

Parton-Based Gribov-Regge Theory

H.J. Drescher¹, M. Hladik^{1,3}, S. Ostapchenko^{2,1}, T. Pierog¹,
and K. Werner¹

¹ *SUBATECH, Université de Nantes – IN2P3/CNRS – EMN, Nantes, France*

² *Moscow State University, Institute of Nuclear Physics, Moscow, Russia*

³ *now at SAP AG, Berlin, Germany*

November 26, 2024

Abstract

We present a new parton model approach for hadron-hadron interactions and, in particular, for the initial stage of nuclear collisions at very high energies (RHIC, LHC and beyond). The most important aspect of our approach is a self-consistent treatment, using the same formalism for calculating cross sections and particle production, based on an effective, QCD-inspired field theory, where many of the inconsistencies of presently used models will be avoided.

In addition, we provide a unified treatment of soft and hard scattering, such that there is no fundamental cutoff parameter any more defining an artificial border between soft and hard scattering.

Our approach cures some of the main deficiencies of two of the standard procedures currently used: the Gribov-Regge theory and the eikonalized parton model. There, cross section calculations and particle production cannot be treated in a consistent way using a common formalism. In particular, energy conservation is taken care of in case of particle production, but not concerning cross section calculations. In addition, hard contributions depend crucially on some cutoff, being divergent for the cutoff being zero. Finally, in case of several elementary scatterings, they are not treated on the same level: the first collision is always treated differently than the subsequent ones. All these problems are solved in our new approach.

For testing purposes, we make very detailed studies of electron-positron annihilation and lepton-nucleon scattering before applying our approach to proton-proton and nucleus-nucleus collisions.

In order to keep a clean picture, we do not consider secondary interactions. We provide a very transparent extrapolation of the physics of more elementary interactions towards nucleus-nucleus scattering, without considering any nuclear effects due to final state interactions. In this sense we consider our model a realistic and consistent approach to describe the initial stage of nuclear collisions.

Contents

1	Introduction	7
1.1	Present Status	8
1.2	Parton-based Gribov-Regge Theory	10
2	The Formalism	13
2.1	Profile Functions	13
2.2	Parton-Parton Scattering	14
2.3	Hadron-Hadron Scattering	19
2.4	Nucleus-Nucleus Scattering	23
2.5	Diffractive Scattering	27
2.6	AGK Cancelations in Hadron-Hadron Scattering	27
2.7	AGK Cancelations in Nucleus-Nucleus Scattering	28
2.8	Outlook	29
3	Virtual Emissions	31
3.1	Parameterizing the Elementary Interaction	31
3.2	Calculating Φ for proton-proton collisions	34
3.3	Unitarity Problems	35
3.4	A Phenomenological Solution: Unitarization of Φ	37
3.5	Properties of the Unitarized Theory	40
3.6	Comparison with the Conventional Approach	44
3.7	Unitarization for Nucleus-Nucleus Scattering	46
3.8	Profile Functions in Nucleus-Nucleus Scattering	47
3.9	Inclusive Cross Sections in Nucleus-Nucleus Scattering	48
4	Markov Chain Techniques	51
4.1	Probability Distributions for Configurations	51
4.2	The Interaction Matrix	52
4.3	The Markov Chain Method	54
4.4	Convergence	55
4.5	Some Tests for Proton-Proton Scattering	57
5	Enhanced Pomeron diagrams	61
5.1	Calculating lowest order enhanced diagrams	62
5.2	Cutting Enhanced Diagrams	66
5.3	Important Features of Enhanced Diagrams	69
6	Parton Configurations	73
6.1	General Procedure of Parton Generation	73
6.2	Generating the Parton Ladder	75
6.3	The Time-like Parton Cascade	77

7	Hadronization	81
7.1	Hadronic Structure of Cut Pomerons	81
7.2	Lagrange Formalism for Strings	87
7.3	Identifying Partons and Kinks	88
7.4	Momentum Bands in Parameter Space	90
7.5	Area Law	91
7.6	Generating Break Points	92
7.7	From String Fragments to Hadrons	96
7.8	Transverse Momentum	100
7.9	The Fragmentation Algorithm	101
8	Parameters	103
8.1	Hadronization	103
8.2	Time-Like Cascade	104
8.3	Parton-Parton Scattering	106
8.4	Hadron-Hadron Scattering	106
9	Testing Time-like Cascade and Hadronization: Electron-Positron Annihilation	109
9.1	The Basic Diagram	110
9.2	The Time-like Parton Cascade and String Formation	111
9.3	Event Shape Variables	112
9.4	The Charged Particle Distributions	117
9.5	Identified Particles	124
9.6	Jet Rates	129
10	Testing the Semi-hard Pomeron: Photon-Proton Scattering	131
10.1	Kinematics	132
10.2	Cross Sections	133
10.3	Parton Momentum Distributions	135
10.4	The Structure Function F_2	139
10.5	Parton Configurations: Basic Formulas	142
10.6	Generating Initial Conditions for the Perturbative Evolution	145
10.7	Generating the Ladder Partons	147
10.8	Hadron Production	150
10.9	Results	151
11	Results for Proton-Proton Scattering	159
11.1	Energy dependence	159
11.2	Charged Particle and Pion Spectra	161
11.3	Proton spectra	164
11.4	Strange particle spectra	166
12	Results for Collisions Involving Nuclei	167
12.1	Proton-Nucleus Scattering	167
12.2	Nucleus-Nucleus Scattering	171
13	Summary	179
A	Kinematics of Two Body Collisions	181
A.1	Conventions	181
A.2	Proof of the Impossibility of Longitudinal Excitations	181

B Partonic Interaction Amplitudes	183
B.1 Semi-hard Parton-Parton Scattering	183
B.2 Parton Evolution	187
B.3 Time-Like Parton Splitting	188
C Hadron-Hadron Amplitudes	191
C.1 Neglecting Valence Quark Scatterings	191
C.2 Including Valence Quark Hard Scatterings	194
C.3 Enhanced Diagrams	196
C.4 Parton Generation for Triple-Pomeron Diagrams	199
D Calculation of Φ and H	201
D.1 Calculation of Φ_{pp}	201
D.2 Calculation of H	203
D.3 Calculation of Φ_{AB}	206
D.4 Exponentiation of Φ_{AB}	208

Chapter 1

Introduction

The purpose of this paper is to provide the theoretical framework to treat hadron-hadron scattering and the **initial stage of nucleus-nucleus collisions** at ultra-relativistic energies, in particular with view to RHIC and LHC. The knowledge of these initial collisions is crucial for any theoretical treatment of a possible parton-hadron phase transition, the detection of which being the ultimate aim of all the efforts of colliding heavy ions at very high energies.

It is quite clear that coherence is crucial for the very early stage of nuclear collisions, so a real quantum mechanical treatment is necessary and any attempt to use a **transport theoretical parton approach** with incoherent quasi-classical partons should not be considered at this point. Also **semi-classical hadronic cascades** cannot be stretched to account for the very first interactions, even when this is considered to amount to a string excitation, since it is well known [1] that such longitudinal excitation is simply kinematically impossible (see appendix A.2). There is also the very unpleasant feature of having to treat formation times of leading and non-leading particles very different. Otherwise, due to a large gamma factor, it would be impossible for a leading particle to undergo multiple collisions.

So what are the currently used fully quantum mechanical approaches? There are presently considerable efforts to describe nuclear collisions via solving **classical Yang-Mills equations**, which allows to calculate inclusive parton distributions [2]. This approach is to some extent orthogonal to ours: here, screening is due to perturbative processes, whereas we claim to have good reasons to consider soft processes to be at the origin of screening corrections.

Provided factorization works for nuclear collisions, one may employ the **parton model**, which allows to calculate inclusive cross sections as a convolution of an elementary cross section with parton distribution functions, with these distribution function taken from deep inelastic scattering. In order to get exclusive parton level cross sections, some additional assumptions are needed, as discussed later.

Another approach is the so-called **Gribov-Regge theory** [3]. This is an effective field theory, which allows multiple interactions to happen “in parallel”, with the phenomenological object called “Pomeron” representing an elementary interaction. Using the general rules of field theory, one may express cross sections in terms of a couple of parameters characterizing the Pomeron. Interference terms are crucial, they assure the unitarity of the theory. A disadvantage is the fact that cross sections and particle production are not calculated consistently: the fact that energy needs to be shared between many Pomerons in case of multiple scattering is well taken into account when calculating particle production (in particular in Monte Carlo applications), but energy conservation is not taken care of for cross section calculations. This is a serious problem and makes the whole approach inconsistent. Also a problem is the question of how to include in a consistent way hard processes, which are usually treated in the parton model approach. Another unpleasant feature is the fact that different elementary interactions in case of multiple scattering are usually not treated equally, so the first interaction is usually considered to be quite different compared to the

subsequent ones.

Here, we present a new approach which we call “**Parton-based Gribov-Regge Theory**”, where we solve some of the above-mentioned problems: we have a consistent treatment for calculating cross sections and particle production considering energy conservation in both cases; we introduce hard processes in a natural way, and, compared to the parton model, we can deal with exclusive cross sections without arbitrary assumptions. A single set of parameters is sufficient to fit many basic spectra in proton-proton and lepton-nucleon scattering, as well as for electron-positron annihilation (with the exception of one parameter which needs to be changed in order to optimize electron-positron transverse momentum spectra).

The basic guideline of our approach is theoretical consistency. We cannot derive everything from first principles, but we use rigorously the language of field theory to make sure not to violate basic laws of physics, which is easily done in more phenomenological treatments (see discussion above).

There are still problems and open questions: there is clearly a problem with unitarity at very high energies, which should be cured by considering screening corrections due to so-called triple-Pomeron interactions, which we do not treat rigorously at present but which is our next project.

1.1 Present Status

Before presenting new theoretical ideas, we want to discuss a little bit more in detail the present status and, in particular, the open problems in the parton model approach and in Gribov-Regge theory.

Gribov-Regge Theory

Gribov-Regge theory is by construction a multiple scattering theory. The elementary interactions are realized by complex objects called “Pomerons”, whose precise nature is not known, and which are therefore simply parameterized: the elastic amplitude T corresponding to a single Pomeron exchange is given as

$$T(s, t) \sim i s^{\alpha_0 + \alpha' t} \quad (1.1)$$

with a couple of parameters to be determined by experiment. Even in hadron-hadron scattering, several of these Pomerons are exchanged in parallel, see fig. 1.1. Using general rules of field theory

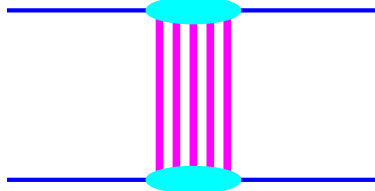


Figure 1.1: Hadron-hadron scattering in GRT. The thick lines between the hadrons (incoming lines) represent a Pomeron each. The different Pomeron exchanges occur in parallel.

(cutting rules), one obtains an expression for the inelastic cross section,

$$\sigma_{\text{inel}}^{h_1 h_2} = \int d^2 b \{1 - \exp(-G(s, b))\}, \quad (1.2)$$

where the so-called eikonal $G(s, b)$ (proportional to the Fourier transform of $T(s, t)$) represents one elementary interaction (a thick line in fig. 1.1). One can generalize to nucleus-nucleus collisions, where corresponding formulas for cross sections may be derived.

In order to calculate exclusive particle production, one needs to know how to share the energy between the individual elementary interactions in case of multiple scattering. We do not want to discuss the different recipes used to do the energy sharing (in particular in Monte Carlo applications). The point is, whatever procedure is used, this is not taken into account in calculation of cross sections discussed above. So, actually, one is using two different models for cross section calculations and for treating particle production. Taking energy conservation into account in exactly the same way will modify the cross section results considerably, as we are going to demonstrate later.

This problem has first been discussed in [4], [5]. The authors claim that following from the non-planar structure of the corresponding diagrams, conserving energy and momentum in a consistent way is crucial, and therefore the incident energy has to be shared between the different elementary interactions, both real and virtual ones.

Another very unpleasant and unsatisfactory feature of most “recipes” for particle production is the fact, that the second Pomeron and the subsequent ones are treated differently than the first one, although in the above-mentioned formula for the cross section all Pomerons are considered to be identical.

The Parton Model

The standard parton model approach to hadron-hadron or also nucleus-nucleus scattering amounts to presenting the partons of projectile and target by momentum distribution functions, f_{h_1} and f_{h_2} , and calculating inclusive cross sections for the production of parton jets with the squared transverse momentum p_\perp^2 larger than some cutoff Q_0^2 as

$$\sigma_{\text{incl}}^{h_1 h_2} = \sum_{ij} \int dp_\perp^2 \int dx^+ \int dx^- f_{h_1}^i(x^+, p_\perp^2) f_{h_2}^j(x^-, p_\perp^2) \frac{d\hat{\sigma}_{ij}}{dp_\perp^2}(x^+ x^- s) \theta(p_\perp^2 - Q_0^2), \quad (1.3)$$

where $d\hat{\sigma}_{ij}/dp_\perp^2$ is the elementary parton-parton cross section and i, j represent parton flavors.

This simple factorization formula is the result of cancelations of complicated diagrams (AGK cancelations) and hides therefore the complicated multiple scattering structure of the reaction. The most obvious manifestation of such a structure is the fact that at high energies ($\sqrt{s} \gg 10$ GeV) the inclusive cross section in proton-(anti)proton scattering exceeds the total one, so the average number $\bar{N}_{\text{int}}^{pp}$ of elementary interactions must be bigger than one:

$$\bar{N}_{\text{int}}^{h_1 h_2} = \sigma_{\text{incl}}^{h_1 h_2} / \sigma_{\text{tot}}^{h_1 h_2} > 1 \quad (1.4)$$

The usual solution is the so-called eikonalization, which amounts to re-introducing multiple scattering, based on the above formula for the inclusive cross section:

$$\sigma_{\text{incl}}^{h_1 h_2}(s) = \int d^2b \left\{ 1 - \exp \left(-A(b) \sigma_{\text{incl}}^{h_1 h_2}(s) \right) \right\} = \sum \sigma_m^{h_1 h_2}(s), \quad (1.5)$$

with

$$\sigma_m^{h_1 h_2}(s) = \int d^2b \frac{\left(A(b) \sigma_{\text{incl}}^{h_1 h_2}(s) \right)^m}{m!} \exp \left(-A(b) \sigma_{\text{incl}}^{h_1 h_2}(s) \right) \quad (1.6)$$

representing the cross section for m scatterings; $A(b)$ being the proton-proton overlap function (the convolution of the two proton profiles). In this way the multiple scattering is “recovered”. The disadvantage is that this method does not provide any clue how to proceed for nucleus-nucleus (AB) collisions. One usually assumes the proton-proton cross section for each individual nucleon-nucleon pair of a AB system. We are going to demonstrate that this assumption is incorrect.

Another problem, in fact the same one as discussed earlier for the GRT, arises in case of exclusive calculations (event generation), since the above formulas do not provide any information on how

to share the energy between the many elementary interactions. The Pythia-method [6] amounts to generating the first elementary interaction according to the inclusive differential cross section, then taking the remaining energy for the second one and so on. In this way, the event generation will reproduce the theoretical inclusive spectrum for hadron-hadron interaction (by construction), as it should be. The method is, however, very arbitrary, and is certainly not a convincing procedure for the multiple scattering aspects of the collisions.

1.2 Parton-based Gribov-Regge Theory

In this paper, we present a new approach for hadronic interactions and for the initial stage of nuclear collisions, which is able to solve several of the above-mentioned problems. We provide a rigorous treatment of the multiple scattering aspect, such that questions as energy conservation are clearly determined by the rules of the field theory, both for cross section and particle production calculations. In both (!) cases, energy is properly shared between the different interactions happening in parallel, see fig. 1.2. for proton-proton and fig. 1.3 for proton-nucleus collisions

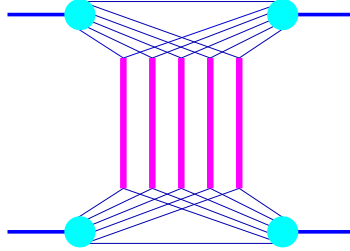


Figure 1.2: Graphical representation of a contribution to the elastic amplitude of proton-proton scattering. Here, energy conservation is taken into account: the energy of the incoming protons is shared among several “constituents” (shown by splitting the nucleon lines into several constituent lines), and so each Pomeron disposed only a fraction of the total energy, such that the total energy is conserved.

(generalization to nucleus-nucleus is obvious). This is the most important and new aspect of our

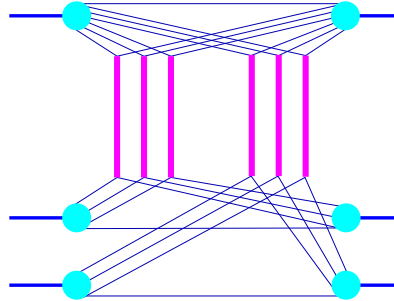


Figure 1.3: Graphical representation of a contribution to the elastic amplitude of proton-nucleus scattering, or more precisely a proton interacting with (for simplicity) two target nucleons, taking into account energy conservation. Here, the energy of the incoming proton is shared between all the constituents, which now provide the energy for interacting with two target nucleons.

approach, which we consider to be a first necessary step to construct a consistent model for high energy nuclear scattering.

The elementary interactions, shown as the thick lines in the above figures, are in fact a sum of a soft, a hard, and a semi-hard contribution, providing a consistent treatment of soft and hard scattering. To some extent, our approach provides a link between the Gribov-Regge approach and the parton model, we call it “Parton-based Gribov-Regge Theory”.

There are still many problems to be solved: as we are going to show later, a rigorous treatment of energy conservation will lead to unitarity problems (increasingly severe with increasing energy), which is nothing but a manifestation of the fact that screening corrections will be increasingly important. In this paper we will employ a “unitarization procedure” to solve this problem, but this is certainly not the final answer. The next step should be a consistent approach, taking into account both energy conservation and screening corrections due to multi-Pomeron interactions.

Our approach is realized as the Monte Carlo code NEXUS, which is nothing but the direct implementation of the formalism described in this paper. All our numerical results are calculated with NEXUS version 2.00.

Chapter 2

The Formalism

We want to calculate cross sections and particle production in a consistent way, in both cases based on the same formalism, with energy conservation being ensured. The formalism operates with Feynman diagrams of the QCD-inspired effective field theory, such that calculations follow the general rules of the field theory. A graphical representation of a contribution to the elastic amplitude of nucleus-nucleus scattering (related to particle production via the optical theorem) is shown in fig. 2.1: here the nucleons are split into several “constituents”, each one carrying a frac-

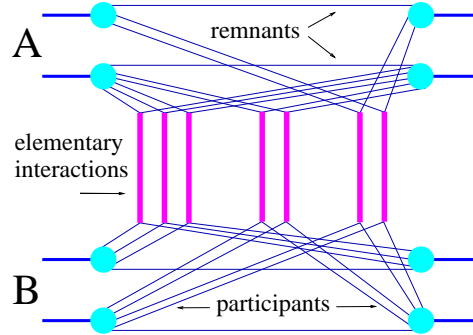


Figure 2.1: A contribution to the elastic amplitude of a nucleus-nucleus collision, or more precisely two nucleons from projectile A interacting with two nucleons from target B , taking into account energy conservation. The energy of the incoming nucleons is shared between all the constituents.

tion of the incident momentum, such that the sum of the momentum fractions is one (momentum conservation). Per nucleon there are one or several “participants” and exactly one “spectator” or “remnant”, where the former ones interact with constituents from the other side via some “elementary interaction” (vertical lines in the figure 2.1). The remnant is just all the rest, i.e. the nucleon minus the participants.

After a technical remark concerning profile functions, we are going to discuss parton-parton scattering, before we develop the multiple scattering theory for hadron-hadron and nucleus-nucleus scattering.

2.1 Profile Functions

Profile functions play a fundamental role in our formalism, so we briefly sketch their definition and physical meaning.

Let T be the elastic scattering amplitude T for the two-body scattering depicted in fig.2.2. The 4-momenta p and p' are the ones for the incoming particles, $\tilde{p} = p + q$ and $\tilde{p}' = p' - q$ the ones

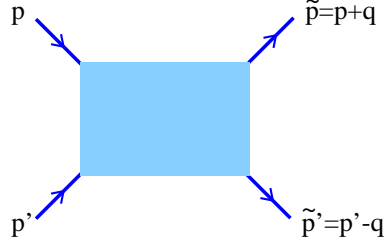


Figure 2.2: The general elastic scattering amplitude T .

for the outgoing particles, and q the 4-momentum transfer in the process. We define as usual the Mandelstam variables s and t (see appendix A.1). Using the optical theorem, we may write the total cross section as

$$\sigma_{\text{tot}}(s) = \frac{1}{2s} 2\text{Im} T(s, t=0). \quad (2.1)$$

We define the Fourier transform \tilde{T} of T as

$$\tilde{T}(s, b) = \frac{1}{4\pi^2} \int d^2 q_{\perp} e^{-i\vec{q}_{\perp} \vec{b}} T(s, t), \quad (2.2)$$

using $t = -q_{\perp}^2$ (see appendix A.2), and a so-called “profile function” $G(s, b)$ as

$$G(s, b) = \frac{1}{2s} 2\text{Im} \tilde{T}(s, b). \quad (2.3)$$

One can easily verify that

$$\sigma_{\text{tot}}(s) = \int d^2 b G(s, b), \quad (2.4)$$

which allows an interpretation of $G(s, b)$ to be the probability of an interaction at impact parameter b .

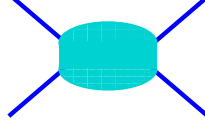
In the following, we are working with partonic, hadronic, and even nuclear profile functions. The central result to be derived in the following sections is the fact that hadronic and also nuclear profile functions can be expressed in terms of partonic ones, allowing a clean formulation of a multiple scattering theory.

2.2 Parton-Parton Scattering

We distinguish three types of elementary parton-parton scatterings, referred to as “soft”, “hard” and “semi-hard”, which we are going to discuss briefly in the following. The detailed derivations can be found in appendix B.1.

The Soft Contribution

Let us first consider the pure non-perturbative contribution to the process of the fig. 2.2, where all virtual partons appearing in the internal structure of the diagram have restricted virtualities $Q^2 < Q_0^2$, where $Q_0^2 \sim 1 \text{ GeV}^2$ is a reasonable cutoff for perturbative QCD being applicable. Such soft non-perturbative dynamics is known to dominate hadron-hadron interactions at not too high energies. Lacking methods to calculate this contribution from first principles, it is simply parameterized and graphically represented as a ‘blob’, see fig. 2.3. It is traditionally assumed to

**Figure 2.3:** The soft contribution.

correspond to multi-peripheral production of partons (and final hadrons) [7] and is described by the phenomenological soft Pomeron exchange contribution [3]:

$$T_{\text{soft}}(\hat{s}, t) = 8\pi s_0 \eta(t) \gamma_{\text{part}}^2 \left(\frac{\hat{s}}{s_0} \right)^{\alpha_{\text{soft}}(0)} \exp\left(\lambda_{\text{soft}}^{(2)}(\hat{s}/s_0) t\right), \quad (2.5)$$

with

$$\lambda_{\text{soft}}^{(n)}(z) = n R_{\text{part}}^2 + \alpha'_{\text{soft}} \ln z, \quad (2.6)$$

where $\hat{s} = (p + p')^2$. The parameters $\alpha_{\text{soft}}(0)$, α'_{soft} are the intercept and the slope of the Pomeron trajectory, γ_{part} and R_{part}^2 are the vertex value and the slope for the Pomeron-parton coupling, and $s_0 \simeq 1 \text{ GeV}^2$ is the characteristic hadronic mass scale. The so-called signature factor η is given as

$$\eta(t) = i - \cot \frac{\pi \alpha_P(t)}{2} \simeq i. \quad (2.7)$$

Cutting the diagram of the fig. 2.3 corresponds to the summation over multi-peripheral intermediate hadronic states, connected via unitarity to the imaginary part of the amplitude (2.5),

$$\frac{1}{i} \text{disc}_{\hat{s}} T_{\text{soft}}(\hat{s}, t) = \frac{1}{i} [T_{\text{soft}}(\hat{s} + i0, t) - T_{\text{soft}}(\hat{s} - i0, t)] \quad (2.8)$$

$$= 2\text{Im} T_{\text{soft}}(\hat{s}, t) \quad (2.9)$$

$$= \sum_{n, \text{spins}, \dots} \int d\tau_n T_{p, p' \rightarrow X_n} T_{\bar{p}, \bar{p}' \rightarrow X_n}^*, \quad (2.10)$$

where $T_{p, p' \rightarrow X_n}$ is the amplitude for the transition of the initial partons p, p' into the n -particle state X_n , $d\tau_n$ is the invariant phase space volume for the n -particle state X_n and the summation is done over the number of particles n and over their spins and species, the averaging over initial parton colors and spins is assumed; $\text{disc}_{\hat{s}} T_{\text{soft}}(\hat{s}, t)$ denotes the discontinuity of the amplitude $T_{\text{soft}}(\hat{s}, t)$ on the right-hand cut in the variable \hat{s} .

For $t = 0$ one obtains via the optical theorem the contribution σ_{soft} of the soft Pomeron exchange to the total parton interaction cross section,

$$\sigma_{\text{soft}}(\hat{s}) = \frac{1}{2\hat{s}} 2\text{Im} T_{\text{soft}}(\hat{s}, 0) = 8\pi \gamma_{\text{part}}^2 \left(\frac{\hat{s}}{s_0} \right)^{\alpha_{\text{soft}}(0)-1}, \quad (2.11)$$

where $2\hat{s}$ defines the initial parton flux.

The corresponding profile function for parton-parton interaction is expressed via the Fourier transform \tilde{T} of T divided by the flux $2s$,

$$D_{\text{soft}}(\hat{s}, b) = \frac{1}{2\hat{s}} 2\text{Im} \tilde{T}_{\text{soft}}(\hat{s}, b), \quad (2.12)$$

which gives

$$D_{\text{soft}}(\hat{s}, b) = \frac{1}{8\pi^2 \hat{s}} \int d^2 q_{\perp} \exp(-i \vec{q}_{\perp} \vec{b}) 2\text{Im} T_{\text{soft}}(\hat{s}, -q_{\perp}^2) \quad (2.13)$$

$$= \frac{2\gamma_{\text{part}}^2}{\lambda_{\text{soft}}^{(2)}(\hat{s}/s_0)} \left(\frac{\hat{s}}{s_0}\right)^{\alpha_{\text{soft}}(0)-1} \exp\left(-\frac{b^2}{4\lambda_{\text{soft}}^{(2)}(\hat{s}/s_0)}\right). \quad (2.14)$$

The external legs of the diagram of fig. 2.3 are ‘partonic constituents’, which are assumed to be quark-antiquark pairs.

The Hard Contribution

Let us now consider the other extreme, when all the processes in the ‘box’ of the fig. 2.2 are perturbative, i.e. all internal intermediate partons are characterized by large virtualities $Q^2 > Q_0^2$. In that case, the corresponding hard parton-parton scattering amplitude $T_{\text{hard}}^{jk}(\hat{s}, t)$ (j, k denote the types (flavors) of the initial partons) can be calculated using the perturbative QCD techniques [8, 9], and the intermediate states contributing to the absorptive part of the amplitude of the fig. 2.2 can be defined in the parton basis. In the leading logarithmic approximation of QCD, summing up terms where each (small) running QCD coupling constant $\alpha_s(Q^2)$ appears together with a large logarithm $\ln(Q^2/\lambda_{\text{QCD}}^2)$ (with λ_{QCD} being the infrared QCD scale), and making use of the factorization hypothesis, one obtains the contribution of the corresponding cut diagram for $t = q^2 = 0$ as the cut parton ladder cross section $\sigma_{\text{hard}}^{jk}(\hat{s}, Q_0^2)$ ¹, which will correspond to the cut diagram of fig. 2.4, where all horizontal rungs are the final (on-shell) partons and the virtualities of

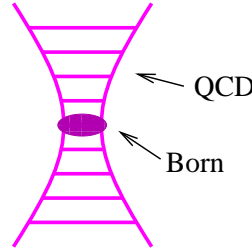


Figure 2.4: The hard (or val-val) contribution.

the virtual t -channel partons increase from the ends of the ladder towards the largest momentum transfer parton-parton process (indicated symbolically by the ‘blob’ in the middle of the ladder):

$$\begin{aligned} \sigma_{\text{hard}}^{jk}(\hat{s}, Q_0^2) &= \frac{1}{2\hat{s}} 2\text{Im} T_{\text{hard}}^{jk}(\hat{s}, t=0) \\ &= K \sum_{ml} \int dx_B^+ dx_B^- dp_{\perp}^2 \frac{d\sigma_{\text{Born}}^{ml}}{dp_{\perp}^2}(x_B^+ x_B^- \hat{s}, p_{\perp}^2) \\ &\times E_{\text{QCD}}^{jm}(x_B^+, Q_0^2, M_F^2) E_{\text{QCD}}^{kl}(x_B^-, Q_0^2, M_F^2) \theta(M_F^2 - Q_0^2), \end{aligned} \quad (2.15)$$

Here $d\sigma_{\text{Born}}^{ml}/dp_{\perp}^2$ is the differential $2 \rightarrow 2$ parton scattering cross section, p_{\perp}^2 is the parton transverse momentum in the hard process, m, l and x_B^{\pm} are correspondingly the types and the shares of the light cone momenta of the partons participating in the hard process, and M_F^2 is the factorization scale for the process (we use $M_F^2 = p_{\perp}^2/4$). The ‘evolution function’ $E_{\text{QCD}}^{jm}(Q_0^2, M_F^2, z)$ represents the evolution of a parton cascade from the scale Q_0^2 to M_F^2 , i.e. it gives the number density of

¹ Strictly speaking, one obtains the ladder representation for the process only using axial gauge.

partons of type m with the momentum share z at the virtuality scale M_F^2 , resulted from the evolution of the initial parton j , taken at the virtuality scale Q_0^2 . The evolution function satisfies the usual DGLAP equation [10] with the initial condition $E_{\text{QCD}}^{jm}(Q_0^2, Q_0^2, z) = \delta_m^j \delta(1-z)$, as discussed in detail in appendix B.3. The factor $K \simeq 1.5$ takes effectively into account higher order QCD corrections.

In the following we shall need to know the contribution of the uncut parton ladder $T_{\text{hard}}^{jk}(\hat{s}, t)$ with some momentum transfer q along the ladder (with $t = q^2$). The behavior of the corresponding amplitudes was studied in [11] in the leading logarithmic ($1/x$) approximation of QCD. The precise form of the corresponding amplitude is not important for our application; we just use some of the results of [11], namely that one can neglect the real part of this amplitude and that it is nearly independent on t , i.e. that the slope of the hard interaction R_{hard}^2 is negligible small, i.e. compared to the soft Pomeron slope one has $R_{\text{hard}}^2 \simeq 0$. So we parameterize $T_{\text{hard}}^{jk}(\hat{s}, t)$ in the region of small t as [12]

$$T_{\text{hard}}^{jk}(\hat{s}, t) = i\hat{s} \sigma_{\text{hard}}^{jk}(\hat{s}, Q_0^2) \exp(R_{\text{hard}}^2 t) \quad (2.16)$$

The corresponding profile function is obtained by calculating the Fourier transform \tilde{T}_{hard} of T_{hard} and dividing by the initial parton flux $2\hat{s}$,

$$D_{\text{hard}}^{jk}(\hat{s}, b) = \frac{1}{2\hat{s}} 2\text{Im} \tilde{T}_{\text{hard}}^{jk}(\hat{s}, b), \quad (2.17)$$

which gives

$$\begin{aligned} D_{\text{hard}}^{jk}(\hat{s}, b) &= \frac{1}{8\pi^2 \hat{s}} \int d^2 q_{\perp} \exp(-i\vec{q}_{\perp} \vec{b}) 2\text{Im} T_{\text{hard}}^{jk}(\hat{s}, -q_{\perp}^2) \\ &= \sigma_{\text{hard}}^{jk}(\hat{s}, Q_0^2) \frac{1}{4\pi R_{\text{hard}}^2} \exp\left(-\frac{b^2}{4R_{\text{hard}}^2}\right), \end{aligned} \quad (2.18)$$

In fact, the above considerations are only correct for valence quarks, as discussed in detail in the next section. Therefore, we also talk about “valence-valence” contribution and we use $D_{\text{val-val}}$ instead of D_{hard} :

$$D_{\text{val-val}}^{jk}(\hat{s}, b) \equiv D_{\text{hard}}^{jk}(\hat{s}, b), \quad (2.19)$$

so these are two names for one and the same object.

The Semi-hard Contribution

The discussion of the preceding section is not valid in case of sea quarks and gluons, since here the momentum share x_1 of the “first” parton is typically very small, leading to an object with a large mass of the order Q_0^2/x_1 between the parton and the proton [13]. Microscopically, such ‘slow’ partons with $x_1 \ll 1$ appear as a result of a long non-perturbative parton cascade, where each individual parton branching is characterized by a small momentum transfer squared $Q^2 < Q_0^2$ and nearly equal partition of the parent parton light cone momentum [7, 14]. When calculating proton structure functions or high- p_t jet production cross sections that non-perturbative contribution is usually included into parameterized initial parton momentum distributions at $Q^2 = Q_0^2$. However, the description of inelastic hadronic interactions requires to treat it explicitly in order to account for secondary particles produced during such non-perturbative parton pre-evolution, and to describe correctly energy-momentum sharing between multiple elementary scatterings. As the underlying dynamics appears to be identical to the one of soft parton-parton scattering considered above, we treat this soft pre-evolution as the usual soft Pomeron emission, as discussed in detail in appendix B.1.

So for sea quarks and gluons, we consider so-called semi-hard interactions between parton constituents of initial hadrons, represented by a parton ladder with “soft ends”, see fig. 2.5. As in

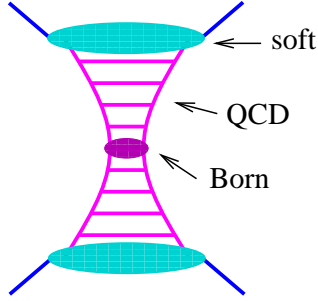


Figure 2.5: The semi-hard “sea-sea” contribution: parton ladder plus “soft ends”.

case of soft scattering, the external legs are quark-antiquark pairs, connected to soft Pomerons. The outer partons of the ladder are on both sides sea quarks or gluons (therefore the index “sea-sea”). The central part is exactly the hard scattering considered in the preceding section. As discussed in length in the appendix B.1, the mathematical expression for the corresponding amplitude is given as

$$iT_{\text{sea-sea}}(\hat{s}, t) = \sum_{jk} \int_0^1 \frac{dz^+}{z^+} \frac{dz^-}{z^-} \text{Im} T_{\text{soft}}^j\left(\frac{s_0}{z^+}, t\right) \text{Im} T_{\text{soft}}^k\left(\frac{s_0}{z^-}, t\right) iT_{\text{hard}}^{jk}(z^+ z^- \hat{s}, t), \quad (2.20)$$

with z^\pm being the momentum fraction of the external leg-partons of the parton ladder relative to the momenta of the initial (constituent) partons. The indices j and k refer to the flavor of these external ladder partons. The amplitudes T_{soft}^j are the soft Pomeron amplitudes discussed earlier, but with modified couplings, since the Pomerons are now connected to the ladder on one side. The arguments s_0/z^\pm are the squared masses of the two soft Pomerons, $z^+ z^- \hat{s}$ is the squared mass of the hard piece.

Performing as usual the Fourier transform to the impact parameter representation and dividing by $2\hat{s}$, we obtain the profile function

$$D_{\text{sea-sea}}(\hat{s}, b) = \frac{1}{2\hat{s}} 2\text{Im} \tilde{T}_{\text{sea-sea}}(\hat{s}, b), \quad (2.21)$$

which may be written as

$$D_{\text{sea-sea}}(\hat{s}, b) = \sum_{jk} \int_0^1 dz^+ dz^- E_{\text{soft}}^j(z^+) E_{\text{soft}}^k(z^-) \sigma_{\text{hard}}^{jk}(z^+ z^- \hat{s}, Q_0^2) \times \frac{1}{4\pi \lambda_{\text{soft}}^{(2)}(1/(z^+ z^-))} \exp\left(-\frac{b^2}{4\lambda_{\text{soft}}^{(2)}(1/(z^+ z^-))}\right) \quad (2.22)$$

with the soft Pomeron slope $\lambda_{\text{soft}}^{(2)}$ and the cross section $\sigma_{\text{hard}}^{jk}$ being defined earlier. The functions $E_{\text{soft}}^j(z^\pm)$ representing the “soft ends” are defined as

$$E_{\text{soft}}^j(z^\pm) = \text{Im} T_{\text{soft}}^j\left(\frac{s_0}{z^\pm}, t=0\right), \quad (2.23)$$

or explicitly

$$E_{\text{soft}}^g(z) = 8\pi s_0 \gamma_{\text{part}} \gamma_g z^{-\alpha_{\text{soft}}(0)} (1-z)^{\beta_g}, \quad (2.24)$$

$$E_{\text{soft}}^q(z) = \gamma_{qg} \int_z^1 d\xi P_g^q(\xi) E_{\text{soft}}^g\left(\frac{z}{\xi}\right), \quad (2.25)$$

with

$$\gamma_{qg}\gamma_g = w_{\text{split}} \tilde{\gamma}_g, \quad \gamma_g = (1 - w_{\text{split}}) \tilde{\gamma}_g, \quad (2.26)$$

and

$$\tilde{\gamma}_g = \frac{1}{8\pi s_0 \gamma_{\text{part}}} \frac{\Gamma(3 - \alpha_{\text{soft}}(0) + \beta_g)}{\Gamma(2 - \alpha_{\text{soft}}(0)) \Gamma(1 + \beta_g)} \quad (2.27)$$

(see appendix B.1). We neglected the small hard scattering slope R_{hard}^2 compared to the Pomeron slope $\lambda_{\text{soft}}^{(2)}$. We call E_{soft} also the “soft evolution”, to indicate that we consider this as simply a continuation of the QCD evolution, however, in a region where perturbative techniques do not apply any more. As discussed in the appendix B.1, $E_{\text{soft}}^j(z)$ has the meaning of the momentum distribution of parton j in the soft Pomeron.

Consistency requires to also consider the mixed semi-hard contributions with a valence quark on one side and a non-valence participant (quark-antiquark pair) on the other one, see fig. 2.6.

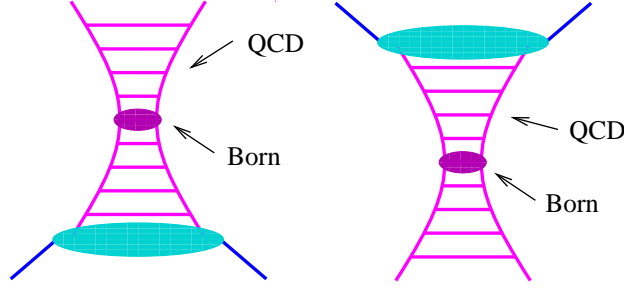


Figure 2.6: Two “mixed” contributions.

We have

$$iT_{\text{val-sea}}^j(\hat{s}, t) = \int_0^1 \frac{dz^-}{z^-} \sum_k \text{Im} T_{\text{soft}}^k\left(\frac{s_0}{z^-}, t\right) iT_{\text{hard}}^{jk}(z^-, \hat{s}, t) \quad (2.28)$$

and

$$D_{\text{val-sea}}^j(\hat{s}, b) = \sum_k \int_0^1 dz^- E_{\text{soft}}^k(z^-) \sigma_{\text{hard}}^{jk}(z^-, \hat{s}, Q_0^2) \times \frac{1}{4\pi \lambda_{\text{soft}}^{(1)}(1/z^-)} \exp\left(-\frac{b^2}{4\lambda_{\text{soft}}^{(1)}(1/z^-)}\right) \quad (2.29)$$

where j is the flavor of the valence quark at the upper end of the ladder and k is the type of the parton on the lower ladder end. Again, we neglected the hard scattering slope R_{hard}^2 compared to the soft Pomeron slope. A contribution $D_{\text{sea-val}}^j(\hat{s}, b)$, corresponding to a valence quark participant from the target hadron, is given by the same expression,

$$D_{\text{sea-val}}^j(\hat{s}, b) = D_{\text{val-sea}}^j(\hat{s}, b), \quad (2.30)$$

since eq. (2.29) stays unchanged under replacement $z^- \rightarrow z^+$ and only depends on the total c.m. energy squared \hat{s} for the parton-parton system.

2.3 Hadron-Hadron Scattering

Let us now consider hadron-hadron interactions (a more detailed treatment can be found in appendix C). We ignore first contributions involving valence quark scatterings. In the general case,

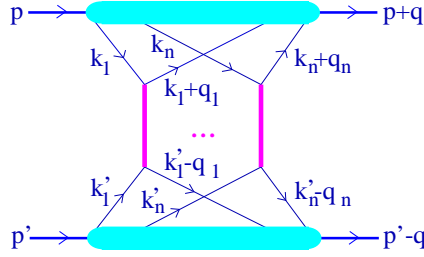


Figure 2.7: Hadron-hadron interaction amplitude.

the expression for the hadron-hadron scattering amplitude includes contributions from multiple scattering between different parton constituents of the initial hadrons, as shown in fig. 2.7, and can be written according to the standard rules [3, 14] as

$$i T_{h_1 h_2}(s, t) = \sum_{n=1}^{\infty} \frac{1}{n!} \int \prod_{l=1}^n \left[\frac{d^4 k_l}{(2\pi)^4} \frac{d^4 k'_l}{(2\pi)^4} \frac{d^4 q_l}{(2\pi)^4} \right] N_{h_1}^{(n)}(p, k_1, \dots, k_n, q_1, \dots, q_n) \quad (2.31)$$

$$\times \prod_{l=1}^n [i T_{1\mathbb{P}}(\hat{s}_l, q_l^2)] N_{h_2}^{(n)}(p', k'_1, \dots, k'_n, -q_1, \dots, -q_n) (2\pi)^4 \delta^{(4)}\left(\sum_{k=1}^n q_k - q\right),$$

with $t = q^2$, $s = (p + p')^2 \simeq p^+ p'^-$, with p, p' being the 4-momenta of the initial hadrons, and with $\hat{s}_l = (k_l + k'_l)^2 \simeq k_l^+ k'^l_-$. $T_{1\mathbb{P}}$ is the sum of partonic one-Pomeron-exchange scattering amplitudes, discussed in the preceding section, $T_{1\mathbb{P}} = T_{\text{soft}} + T_{\text{sea-sea}}$. The momenta k_l, k'_l and q_l denote correspondingly the 4-momenta of the initial partonic constituents (quark-antiquark pairs) for the l -th scattering and the 4-momentum transfer in that partial process. The factor $1/n!$ takes into account the identical nature of the n re-scattering contributions. $N_h^{(n)}(p, k_1, \dots, k_n, q_1, \dots, q_n)$ denotes the contribution of the vertex for n -parton coupling to the hadron h .

As discussed in appendix C, the hadron-hadron amplitude (2.31) may be written as

$$i T_{h_1 h_2}(s, t) = 8\pi^2 s \sum_{n=1}^{\infty} \frac{1}{n!} \int_0^1 \prod_{l=1}^n dx_l^+ dx_l^- \prod_{l=1}^n \left[\frac{1}{8\pi^2 \hat{s}_l} \int d^2 q_{l\perp} i T_{1\mathbb{P}}^{h_1 h_2}(x_l^+, x_l^-, s, -q_{l\perp}^2) \right] \quad (2.32)$$

$$\times F_{\text{remn}}^{h_1} \left(1 - \sum_{j=1}^n x_j^+ \right) F_{\text{remn}}^{h_2} \left(1 - \sum_{j=1}^n x_j^- \right) \delta^{(2)} \left(\sum_{k=1}^n \vec{q}_{k\perp} - \vec{q}_{\perp} \right).$$

(see eq. (C.22)), where the partonic amplitudes are defined as $T_{1\mathbb{P}}^{h_1 h_2} = T_{\text{soft}}^{h_1 h_2} + T_{\text{sea-sea}}^{h_1 h_2}$, with

$$T_{\text{soft/sea-sea}}^{h_1 h_2}(x^+, x^-, s, -q_{\perp}^2) = T_{\text{soft/sea-sea}}(x^+ x^- s, -q_{\perp}^2) F_{\text{part}}^{h_1}(x^+) F_{\text{part}}^{h_2}(x^-) \times \exp(-[R_{h_1}^2 + R_{h_2}^2] q_{\perp}^2) \quad (2.33)$$

representing the contributions of “elementary interactions plus external legs”; the functions $F_{\text{remn}}^h, F_{\text{part}}^h$ are defined in (C.18-C.21) as

$$F_{\text{part}}^h(x) = \gamma_h x^{-\alpha_{\text{part}}}, \quad (2.34)$$

$$F_{\text{remn}}^h(x) = x^{\alpha_{\text{remn}}^h}. \quad (2.35)$$

Formula (2.32) is also correct if one includes valence quarks (see appendix C), if one defines

$$T_{1\mathbb{P}}^{h_1 h_2} = T_{\text{soft}}^{h_1 h_2} + T_{\text{sea-sea}}^{h_1 h_2} + T_{\text{val-val}}^{h_1 h_2} + T_{\text{val-sea}}^{h_1 h_2} + T_{\text{sea-val}}^{h_1 h_2}, \quad (2.36)$$

with the hard contribution

$$T_{\text{val-val}}^{h_1 h_2}(x^+, x^-, s, -q_\perp^2) = \int_0^{x^+} dx_v^+ \frac{x^+}{x_v^+} \int_0^{x^-} dx_v^- \frac{x^-}{x_v^-} \sum_{j,k} T_{\text{hard}}^{jk}(x_v^+ x_v^- s, -q_\perp^2) \quad (2.37)$$

$$\times \bar{F}_{\text{part}}^{h_1, j}(x_v^+, x^+ - x_v^+) \bar{F}_{\text{part}}^{h_2, k}(x_v^-, x^- - x_v^-) \exp(-[R_{h_1}^2 + R_{h_2}^2] q_\perp^2),$$

with the mixed semi-hard “val-sea” contribution

$$T_{\text{val-sea}}^{h_1 h_2}(x^+, x^-, s, -q_\perp^2) = \int_0^{x^+} dx_v^+ \frac{x^+}{x_v^+} \sum_j T_{\text{val-sea}}^j(x_v^+ x^- s, -q_\perp^2) \quad (2.38)$$

$$\times \bar{F}_{\text{part}}^{h_1, j}(x_v^+, x^+ - x_v^+) F_{\text{part}}^{h_2}(x^-) \exp(-[R_{h_1}^2 + R_{h_2}^2] q_\perp^2),$$

and with the contribution “sea-val” obtained from “val-sea” by exchanging variables,

$$T_{\text{sea-val}}^{h_1 h_2}(x^+, x^-, s, -q_\perp^2) = T_{\text{val-sea}}^{h_2 h_1}(x^-, x^+, s, -q_\perp^2).$$

Here, we allow formally any number of valence type interactions (based on the fact that multiple valence type processes give negligible contribution). In the valence contributions, we have convolutions of hard parton scattering amplitudes T_{hard}^{jk} and valence quark distributions \bar{F}_{part}^j over the valence quark momentum share x_v^\pm rather than a simple product, since only the valence quarks are involved in the interactions, with the anti-quarks staying idle (the external legs carrying momenta x^+ and x^- are always quark-antiquark pairs). The functions \bar{F} are given as

$$\bar{F}_{\text{part}}^{h, i}(x_v, x_{\bar{q}}) = N^{-1} q_{\text{val}}^i(x_v, Q_0^2) (1 - x_v)^{\alpha_{\mathbb{R}} - 1 - \alpha_{\text{remn}}} (x_{\bar{q}})^{-\alpha_{\mathbb{R}}}, \quad (2.39)$$

with the normalization factor

$$N = \frac{\Gamma(1 + \alpha_{\text{remn}}) \Gamma(1 - \alpha_{\mathbb{R}})}{\Gamma(2 + \alpha_{\text{remn}} - \alpha_{\mathbb{R}})}, \quad (2.40)$$

where q_{val}^i is a usual valence quark distribution function.

The Fourier transform $\tilde{T}_{h_1 h_2}$ of the amplitude (2.32) is given as

$$\begin{aligned} \frac{i}{2s} \tilde{T}_{h_1 h_2}(s, b) &= \sum_{n=1}^{\infty} \frac{1}{n!} \int_0^1 \prod_{l=1}^n dx_l^+ dx_l^- \prod_{l=1}^n \frac{i}{2\hat{s}_l} \tilde{T}_{1\mathbb{P}}^{h_1 h_2}(x_l^+, x_l^-, s, b) \\ &\times F_{\text{remn}}^{h_1} \left(1 - \sum_{j=1}^n x_j^+ \right) F_{\text{remn}}^{h_2} \left(1 - \sum_{j=1}^n x_j^- \right), \end{aligned} \quad (2.41)$$

with $\tilde{T}_{1\mathbb{P}}^{h_1 h_2}$ being the Fourier transform of $T_{1\mathbb{P}}^{h_1 h_2}$. The profile function γ is as usual defined as

$$\gamma_{h_1 h_2}(s, b) = \frac{1}{2s} 2\text{Im} \tilde{T}_{h_1 h_2}(s, b), \quad (2.42)$$

which may be evaluated using the AGK cutting rules [15],

$$\begin{aligned} \gamma_{h_1 h_2}(s, b) &= \sum_{m=1}^{\infty} \frac{1}{m!} \int_0^1 \prod_{\mu=1}^m dx_\mu^+ dx_\mu^- \prod_{\mu=1}^m \frac{1}{2\hat{s}_\mu} 2\text{Im} \tilde{T}_{1\mathbb{P}}^{h_1 h_2}(x_\mu^+, x_\mu^-, s, b) \\ &\times \sum_{l=0}^{\infty} \frac{1}{l!} \int_0^1 \prod_{\lambda=1}^l d\tilde{x}_\lambda^+ d\tilde{x}_\lambda^- \prod_{\lambda=1}^l \frac{1}{2\hat{s}_\lambda} (-2) \text{Im} \tilde{T}_{1\mathbb{P}}^{h_1 h_2}(\tilde{x}_\lambda^+, \tilde{x}_\lambda^-, s, b) \\ &\times F_{\text{remn}}^{h_1} \left(1 - \sum_{j=1}^m x_j^+ - \sum_{k=1}^l \tilde{x}_k^+ \right) F_{\text{remn}}^{h_2} \left(1 - \sum_{j=1}^m x_j^- - \sum_{k=1}^l \tilde{x}_k^- \right), \end{aligned} \quad (2.43)$$

where $2\text{Im}\tilde{T}^{h_1h_2}$ represents a cut elementary diagram and $-2\text{Im}\tilde{T}^{h_1h_2}$ an uncut one (taking into account that the uncut contribution may appear on either side from the cut plane). It is therefore useful to define a partonic profile function G via

$$G_{1\mathbb{P}}^{h_1h_2}(x_\lambda^+, x_\lambda^-, s, b) = \frac{1}{2x_\lambda^+ x_\lambda^- s} 2\text{Im}\tilde{T}_{1\mathbb{P}}^{h_1h_2}(x_\lambda^+, x_\lambda^-, s, b), \quad (2.44)$$

which allows to write the integrand of the right-hand-side of eq. (2.43) as a product of G and $(-G)$ terms:

$$\begin{aligned} \gamma_{h_1h_2}(s, b) &= \sum_{m=1}^{\infty} \frac{1}{m!} \int_0^1 \prod_{\mu=1}^m dx_\mu^+ dx_\mu^- \prod_{\mu=1}^m G_{1\mathbb{P}}^{h_1h_2}(x_\mu^+, x_\mu^-, s, b) \\ &\times \sum_{l=0}^{\infty} \frac{1}{l!} \int_0^1 \prod_{\lambda=1}^l d\tilde{x}_\lambda^+ d\tilde{x}_\lambda^- \prod_{\lambda=1}^l -G_{1\mathbb{P}}^{h_1h_2}(\tilde{x}_\lambda^+, \tilde{x}_\lambda^-, s, b) \\ &\times F_{\text{remn}}\left(x^{\text{proj}} - \sum_{\lambda} \tilde{x}_\lambda^+\right) F_{\text{remn}}\left(x^{\text{targ}} - \sum_{\lambda} \tilde{x}_\lambda^-\right), \end{aligned} \quad (2.45)$$

see fig. 2.8, with

$$x^{\text{proj/targ}} = 1 - \sum x_\mu^\pm$$

being the momentum fraction of the projectile/target remnant. This is a very important result,

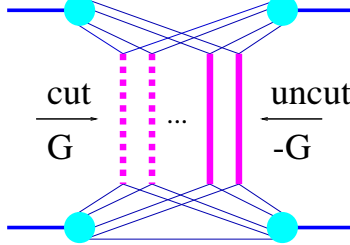


Figure 2.8: The hadronic profile function γ expressed in terms of partonic profile functions $G \equiv G_{1\mathbb{P}}^{h_1h_2}$.

allowing to express the total profile function $\gamma_{h_1h_2}$ via the elementary profile functions $G_{1\mathbb{P}}^{h_1h_2}$.

Based on the above definitions, we may write the profile function $G_{1\mathbb{P}}^{h_1h_2}$ as

$$G_{1\mathbb{P}}^{h_1h_2} = G_{\text{soft}}^{h_1h_2} + G_{\text{sea-sea}}^{h_1h_2} + G_{\text{val-val}}^{h_1h_2} + G_{\text{val-sea}}^{h_1h_2} + G_{\text{sea-val}}^{h_1h_2}, \quad (2.46)$$

with

$$G_{\text{soft/sea-sea}}^{h_1h_2}(x^+, x^-, s, b) = D_{\text{soft/sea-sea}}^{h_1h_2}(x^+ x^- s, b) F_{\text{part}}^{h_1}(x^+) F_{\text{part}}^{h_2}(x^-) \quad (2.47)$$

for the soft and semi-hard “sea-sea” contribution, with

$$\begin{aligned} G_{\text{val-val}}^{h_1h_2}(x^+, x^-, s, b) &= \int dx_{q_v}^+ dx_{q_v}^- \sum_{i,j} D_{\text{val-val}}^{h_1h_2,ij}(x_{q_v}^+ x_{q_v}^- s, b) \\ &\times \bar{F}_{\text{part}}^{h_1,i}(x_{q_v}^+, x^+ - x_{q_v}^+) \bar{F}_{\text{part}}^{h_2,j}(x_{q_v}^-, x^- - x_{q_v}^-) \end{aligned} \quad (2.48)$$

for the hard “val-val” contribution, and with

$$G_{\text{val-sea}}^{h_1h_2}(x^+, x^-, s, b) = \int dx_{q_v}^+ \sum_i D_{\text{val-sea}}^{h_1h_2,i}(x_{q_v}^+ x^- s, b) \bar{F}_{\text{part}}^{h_1,i}(x_{q_v}^+, x^+ - x_{q_v}^+) F_{\text{part}}^{h_2}(x^-) \quad (2.49)$$

and

$$G_{\text{sea-val}}^{h_1 h_2}(x^+, x^-, s, b) = \int dx_{q_v}^- \sum_i D_{\text{val-sea}}^{h_2 h_1, i}(x^+ x_{q_v}^- s, b) \bar{F}_{\text{part}}^{h_2, i}(x_{q_v}^-, x^- - x_{q_v}^-) F_{\text{part}}^{h_1}(x^+), \quad (2.50)$$

for the mixed semi-hard “val-sea” and “sea-val” contributions. For the soft and “sea-sea” contributions, the D -functions are given as

$$D_{\text{soft/sea-sea}}^{h_1 h_2}(\hat{s}, b) = \int d^2 b' D_{\text{soft/sea-sea}}(\hat{s}, |\vec{b} - \vec{b}'|) \frac{1}{4\pi (R_{h_1}^2 + R_{h_2}^2)} \exp\left[-\frac{b'^2}{4(R_{h_1}^2 + R_{h_2}^2)}\right], \quad (2.51)$$

which means that $D_{\text{soft/sea-sea}}^{h_1 h_2}$ has the same functional form as $D_{\text{soft/sea-sea}}$, with $\lambda_{\text{soft}}^{(2)}(\xi)$ being replaced by

$$\lambda_{\text{soft}}^{h_1 h_2}(\xi) = \lambda_{\text{soft}}^{(2)}(\xi) + R_{h_1}^2 + R_{h_2}^2 \quad (2.52)$$

$$\simeq R_{h_1}^2 + R_{h_2}^2 + \alpha'_{\text{soft}} \ln \xi, \quad (2.53)$$

where we neglected the parton slope R_{part}^2 compared to the hadron slope R_h^2 .

For the hard contribution, we have correspondingly $D_{\text{val-val}}^{h_1 h_2, ij}(\hat{s}, b)$ being given in eq. (2.18) with R_{hard}^2 being replaced by $R_{h_1}^2 + R_{h_2}^2$ (neglecting the hard scattering slope R_{hard}^2 as compared to the hadron Regge slopes $R_{h_1}^2, R_{h_2}^2$). In case of mixed Pomerons, we have $D_{\text{val-sea}}^{h_1 h_2, i}(\hat{s}, b)$ given in eq. (2.29) with R_{part}^2 being replaced by $R_{h_1}^2 + R_{h_2}^2$.

2.4 Nucleus-Nucleus Scattering

We generalize the discussion of the last section in order to treat nucleus-nucleus scattering. In the Glauber-Gribov approach [16, 17], the nucleus-nucleus scattering amplitude is defined by the sum of contributions of diagrams, shown at fig.2.1, corresponding to multiple scattering processes between parton constituents of projectile and target nucleons. Nuclear form factors are supposed to be defined by the nuclear ground state wave functions. Assuming the nucleons to be uncorrelated, one can make the Fourier transform to obtain the amplitude in the impact parameter representation. Then, for given impact parameter \vec{b}_0 between the nuclei, the only formal differences from the hadron-hadron case will be the possibility for a given nucleon to interact with a number of nucleons from the partner nucleus as well as the averaging over nuclear ground states, which amounts to an integration over transverse nucleon coordinates \vec{b}_i^A and \vec{b}_j^B in the projectile and in the target correspondingly. We write this integration symbolically as

$$\int dT_{AB} := \int \prod_{i=1}^A d^2 b_i^A T_A(b_i^A) \prod_{j=1}^B d^2 b_j^B T_B(b_j^B), \quad (2.54)$$

with A, B being the nuclear mass numbers and with the so-called nuclear thickness function $T_A(b)$ being defined as the integral over the nuclear density $\rho_{A(B)}$,

$$T_A(b) := \int dz \rho_A(\sqrt{b^2 + z^2}). \quad (2.55)$$

For the nuclear densities, we use a parameterization of experimental data of [18],

$$\rho_A(r) \propto \begin{cases} \exp\{-r^2/1.72^2\} & \text{if } A = 2, \\ \exp\{-r^2/(0.9A^{1/3})^2\} & \text{if } 2 < A < 10, \\ 1/\left\{1 + \exp\left(\frac{r-0.7A^{0.446}}{0.545}\right)\right\} & \text{if } A \geq 10. \end{cases} \quad (2.56)$$

It is convenient to use the transverse distance b_k between the two nucleons from the k -th nucleon-nucleon pair, i.e.

$$b_k = \left| \vec{b}_0 + \vec{b}_{\pi(k)}^A - \vec{b}_{\tau(k)}^B \right|, \quad (2.57)$$

where the functions $\pi(k)$ and $\tau(k)$ refer to the projectile and the target nucleons participating in the k^{th} interaction (pair k). In order to simplify the notation, we define a vector b whose components are the overall impact parameter b_0 as well as the transverse distances b_1, \dots, b_{AB} of the nucleon pairs,

$$b = \{b_0, b_1, \dots, b_{AB}\}. \quad (2.58)$$

Then the nucleus-nucleus interaction cross section can be obtained applying the cutting procedure to elastic scattering diagrams of fig.2.1 and written in the form

$$\sigma_{\text{inel}}^{AB}(s) = \int d^2 b_0 \int dT_{AB} \gamma_{AB}(s, b), \quad (2.59)$$

where the so-called nuclear profile function γ_{AB} represents an interaction for given transverse coordinates of the nucleons.

The calculation of the profile function γ_{AB} as the sum over all cut diagrams of the type shown in fig.2.9 does not differ from the hadron-hadron case and follows the rules formulated in the

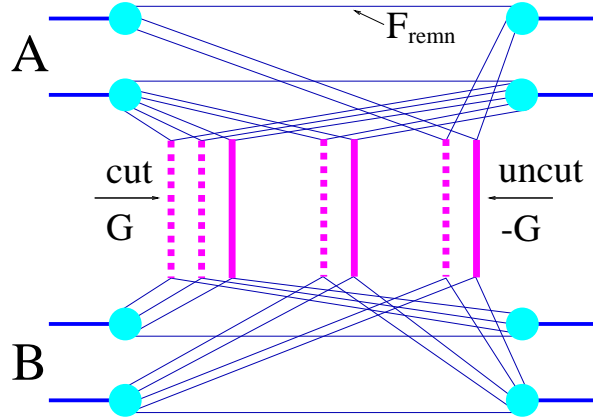


Figure 2.9: Example for a cut multiple scattering diagram, with cut (dashed lines) and uncut (full lines) elementary diagrams. This diagram can be translated directly into a formula for the inelastic cross section (see text).

preceding section:

- For a remnant carrying the light cone momentum fraction x (x^+ in case of projectile, or x^- in case of target), one has a factor $F_{\text{remn}}(x)$, defined in eq. (2.35).
- For each cut elementary diagram (real elementary interaction = dashed vertical line) attached to two participants with light cone momentum fractions x^+ and x^- , one has a factor $G(x^+, x^-, s, b)$, given by eqs. (2.46-2.50). Apart of x^+ and x^- , G is also a function of the total squared energy s and of the relative transverse distance b between the two corresponding nucleons (we use G as an abbreviation for G_{NP}^{NN} for nucleon-nucleon scattering).
- For each uncut elementary diagram (virtual emissions = full vertical line) attached to two participants with light cone momentum fractions x^+ and x^- , one has a factor $-G(x^+, x^-, s, b)$, with the same G as used for the cut diagrams.
- Finally one sums over all possible numbers of cut and uncut Pomerons and integrates over the light cone momentum fractions.

So we find

$$\begin{aligned}
\gamma_{AB}(s, b) &= \sum_{m_1 l_1} \dots \sum_{m_{AB} l_{AB}} (1 - \delta_{0\Sigma m_k}) \int \prod_{k=1}^{AB} \left\{ \prod_{\mu=1}^{m_k} dx_{k,\mu}^+ dx_{k,\mu}^- \prod_{\lambda=1}^{l_k} d\tilde{x}_{k,\lambda}^+ d\tilde{x}_{k,\lambda}^- \right\} \\
&\times \prod_{k=1}^{AB} \left\{ \frac{1}{m_k!} \frac{1}{l_k!} \prod_{\mu=1}^{m_k} G(x_{k,\mu}^+, x_{k,\mu}^-, s, b_k) \prod_{\lambda=1}^{l_k} -G(\tilde{x}_{k,\lambda}^+, \tilde{x}_{k,\lambda}^-, s, b_k) \right\} \\
&\times \prod_{i=1}^A F_{\text{remn}} \left(x_i^+ - \sum_{\pi(k)=i} \tilde{x}_{k,\lambda}^+ \right) \prod_{j=1}^B F_{\text{remn}} \left(x_j^- - \sum_{\tau(k)=j} \tilde{x}_{k,\lambda}^- \right) \quad (2.60)
\end{aligned}$$

with

$$x_i^{\text{proj}} = 1 - \sum_{\pi(k)=i} x_{k,\mu}^+, \quad (2.61)$$

$$x_j^{\text{targ}} = 1 - \sum_{\tau(k)=j} x_{k,\mu}^-. \quad (2.62)$$

The summation indices m_k refer to the number of cut elementary diagrams and l_k to the number of uncut elementary diagrams, related to nucleon pair k . For each possible pair k (we have altogether AB pairs), we allow for any number of cut and uncut diagrams. The integration variables $x_{k,\mu}^\pm$ refer to the μ^{th} elementary interaction of the k^{th} pair for the cut elementary diagrams, the variables $\tilde{x}_{k,\lambda}^\pm$ refer to the corresponding uncut elementary diagrams. The arguments of the remnant functions F_{remn} are the remnant light cone momentum fractions, i.e. unity minus the momentum fractions of all the corresponding elementary contributions (cut and uncut ones). We also introduce the variables x_i^+ and x_j^- , defined as unity minus the momentum fractions of all the corresponding cut contributions, in order to integrate over the uncut ones (see below).

The expression for $\gamma_{AB}(\dots)$ sums up all possible numbers of cut Pomerons m_k with one exception due to the factor $(1 - \delta_{0\Sigma m_k})$: one does not consider the case of all m_k 's being zero, which corresponds to “no interaction” and therefore does not contribute to the inelastic cross section. We may therefore define a quantity $\bar{\gamma}_{AB}(\dots)$, representing “no interaction”, by taking the expression for $\gamma_{AB}(\dots)$ with $(1 - \delta_{0\Sigma m_k})$ replaced by $(\delta_{0\Sigma m_k})$:

$$\begin{aligned}
\bar{\gamma}_{AB}(s, b) &= \sum_{l_1} \dots \sum_{l_{AB}} \int \prod_{k=1}^{AB} \left\{ \prod_{\lambda=1}^{l_k} d\tilde{x}_{k,\lambda}^+ d\tilde{x}_{k,\lambda}^- \right\} \prod_{k=1}^{AB} \left\{ \frac{1}{l_k!} \prod_{\lambda=1}^{l_k} -G(\tilde{x}_{k,\lambda}^+, \tilde{x}_{k,\lambda}^-, s, b_k) \right\} \\
&\times \prod_{i=1}^A F^+ \left(1 - \sum_{\pi(k)=i} \tilde{x}_{k,\lambda}^+ \right) \prod_{j=1}^B F^- \left(1 - \sum_{\tau(k)=j} \tilde{x}_{k,\lambda}^- \right). \quad (2.63)
\end{aligned}$$

One now may consider the sum of “interaction” and “no interaction”, and one obtains easily

$$\gamma_{AB}(s, b) + \bar{\gamma}_{AB}(s, b) = 1. \quad (2.64)$$

Based on this important result, we consider γ_{AB} to be the probability to have an interaction and correspondingly $\bar{\gamma}_{AB}$ to be the probability of no interaction, for fixed energy, impact parameter and nuclear configuration, specified by the transverse distances b_k between nucleons, and we refer to eq. (2.64) as “unitarity relation”. But we want to go even further and use an expansion of γ_{AB} in order to obtain probability distributions for individual processes, which then serves as a basis for the calculations of exclusive quantities.

The expansion of γ_{AB} in terms of cut and uncut Pomerons as given above represents a sum of a large number of positive and negative terms, including all kinds of interferences, which excludes

any probabilistic interpretation. We have therefore to perform summations of interference contributions - sum over any number of virtual elementary scatterings (uncut Pomerons) - for given non-interfering classes of diagrams - with given numbers of real scatterings (cut Pomerons) [15]. Let us write the formulas explicitly. We have

$$\begin{aligned} \gamma_{AB}(s, b) &= \sum_{m_1} \dots \sum_{m_{AB}} (1 - \delta_0 \sum m_k) \int \prod_{k=1}^{AB} \left\{ \prod_{\mu=1}^{m_k} dx_{k,\mu}^+ dx_{k,\mu}^- \right\} \\ &\times \prod_{k=1}^{AB} \left\{ \frac{1}{m_k!} \prod_{\mu=1}^{m_k} G(x_{k,\mu}^+, x_{k,\mu}^-, s, b_k) \right\} \Phi_{AB}(x^{\text{proj}}, x^{\text{targ}}, s, b), \end{aligned} \quad (2.65)$$

where the function Φ representing the sum over virtual emissions (uncut Pomerons) is given by the following expression

$$\begin{aligned} \Phi_{AB}(x^{\text{proj}}, x^{\text{targ}}, s, b) &= \sum_{l_1} \dots \sum_{l_{AB}} \int \prod_{k=1}^{AB} \left\{ \prod_{\lambda=1}^{l_k} d\tilde{x}_{k,\lambda}^+ d\tilde{x}_{k,\lambda}^- \right\} \prod_{k=1}^{AB} \left\{ \frac{1}{l_k!} \prod_{\lambda=1}^{l_k} -G(\tilde{x}_{k,\lambda}^+, \tilde{x}_{k,\lambda}^-, s, b_k) \right\} \\ &\times \prod_{i=1}^A F_{\text{remn}} \left(x_i^{\text{proj}} - \sum_{\pi(k)=i} \tilde{x}_{k,\lambda}^+ \right) \prod_{j=1}^B F_{\text{remn}} \left(x_j^{\text{targ}} - \sum_{\tau(k)=j} \tilde{x}_{k,\lambda}^- \right). \end{aligned} \quad (2.66)$$

This summation has to be carried out, before we may use the expansion of γ_{AB} to obtain probability distributions. This is far from trivial, as we are going to discuss in the next section, but let us assume for the moment that it can be done. To make the notation more compact, we define matrices X^+ and X^- , as well as a vector m , via

$$X^+ = \{x_{k,\mu}^+\}, \quad (2.67)$$

$$X^- = \{x_{k,\mu}^-\}, \quad (2.68)$$

$$m = \{m_k\}, \quad (2.69)$$

which leads to

$$\gamma_{AB}(s, b) = \sum_m (1 - \delta_{0m}) \int dX^+ dX^- \Omega_{AB}^{(s,b)}(m, X^+, X^-), \quad (2.70)$$

$$\bar{\gamma}_{AB}(s, b) = \Omega_{AB}^{(s,b)}(0, 0, 0), \quad (2.71)$$

with

$$\Omega_{AB}^{(s,b)}(m, X^+, X^-) = \prod_{k=1}^{AB} \left\{ \frac{1}{m_k!} \prod_{\mu=1}^{m_k} G(x_{k,\mu}^+, x_{k,\mu}^-, s, b_k) \right\} \Phi_{AB}(x^{\text{proj}}, x^{\text{targ}}, s, b). \quad (2.72)$$

This allows to rewrite the unitarity relation eq. (2.64) in the following form,

$$\sum_m \int dX^+ dX^- \Omega_{AB}^{(s,b)}(m, X^+, X^-) = 1. \quad (2.73)$$

This equation is of fundamental importance, because it allows us to interpret $\Omega^{(s,b)}(m, X^+, X^-)$ as probability density of having an interaction configuration characterized by m , with the light cone momentum fractions of the Pomerons being given by X^+ and X^- .

2.5 Diffractive Scattering

We do not have a consistent treatment of diffractive scattering at the moment, this is left to a future project in connection with a complete treatment of enhanced diagrams. For the moment, we introduce diffraction “by hand”: in case of no interaction in pp or pA scattering, we consider the projectile to be diffractively excited with probability

$$w_{\text{diff}} \frac{\left(1 - \sqrt{\Phi(1, x^{\text{targ}}, s, b)}\right)^2}{\Phi(1, x^{\text{targ}}, s, b)}, \quad (2.74)$$

with a fit parameter w_{diff} . Nucleus-nucleus scattering is here (but only here!) considered as composed of pA or Ap collisions.

2.6 AGK Cancelations in Hadron-Hadron Scattering

As a first application, we are going to prove that AGK cancelations apply perfectly in our model².

As we showed above, the description of high energy hadronic interaction requires to consider explicitly a great number of contributions, corresponding to multiple scattering process, with a number of elementary parton-parton interactions happening in parallel. However, when calculating inclusive spectra of secondary particles, it is enough to consider the simplest hadron-hadron (nucleus-nucleus) scattering diagrams containing a single elementary interaction, as the contributions of multiple scattering diagrams with more than one elementary interaction exactly cancel each other. This so-called AGK-cancelation is a consequence of the general Abramovskii-Gribov-Kancheli cutting rules [15].

Let us consider the most fundamental inclusive distribution, where all other inclusive spectra may be derived from: the distribution $dn_{\text{Pom}}^{h_1 h_2}/dx^+ dx^-$, with $dn_{\text{Pom}}^{h_1 h_2}$ being the number of Pomerons with light cone momentum fractions between x^+ and $x^+ + dx^+$ and between x^- and $x^- + dx^-$ respectively, at a given value of b and s . If AGK cancelations apply, the result for $dn_{\text{Pom}}^{h_1 h_2}/dx^+ dx^-$ should coincide with the contribution coming from exactly one elementary interaction (see eq. (2.45)):

$$\frac{dn_{\text{Pom}}^{(1)h_1 h_2}}{dx^+ dx^-}(x^+, x^-, s, b) = G_{\text{IP}}^{h_1 h_2}(x^+, x^-, s, b) F_{\text{remn}}^{h_1}(1 - x^+) F_{\text{remn}}^{h_2}(1 - x^-), \quad (2.75)$$

and the contributions from multiple scattering should exactly cancel. We have per definition

$$\begin{aligned} \frac{dn_{\text{Pom}}^{h_1 h_2}}{dx^+ dx^-}(x^+, x^-, s, b) &= \sum_{m=1}^{\infty} \sum_{l=0}^{\infty} \int \prod_{\mu=1}^m dx_{\mu}^+ dx_{\mu}^- \prod_{\lambda=m+1}^{m+l} dx_{\lambda}^+ dx_{\lambda}^- \\ &\times \frac{1}{m!} \frac{1}{l!} \prod_{\mu=1}^m G_{\text{IP}}^{h_1 h_2}(x_{\mu}^+, x_{\mu}^-, s, b) \prod_{\lambda=m+1}^{m+l} -G_{\text{IP}}^{h_1 h_2}(x_{\lambda}^+, x_{\lambda}^-, s, b) \\ &\times F_{\text{remn}}^{h_1}\left(1 - \sum_{\nu=1}^{m+l} x_{\nu}^+\right) F_{\text{remn}}^{h_2}\left(1 - \sum_{\nu=1}^{m+l} x_{\nu}^-\right) \\ &\times \sum_{\mu'=1}^m \delta(x^+ - x_{\mu'}^+) \delta(x^- - x_{\mu'}^-). \end{aligned} \quad (2.76)$$

² We speak here about the contribution of elementary interactions (Pomeron exchanges) to the secondary particle production; the AGK cancellations do not hold for the contribution of remnant states (spectator partons) hadronization [4].

Due to the symmetry of the integrand in the r.h.s. of eq. (2.76) in the variables x_1^\pm, \dots, x_m^\pm , the sum of delta functions produces a factor $mG(x^+, x^-, s, b)$, and removes one $dx_\mu^+ dx_\mu^-$ integration. Using

$$m \sum_{m=1}^{\infty} \dots \frac{1}{m!} \prod_{\mu=1}^{m-1} \dots = \sum_{m'=0}^{\infty} \dots \frac{1}{m'!} \prod_{\mu=1}^{m'} \dots, \quad (2.77)$$

with $m' = m - 1$, we get

$$\begin{aligned} \frac{dn_{\text{Pom}}^{h_1 h_2}}{dx^+ dx^-}(x^+, x^-, s, b) &= G_{1\mathbb{P}}^{h_1 h_2}(x^+, x^-, s, b) \frac{1}{n!} \sum_{n=0}^{\infty} \int \prod_{\nu=1}^n dx_\nu^+ dx_\nu^- \\ &\times \left\{ \sum_{m=0}^n \binom{n}{m} \prod_{\mu=1}^m G_{1\mathbb{P}}^{h_1 h_2}(x_\mu^+, x_\mu^-, s, b) \prod_{\lambda=m+1}^n -G_{1\mathbb{P}}^{h_1 h_2}(x_\lambda^+, x_\lambda^-, s, b) \right\} \\ &\times F_{\text{remn}}^{h_1}(1 - x^+ - \sum_{\nu=1}^n x_\nu^+) F_{\text{remn}}^{h_2}(1 - x^- - \sum_{\nu=1}^n x_\nu^-). \end{aligned} \quad (2.78)$$

The term in curly brackets $\{\dots\}$ is 1 for $n = 0$ and zero otherwise, so we get the important final result

$$\frac{dn_{\text{Pom}}^{h_1 h_2}}{dx^+ dx^-}(x^+, x^-, s, b) = \frac{dn_{\text{Pom}}^{(1)h_1 h_2}}{dx^+ dx^-}(x^+, x^-, s, b), \quad (2.79)$$

which corresponds to one single elementary interaction; the multiple scattering aspects completely disappeared, so AGK cancelations indeed apply in our approach. AGK cancelations are closely related to the factorization formula for jet production cross section, since as a consequence of eq. (2.79), we may obtain the inclusive jet cross section in a factorized form as

$$\sigma_{\text{jet}}^{h_1 h_2} = \sum_{j,k} \int dp_\perp^2 \int dz^+ \int dz^- f_j^{h_1}(z^+, M_F^2) f_k^{h_2}(z^-, M_F^2) \frac{d\sigma_{\text{Born}}^{jk}}{dp_\perp^2}(z^+ z^- s, p_\perp^2), \quad (2.80)$$

with $f_j^{h_1}$ and $f_k^{h_2}$ representing the parton distributions of the two hadrons.

2.7 AGK Cancelations in Nucleus-Nucleus Scattering

We have shown in the previous section that for hadron-hadron scattering AGK cancelations apply, which means that inclusive spectra coincide with the contributions coming from exactly one elementary interaction. For multiple Pomeron exchanges we have a complete destructive interference, they do not contribute at all. Here, we are going to show that AGK cancelations also apply for nucleus-nucleus scattering, which means that the inclusive cross section for $A + B$ scattering is AB times the corresponding inclusive cross section for proton-proton interaction.

The inclusive cross section for forming a Pomeron with light cone momentum fractions x^+ and x^- in nucleus-nucleus scattering is given as

$$\begin{aligned} \frac{d\sigma_{\text{Pom}}^{AB}}{dx^+ dx^-}(x^+, x^-, s) &= \int d^2 b_0 \int dT_{AB} \\ &\times \sum_{m_1 l_1} \dots \sum_{m_{AB} l_{AB}} (1 - \delta_0 \sum m_k) \int \prod_{k=1}^{AB} \left\{ \prod_{\mu=1}^{m_k + l_k} dx_{k,\mu}^+ dx_{k,\mu}^- \right\} \\ &\times \prod_{k=1}^{AB} \left\{ \frac{1}{m_k! l_k!} \prod_{\mu=1}^{m_k} G(x_{k,\mu}^+, x_{k,\mu}^-, s, b_k) \prod_{\lambda=m_k+1}^{m_k+l_k} -G(x_{k,\lambda}^+, x_{k,\lambda}^-, s, b_k) \right\} \end{aligned}$$

$$\begin{aligned}
& \times \prod_{i=1}^A F_{\text{remn}} \left(1 - \sum_{\pi(k)=i} x_{k,\lambda}^+ \right) \prod_{j=1}^B F_{\text{remn}} \left(1 - \sum_{\tau(k)=j} x_{k,\lambda}^- \right) \\
& \times \sum_{k'=1}^{AB} \sum_{\mu'=1}^{m_k} \delta(x^+ - x_{k'\mu'}^+) \delta(x^- - x_{k'\mu'}^-). \tag{2.81}
\end{aligned}$$

The factor $(1 - \delta_0 \sum m_k)$ makes sure that at least one of the indices m_k is bigger than zero. Integrating over the variables appearing in the delta functions, we obtain a factor $\sum_{k'} G(x^+, x^-, s, b_k) \cdot m_{k'}$ which may be written in front of $\sum_{m_1 l_1} \dots$. In the following expression one may rename the integration variables such that the variables $x_{k'\mu'}^+$ and $x_{k'\mu'}^-$ disappear. This means for the arguments of the functions F_{remn} that for $i = \pi(k')$ and $j = \tau(k')$ one replaces 1 by $1 - x^+$ and $1 - x^-$ respectively. Then one uses the factor $m_{k'}$ mentioned above to replace $m_{k'}!$ by $(m_{k'} - 1)!$. One finally renames $(m_{k'} - 1)$ by $m_{k'}$, as a consequence of which one may drop the factor $(1 - \delta_0 \sum m_k)$. This is crucial, since now we have factors of the form

$$\sum_{m_k=0}^{\infty} \sum_{l_k=0}^{\infty} \dots \frac{1}{m_k! l_k!} \prod_{\mu=1}^{m_k} G(x_{k,\mu}^+, x_{k,\mu}^-, s, b) \prod_{\lambda=m_k+1}^{m_k+l_k} -G(x_{k,\lambda}^+, x_{k,\lambda}^-, s, b) \dots \tag{2.82}$$

In this sum only the term for $m_k = 0$ and $l_k = 0$ is different from zero, namely 1, and so we get

$$\frac{d\sigma_{\text{Pom}}^{AB}}{dx^+ dx^-}(x^+, x^-, s, b) = \int d^2 b_0 \int dT_{AB} \sum_{k'} G(x^+, x^-, s, b_{k'}) F_{\text{remn}}(1 - x^+) F_{\text{remn}}(1 - x^-). \tag{2.83}$$

Using the definition of dT_{AB} , writing $b_{k'}$ explicitly as $|\vec{b}_0 + \vec{b}_{\pi(k)}^A - \vec{b}_{\tau(k)}^B|$, we obtain

$$\begin{aligned}
\frac{d\sigma_{\text{Pom}}^{AB}}{dx^+ dx^-}(x^+, x^-, s) &= AB \int d^2 b_0 \int d^2 b_+ T(b_+) \int d^2 b_- T(b_-) G(x^+, x^-, s, |\vec{b}_0 + \vec{b}_+ - \vec{b}_-|) \\
&\times F_{\text{remn}}(1 - x^+) F_{\text{remn}}(1 - x^-). \tag{2.84}
\end{aligned}$$

Changing the order of the integrations, we obtain finally

$$\frac{d\sigma_{\text{Pom}}^{AB}}{dx^+ dx^-}(x^+, x^-, s) = AB \frac{d\sigma_{\text{Pom}}^{pp}}{dx^+ dx^-}(x^+, x^-, s) \tag{2.85}$$

with

$$\frac{d\sigma_{\text{Pom}}^{pp}}{dx^+ dx^-}(x^+, x^-, s) = \int d^2 b G(x^+, x^-, s, b) F_{\text{remn}}(1 - x^+) F_{\text{remn}}(1 - x^-). \tag{2.86}$$

Since any other inclusive cross section $d\sigma_{\text{incl}}/dq$ may be obtained from the inclusive Pomeron distribution via convolution, we obtain the very general result

$$\frac{d\sigma_{\text{incl}}^{AB}}{dq}(q, s, b) = AB \frac{d\sigma_{\text{incl}}^{pp}}{dq}(q, s, b), \tag{2.87}$$

so nucleus-nucleus inclusive cross sections are just AB times the proton-proton ones. So, indeed, AGK cancelations appear perfectly in our approach.

2.8 Outlook

What did we achieve so far? We have a well defined model, introduced by using the language of field theory (Feynman diagrams). We were able to prove some elementary properties (AGK cancelations in case of proton-proton and nucleus-nucleus scattering). To proceed further, we have to solve (at least) two fundamental problems:

- the sum over virtual emissions has to be performed,
- tools have to be developed to deal with the multidimensional probability distribution $\Omega_{AB}^{(s,b)}(m, X^+, X^-)$,

both being very difficult tasks.

Calculating the sum over virtual emissions (Φ_{AB}) is not only technically difficult, there are also conceptual problems. By studying the properties of Φ_{AB} , we find that at very high energies the theory is no longer unitary without taking into account additional screening corrections. In this sense, we consider our work as a first step to construct a consistent model for high energy nuclear scattering, but there is still work to be done.

Concerning the multidimensional probability distribution $\Omega_{AB}^{(s,b)}(m, X^+, X^-)$, we are going to develop methods well known in statistical physics (Markov chain techniques), which we also are going to discuss in detail later. So finally, we are able to calculate the probability distribution $\Omega_{AB}^{(s,b)}(m, X^+, X^-)$, and are able to generate (in a Monte Carlo fashion) configurations (m, X^+, X^-) according to this probability distribution.

The two above mentioned problems will be discussed in detail in the following chapters.

Chapter 3

Virtual Emissions

In order to proceed, we need to calculate the sum over virtual emissions, represented by the function Φ_{AB} . Understanding the behavior of Φ_{AB} is crucial, since this function is related to $\bar{\gamma}_{AB}$ and plays therefore a crucial role in connection with unitarity, the unitarity equation being given as $\gamma_{AB} + \bar{\gamma}_{AB} = 1$. By studying the properties of Φ_{AB} , we find inconsistencies in the limit of high energies, in the sense that the individual terms appearing in the unitarity equation are not necessarily positive. Attempting to understand this unphysical behavior, we find that any model where AGK cancelations apply (so most of the models used presently) has to run asymptotically into this problem. So eventually one needs to construct models, where AGK cancelations are violated, which is going to be expected when contributions of Pomeron-Pomeron interactions are taken into consideration.

As a first phenomenological solution of the unitarity problem, we are going to “unitarize” the “bare theory” introduced in the preceding chapter “by hand”, such that the theory is changed as little as possible, but the asymptotic problems disappear. The next step should of course be a consistent treatment including contributions of enhanced Pomeron diagrams.

In the following, we are going to present the calculation of Φ_{AB} , we discuss the unitarity problems and the phenomenological solution, as well as properties of the “unitarized theory”.

3.1 Parameterizing the Elementary Interaction

The basis for all the calculations which follow is the function $G_{1\text{IP}}^{NN}$, which is the profile function representing a single elementary nucleon-nucleon (NN) interaction. For simplicity, we write simply $G \equiv G_{1\text{IP}}^{NN}$. This function G is a sum of several terms, representing soft, semi-hard, valence, and screening contributions. In case of soft and semi-hard, one has $G = (x^+x^-)^{-\alpha_{\text{part}}} D$, where D represents the Pomeron exchange and the factor in front of D the “external legs”, the nucleon participants. For the other contributions the functional dependence on x^+, x^- is somewhat more complicated, but nevertheless it is convenient to define a function

$$D(x^+, x^-, s, b) = \frac{G(x^+, x^-, s, b)}{(x^+x^-)^{-\alpha_{\text{part}}}}. \quad (3.1)$$

We obtain G and therefore D as the result of a quite involved numerical calculation, which means that these functions are given in a discretized fashion. Since this is not very convenient and since the dependence of x^+, x^- , and b are quite simple, we are going to parameterize our numerical results and use this analytical expression for further calculations. This makes the following discussions much easier and more transparent.

We first consider the case of zero impact parameter ($b = 0$). In fig. 3.1, we plot the function D together with the individual contributions as functions of $x = x^+x^-$, for $b = 0$ and for different values of s . To fit the function D , we make the following ansatz,

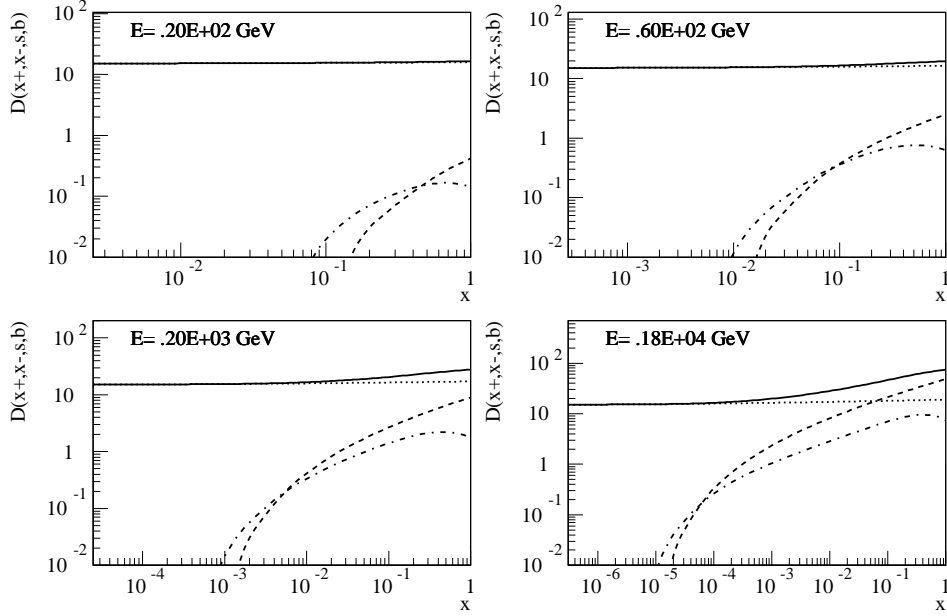


Figure 3.1: The function D (solid line) as well as the different contributions to D as a function of $x = x^+ x^-$, for $b = 0$, at different energies $E = \sqrt{s}$. We show D_{soft} (dotted), D_{semi} (dashed), and D_{valence} (dashed-dotted).

$$D(x^+, x^-, s, b = 0) = \sum_{i=1}^N \underbrace{\left\{ \alpha_{D_i} + \alpha_{D_i}^* (x^+ x^-)^{\beta_{D_i}^*} \right\}}_{D_i} (x^+ x^- s)^{\beta_{D_i}}, \quad (3.2)$$

where the parameters may depend on s , and the parameters marked with a star are non-zero for a given i only if the corresponding α_{D_i} is zero. This parameterization works very well, as shown in fig. 3.2, where we compare the original D function with the fit according to eq. (3.2).

Let us now consider the b -dependence for fixed x^+ and x^- . Since we observe almost a Gaussian shape with a weak (logarithmic) dependence of the width on $x = x^+ x^-$, we could make the following ansatz:

$$D(x^+, x^-, s, b) = \sum_{i=1}^N \left\{ \alpha_{D_i} + \alpha_{D_i}^* (x^+ x^-)^{\beta_{D_i}^*} \right\} (x^+ x^- s)^{\beta_{D_i}} \exp \left(\frac{-b^2}{\delta_{D_i} + \epsilon_{D_i} \ln(x^+ x^- s)} \right). \quad (3.3)$$

However, we can still simplify the parameterization. We have

$$\exp \left(\frac{-b^2}{\delta + \epsilon \ln x} \right) \approx \exp \left(\frac{-b^2}{\delta} \left(1 - \frac{\epsilon}{\delta} \ln(x^+ x^- s) \right) \right) \quad (3.4)$$

$$= \exp \left(\frac{-b^2}{\delta} \right) (x^+ x^- s)^{\gamma_{b^2}} \quad (3.5)$$

So we make finally the ansatz

$$D(x^+, x^-, s, b) = \sum_{i=1}^N \left\{ \alpha_{D_i} + \alpha_{D_i}^* (x^+ x^-)^{\beta_{D_i}^*} \right\} (x^+ x^- s)^{\beta_{D_i} + \gamma_{D_i} b^2} e^{-\frac{b^2}{\delta_{D_i}}}, \quad (3.6)$$

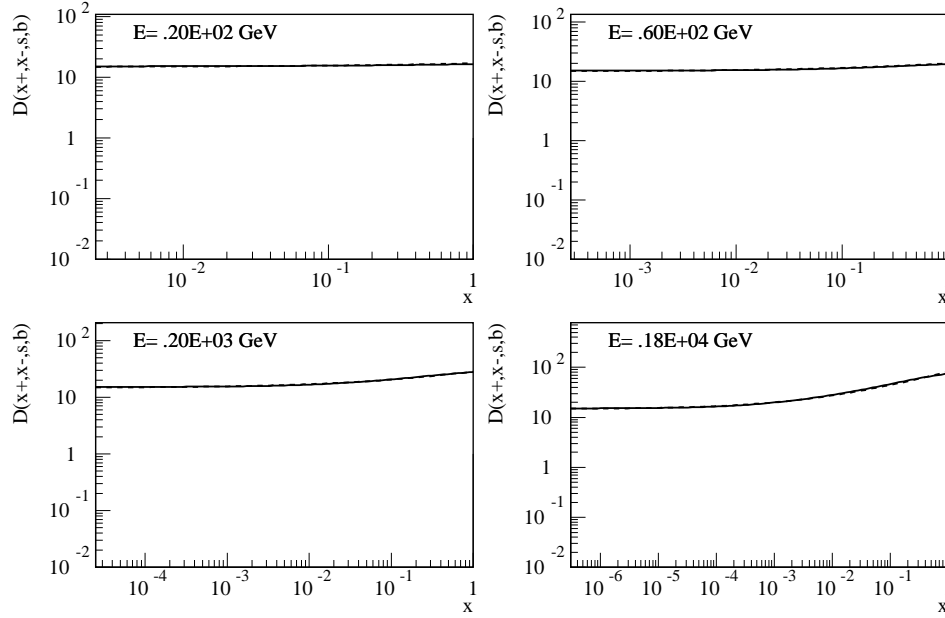


Figure 3.2: The exact (full) and the parameterized (dashed) function D as a function of $x = x^+x^-$, for $b = 0$, at different energies $E = \sqrt{s}$.

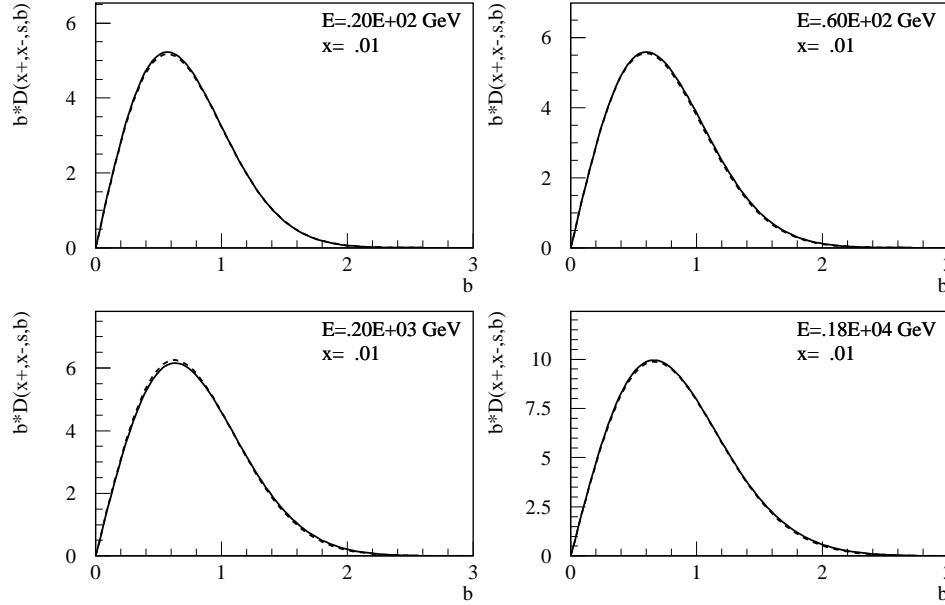


Figure 3.3: The b -dependence of $b \cdot D(x^+, x^-, s, b)$ for a fixed value of $x = x^+x^-$, with $x^+ = x^-$, at different energies $E = \sqrt{s}$. Exact results are represented as solid lines, the parameterized ones by dashed lines.

which provides a very good analytical representation of the numerically obtained function D , as shown in fig. 3.3.

3.2 Calculating Φ for proton-proton collisions

We first consider proton-proton collisions. To be more precise, we are going to derive an expression for Φ_{pp} which can be evaluated easily numerically and which will serve as the basis to investigate the properties of Φ_{pp} . We have

$$\begin{aligned} \Phi_{pp}(x^+, x^-, s, b) &= \sum_{l=0}^{\infty} \int dx_1^+ dx_1^- \dots dx_l^+ dx_l^- \left\{ \frac{1}{l!} \prod_{\lambda=1}^l -G(x_\lambda^+, x_\lambda^-, s, b) \right\} \\ &\times F_{\text{remn}}\left(x^+ - \sum x_\lambda^+\right) F_{\text{remn}}\left(x^- - \sum x_\lambda^-\right). \end{aligned} \quad (3.7)$$

with

$$F_{\text{remn}}(x) = x^{\alpha_{\text{remn}}} \Theta(x) \Theta(1-x), \quad (3.8)$$

where $\Theta(x)$ is the Heavyside function, and

$$G(x_\lambda^+, x_\lambda^-, s, b) = (x_\lambda^+ x_\lambda^-)^{-\alpha_{\text{part}}} D(x_\lambda^+, x_\lambda^-, s, b). \quad (3.9)$$

Using eq. (3.6), we have

$$G(x_\lambda^+, x_\lambda^-, s, b) = \sum_{i=1}^N \underbrace{\alpha_i (x_\lambda^+ x_\lambda^-)^{\beta_i}}_{G_{i,\lambda}} \quad (3.10)$$

with

$$\alpha_i = (\alpha_{D_i} + \alpha_{D_i}^*) s^{(\beta_{D_i} + \gamma_{D_i} b^2)} e^{-\frac{b^2}{\delta_{D_i}}}, \quad (3.11)$$

$$\beta_i = \beta_{D_i} + \beta_{D_i}^* + \gamma_{D_i} b^2 - \alpha_{\text{part}}, \quad (3.12)$$

with $\alpha_{D_i}^* \neq 0$ and $\beta_{D_i}^* \neq 0$ only if $\alpha_{D_i} = 0$. Using eq. (3.10), we obtain from eq. (3.7) the following expression

$$\begin{aligned} \Phi_{pp}(x^+, x^-, s, b) &= \sum_{r_1=0}^{\infty} \dots \sum_{r_N=0}^{\infty} \frac{1}{r_1!} \dots \frac{1}{r_N!} \int \prod_{\lambda=1}^{r_1+\dots+r_N} dx_\lambda^+ dx_\lambda^- \\ &\times \prod_{\rho_1=1}^{r_1} -G_{1,\rho_1} \dots \prod_{\rho_N=r_1+\dots+r_{N-1}+1}^{r_1+\dots+r_N} -G_{N,\rho_N} \\ &\times F_{\text{remn}}\left(x^+ - \sum_{\lambda} x_\lambda^+\right) F_{\text{remn}}\left(x^- - \sum_{\lambda} x_\lambda^-\right). \end{aligned} \quad (3.13)$$

Using the fact that the functions $G_{i,\lambda}$ are separable,

$$G_{i,\lambda} = \alpha_i (x_\lambda^+)^{\beta_i} (x_\lambda^-)^{\beta_i}, \quad (3.14)$$

one finds finally (see appendix D.1)

$$\begin{aligned} \Phi_{pp}(x^+, x^-, s, b) &= x^{\alpha_{\text{remn}}} \sum_{r_1=0}^{\infty} \dots \sum_{r_N=0}^{\infty} \left\{ \frac{\Gamma(1 + \alpha_{\text{remn}})}{\Gamma(1 + \alpha_{\text{remn}} + r_1 \tilde{\beta}_1 + \dots + r_N \tilde{\beta}_N)} \right\}^2 \\ &\times \frac{(-\alpha_1 x^{\tilde{\beta}_1} \Gamma^2(\tilde{\beta}_1))^r}{r_1!} \dots \frac{(-\alpha_N x^{\tilde{\beta}_N} \Gamma^2(\tilde{\beta}_N))^t}{r_N!} \end{aligned} \quad (3.15)$$

with $x = x^+ x^-$ and $\tilde{\beta}_i = \beta_i + 1$. Since the sums converge very fast, this expression can be easily evaluated numerically.

3.3 Unitarity Problems

In this section, we are going to present numerical results for Φ_{pp} , based on equation (3.15). We will observe an unphysical behavior in certain regions of phase space, which amounts to a violation of unitarity. Trying to understand its physical origin, we find that AGK cancelations, which apply in our model, automatically lead to unitarity violations. This means on the other hand that a fully consistent approach requires explicit violation of AGK cancelations, which should occur in case of considering contributions of enhanced Pomeron diagrams.

In which way is Φ_{pp} related to unitarity? We have shown in the preceding chapter that the inelastic non-diffractive cross section $\sigma_{\text{inel}}(s)$ may be written as

$$\sigma_{\text{inel}}(s) = \int d^2b \gamma_{pp}(s, b), \quad (3.16)$$

with the profile function $\gamma_{pp}(s, b)$ representing all diagrams with at least one cut Pomeron. We defined as well the corresponding quantity $\bar{\gamma}_{pp}(s, b)$ representing all diagrams with zero cut Pomerons. We demonstrated that the sum of these two quantities is one (2.64),

$$\gamma_{pp}(s, b) + \bar{\gamma}_{pp}(s, b) = 1, \quad (3.17)$$

which represents a unitarity relation. The function Φ_{pp} enters finally, since we have the relation

$$\bar{\gamma}_{pp}(s, b) = \Phi_{pp}(1, 1, s, b). \quad (3.18)$$

Based on these formulas, we interpret $\bar{\gamma}_{pp}(s, b) = \Phi_{pp}(1, 1, s, b)$ as the probability of having no interaction, whereas $\gamma_{pp}(s, b) = 1 - \Phi_{pp}(1, 1, s, b)$ represents the probability to have an interaction, at given impact parameter and energy. Such an interpretation of course only makes sense as long as any of the γ 's is positive, otherwise unitarity is said to be violated, even if the equation (3.17) still holds.

In fig. 3.4, we plot Φ_{pp} as a function of $x = x^+x^-$ for $\sqrt{s} = 200$ GeV for two different values of b . The curve for $b = 1.5$ fm (solid curve) is close to one with a minimum of about 0.8 at $x = 1$. The x -dependence for $b = 0$ fm (dashed curve) is much more dramatic: the curve deviates from 1 already at relatively small values of x and drops finally to negative values at $x = 1$. The values for

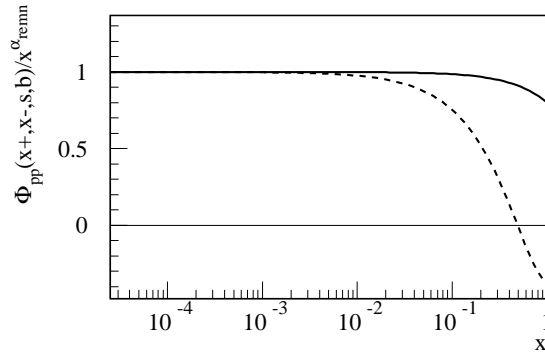


Figure 3.4: The expression $\Phi_{pp}(x^+, x^-, s, b) / x^{\alpha_{\text{remn}}}$ as a function of $x = x^+x^-$ for $b = 0$ (dashed) and for $b = 1.5$ fm (solid curve).

$x = 1$ are of particular interest, since $1 - \Phi_{pp}(1, 1, s, b) = \gamma_{pp}(s, b)$ represents the profile function in the sense that the integration over b provides the inelastic non-diffractive cross section. Therefore, in fig. 3.5, we plot the b -dependence of $1 - \Phi_{pp}(1, 1, s, b)$, which increases beyond 1 for small values

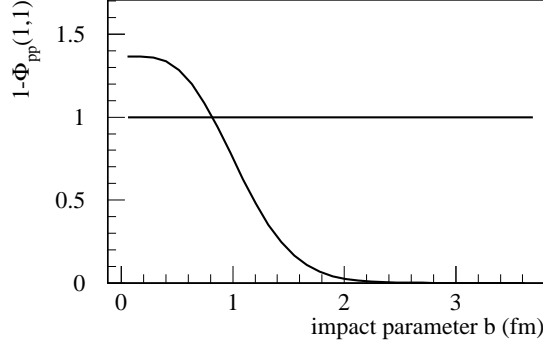


Figure 3.5: The profile function $1 - \Phi_{pp}(1, 1, s, b)$ as a function of impact parameter b . This function should represent the probability to have an interaction at a given impact parameter.

of b , since Φ_{pp} is negative in this region, as discussed above for the case of $b = 0$ fm. On the other hand, an upper limit of 1 is really necessary in order to assure unitarity. So the fact that Φ_{pp} grows to values bigger than one is a manifestation of unitarity violation.

In the following, we try to understand the physical reason for this unitarity problem. We are going to show, that it is intimately related to the fact that in our approach AGK cancelations are fulfilled, as shown earlier, which means that any approach where AGK cancelations apply will have exactly the same problem.

We are going to demonstrate in the following that AGK cancelations imply automatically unitarity violation. The average light cone momentum taken by a Pomeron may be calculated from the Pomeron inclusive spectrum dn_{Pom}/dx^+dx^- as

$$\langle x^+ \rangle = \int dx^+ x^+ \left\{ \frac{1}{\sigma_{\text{inel}}(s)} \int d^2b \int dx^- \frac{dn_{\text{Pom}}}{dx^+dx^-}(x^+, x^-, s, b) \right\}. \quad (3.19)$$

If AGK cancelations apply, we have

$$dn_{\text{Pom}}/dx^+dx^- = dn_{\text{Pom}}^{(1)}/dx^+dx^- = G(x^+, x^-, s, b) F_{\text{remn}}(x^+) F_{\text{remn}}(x^-), \quad (3.20)$$

and therefore

$$\frac{dn_{\text{Pom}}}{dx^+dx^-}(x^+, x^-, s, b) = \mu(s) (x^+ x^- s)^{\Delta(s)} e^{-\frac{b^2}{\lambda(s)}} f(x^+) f(x^-), \quad (3.21)$$

where $\Delta(s)$ is bigger than zero and increases with energy and $\mu(s)$ and $\lambda(s)$ depend weakly (logarithmically) on s , whereas f is an energy independent function. We obtain

$$\langle x^+ \rangle = \frac{\gamma(s) s^{\Delta(s)}}{\sigma_{\text{inel}}(s)}, \quad (3.22)$$

where $\gamma(s)$ depends only logarithmically on s . Since $\langle x^+ \rangle$ must be smaller or equal to one, we find

$$\sigma_{\text{inel}}(s) \geq \gamma(s) s^{\Delta(s)}, \quad (3.23)$$

which violates the Froissard bound and therefore unitarity. This problem is related to the old problem of unitarity violation in case of single Pomeron exchange. The solution appeared to be the observation that one needs to consider multiple scattering such that virtual multiple emissions provide sufficient screening to avoid the unreasonably fast increase of the cross section. If AGK cancelations apply (as in our model), the problem comes back by considering inclusive spectra, since these are determined by single scattering.

Thus, we have shown that *a consistent application of the eikonal Pomeron scheme both to interaction cross sections and to particle production calculations unavoidably leads to the violation of the unitarity*. This problem is not observed in many models currently used, since there simply no consistent treatment is provided, and the problem is therefore hidden. The solution of the unitarity problem requires to employ the full Pomeron scheme, which includes also so-called enhanced Pomeron diagrams, to be discussed later. The simplest diagram of that kind - so-called Y-diagram, for example, contributes a negative factor to all inclusive particle distributions in the particle rapidity region $y_0 < y < Y$, where Y is the total rapidity range for the interaction and y_0 corresponds to the rapidity position of the Pomeron self-interaction vertex. Thus, one speaks about breaking of the AGK-cancellations in the sense that one gets corrections to all inclusive quantities calculated from just one Pomeron exchange graph [19]. In particular, presenting the inclusive Pomeron distribution $d\sigma_{\text{Pom}}(x^+, x^-)/dx^+ dx^-$ by the formula (2.75) implies that the functions $f(x^\pm)$ acquire a dependence on the energy of the interaction s . It is this dependence which is expected to slow down the energy increase of the Pomeron number and thus to cure the unitarity problem.

So we think it is mandatory to proceed in the following way: first one needs to provide a consistent treatment of cross sections and particle production, which will certainly lead to unitarity problems, and second one has to refine the theory to solve the unitarity problem in a consistent way, via screening corrections. The first part of this program is provided in this paper, the second one will be treated in some approximate fashion later, but a rigorous, self-consistent treatment of this second has still to be done.

3.4 A Phenomenological Solution: Unitarization of Φ

As we have seen in the preceding sections, unitarity violation manifests itself by the fact that the virtual emission function Φ_{pp} appears to be negative at high energies and small impact parameter for large values of x^+ and x^- , particularly for $x^+ = x^- = 1$. What is the mathematical origin of these negative values? In eq. (3.15), the sums over r_i contains terms of the form $(\dots)^{r_i}/r_i!$ and an additional factor of the form

$$\left\{ \frac{\Gamma(1 + \alpha_{\text{remn}})}{\Gamma(1 + \alpha_{\text{remn}} + r_1 \tilde{\beta}_1 + \dots + r_N \tilde{\beta}_N)} \right\}. \quad (3.24)$$

It is this factor which causes the problem, as it strongly suppresses contributions of terms with large r_i , which are important when the interaction energy s increases. Physically it is connected to the reduced phase space in case of too many virtual Pomerons emitted. By dropping this factor one would obtain a simple exponential function which is definitely positive.

Our strategy is to modify the scheme such that Φ_{pp} stays essentially unchanged for values of s , b , x^+ , and x^- , where Φ_{pp} is positive and that Φ_{pp} is “corrected” to assure positive values in regions where it is negative. We call this procedure “unitarization”, which should not be considered as an approximation, since one is really changing the physical content of the theory. This is certainly only a phenomenological solution of the problem, the correct procedure should amount to taking into account the mentioned screening corrections due to enhanced Pomeron diagrams, which should provide a “natural unitarization”. Nevertheless we consider our approach as a necessary first step towards a consistent formulation of multiple scattering theory in nuclear (including hadron-hadron) collisions at very high energies.

Let us explain our “unitarization” in the following. We define

$$g(z) = \frac{\Gamma(1 + \alpha_{\text{remn}})}{\Gamma(1 + \alpha_{\text{remn}} + z)} \quad (3.25)$$

such that

$$g(r_1 \tilde{\beta}_1 + \dots + r_N \tilde{\beta}_N) \quad (3.26)$$

is the factor causing unitarity problems. This expression should be of the form

$$(\dots)^{r_1} \dots (\dots)^{r_N},$$

which would make Φ_{AB} a well behaved exponential function. In order to achieve this, the function g should be an exponential. So we replace $g(z)$ by $g_e(z)$, where the latter function is defined as

$$g_e(z) = e^{-\epsilon_e z}, \quad (3.27)$$

where the parameter ϵ_e should be chosen such that $g(z)$ is well approximated for values of z between (say) 0 and 0.5 (see fig. 3.6). The index “e” refers to “exponentiation”. So, we replace the factor

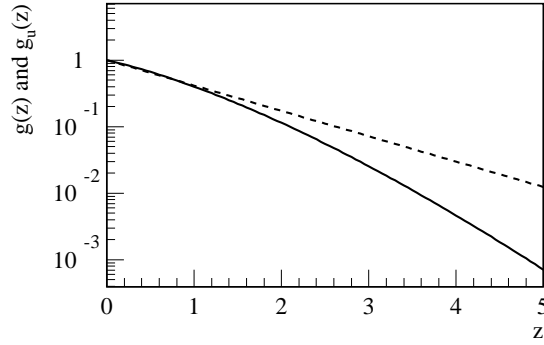


Figure 3.6: Function $g(z)$ (full line) and unitarized function $g_u(z)$ (dashed).

$g(r_1\tilde{\beta}_1 + \dots + r_N\tilde{\beta}_N)$ by

$$g_e(r_1\tilde{\beta}_1 + \dots + r_N\tilde{\beta}_N) = e^{-\epsilon_e(r_1\tilde{\beta}_1 + \dots + r_N\tilde{\beta}_N)} \quad (3.28)$$

$$= \left(e^{-\epsilon_e\tilde{\beta}_1}\right)^{r_1} \dots \left(e^{-\epsilon_e\tilde{\beta}_N}\right)^{r_N}, \quad (3.29)$$

and obtain correspondingly instead of Φ_{pp}

$$\begin{aligned} \Phi_{e_{pp}}(x^+, x^-, s, b) &= x^{\alpha_{\text{remn}}} \sum_{r_1=0}^{\infty} \dots \sum_{r_N=0}^{\infty} \left(e^{-2\epsilon_e\tilde{\beta}_1}\right)^{r_1} \dots \left(e^{-2\epsilon_e\tilde{\beta}_N}\right)^{r_N} \\ &\times \frac{(-\alpha_1 x^{\tilde{\beta}_1} \Gamma^2(\tilde{\beta}_1))^{r_1}}{r_1!} \dots \frac{(-\alpha_N x^{\tilde{\beta}_N} \Gamma^2(\tilde{\beta}_N))^{r_N}}{r_N!}. \end{aligned} \quad (3.30)$$

Now the sums can be performed and we get

$$\Phi_{e_{pp}}(x^+, x^-, s, b) = x^{\alpha_{\text{remn}}} \prod_{i=1}^N \exp \left\{ -\alpha_i x^{\tilde{\beta}_i} \Gamma^2(\tilde{\beta}_i) e^{-2\epsilon_e\tilde{\beta}_i} \right\} \quad (3.31)$$

which may be written as

$$\Phi_{e_{pp}}(x^+, x^-, s, b) = (x^+ x^-)^{\alpha_{\text{remn}}} \exp \left\{ -\tilde{G}(x^+ x^-, s, b) \right\} \quad (3.32)$$

with

$$\tilde{G}(x, s, b) = \sum_{i=1}^N \tilde{\alpha}_i x^{\tilde{\beta}_i} \quad (3.33)$$

with

$$\tilde{\alpha}_i = \alpha_i \Gamma^2(\tilde{\beta}_i) e^{-2\epsilon_e \tilde{\beta}_i} \quad (3.34)$$

$$\tilde{\beta}_i = \beta_i + 1, \quad (3.35)$$

where α_i and β_i are given as

$$\alpha_i = (\alpha_{D_i} + \alpha_{D_i}^*) s^{(\beta_{D_i} + \gamma_{D_i} b^2)} e^{-\frac{b^2}{\beta_{D_i}}}, \quad (3.36)$$

$$\beta_i = \beta_{D_i} + \beta_{D_i}^* + \gamma_{D_i} b^2 - \alpha_{\text{part}}, \quad (3.37)$$

with $\alpha_{D_i}^* \neq 0$ and $\beta_{D_i}^* \neq 0$ only if $\alpha_{D_i} \neq 0$.

We are not yet done. We modified Φ_{pp} such that the new function $\Phi_{e_{pp}}$ is surely positive. But what happened to our unitarity equation? If we replace Φ_{pp} by $\Phi_{e_{pp}}$, we obtain

$$\bar{\gamma}_{pp} + \gamma_{pp} = \sum_{m=0}^{\infty} \int dX^+ dX^- \Omega_{e_{pp}}^{(s,b)}(m, X^+, X^-), \quad (3.38)$$

with

$$\Omega_{e_{pp}}^{(s,b)}(m, X^+, X^-) = \left\{ \frac{1}{m!} \prod_{\mu=1}^m G(s, x_{\mu}^+, x_{\mu}^-, b) \right\} \Phi_{e_{pp}}(x^+, x^-, s, b), \quad (3.39)$$

where x^+ and x^- refer to the remnant light cone momenta. Since $\Phi_{e_{pp}}$ is always bigger than Φ_{pp} for small values of b , the sum $\gamma_{pp} + \bar{\gamma}_{pp}$ is bigger than one, so the unitarity equation does not hold any more. This is quite natural, since we modified the virtual emissions without caring about the real ones. In order to account for this, we define

$$Z(s, b) = \sum_{m=0}^{\infty} \int dX^+ dX^- \left\{ \frac{1}{m!} \prod_{\mu=1}^m G(s, x_{\mu}^+, x_{\mu}^-, b) \right\} \Phi_{e_{pp}}(x^+, x^-, s, b), \quad (3.40)$$

which is equal to one in the exact case, but which is different from one if we use $\Phi_{e_{pp}}$ instead of Φ_{pp} . In order to recover the unitarity equation, we have to “renormalize” $\Phi_{e_{pp}}$, and we define therefore the “unitarized” virtual emission function $\Phi_{u_{pp}}$ via

$$\Phi_{u_{pp}}(x^+, x^-, s, b) = \frac{\Phi_{e_{pp}}(x^+, x^-, s, b)}{Z(s, b)}. \quad (3.41)$$

Now, the unitarity equation holds,

$$\bar{\gamma}_{pp} + \gamma_{pp} = \sum_{m=0}^{\infty} \int dX^+ dX^- \Omega_{u_{pp}}^{(s,b)}(m, X^+, X^-) = 1, \quad (3.42)$$

with

$$\Omega_{u_{pp}}^{(s,b)}(m, X^+, X^-) = \left\{ \frac{1}{m!} \prod_{\mu=1}^m G(s, x_{\mu}^+, x_{\mu}^-, b) \right\} \Phi_{u_{pp}}(x^+, x^-, s, b) \quad (3.43)$$

being strictly positive, which allows finally the probability interpretation.

3.5 Properties of the Unitarized Theory

We are now going to investigate the consequences of our unitarization, in other words, how the results are affected by this modification. In fig. 3.7 we compare the exact and the exponentiated version of the virtual emission function (Φ_{pp} and Φ_{epp}) for a large value of the impact parameter ($b = 1.5$ fm). The exponentiated result (dashed) is somewhat below the exact one (solid curve), but the difference is quite small. The situation is somewhat different in case of zero impact parameter

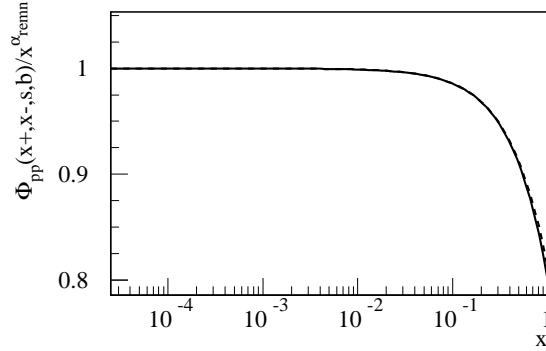


Figure 3.7: Behavior of $\Phi_{pp}(x^+, x^-, s, b) / (x^+ x^-)^{\alpha_{remn}}$ as a function of $x = x^+ x^-$, for the exact function (solid) and the exponentiated one (dashed curve) for impact parameter $b = 1.5$ fm.

b . For small values of x the two curves coincide more or less, however for $x = 1$ the exponentiated result (dashed) is well above the exact one (solid curve). In particular, and this is most important, the dashed curve rests positive and in this sense corrects for the unphysical behavior (negative values) for the exact curve. The behavior for $x = 1$ for different values of b is summarized in

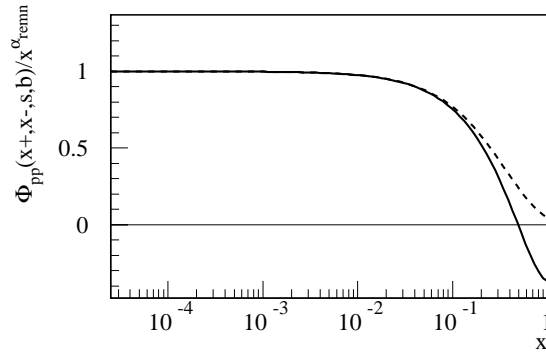


Figure 3.8: Behavior of $\Phi_{pp}(x^+, x^-, s, b) / (x^+ x^-)^{\alpha_{remn}}$ as a function of $x = x^+ x^-$, for the exact function (solid) and the exponentiated one (dashed curve) for impact parameter $b = 0$ fm.

fig. 3.9, where we plot $1 - \Phi_{pp}(1, 1, s, b)$ as a function of b . We clearly observe that for large b exact (solid) and exponentiated (dashed curve) result agree approximately, whereas for small values of b they differ substantially, with the exponentiated version always staying below 1, as it should be. So the effect of our exponentiation is essentially to push the function below 1.

Next we calculate explicitly the normalization function $Z(s, b)$. We have

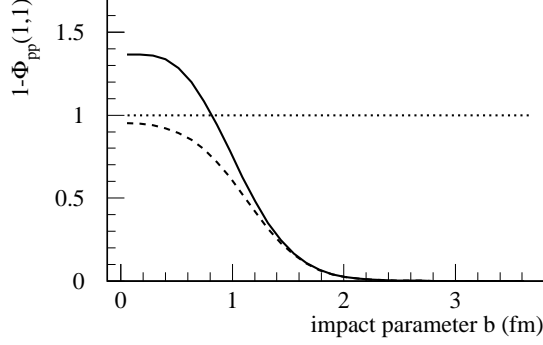


Figure 3.9: The function $1 - \Phi_{pp}(1, 1, s, b)$ as a function of impact parameter b . We show the exact result (solid) as well as the exponentiated one (dashed curve).

$$Z(s, b) = \sum_{m=0}^{\infty} \int \prod_{\mu=1}^m dx_{\mu}^{+} dx_{\mu}^{-} \frac{1}{m!} \prod_{\mu=1}^m G(x_{\mu}^{+}, x_{\mu}^{-}, s, b) \times \Phi_{e_{pp}} \left(1 - \sum_{\nu=1}^m x_{\nu}^{+}, 1 - \sum_{\nu=1}^m x_{\nu}^{-} \right), \quad (3.44)$$

which may be written as

$$Z(s, b) = \Phi_{e_{pp}}(1, 1, s, b) + \int dz^{+} dz^{-} H(z^{+}, z^{-}) \Phi_{e_{pp}}(z^{+}, z^{-}, s, b), \quad (3.45)$$

with

$$H(z^{+}, z^{-}) = \sum_{m=1}^{\infty} \int \prod_{\mu=1}^m dx_{\mu}^{+} dx_{\mu}^{-} \frac{1}{m!} \prod_{\mu=1}^m G(x_{\mu}^{+}, x_{\mu}^{-}, s, b) \times \delta \left(1 - z^{+} - \sum_{\mu=1}^m x_{\mu}^{+} \right) \delta \left(1 - z^{-} - \sum_{\mu=1}^m x_{\mu}^{-} \right). \quad (3.46)$$

Using the analytical form of G , we obtain

$$H(z^{+}, z^{-}) = \underbrace{\sum_{r_1=0}^{\infty} \dots \sum_{r_N=0}^{\infty}}_{r_1 + \dots + r_N \neq 0} \frac{[(1 - z^{+})(1 - z^{-})]^{r_1 \tilde{\beta}_1 + \dots + r_N \tilde{\beta}_N - 1}}{\Gamma(r_1 \tilde{\beta}_1 + \dots + r_N \tilde{\beta}_N)^2} \times \frac{(\alpha_1 \Gamma(\tilde{\beta}_1)^2)^{r_1}}{r_1!} \dots \frac{(\alpha_N \Gamma(\tilde{\beta}_N)^2)^{r_N}}{r_N!} \quad (3.47)$$

(see appendix D.2). This can be calculated, and after numerically doing the integration over z^{+}, z^{-} , we obtain the normalization function $Z(s, b)$, as shown in fig. 3.10. We observe, as expected, a value close to unity at large values of b , whereas for small impact parameter $Z(s, b)$ is bigger than one, since only at small values of b the virtual emission function Φ_{pp} has been changed substantially towards bigger values.

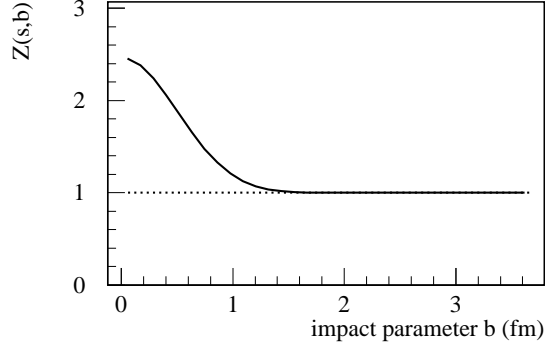


Figure 3.10: The normalization function $Z(s, b)$ as a function of the impact parameter b .

Knowing $\Phi_{e_{pp}}$ and Z , we are ready to calculate the unitarized emission functions $\Phi_{u_{pp}}$ which finally replaces Φ_{pp} in all formulas for cross section calculations. The results are shown in fig. 3.11, where we plot $1 - \Phi_{u_{pp}}$ together with $1 - \Phi_{e_{pp}}$ and $1 - \Phi_{pp}$ for both x^+ and x^- being one. We

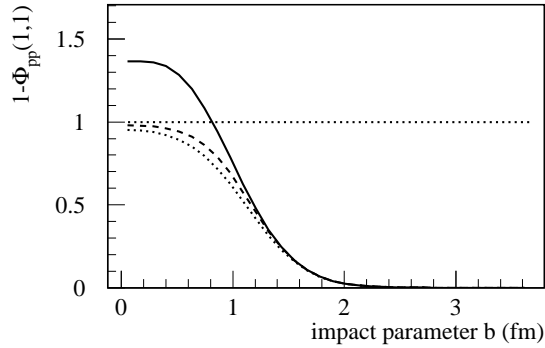


Figure 3.11: The function $1 - \Phi_{pp}(1, 1, s, b)$ as a function of the impact parameter b . We show the exact result $1 - \Phi_{pp}$ (solid line) as well as the unitarized one $1 - \Phi_{u_{pp}}$ (dashed) and the exponentiated one $1 - \Phi_{e_{pp}}$ (dotted).

observe that compared to $1 - \Phi_{e_{pp}}$ the function $1 - \Phi_{u_{pp}}$ is somewhat increased at small values of b due to the fact that here $Z(s, b)$ is bigger than one, whereas for large impact parameters there is no difference.

Since the unitarity equation holds, we may integrate $1 - \Phi_{u_{pp}}(1, 1, s, b)$ over impact parameter, to obtain the inelastic non-diffractive cross section,

$$\sigma_{\text{inel}}(s) = \int d^2b \{1 - \Phi_{u_{pp}}(1, 1, s, b)\}, \quad (3.48)$$

the result being shown in fig. 3.12. Here the exact and the unitarized result (using Φ_{pp} and $\Phi_{u_{pp}}$ respectively) are quite close due to the fact that one has a two-dimensional b -integration, and therefore the small values of b , where we observe the largest differences, do not contribute much to the integral.

We now turn to inclusive spectra. We consider the inclusive x -spectrum of Pomerons, dn_{Pom}/dx , where $x = x^+x^-$ is the squared mass of the Pomeron divided by s . In the exact theory, we may

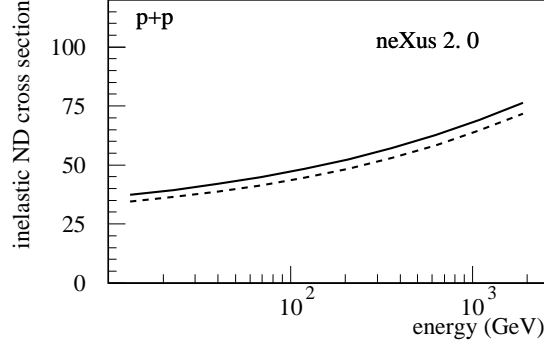


Figure 3.12: The inelastic non-diffractive cross section as a function of the energy, using the exact (solid) and the unitarized (dashed) Φ -function.

take advantage of the AGK cancelations, and obtain

$$\frac{dn_{\text{Pom}}}{dx}(x, s, b) = \int_{+\ln \sqrt{x}}^{-\ln \sqrt{x}} dy \frac{dn_{\text{Pom}}^{(1)}(x^+, x^-, s, b)}{dx^+ dx^-} \Big|_{x^+ = \sqrt{x} e^y, x^- = \sqrt{x} e^{-y}}, \quad (3.49)$$

where $dn_{\text{Pom}}^{(1)}/dx^+ dx^-$ is the corresponding inclusive distribution for one single elementary interaction, which is given in eq. (2.75). The y -integration can be easily performed numerically, and we obtain the results shown in fig. 3.13 as solid curves, the upper one for $b = 0$ fm and the lower one for $b = 1.5$ fm. The calculation of the unitarized result is more involved, since now we cannot use

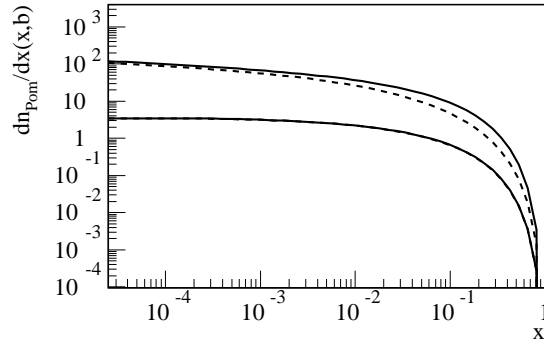


Figure 3.13: Example of an inclusive spectrum: x -distribution of Pomerons. The variable x is defined as $x = x^+ x^-$ and is therefore the squared mass of the Pomeron divided by s . We show the exact (solid) and the unitarized results (dashed) for $b = 0$ fm (upper curves) and $b = 1.5$ fm (lower curves). In fact, for $b = 1.5$ fm the two curves coincide.

the AGK cancelations any more. We have

$$\begin{aligned} \frac{dn_{\text{Pom}}}{dx^+ dx^-}(x^+, x^-, s, b) &= \sum_{m=1}^{\infty} \int \prod_{\mu=1}^m dx_{\mu}^+ dx_{\mu}^- \\ &\times \frac{1}{m!} \prod_{\mu=1}^m \{G(x_{\mu}^+, x_{\mu}^-, s, b)\} \Phi_{u_{pp}}(1 - \sum_{\mu=1}^m x_{\mu}^+, 1 - \sum_{\mu=1}^m x_{\mu}^-, s, b) \end{aligned}$$

$$\times \sum_{\mu'=1}^m \delta(x^+ - x_{\mu'}^+) \delta(x^- - x_{\mu'}^-), \quad (3.50)$$

where we used the unitarized version of Φ_{pp} . We find

$$\begin{aligned} \frac{dn_{\text{Pom}}}{dx^+ dx^-}(x^+, x^-, s, b) &= G(x^+, x^-, s, b) \\ &\times \left[\Phi_{\text{u}pp}(1 - x^+, 1 - x^-, s, b) \right. \\ &\quad \left. + \int dz^+ dz^- H(z^+ + x^+, z^- + x^-) \Phi_{\text{u}pp}(z^+, z^-, s, b) \right], \end{aligned} \quad (3.51)$$

where H is defined in eq. (3.46), with the final result given in eq. (3.47). The integration over z^+, z^- can now be done numerically. Expressing x^+ and x^- via x and y and integrating over y , we finally obtain dn_{Pom}/dx , as shown in fig. 3.13 (dashed curves). In fig. 3.14 we show the b-averaged

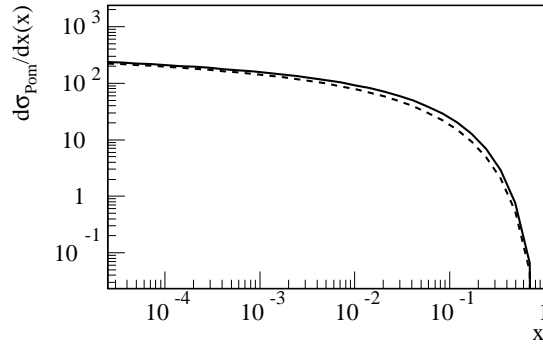


Figure 3.14: The x -distribution of Pomerons, averaged over impact parameter. We show the exact (solid) and the unitarized results (dashed).

inclusive spectra, which are given as

$$\frac{1}{\sigma_{\text{inel}}} \int d^2b \frac{dn_{\text{Pom}}}{dx}(x, s, b) \quad (3.52)$$

for both, the exact and the unitarized version.

3.6 Comparison with the Conventional Approach

At this point it is noteworthy to compare our approach with the conventional one [20, 21]. There one neglects the energy conservation effects in the cross section calculation and sums up virtual Pomeron emissions, each one taken with the initial energy of the interaction s . We can recover the conventional approach by simply considering independent (planar) emission of all the Pomerons, neglecting energy-momentum sharing between them. In the cross section formulas (2.65-3.58) this amounts to perform formally the convolutions of the Pomeron eikonals $G(x^+, x^-, s, b)$ with the remnant functions $F_{\text{remn}}(x^\pm)$ for all the Pomerons. In case of proton-proton scattering, we then get

$$\Phi_{\text{conv}pp}(x^+, x^-, s, b) = e^{-\chi(s, b)}, \quad (3.53)$$

with

$$\chi(s, b) = \int dx^+ dx^- G(x^+, x^-, s, b) F_{\text{remn}}(x^+) F_{\text{remn}}(x^-), \quad (3.54)$$

where Φ does not depend on x^+ and x^- anymore. We obtain a unitarity relation of the form

$$\sum_{m=0}^{\infty} \Omega_m = 1, \quad (3.55)$$

with

$$\Omega_m = \frac{(\chi(s, b))^m}{m!} e^{-\chi(s, b)} \quad (3.56)$$

representing the probability of having m cut Pomerons (Pomeron multiplicity distribution). So in the traditional case, the Pomeron multiplicity distribution is a Poissonian with the mean value given by $\chi(s, b)$. As already mentioned above, that approach is not self-consistent as the AGK rules are assumed to hold when calculating interaction cross sections but are violated at the particle production generation. This inconsistency was already mentioned in [4], where the necessity to develop the correct, Feynman diagram-based scheme, was first argued.

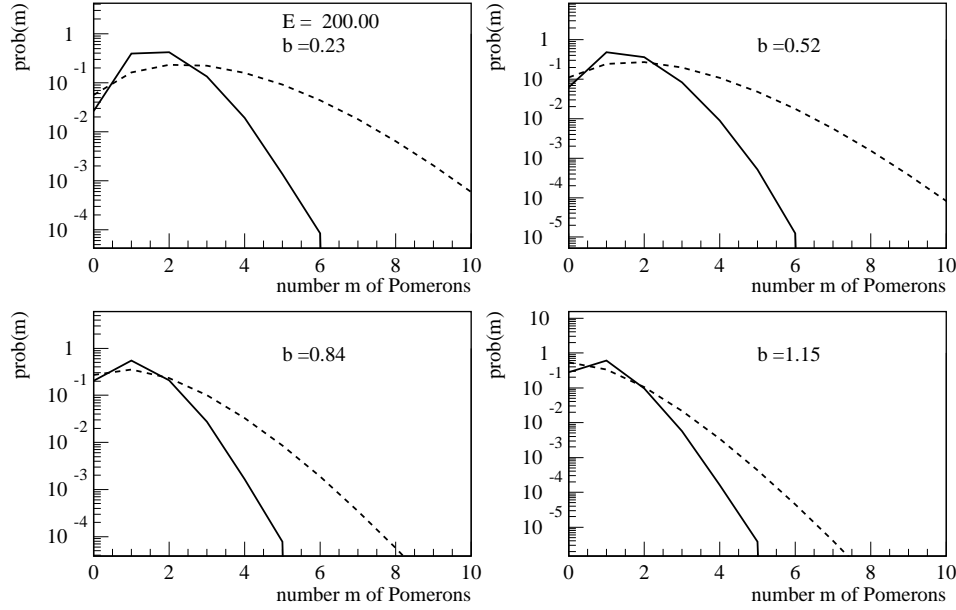


Figure 3.15: Distribution of the number m of Pomerons for different impact parameters. We show the results of a full simulation (solid lines) as well as the Poissonian distribution obtained by ignoring energy conservation (dashed line).

The exact procedure is based on the summation over virtual emissions with the energy-momentum conservation taken into account. This results in the formula (3.7) or, using our parametrization, (3.15) for $\Phi_{pp}(x^+, x^-, s, b)$, explicitly dependent on the momentum, left after cut Pomerons emission, and in the formula

$$\sigma_{\text{inel}}(s) = \int d^2b \{1 - \Phi_{pp}(1, 1, s, b)\} \quad (3.57)$$

for the inelastic cross section; AGK rules are exactly fulfilled both for the cross sections and for the particle production. But with the interaction energy increasing the approach starts to violate the unitarity and is no longer self-consistent.

The "unitarized" procedure, which amounts to replacing Φ_{pp} by $\Phi_{u_{pp}}$, allows to avoid the unitarity problems. The expressions for cross sections and for inclusive spectra are consistent with each other and with the particle generation procedure. The latter one assures the AGK cancelations

validity in the region, where unitarity problems do not appear yet (not too high energies or large impact parameters).

In order to see the effect of energy conservation we calculate χ as given in eq. (3.54) with the same parameters as we use in our approach for different values of b , and we show the corresponding Pomeron multiplicity distribution in fig. 3.15 as dashed lines. We compare this traditional approach with our full simulation, where energy conservation is treated properly (solid lines in the figures). One observes a huge difference between the two approaches. So energy conservation makes the Pomeron multiplicity distributions much narrower, in other words, the mean number of Pomerons is substantially reduced. The reason is that due to energy conservation the phase space of light cone momenta of the Pomeron ends is considerably reduced.

Of course, in the traditional approach one chooses different parameters in order to obtain reasonable values for the Pomeron numbers in order to reproduce the experimental cross sections. But this only “simulates” in some sense the phase space reduction due to energy conservation in an uncontrolled way.

We conclude that considering energy conservation properly in the cross section formulas has an enormous effect and cannot be neglected.

3.7 Unitarization for Nucleus-Nucleus Scattering

In this section, we discuss the unitarization scheme for nucleus-nucleus scattering. The sum over virtual emissions is defined as

$$\begin{aligned} \Phi_{AB}(X^+, X^-, s, b) &= \sum_{l_1} \dots \sum_{l_{AB}} \int \prod_{k=1}^{AB} \left\{ \prod_{\lambda=1}^{l_k} d\tilde{x}_{k,\lambda}^+ d\tilde{x}_{k,\lambda}^- \right\} \prod_{k=1}^{AB} \left\{ \frac{1}{l_k!} \prod_{\lambda=1}^{l_k} -G(\tilde{x}_{k,\lambda}^+, \tilde{x}_{k,\lambda}^-, s, b) \right\} \\ &\times \prod_{i=1}^A F_{\text{remn}} \left(x_i^+ - \sum_{\pi(k)=i} \tilde{x}_{k,\lambda}^+ \right) \prod_{j=1}^B F_{\text{remn}} \left(x_j^- - \sum_{\tau(k)=j} \tilde{x}_{k,\lambda}^- \right). \end{aligned} \quad (3.58)$$

where $X^+ = \{x_1^+ \dots x_A^+\}$, $X^- = \{x_1^- \dots x_B^-\}$ and $\pi(k)$ and $\tau(k)$ represent the projectile or target nucleon linked to pair k . This calculation is very close to the calculation for proton-proton scattering. Using the expression eq. (3.10) of $G(\tilde{x}_{k,\lambda}^+, \tilde{x}_{k,\lambda}^-, s, b)$, the definition eq. (3.8) of $F_{\text{remn}}(x)$, one finally finds

$$\begin{aligned} \Phi_{AB}(X^+, X^-, s, b) &= \\ &\sum_{r_{1,1} \dots r_{N,1}} \dots \sum_{r_{1,AB} \dots r_{N,AB}} \prod_{k=1}^{AB} \frac{(-\alpha_1)^{r_{1,k}}}{r_{1,k}!} \dots \frac{(-\alpha_N)^{r_{N,k}}}{r_{N,k}!} \\ &\prod_{i=1}^A (x_i^+)^{\alpha_{\text{remn}}} \prod_{\pi(k)=i} \left(\Gamma(\tilde{\beta}_1)(x_i^+)^{\tilde{\beta}_1} \right)^{r_{1,k}} \dots \left(\Gamma(\tilde{\beta}_N)(x_i^+)^{\tilde{\beta}_N} \right)^{r_{N,k}} g \left(\sum_{\pi(k)=i} r_{1,k} \tilde{\beta}_1 + \dots + r_{N,k} \tilde{\beta}_N \right) \\ &\prod_{j=1}^B (x_j^-)^{\alpha_{\text{remn}}} \prod_{\tau(k)=j} \left(\Gamma(\tilde{\beta}_1)(x_j^-)^{\tilde{\beta}_1} \right)^{r_{1,k}} \dots \left(\Gamma(\tilde{\beta}_N)(x_j^-)^{\tilde{\beta}_N} \right)^{r_{N,k}} g \left(\sum_{\tau(k)=j} r_{1,k} \tilde{\beta}_1 + \dots + r_{N,k} \tilde{\beta}_N \right) \end{aligned} \quad (3.59)$$

(see appendix D.3), where the function $g(z)$ is defined in eq. (3.25), and the parameters α_i and $\tilde{\beta}_i$ are the same ones as for proton-proton scattering.

In case of nucleus-nucleus scattering, we use the same unitarization prescription as already applied to proton-proton scattering. The first step amounts to replace the function $g(z)$, which

appears in the final expression of Φ_{AB} , by the exponential form $g_e(z)$. This allows to perform the sums in eq. (D.66), and we obtain

$$\Phi_{eAB}(X^+, X^-, s, b) = \prod_{i=1}^A (x_i^+)^{\alpha_{\text{remn}}} \prod_{j=1}^B (x_j^-)^{\alpha_{\text{remn}}} \prod_{k=1}^{AB} e^{-2\tilde{G}(x_{\pi(k)}^+, x_{\tau(k)}^-)} \quad (3.60)$$

(see appendix D.3), where $\tilde{G}(x)$ is defined in eq. (3.33). Having modified Φ , the unitarity equation

$$\sum_m \int dX^+ dX^- \Omega_{eAB}^{(s,b)}(m, X^+, X^-) = 1 \quad (3.61)$$

does not hold any more, since Ω_e depends on Φ_e , and only the exact Φ assures a correct unitarity relation. So as in proton-proton scattering, we need a second step, which amounts to renormalizing Φ_e . So we introduce a normalization factor

$$Z_{AB}(s, b) = \sum_m \int dX^+ dX^- \Omega_{eAB}^{(s,b)}(m, X^+, X^-), \quad (3.62)$$

with Ω_{eAB} defined in the same way as Ω but with Φ_{AB} replaced by Φ_{eAB} , which allows to define the unitarized Φ_{uAB} function as

$$\Phi_{uAB}(x^+, x^-, s, b) = \frac{\Phi_{eAB}(x^+, x^-, s, b)}{Z_{AB}(s, b)}. \quad (3.63)$$

In this way we recover the unitarity relation,

$$\sum_m \int dX^+ dX^- \Omega_{uAB}^{(s,b)}(m, X^+, X^-) = 1, \quad (3.64)$$

with

$$\Omega_{uAB}^{(s,b)}(m, X^+, X^-) = \prod_{k=1}^{AB} \left\{ \frac{1}{m_k!} \prod_{\mu=1}^{m_k} G(s, x_{k,\mu}^+, x_{k,\mu}^-, b) \right\} \Phi_{uAB}(x^+, x^-, s, b), \quad (3.65)$$

and $\Omega_{uAB}^{(s,b)}(m, X^+, X^+)$ may be interpreted as probability distribution for configurations (m, X^+, X^+) .

3.8 Profile Functions in Nucleus-Nucleus Scattering

In case of nucleus-nucleus scattering, the conventional approach [20, 21] represents a ‘‘Glauber-type model’’, where nucleus-nucleus scattering may be considered as a sequence of nucleon-nucleon scatterings with constant cross sections; the nucleons move through the other nucleus along straight line trajectories. In order to test this picture, we consider all pairs of nucleons, which due to their distributions inside the nuclei provide a more or less flat b -distribution. We then simply count, for a given b -bin, the number of interacting pairs and then divide by the number of pairs in the corresponding bin. The resulting distribution, which we call nucleon-nucleon profile function for nucleus-nucleus scattering, represents the probability density of an interaction of a pair of nucleons at given impact parameter. This may be compared with the proton-proton profile function $1 - \Phi_{uPP}(1, 1, s, b)$. In the Glauber model, these two distributions coincide. As demonstrated in fig.3.16 for S+S scattering this is absolutely not the case. The profile function in case of S+S scattering is considerably reduced as compared to the proton-proton one. Since integrating the proton-proton profile function represents the inelastic cross section, one may also define the corresponding integral in nucleus-nucleus scattering as ‘‘individual nucleon-nucleon cross section’’. So we conclude that this cross section is smaller than the proton-proton cross section. This is due to the energy conservation, which reduces the number of Pomerons connected to any nucleon from the projectile and the target and finally affects also the ‘‘individual cross section’’.

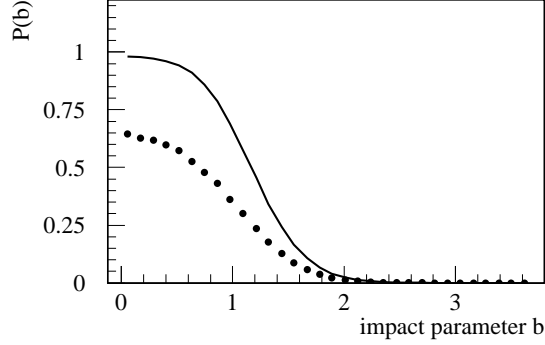


Figure 3.16: The numerically determined profile function in S+S scattering (points) compared to the proton-proton profile function (solid curve).

3.9 Inclusive Cross Sections in Nucleus-Nucleus Scattering

We have shown in the preceding chapter that in the “bare” theory AGK cancelations apply perfectly, which means that nucleus-nucleus inclusive cross sections are just AB times the proton-proton ones,

$$\frac{d\sigma_{\text{incl}}^{AB}}{dq}(q, s, b) = AB \frac{d\sigma_{\text{incl}}^{pp}}{dq}(q, s, b). \quad (3.66)$$

In the unitarized theory, the results is somewhat different. Unfortunately, we cannot calculate cross sections analytically any more, so we perform a numerical calculation using the Markov chain techniques explained later. In order to investigate the deviation from exact AGK cancelations, we calculate the inclusive nucleus-nucleus cross section for Pomeron production (being the basic

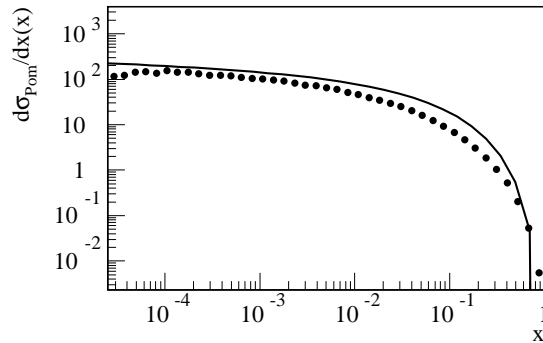


Figure 3.17: Inclusive cross section of Pomeron production for S+S scattering, divided by $AB = 32^2$ (points), compared to the corresponding proton-proton cross section (solid line).

inclusive cross section), divided by AB ,

$$\frac{1}{AB} \frac{d\sigma_{\text{Pom}}^{AB}}{dx}(x, s, b), \quad (3.67)$$

and compare the result with the corresponding proton-proton cross section, see figs. 3.17 and 3.18. For large and for small values of x , we still observe AGK cancelations (the two curves agree), but

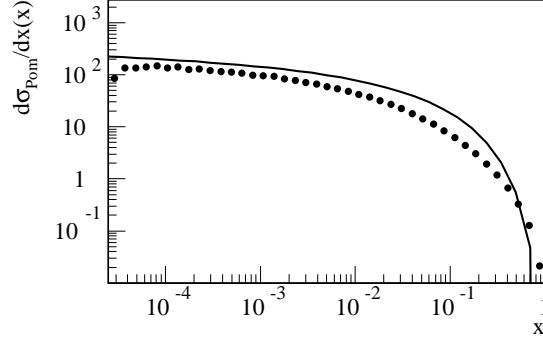


Figure 3.18: Inclusive cross section of Pomeron production for p+ Au scattering, divided by $AB = 197$ (points), compared to the corresponding proton-proton cross section (solid line).

for intermediate values of x , the AGK cancelations are violated, the nucleus-nucleus cross section is smaller than AB times the nucleon-nucleon one. The effect is, however, relatively moderate. If one writes the proton-nucleus cross section as

$$\frac{d\sigma_{\text{Pom}}^{pA}}{dx}(x, s, b) = A^{\alpha(x)} \frac{d\sigma_{\text{Pom}}^{pp}}{dx}, \quad (3.68)$$

we obtain for $\alpha(x)$ values between 0.85 and 1. So one may summarize that “AGK cancelations are violated, but not too strongly”.

Chapter 4

Markov Chain Techniques

In this chapter we discuss how to deal with the multidimensional probability distribution $\Omega_{AB}(K)$ with $K = \{m, X^+, X^-\}$, where the vector m characterizes the type of interaction of each pair of nucleons (the number of elementary interactions per pair), and the matrices X^+ , X^- contain the light cone momenta of all Pomerons (energy sharing between the Pomerons).

4.1 Probability Distributions for Configurations

In this section we essentially repeat the basic formulas of the preceding chapters which allowed us to derive probability distributions for interaction configurations in a consistent way within an effective theory based on Feynman diagrams.

Our basic formula for the inelastic cross section for a nucleus-nucleus collision (which includes also as a particular case proton-proton scattering) could be written in the following form

$$\sigma_{\text{inel}}(s) = \int d^2b_0 \int dT_{AB} \gamma_{AB}(s, b_0, b_1 \dots b_{AB}), \quad (4.1)$$

where dT_{AB} represents the integration over the transverse coordinates b_i^A and b_j^B of projectile and target nucleons, b_0 is the impact parameter between the two nuclei, and $b_k = |\vec{b} + \vec{b}_{\pi(k)}^A - \vec{b}_{\tau(k)}^B|$ is the transverse distance between the nucleons of k^{th} pair. Using the compact notation

$$b = \{b_k\}, \quad m = \{m_k\}, \quad X^+ = \{x_{k,\mu}^+\}, \quad X^- = \{x_{k,\mu}^-\}, \quad (4.2)$$

the function γ_{AB} is given as

$$\gamma_{AB}(s, b) = \sum_m (1 - \delta_{0m}) \int dX^+ dX^- \Omega_{uAB}^{(s,b)}(m, X^+, X^-), \quad (4.3)$$

which represents all diagrams with at least one cut Pomeron. One may define a corresponding quantity $\bar{\gamma}_{AB}$, which represents the configuration with exactly zero cut Pomerons. The latter one can be obtained from (4.3) by exchanging $1 - \delta_{0m}$ by δ_{0m} , which leads to

$$\bar{\gamma}_{AB}(s, b) = \Omega_{uAB}^{(s,b)}(0, 0, 0). \quad (4.4)$$

The expression for Ω is given as

$$\Omega_{uAB}^{(s,b)}(m, X^+, X^-) = \prod_{k=1}^{AB} \left\{ \frac{1}{m_k!} \prod_{\mu=1}^{m_k} G(x_{k,\mu}^+, x_{k,\mu}^-, s, b_k) \right\} \Phi_{uAB}(x^+, x^-, s, b), \quad (4.5)$$

with

$$\begin{aligned} \Phi_{uAB}(x^+, x^-, s, b) &= \frac{1}{Z_{AB}} \prod_{k=1}^{AB} \exp \left(-\tilde{G}(x_{\pi(k)}^+ x_{\tau(k)}^-, s, b_k) \right) \\ &\times \prod_{i=1}^A (x_i^+)^{\alpha_{\text{remn}}} \Theta(x_i^+) \Theta(1 - x_i^+) \prod_{j=1}^B (x_j^-)^{\alpha_{\text{remn}}} \Theta(x_j^-) \Theta(1 - x_j^-). \end{aligned} \quad (4.6)$$

The arguments of Φ_{uAB} are the momentum fractions of projectile and target remnants,

$$x_i^+ = 1 - \sum_{\pi(k)=i} x_{k,\mu}^+, \quad x_j^- = 1 - \sum_{\tau(k)=j} x_{k,\mu}^-, \quad (4.7)$$

where $\pi(k)$ and $\tau(k)$ point to the remnants linked to the k^{th} interaction.

In the following, we perform the analysis for given s and $b = (b_0, b_1, \dots, b_{AB})$, so we do not write these variables explicitly. In addition, we always refer to the unitarized functions, so we will also suppress the subscript “u”. Furthermore, we suppress the index AB .

Crucial for our applications is the probability conservation constraint

$$\gamma + \bar{\gamma} = 1, \quad (4.8)$$

which may be written more explicitly as

$$\sum_m \int dX^+ dX^- \Omega(m, X^+, X^-) = 1. \quad (4.9)$$

This allows us to interpret $\Omega(m, X^+, X^-)$ as the probability distribution for a configuration (m, X^+, X^-) . For any given configuration the function Ω can be easily calculated using the techniques developed in the chapter 2. The difficulty with the Monte Carlo generation of interaction configurations arises from the fact that the configuration space is huge and rather nontrivial in the sense that it cannot be written as a product of single Pomeron contributions. We are going to explain in the next sections, how we deal with this problem.

4.2 The Interaction Matrix

Since $\Omega(m, X^+, X^-)$ is a high-dimensional and nontrivial probability distribution, the only way to proceed amounts to employing dynamical Monte Carlo methods, well known in statistical and solid state physics.

We first need to choose the appropriate framework for our analysis. So we translate our problem into the language of spin systems [22]: we number all nucleon pairs as $1, 2, \dots, AB$ and for each nucleon pair k the possible elementary interactions as $1, 2, \dots, m_k$. Let m_{max} be the maximum number of elementary interactions per nucleon pair one may imagine. We now consider a two dimensional lattice with AB lines and m_{max} columns, see fig. 4.1. Lattice sites are occupied ($= 1$) or empty ($= 0$), representing an elementary interaction (1) or the case of no interaction (0), for the k^{th} pair. In order to represent m_k elementary interactions for the pair k , we need m_k occupied cells (1's) in the k^{th} line. A line containing only empty cells (0's) represents a pair without interaction. Any possible interaction may be represented by this “interaction matrix” M with elements

$$m_{k\mu} \in \{0, 1\}. \quad (4.10)$$

Such an “interaction configuration” is exactly equivalent to a spin configuration of the Ising model. Unfortunately the situation is somewhat more complicated in case of nuclear collisions: we need

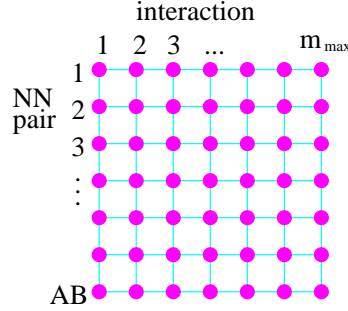


Figure 4.1: The interaction lattice.

to consider the energy available for each elementary interaction, represented via the momentum fractions $x_{k\mu}^+$ and $x_{k\mu}^-$. So we have a “generalized” matrix K ,

$$K = (M, X^+, X^-), \quad (4.11)$$

representing an interaction configuration, with elements

$$K_{k\mu} = \left(m_{k\mu}, x_{k\mu}^+, x_{k\mu}^- \right). \quad (4.12)$$

It is important to note that a number of matrices M represents one and the same vector m . In fact, m is represented by all the matrices M with

$$\sum_{\mu=1}^{m_{\max}} m_{k\mu} = m_k, \quad (4.13)$$

for each k . Since all the corresponding configurations (M, X^+, X^-) should have the same weight, and since there are

$$c = \prod_{k=1}^{AB} \frac{m_{\max}!}{m_k! (m_{\max} - m_k)!} \quad (4.14)$$

configurations (M, X^+, X^-) representing the same configuration (m, X^+, X^-) , the weight for the former is c^{-1} times the weight for the latter, so we obtain the following probability distribution for $K = (M, X^+, X^-)$:

$$\Omega(K) = \prod_{k=1}^{AB} \left\{ \frac{(m_{\max} - m_k)!}{m_{\max}!} \prod_{\mu=1}^{m_k} G(s, x_{k,\mu}^+, x_{k,\mu}^-, b) \right\} \Phi_{u_{AB}}(x^+, x^-, s, b), \quad (4.15)$$

or, using the expression for $\Phi_{u_{AB}}$,

$$\begin{aligned} \Omega(K) &= \frac{1}{Z_{AB}} \prod_{k=1}^{AB} \left\{ \frac{(m_{\max} - m_k)!}{m_{\max}!} \prod_{\mu=1}^{m_k} \left\{ G(s, x_{k,\mu}^+, x_{k,\mu}^-, b_k) \right\} \exp \left(-\tilde{G}(x_{\pi(k)}^+ x_{\tau(k)}^-, s, b_k) \right) \right\} \\ &\times \prod_{i=1}^A (x_i^+)^{\alpha_{\text{remn}}} \Theta(x_i^+) \Theta(1 - x_i^+) \prod_{j=1}^B (x_j^-)^{\alpha_{\text{remn}}} \Theta(x_j^-) \Theta(1 - x_j^-). \end{aligned} \quad (4.16)$$

The probability conservation now reads

$$\sum_K \Omega(K) = \sum_M \int dX^+ dX^- \Omega(M, X^+, X^-) = 1. \quad (4.17)$$

In the following, we shall deal with the “interaction matrix” K , and the probability distribution $\Omega(K)$.

4.3 The Markov Chain Method

In order to generate K according to the given distribution $\Omega(K)$, defined earlier, we construct a Markov chain

$$K^{(0)}, K^{(1)}, K^{(2)}, \dots, K^{(t_{\max})} \quad (4.18)$$

such that the final configurations $K^{(t_{\max})}$ are distributed according to the probability distribution $\Omega(K)$, if possible for a t_{\max} not too large!

Let us discuss how to obtain a new configuration $K^{(t+1)} = L$ from a given configuration $K^{(t)} = K$. We use Metropolis' Ansatz for the transition probability

$$p(K, L) = \text{prob} \left(K^{(t+1)} = L \mid K^{(t)} = K \right) \quad (4.19)$$

as a product of a proposition matrix $w(K, L)$ and an acceptance matrix $u(K, L)$:

$$p(K, L) = \begin{cases} w(K, L) u(K, L) & \text{if } L \neq K \\ w(K, K) + \sum_{L \neq K} w(K, L) \{1 - u(K, L)\} & \text{if } L = K \end{cases}, \quad (4.20)$$

where we use

$$u(K, L) = \min \left(\frac{\Omega(L)}{\Omega(K)} \frac{w(L, K)}{w(K, L)}, 1 \right), \quad (4.21)$$

in order to assure detailed balance. We are free to choose $w(K, L)$, but of course, for practical reasons, we want to minimize the autocorrelation time, which requires a careful definition of w . An efficient procedure requires $u(K, L)$ to be not too small (to avoid too many rejections), so an ideal choice would be $w(K, L) = \Omega(L)$. This is of course not possible, but we choose $w(K, L)$ to be a "reasonable" approximation to $\Omega(L)$ if K and L are reasonably close, otherwise w should be zero. So we define

$$w(K, L) = \begin{cases} \Omega_0(L) & \text{if } d(K, L) \leq 1 \\ 0 & \text{otherwise} \end{cases}, \quad (4.22)$$

where $d(K, L)$ is the number of lattice sites being different in L compared to K , and where $\Omega^{(0)}$ is defined by the same formulas as Ω with one exception: Φ_{uAB} is replaced by 1. So we get

$$\Omega_0(L) \sim \prod_{k=1}^{AB} \left\{ (m_{\max} - m_k)! \prod_{\mu=1}^{m_k} G(x_{k,\mu}^+, x_{k,\mu}^-, s, b_k) \right\}. \quad (4.23)$$

The above definition of $w(K, L)$ may be realized by the following algorithm:

- choose randomly a lattice site (k, μ) ,
- propose a new matrix element $(m_{k\mu}, x_{k\mu}^+, x_{k\mu}^-)$ according to the probability distribution $\rho(m_{k\mu}, x_{k\mu}^+, x_{k\mu}^-)$,

where we are going to derive the form of ρ in the following. From eq. (4.23), we know that ρ should be of the form

$$\rho(m, x^+, x^-) \sim m_0! \begin{cases} G(x^+, x^-, s, b) & \text{if } m = 1 \\ 1 & \text{if } m = 0 \end{cases}, \quad (4.24)$$

where $m_0 = m_{\max} - m$ is the number of zeros in the row k . Let us define \bar{m}_0 as the number of zeros (empty cells) in the row k not counting the current site (k, μ) . Then the factor $m_0!$ is given as $\bar{m}_0!$ in case of $m \neq 0$ and as $\bar{m}_0!(\bar{m}_0 + 1)$ in case of $m = 0$, and we obtain

$$\rho(m, x^+, x^-) \sim (\bar{m}_0 + 1)\delta_{m0} + G(x^+, x^-, s, b)\delta_{m1}. \quad (4.25)$$

Properly normalized, we obtain

$$\rho(m, x^+, x^-) = p_0 \delta_{m0} + (1 - p_0) \frac{G(x^+, x^-, s, b)}{\chi} \delta_{m1}, \quad (4.26)$$

where the probability p_0 of proposing no interaction is given as

$$p_0 = \frac{\bar{m}_0 + 1}{\bar{m}_0 + 1 + \chi(s, b)}, \quad (4.27)$$

with χ being obtained by integrating G over x^+ and x^- ,

$$\chi(s, b) = \int_0^1 dx^+ dx^- G(x^+, x^-, s, b). \quad (4.28)$$

Having proposed a new configuration L , which amounts to generating the values $m_{k\mu}, x_{k\mu}^+, x_{k\mu}^-$ for a randomly chosen lattice site as described above, we accept this proposal with the probability

$$u(K, L) = \min(z_1 z_2, 1), \quad (4.29)$$

with

$$z_1 = \frac{\Omega(L)}{\Omega(K)}, \quad z_2 = \frac{w(L, K)}{w(K, L)}. \quad (4.30)$$

Since K and L differ in at most one lattice site, say (k, μ) , we do not need to evaluate the full formula for the distribution Ω to calculate z_1 , we rather calculate

$$z_1 = \frac{\Omega^{k\mu}(L)}{\Omega^{k\mu}(K)}, \quad (4.31)$$

with

$$\begin{aligned} \Omega^{k\mu}(K) &= \rho(m_{k\mu}, x_{k\mu}^+, x_{k\mu}^-) \exp \left(- \sum_{l \text{ linked to } k} \tilde{G}(x_{\pi(l)}^+ x_{\tau(l)}^-, s, b_l) \right) \\ &\times (x_{\pi(k)}^+)^{\alpha_{\text{remn}}} \Theta(x_{\pi(k)}^+) \Theta(1 - x_{\pi(k)}^+) (x_{\tau(k)}^-)^{\alpha_{\text{remn}}} \Theta(x_{\tau(k)}^-) \Theta(1 - x_{\tau(k)}^-), \end{aligned} \quad (4.32)$$

which is technically quite easy. Our final task is the calculation of the asymmetry z_2 . In many applications of the Markov chain method one uses symmetric proposal matrices, in which case this factor is simply one. This is not the case here. We have

$$z_2 = \frac{\Omega_0(K)}{\Omega_0(L)} = \frac{\Omega_0^{k\mu}(K)}{\Omega_0^{k\mu}(L)}, \quad (4.33)$$

with

$$\Omega_0^{k\mu}(K) = \rho(m_{k\mu}, x_{k\mu}^+, x_{k\mu}^-), \quad (4.34)$$

which is also easily calculated. So we accept the proposal L with the probability $\min(z_1 z_2, 1)$, in which case we have $K^{(t+1)} = L$, otherwise we keep the old configuration K , which means $K^{(t+1)} = K$.

4.4 Convergence

A crucial item is the question of how to determine the number of iterations, which are sufficient to reach the stationary region. In principle one could calculate the autocorrelation time, or better one could estimate it based on an actual iteration. One could then multiply it with some “reasonable

number”, between 10 and 20, in order to obtain the number of iterations. Since this “reasonable number” is not known anyway, we proceed differently. We consider a number of quantities like the number of binary interactions, the number of Pomerons, and other observables, and we monitor their values during the iterations. Simply by inspecting the results for many events, one can quite easily convince oneself if the numbers of iterations are sufficiently large. As a final check one makes sure that the distributions of some relevant observables do not change by doubling the number of iterations. In fig. 4.2, we show the number of collisions (left) and the number of Pomerons (right)

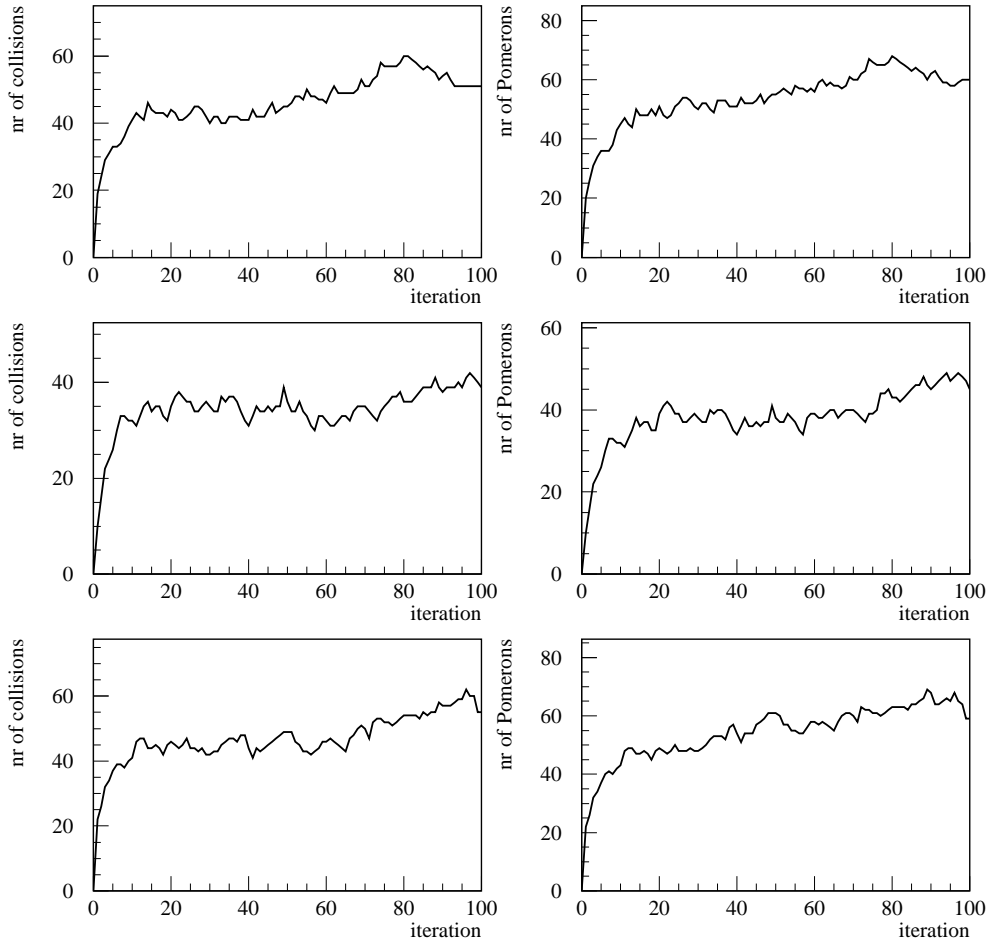


Figure 4.2: Number of collisions (left) and number of Pomerons (right) as a function of the iteration step t (in percent relative to the maximum number of iterations) for three different S+S events.

as a function of the iteration step t for a S+S collision, where the number of iterations t_{\max} has been determined according to some empirical procedure described below. We observe that these two quantities approach very quickly the stationary region. In order to determine the number t_{\max} of iterations for a given reaction $A + B$, we first calculate the upper limit for the number of possibly interacting nucleon pairs as the number of pairs k_{\max} with a transverse distance smaller than some value b_{\max} being defined as

$$1 - e^{-\chi(s, b_{\max})} = 0.001, \quad (4.35)$$

and we then define

$$t_{\max} = 100 \cdot \frac{2}{3} k_{\max}. \quad (4.36)$$

Actually, in the real calculations, we never consider sums of nucleon pairs from 1 to AB , but only from 1 to k_{\max} , because for the other ones the chance to be involved in an interaction is so small that one can safely ignore it.

4.5 Some Tests for Proton-Proton Scattering

As a first test, we check whether the Monte Carlo procedure reproduces the theoretical profile function γ_{inel} . So we make a large number of simulations of proton-proton collisions at a given energy \sqrt{s} , where the impact parameters are chosen randomly between zero and the earlier defined maximum impact parameter b_{\max} . We then count simply the number $\Delta n_{\text{inel}}(b)$ of inelastic interactions in a given impact parameter bin $[b - \Delta b/2, b + \Delta b/2]$, and divide this by the number $\Delta n_{\text{tot}}(b)$ of simulations in this impact parameter interval. Since the total number $\Delta n_{\text{tot}}(b)$ of simulated configurations for the given b -bin splits into the number $\Delta n_{\text{inel}}(b)$ of “interactions” and the number $\Delta n_{\text{nonint}}(b)$ of “non-interactions”, with $\Delta n_{\text{tot}}(b) = \Delta n_{\text{inel}}(b) + \Delta n_{\text{nonint}}(b)$, the result

$$P(b) = \frac{\Delta n_{\text{inel}}(b)}{\Delta n_{\text{tot}}(b)} \quad (4.37)$$

represents the probability to have an interaction at a given impact parameter b , which should coincide with the profile function

$$\gamma_{AB}(s, b) = 1 - \Phi_{u_{AB}}(1, 1, s, b) \quad (4.38)$$

for the corresponding energy. In fig. 4.3, we compare the two quantities for a proton-proton collision

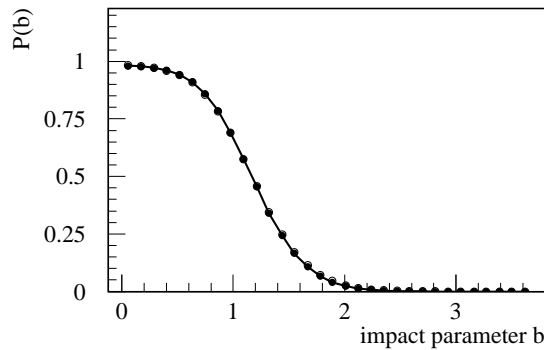


Figure 4.3: The simulated probability $P(b)$ (points) of an inelastic interaction for a proton-proton collision at $\sqrt{s} = 200$ GeV compared to the profile function $\gamma_{AB}(s, b)$ (solid line).

at $\sqrt{s} = 200$ GeV and we find an excellent agreement, as it should be.

Another elementary quantity is the inclusive momentum spectrum of Pomerons. Pomerons, representing elementary interactions, are characterized by their light cone momentum fractions x^+ and x^- , so one might study two dimensional distributions, or for example a distribution in $x = x^+x^-$, where the second variable $y = 0.5 \log(x^+/x^-)$ is integrated over. So again we simulate many proton-proton events at a given energy \sqrt{s} and we count the number of Pomerons ΔN_{Pom} within a certain interval $[x - \Delta x/2, x + \Delta x/2]$ and we calculate

$$\frac{dn_{\text{Pom}}^{\text{MC}}}{dx} = \frac{1}{N_{\text{events}}} \frac{\Delta N_{\text{Pom}}}{\Delta x}, \quad (4.39)$$

representing the Monte Carlo Pomeron x -distribution, which may be compared with the analytical result calculated earlier, as shown in fig. 4.4. The analytical results of course refer to the unitarized

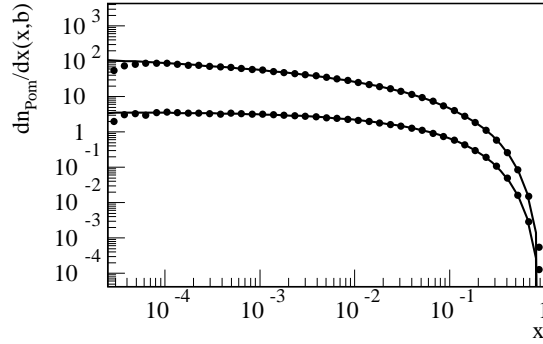


Figure 4.4: Inclusive x -distribution of Pomerons. The variable x is defined as $x = x^+x^-$ and is therefore the squared mass of the Pomeron divided by s . We show unitarized analytical results (solid lines) for $b = 0$ fm (upper curves) and $b = 1.5$ fm (lower curves) and the corresponding simulation results (points).

theory. Again we find perfect agreement between Monte Carlo simulations and analytical curves, as it should be. In fig. 4.5, we compare inclusive Pomeron cross sections (integrated over impact

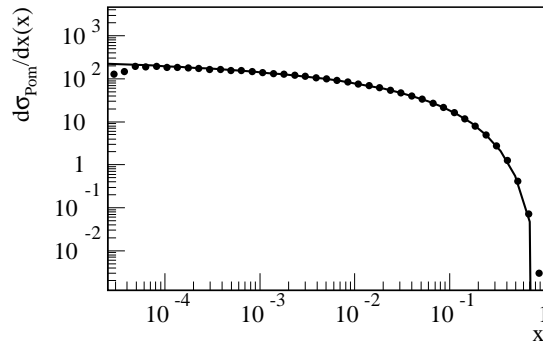


Figure 4.5: Inclusive cross section of Pomerons versus x . The variable x is defined as $x = x^+x^-$ and is therefore the squared mass of the Pomeron divided by s . We show unitarized analytical results (solid line) and the corresponding simulation results (points).

parameter). Here, the impact parameters are generated randomly between 1 and some b_{\max} , one counts the number of Pomerons ΔN_{Pom} within a certain interval of size Δx , and one calculates

$$\frac{d\sigma_{\text{Pom}}^{\text{MC}}}{dx} = \frac{\pi r_{\max}^2}{N_{\text{events}}} \frac{\Delta N_{\text{Pom}}}{\Delta x}, \quad (4.40)$$

which is compared with the analytical result

$$\frac{d\sigma_{\text{Pom}}}{dx}(x, s) = \int d^2b \frac{dn_{\text{Pom}}}{dx}(x, s, b), \quad (4.41)$$

which again show an excellent agreement.

These Pomeron distributions are of particular interest, because they are elementary distributions based on which other inclusive spectra like a transverse momentum distribution of pions may be obtained via convolution.

The two examples of this section provide on one hand a check that the numerical procedures work properly, on the other hand they demonstrate nicely that our Monte Carlo procedure is a very well defined numerical method to solve a particular mathematical problem. In simple cases where analytical results exist, they may be compared with the Monte Carlo results, and they must absolutely agree.

Chapter 5

Enhanced Pomeron diagrams

The eikonal type diagrams shown at fig. 5.1, considered in the previous chapters, correspond to pair-like scatterings between hadron constituents and form the basis for the description of hadronic interactions at not too high energies. However, when the interaction energy increases,

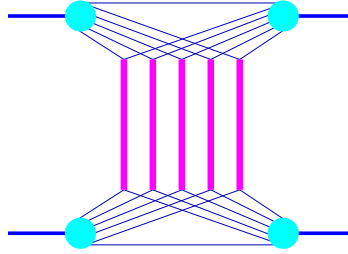


Figure 5.1: Eikonal type diagrams.

the contribution of so-called enhanced Pomeron diagrams as, for example, the diagrams shown in fig. 5.2, become more and more important. The latter ones take into account interactions of

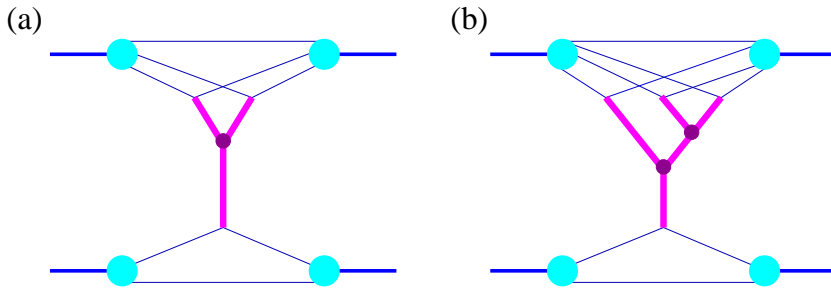


Figure 5.2: Enhanced diagrams.

Pomerons with each other. The corresponding amplitudes increase asymptotically much faster than the usual eikonal type contributions considered so far. In this paper, we restrict ourselves to the lowest order diagrams (Y -diagrams and inverted Y -diagrams).

In the following sections, we discuss the amplitudes corresponding to the lowest order enhanced diagrams and the modification of the hadronic profile function in the presence of these diagrams, before we discuss their most important features.

5.1 Calculating lowest order enhanced diagrams

To introduce enhanced type diagrams let us come back to the process of double soft Pomeron exchange, which is a particular case of the diagram of fig. 2.7. The corresponding contribution to the elastic scattering amplitude is given in eqs. (2.31), (C.11) with $n = 2$ and with $T_{1\mathbb{P}}$ being replaced by T_{soft} :

$$\begin{aligned}
 iT_{h_1 h_2}^{(2)}(s, t) &= \frac{1}{2} \int \frac{d^4 k_1}{(2\pi)^4} \frac{d^4 k'_1}{(2\pi)^4} \frac{d^4 k_2}{(2\pi)^4} \frac{d^4 k'_2}{(2\pi)^4} \frac{d^4 q_1}{(2\pi)^4} \Theta(s_1^+) \Theta(s_1^-) \Theta(s_2^+) \Theta(s_2^-) \Theta(s_{q_1}^+) \Theta(s_{q_1}^-) \\
 &\quad \times \text{disc}_{s_1^+, s_2^+, s_{q_1}^+} N_{h_1}^{(2)}(p, k_1, k_2, q_1, q - q_1) \\
 &\quad \times \prod_{l=1}^2 [iT_{\text{soft}}(\hat{s}_l, q_l^2)] \text{disc}_{s_1^-, s_2^-, s_{q_1}^-} N_{h_2}^{(2)}(p', k'_1, k'_2, -q_1, -q + q_1) \quad (5.1)
 \end{aligned}$$

see fig. 5.3.

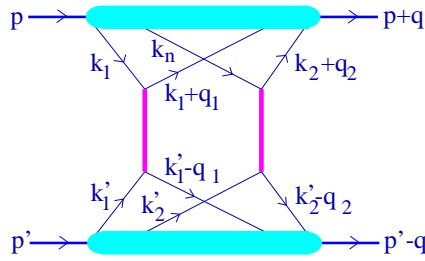


Figure 5.3: Double Pomeron exchange.

We are now interested in the contribution with some of the invariants

$$s_1^+ = (p - k_1)^2 \simeq -p^+ k_1^-, \quad (5.2)$$

$$s_2^+ = (p - k_1 - k_2)^2 \simeq -p^+ (k_1^- + k_2^-), \quad (5.3)$$

$$s_{q_1}^+ = (p + q_1)^2 \simeq p^+ q_1^-, \quad (5.4)$$

being large, implying k_i^-, q_1^- to be not too small. As shown in appendix C.3, in that case the above amplitude may be written as

$$iT_{h_1 h_2}^{3\mathbb{P}^-}(s, t) = \int_0^1 \frac{dx^+}{x^+} \frac{dx^-}{x^-} F_{\text{remn}}^{h_1}(1 - x^+) F_{\text{remn}}^{h_2}(1 - x^-) iT_{3\mathbb{P}^-}^{h_1 h_2}(x^+, x^-, s, t) \quad (5.5)$$

with

$$\begin{aligned}
 iT_{3\mathbb{P}^-}^{h_1 h_2}(x^+, x^-, s, t) &= 8\pi^2 x^+ x^- s \frac{r_{3\mathbb{P}}}{2} \int_{s_0/x^-}^{x^+} \frac{dx_{12}^+}{x_{12}^+} \left[\frac{1}{2s^+} \text{Im} T^{h_1}(x^+, s^+, -q_\perp^2) \right] \\
 &\quad \times \int dz^+ \int d^2 q_{1\perp} d^2 q_{2\perp} \int_0^{x^-} dx_1^- dx_2^- \prod_{l=1}^2 \left[\frac{1}{8\pi^2 \hat{s}_l} iT^{h_2}(x_l^-, \hat{s}_l, -q_{l\perp}^2) \right] \\
 &\quad \times \delta(x^- - x_1^- - x_2^-) \delta^{(2)}(\vec{q}_\perp - \vec{q}_{1\perp} - \vec{q}_{2\perp}), \quad (5.6)
 \end{aligned}$$

with

$$T^h(x, s, -q_\perp^2) = T_{\text{soft}}^h(x, s, -q_\perp^2) = T_{\text{soft}}(s, -q_\perp^2) F_{\text{part}}^h(x) \exp(-R_h^2 q_\perp^2) \quad (5.7)$$

and

$$\hat{s}_1 = x_{12}^+ z^+ x_1^- s, \quad \hat{s}_2 = x_{12}^+ (1 - z^+) x_2^- s, \quad (5.8)$$

where the following definitions have been used

$$x^+ = k^+/p^+, \quad (5.9)$$

$$x_{12}^+ = k_{12}^+/p^+, \quad (5.10)$$

$$x_1^+ = k_1^+/p^+, \quad (5.11)$$

$$x_{12}^+ - x_1^+ = (k_{12}^+ - k_1^+)/p^+ = k_2^+/p^+, \quad (5.12)$$

$$z^+ = k_1^+/k_{12}^+ = x_1^+/x_{12}^+, \quad (5.13)$$

$$s^+ = (k - k_{12})^2 \simeq -k^+ k_{12}^- \simeq s_0 k^+/k_{12}^+ = s_0 x^+/x_{12}^+, \quad (5.14)$$

see fig. 5.4. The sign “−” in “3P−” refers to the Pomeron “splitting” towards the target hadron

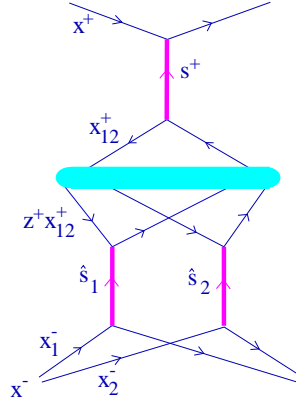


Figure 5.4: Kinematical variables for the triple Pomeron contribution.

(reversed Y-diagram); the lower limit for the integral dx_{12}^+ is due to $x_{12}^- \simeq s_0/x_{12}^+ < x^-$.

The triple-Pomeron contribution (5.6) is by construction expressed via amplitudes T_{soft}^h for parton-parton scattering due to soft Pomeron exchange, each one corresponding to non-perturbative parton dynamics, characterized by restricted parton virtualities $Q^2 < Q_0^2$. We can also take into account contributions to the triple-Pomeron diagram from semi-hard processes, when some part of the parton cascade mediating the scattering between partons of momenta k_l and k_l' at fig. C.3 (k and $-k_{12}$) develops in the perturbative region $Q^2 > Q_0^2$. Then, according to the general discussion of chapter 2, the amplitudes T^h obtain also contributions from semi-hard sea-type parton-parton scattering $T_{\text{sea-sea}}^h$ and from valence quark scattering $T_{\text{val-sea}}^h$:

$$T^h = T_{\text{soft}}^h + T_{\text{sea-sea}}^h + T_{\text{val-sea}}^h, \quad (5.15)$$

with

$$T_{\text{soft/sea-sea}}^h(x, \hat{s}, -q_{\perp}^2) = T_{\text{soft/sea-sea}}(\hat{s}, -q_{\perp}^2) F_{\text{part}}^h(x) \exp(-R_h^2 q_{\perp}^2) \quad (5.16)$$

and

$$T_{\text{val-sea}}^h(x, \hat{s}, -q_{\perp}^2) = \int_0^x dx_v \frac{x}{x_v} \sum_k T_{\text{val-sea}}^k\left(\frac{x_v}{x} \hat{s}, -q_{\perp}^2\right) \exp(-R_h^2 q_{\perp}^2) \times \bar{F}_{\text{part}}^{h,k}(x_v, x - x_v). \quad (5.17)$$

We have to stress again that we do not consider the possibility of Pomeron-Pomeron coupling in the perturbative region $Q^2 > Q_0^2$. Therefore in our scheme hard parton processes can only contribute into internal structure of elementary parton-parton scattering amplitudes but do not influence the triple-Pomeron coupling.

A similar contribution $T_{3\mathbb{P}+}^{h_1 h_2}$ of the Y-diagram can be obtained via interchanging $x^+ \leftrightarrow x^-$ and $h_1 \leftrightarrow h_2$:

$$T_{3\mathbb{P}+}^{h_1 h_2}(x^+, x^-, s, t) = T_{3\mathbb{P}-}^{h_2 h_1}(x^-, x^+, s, t). \quad (5.18)$$

One can repeat the above derivation for the case of a general soft multiple scattering process, see eq. (2.31), where some of the energy invariants $s_{q_l}^+$, $s_{q_l}^-$ are large [14]. One then obtains finally the general multiple scattering expression (C.22), with the contribution of corresponding pairs of Pomerons being replaced by expressions

$$\frac{1}{8\pi^2 x^+ x^- s} \int d^2 q_\perp i T_{3\mathbb{P}\pm}^{h_1 h_2}(x^+, x^-, s, t), \quad (5.19)$$

where x^\pm refers to the summary light cone momentum share of the constituent partons participating in the triple-Pomeron process. So we get

$$\begin{aligned} iT_{h_1 h_2}(s, t) &= 8\pi^2 s \sum_{n=1}^{\infty} \frac{1}{n!} \int_0^1 \prod_{l=1}^n dx_l^+ dx_l^- \prod_{l=1}^n \left[\frac{1}{8\pi^2 \hat{s}_l} \int d^2 q_{l\perp} i T_{\mathbb{P}}^{h_1 h_2}(\hat{s}_l, -q_{l\perp}^2) \right] \\ &\times F_{\text{remn}}^{h_1} \left(1 - \sum_{j=1}^n x_j^+ \right) F_{\text{remn}}^{h_2} \left(1 - \sum_{j=1}^n x_j^- \right) \delta^{(2)} \left(\sum_{k=1}^n \vec{q}_{k\perp} - \vec{q}_\perp \right). \end{aligned} \quad (5.20)$$

with

$$T_{\mathbb{P}}^{h_1 h_2} = T_{1\mathbb{P}}^{h_1 h_2} + T_{3\mathbb{P}-}^{h_1 h_2} + T_{3\mathbb{P}+}^{h_1 h_2} \quad (5.21)$$

Here, we allow any number of simple triple-Pomeron diagrams; thus we restrict ourselves to the contributions of double Pomeron iteration in the t -channel rather than to the first order in $r_{3\mathbb{P}}$.

The Fourier transform \tilde{T} of the amplitude (5.20) is given as

$$\begin{aligned} \frac{i}{2s} \tilde{T}_{h_1 h_2}(s, b) &= \sum_{n=1}^{\infty} \frac{1}{n!} \int_0^1 \prod_{l=1}^n dx_l^+ dx_l^- \prod_{l=1}^n \frac{i}{2s} \tilde{T}_{\mathbb{P}}^{h_1 h_2}(x_l^+, x_l^-, s, b) \\ &\times F_{\text{remn}}^{h_1} \left(1 - \sum_{j=1}^n x_j^+ \right) F_{\text{remn}}^{h_2} \left(1 - \sum_{j=1}^n x_j^- \right), \end{aligned} \quad (5.22)$$

with $\tilde{T}_{\mathbb{P}}^{h_1 h_2}$ being the Fourier transform of $T_{\mathbb{P}}^{h_1 h_2}$,

$$\tilde{T}_{\mathbb{P}}^{h_1 h_2} = \tilde{T}_{1\mathbb{P}}^{h_1 h_2} + \tilde{T}_{3\mathbb{P}-}^{h_1 h_2} + \tilde{T}_{3\mathbb{P}+}^{h_1 h_2}, \quad (5.23)$$

where the Fourier transform $\tilde{T}_{3\mathbb{P}-}^{h_1 h_2}$ of the triple Pomeron amplitude $T_{3\mathbb{P}-}^{h_1 h_2}$ is given as

$$\begin{aligned} \frac{i}{2\hat{s}} \tilde{T}_{3\mathbb{P}-}^{h_1 h_2}(x^+, x^-, s, b) &= \frac{r_{3\mathbb{P}}}{2} \int d^2 b_1 \int_{s_0/x^-}^{x^+} \frac{dx_{12}^+}{x_{12}^+} \left[\frac{1}{2s^+} \text{Im} \tilde{T}^{h_1}(x^+, s^+, |\vec{b} - \vec{b}_1|) \right] \\ &\times \int dz^+ \int_0^{x^-} dx_1^- dx_2^- \prod_{l=1}^2 \left[\frac{1}{2\hat{s}_l} i \tilde{T}^{h_2}(x_l^-, \hat{s}_l, b_1) \right] \delta(x^- - x_1^- - x_2^-), \end{aligned} \quad (5.24)$$

with $\hat{s} = x^+ x^- s$ (and similarly for $\tilde{T}_{3\mathbb{P}+}^{h_1 h_2}$).

Here we used

$$\delta^{(2)}(\vec{q}_\perp - \vec{q}_{1\perp} - \vec{q}_{2\perp}) = \frac{1}{4\pi^2} \int d^2 b_1 \exp\left(i(\vec{q}_\perp - \vec{q}_{1\perp} - \vec{q}_{2\perp}) \vec{b}_1\right). \quad (5.25)$$

The profile function γ for hadron-hadron interaction is as usual defined as

$$\gamma_{h_1 h_2}(s, b) = \frac{1}{2s} 2\text{Im} \tilde{T}_{h_1 h_2}(s, b), \quad (5.26)$$

which may be evaluated using the AGK cutting rules,

$$\begin{aligned}
\gamma_{h_1 h_2}(s, b) &= \sum_{m=1}^{\infty} \frac{1}{m!} \int \prod_{\mu=1}^m dx_{\mu}^+ dx_{\mu}^- \prod_{\mu=1}^m G_{\mathbb{P}}^{h_1 h_2}(x_{\mu}^+, x_{\mu}^-, s, b) \\
&\times \sum_{l=1}^{\infty} \frac{1}{l!} \int \prod_{\lambda=1}^l d\tilde{x}_{\lambda}^+ d\tilde{x}_{\lambda}^- \prod_{\lambda=1}^l -G_{\mathbb{P}}^{h_1 h_2}(\tilde{x}_{\lambda}^+, \tilde{x}_{\lambda}^-, s, b) \\
&\times F_{\text{remn}} \left(x^{\text{proj}} - \sum_{\lambda} \tilde{x}_{\lambda}^+ \right) F_{\text{remn}} \left(x^{\text{targ}} - \sum_{\lambda} \tilde{x}_{\lambda}^- \right), \tag{5.27}
\end{aligned}$$

with $x^{\text{proj/targ}} = 1 - \sum x_{\mu}^{\pm}$ being the momentum fraction of the projectile/target remnant, and with

$$G_{\mathbb{P}}^{h_1 h_2} = G_{1\mathbb{P}}^{h_1 h_2} + G_{3\mathbb{P}^-}^{h_1 h_2} + G_{3\mathbb{P}^+}^{h_1 h_2}, \tag{5.28}$$

where $G_{3\mathbb{P}^{\pm}}^{h_1 h_2}$ is twice the imaginary part of the Fourier transformed triple-Pomeron amplitude $\tilde{T}_{3\mathbb{P}^{\pm}}^{h_1 h_2}$ divided by $2\hat{s}$,

$$G_{3\mathbb{P}^{\pm}}^{h_1 h_2}(x^+, x^-, s, b) = \frac{1}{2x^+ x^- s} 2\text{Im} \tilde{T}_{3\mathbb{P}^{\pm}}^{h_1 h_2}(x^+, x^-, s, b), \tag{5.29}$$

which gives, assuming imaginary amplitudes,

$$\begin{aligned}
G_{3\mathbb{P}^-}^{h_1 h_2}(x^+, x^-, s, b) &= -\frac{r_{3\mathbb{P}}}{8} \int d^2 b_1 \int_{s_0/x^-}^{x^+} \frac{dx_{12}^+}{x_{12}^+} G^{h_1}(x^+, s^+, |\vec{b} - \vec{b}_1|) \\
&\times \int_0^1 dz^+ \int_0^{x^-} dx_1^- G^{h_2}(x_1^-, \hat{s}_1, b_1) G^{h_2}(x^- - x_1^-, \hat{s}_2, b_1), \tag{5.30}
\end{aligned}$$

see fig. 5.5, with

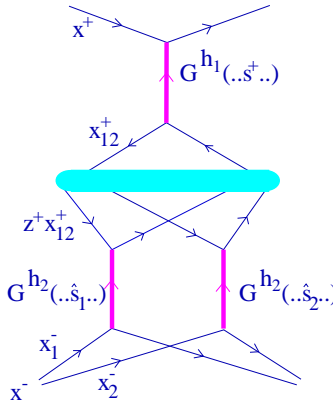


Figure 5.5: Triple Pomeron contribution.

$$s^+ = s_0 \frac{x^+}{x_{12}^+}, \quad \hat{s}_1 = x_{12}^+ z^+ x_1^- s, \quad \hat{s}_2 = x_{12}^+ (1 - z^+) (x^- - x_1^-) s. \tag{5.31}$$

The functions G^h are defined as

$$G^h(x, \hat{s}, b) = \frac{1}{2\hat{s}} 2\text{Im} \tilde{T}^h(x, \hat{s}, b), \tag{5.32}$$

with \tilde{T}^h being the Fourier transform of T^h , which gives

$$G^h = G_{\text{soft}}^h + G_{\text{sea-sea}}^h + G_{\text{val-sea}}^h, \quad (5.33)$$

with

$$G_{\text{soft}}^h(x, \hat{s}, b) = \frac{2\gamma_{\text{part}}}{\lambda_{\text{soft}}^h(\frac{\hat{s}}{s_0})} \left(\frac{\hat{s}}{s_0}\right)^{\alpha_{\text{soft}}(0)-1} \exp\left(-\frac{b^2}{4\lambda_{\text{soft}}^h(\frac{\hat{s}}{s_0})}\right) F_{\text{part}}(x) \quad (5.34)$$

$$G_{\text{sea-sea}}^h(x, \hat{s}, b) = \frac{1}{4\pi} \sum_{jk} \int_0^1 dz^+ dz^- E_{\text{soft}}^j(z^+) E_{\text{soft}}^k(z^-) \sigma_{\text{ladder}}^{jk}(z^+ z^- \hat{s}, Q_0^2) \times \quad (5.35)$$

$$\begin{aligned} & \times \frac{1}{\lambda_{\text{soft}}^h(1/z^+ z^-)} \exp\left(-\frac{b^2}{4\lambda_{\text{soft}}^h(1/z^+ z^-)}\right) F_{\text{part}}(x) \\ G_{\text{val-sea}}^h(x, \hat{s}, b) &= \frac{1}{4\pi} \sum_{jk} \int_0^x dx_v \int_0^1 dz^+ E_{\text{soft}}^j(z^+) \sigma_{\text{ladder}}^{jk}\left(\frac{x_v}{x} z^+ \hat{s}, Q_0^2\right) \\ & \times \frac{1}{\lambda_{\text{soft}}^h(1/z^+)} \exp\left(-\frac{b^2}{4\lambda_{\text{soft}}^h(1/z^+)}\right) \bar{F}_{\text{part}}^k(x_v, x - x_v), \end{aligned} \quad (5.36)$$

with

$$\lambda_{\text{soft}}^h(z) = R_h^2 + \alpha'_{\text{soft}} \ln z. \quad (5.37)$$

5.2 Cutting Enhanced Diagrams

To treat particle production, we have to investigate the different cuts of an enhanced diagram. We consider the inverted Y-diagram here, the same arguments apply to the Y-diagram. We employ the cutting rules to eq. (5.24),

$$G_{3\mathbb{P}^-}^{h_1 h_2} = \frac{1}{2\hat{s}} 2\text{Im}\tilde{T}_{3\mathbb{P}^-}^{h_1 h_2} = \langle \text{sum over cut diagrams} \rangle = \sum_i G_{3\mathbb{P}^-(i)}^{h_1 h_2}, \quad (5.38)$$

where the index i counts the different cuts. We take into account that the cutting procedure only influences the two Pomerons exchanged “in parallel” in the triple-Pomeron graph (the lower Pomerons) with the third Pomeron already being cut [14], so that we have three contributions: none of the lower Pomerons cut ($i = 0$, diffraction), one of these Pomerons cut ($i = 1$, screening), and both Pomerons cut ($i = 2$, Pomeron-Pomeron fusion), see fig. 5.6. So we have

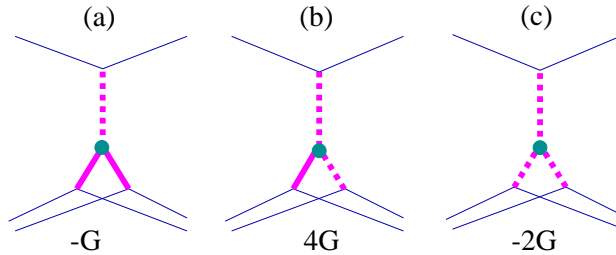


Figure 5.6: The different cuts of the triple Pomeron inverted Y-diagram: none of the lower Pomerons cut (a), one of these Pomerons cut (b), and both Pomerons cut (c). We also indicate their relations with $G = G_{3\mathbb{P}^-}^{h_1 h_2}$.

$$G_{3\mathbb{P}^-}^{h_1 h_2} = G_{3\mathbb{P}^-(0)}^{h_1 h_2} + G_{3\mathbb{P}^-(1)}^{h_1 h_2} + G_{3\mathbb{P}^-(2)}^{h_1 h_2}, \quad (5.39)$$

with

$$\begin{aligned}
G_{3\mathbb{P}^-(0)}^{h_1 h_2} &= \left\{ \frac{i}{2\hat{s}} \tilde{T}_{3\mathbb{P}^-}^{h_1 h_2} \right\} \times 2, \\
G_{3\mathbb{P}^-(1)}^{h_1 h_2} &= \left\{ \frac{i}{2\hat{s}} \tilde{T}_{3\mathbb{P}^-}^{h_1 h_2} \right\} \times (-2) \times 2 \times 2, \\
G_{3\mathbb{P}^-(2)}^{h_1 h_2} &= \left\{ \frac{i}{2\hat{s}} \tilde{T}_{3\mathbb{P}^-}^{h_1 h_2} \right\} \times 2 \times 2.
\end{aligned} \tag{5.40}$$

Here, we assumed imaginary amplitudes, and we replace as usual a factor $i\tilde{T}^h$ in eq. (5.24) by $2\text{Im}\tilde{T}^h = -2i\tilde{T}^h$ for a cut Pomeron, and by $(i\tilde{T}^h)^* = i\tilde{T}^h$ for an uncut Pomeron being to the left of the cut plane, and by $i\tilde{T}^h$ for an uncut Pomeron being to the right of the cut plane. Using (see eq. (5.29))

$$\frac{i}{2\hat{s}} \tilde{T}_{3\mathbb{P}^-}^{h_1 h_2} = -\frac{1}{2} G_{3\mathbb{P}^-}^{h_1 h_2}, \tag{5.41}$$

we get

$$\begin{aligned}
G_{3\mathbb{P}^-(0)}^{h_1 h_2} &= -1 \times G_{3\mathbb{P}^-}^{h_1 h_2}, \\
G_{3\mathbb{P}^-(1)}^{h_1 h_2} &= +4 \times G_{3\mathbb{P}^-}^{h_1 h_2}, \\
G_{3\mathbb{P}^-(2)}^{h_1 h_2} &= -2 \times G_{3\mathbb{P}^-}^{h_1 h_2},
\end{aligned} \tag{5.42}$$

which means that each cut contribution is equal to the profile function, up to a pre-factor, see fig. 5.6. The sum of the three contributions is $G_{3\mathbb{P}^-}^{h_1 h_2}$, as it should be.

There is a substantial difference between the different cuts of triple-Pomeron contributions: in the case of both lower Pomerons being cut ($i = 2$) all the momentum of the constituent partons, participating in the process, is transferred to secondary hadrons produced, whereas for the cut between these Pomerons ($i = 0$) only the light cone momentum fractions of the cut Pomeron (x^+ , $x_{12}^- = s_0/x_{12}^+$ in eq. (5.30)) are available for hadron production, the momentum share $x^- - x_{12}^-$ of the partons, connected to the uncut (virtual) Pomerons is given back to the remnant state. Correspondingly, the contribution with one of the two lower Pomerons being cut ($i = 1$) defines the screening correction to the elementary rescattering with the momentum fractions x^+ , x_1^- (considering the first of the two Pomerons being cut). It is therefore useful to rewrite the expression for the profile function as

$$\begin{aligned}
\gamma_{h_1 h_2}(s, b) &= \sum_m \frac{1}{m!} \int \prod_{\mu=1}^m dx_\mu^+ dx_\mu^- d\hat{x}_\mu^+ d\hat{x}_\mu^- \prod_{\mu=1}^m \hat{G}_{\mathbb{P}}^{h_1 h_2}(x_\mu^+, x_\mu^-, \hat{x}_\mu^+, \hat{x}_\mu^-, s, b) \\
&\times \sum_l \frac{1}{l!} \int \prod_{\lambda=1}^l d\tilde{x}_\lambda^+ d\tilde{x}_\lambda^- \prod_{\lambda=1}^l -G_{\mathbb{P}}^{h_1 h_2}(\tilde{x}_\lambda^+, \tilde{x}_\lambda^-, s, b) \\
&\times F_{\text{remn}} \left(x^{\text{proj}} - \sum_\mu \hat{x}_\mu^+ - \sum_\lambda \tilde{x}_\lambda^+ \right) F_{\text{remn}} \left(x^{\text{targ}} - \sum_\mu \hat{x}_\mu^- - \sum_\lambda \tilde{x}_\lambda^- \right), \tag{5.43}
\end{aligned}$$

with $G_{\mathbb{P}}^{h_1 h_2}$ being defined earlier, and with

$$\hat{G}_{\mathbb{P}}^{h_1 h_2}(x_\mu^+, x_\mu^-, \hat{x}_\mu^+, \hat{x}_\mu^-, s, b) = G_{1\mathbb{P}}(x_\mu^+, x_\mu^-, s, b) \delta(\hat{x}_\mu^+) \delta(\hat{x}_\mu^-) + \sum_{\sigma=\pm} \sum_{i=0}^2 \hat{G}_{3\mathbb{P}\sigma(i)}^{h_1 h_2}(x_\mu^+, x_\mu^-, \hat{x}_\mu^+, \hat{x}_\mu^-, s, b), \tag{5.44}$$

where we used

$$x^{\text{proj/targ}} = 1 - \sum_\mu x_\mu^\pm. \tag{5.45}$$

The variables x_μ^\pm are now the momentum fractions for the individual cut contributions, which define the energy for the production of secondary hadrons resulting from a given elementary interaction. The expressions for the functions $\hat{G}_{3\mathbb{P}\sigma(i)}^{h_1 h_2}$ are obtained from eqs. (5.27, 5.30, 5.55, 5.56), by changing the variables properly. Simplest is the case of all Pomerons being cut, no changing of variables is necessary, we have simply

$$\hat{G}_{3\mathbb{P}-(2)}^{h_1 h_2}(x^+, x^-, \hat{x}^+, \hat{x}^-, s, b) = -2G_{3\mathbb{P}-}^{h_1 h_2}(x^+, x^-, s, b) \delta(\hat{x}^+) \delta(\hat{x}^-) \quad (5.46)$$

$$\begin{aligned} &= \frac{r_{3\mathbb{P}}}{4} \int d^2 b_1 \int_{s_0/x^-}^{x^+} \frac{dx_{12}^+}{x_{12}^+} G^{h_1}(x^+, s^+, |\vec{b} - \vec{b}_1|) \\ &\times \int_0^1 dz^+ \int_0^{x^-} dx_1^- G^{h_2}(x_1^-, \hat{s}_1, b_1) G^{h_2}(x^- - x_1^-, \hat{s}_2, b_1) \\ &\times \delta(\hat{x}^+) \delta(\hat{x}^-), \end{aligned} \quad (5.47)$$

For none of the two lower Pomerons being cut, we rename x_{12}^- into x^- and $x^- - x_{12}^-$ into \hat{x}^- , so we get

$$\begin{aligned} \hat{G}_{3\mathbb{P}-(0)}^{h_1 h_2}(x^+, x^-, \hat{x}^+, \hat{x}^-, s, b) &= \frac{r_{3\mathbb{P}}}{8} \int d^2 b_1 \frac{1}{x^-} G^{h_1}(x^+, x^+ x^- s, |\vec{b} - \vec{b}_1|) \\ &\times \int_0^1 dz^+ \int_0^{\hat{x}^- + x^-} dx_1^- G^{h_2}(x_1^-, x_1^- \frac{s_0}{x^-} z^+ s, b_1) \\ &\times G^{h_2}(\hat{x}^- + x^- - x_1^-, (\hat{x}^- + x^- - x_1^-) \frac{s_0}{x^-} (1 - z^+) s, b_1) \delta(\hat{x}^+). \end{aligned} \quad (5.48)$$

For one of the two lower Pomerons being cut, we rename x_1^- into x^- and $x^- - x_1^-$ into \hat{x}^- , and we get

$$\begin{aligned} \hat{G}_{3\mathbb{P}-(1)}^{h_1 h_2}(x^+, x^-, \hat{x}^+, \hat{x}^-, s, b) &= -\frac{r_{3\mathbb{P}}}{2} \int d^2 b_1 \int_{s_0/x^-}^{x^+} \frac{dx_{12}^+}{x_{12}^+} G^{h_1}(x^+, s^+, |\vec{b} - \vec{b}_1|) \\ &\times \int_0^1 dz^+ G^{h_2}(x^-, x_{12}^+ z^+ x^- s, b_1) G^{h_2}(\hat{x}^-, x_{12}^+ (1 - z^+) \hat{x}^- s, b_1) \delta(\hat{x}^+). \end{aligned} \quad (5.49)$$

The contributions $G_{3\mathbb{P}+(i)}^{h_1 h_2}$ can be obtained via interchanging $x^+ \leftrightarrow x^-$, $\hat{x}^+ \leftrightarrow \hat{x}^-$ and $h_1 \leftrightarrow h_2$ in the above formulas:

$$G_{3\mathbb{P}+(i)}^{h_1 h_2}(x^+, x^-, \hat{x}^+, \hat{x}^-, s, b) = G_{3\mathbb{P}-(i)}^{h_2 h_1}(x^-, x^+, \hat{x}^-, \hat{x}^+, s, b). \quad (5.50)$$

We define as in the usual eikonal case the virtual emission function

$$\begin{aligned} \Phi_{h_1 h_2}(x^{\text{proj}}, x^{\text{targ}}, s, b) &= \sum_l \int \prod_{\lambda=1}^l d\tilde{x}_\lambda^+ d\tilde{x}_\lambda^- \frac{1}{l!} \prod_{\lambda=1}^l -G_{\mathbb{P}}^{h_1 h_2}(\tilde{x}_\lambda^+, \tilde{x}_\lambda^-, s, b) \\ &\times F_{\text{remn}}\left(x^{\text{proj}} - \sum_\lambda \tilde{x}_\lambda^+\right) F_{\text{remn}}\left(x^{\text{targ}} - \sum_\lambda \tilde{x}_\lambda^-\right), \end{aligned} \quad (5.51)$$

which allows to write the profile functions eq. (5.43) as

$$\begin{aligned} \gamma_{h_1 h_2}(s, b) &= \sum_m \frac{1}{m!} \int \prod_{\mu=1}^m dx_\mu^+ dx_\mu^- d\hat{x}_\mu^+ d\hat{x}_\mu^- \prod_{\mu=1}^m \hat{G}_{\mathbb{P}}^{h_1 h_2}(x_\mu^+, x_\mu^-, \hat{x}_\mu^+, \hat{x}_\mu^-, s, b) \\ &\times \Phi_{h_1 h_2}\left(x^{\text{proj}} - \sum_\mu \hat{x}_\mu^+, x^{\text{targ}} - \sum_\mu \hat{x}_\mu^-, s, b\right), \end{aligned} \quad (5.52)$$

which may be approximated as

$$\gamma_{h_1 h_2}(s, b) = \sum_m \frac{1}{m!} \int \prod_{\mu=1}^m dx_{\mu}^+ dx_{\mu}^- \prod_{\mu=1}^m \hat{G}_{\mathbb{P}}^{h_1 h_2}(x_{\mu}^+, x_{\mu}^-, x^{\text{proj}}, x^{\text{targ}}, s, b) \times \Phi_{h_1 h_2}(x^{\text{proj}}, x^{\text{targ}}, s, b), \quad (5.53)$$

with

$$\hat{G}_{\mathbb{P}}^{h_1 h_2}(x^+, x^-, x^{\text{proj}}, x^{\text{targ}}, s, b) = \frac{1}{F_{\text{remn}}(x^{\text{proj}}) F_{\text{remn}}(x^{\text{targ}})} \times \int d\hat{x}^+ d\hat{x}^- \hat{G}_{\mathbb{P}}^{h_1 h_2}(x^+, x^-, \hat{x}^+, \hat{x}^-, s, b) F_{\text{remn}}(x^{\text{proj}} - \hat{x}^+) F_{\text{remn}}(x^{\text{targ}} - \hat{x}^-). \quad (5.54)$$

Based on eq. (5.53), we proceed as in the eikonal case. We unitarize the theory by replacing $\Phi_{h_1 h_2}$ by $\Phi_{\text{u}_{h_1 h_2}}$ in a complete analogy to the eikonal model. The numerical Markov chain procedures have to be modified slightly due to the fact that the \hat{G} functions contain x^{proj} and x^{targ} as arguments. One can no longer restrict oneself to considering one single site of the interaction matrix, since changing x^+ and x^- modifies as well x^{proj} and x^{targ} and affects therefore the other sites as well (in case of nucleus-nucleus all the sites related to the same projectile and target nucleon). But this does not pose major problems.

5.3 Important Features of Enhanced Diagrams

The amplitude corresponding to a single Pomeron exchange as shown at fig. 5.7(a) behaves as a function of energy approximately as s^{Δ} , where s is the c.m. energy squared for hadron-hadron interaction and Δ is some effective exponent. At the same moment, the amplitude of the so-called Y-diagram shown in fig. 5.7(b) increases asymptotically as $s^{2\Delta}$, as can be seen from eq. (5.30). The amplitude corresponding to the diagram in fig. 5.7(c) behaves as $s^{3\Delta}$. This indicates very

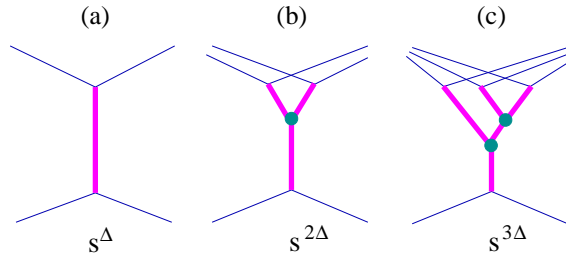


Figure 5.7: Energy dependence of Pomeron diagrams.

important property of enhanced diagrams, namely that they increase with energy much faster than the usual eikonal ones.

In the following, we discuss exclusively enhanced Y-diagrams for given hadron types h_1 and h_2 , and to simplify the notation, we use simply G to refer to the corresponding profile function, omitting all indices referring to the initial hadron types and the Pomeron type.

In order to calculate contributions of enhanced graphs to the total interaction cross section, one has to consider different cuts of elastic scattering diagrams. We have

$$G \equiv \frac{1}{2s} 2\text{Im}\tilde{T}(s, t=0) = G_{(0)} + G_{(1)} + G_{(2)}, \quad (5.55)$$

where $G_{(i)}$ refers to the different cut diagrams, as shown in fig. 5.8. We use our convention employed

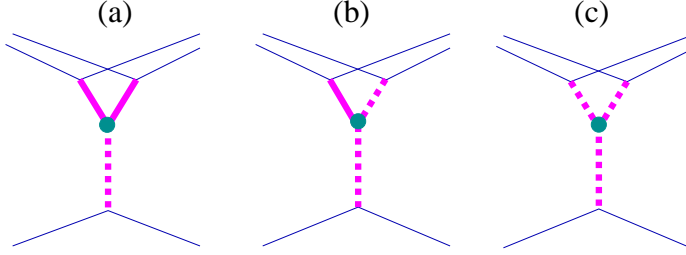


Figure 5.8: The different cuts of the Y-diagram.

already earlier to plot cut Pomerons as dashed and uncut ones as full vertical lines. The diagram in fig. 5.8(a) gives rise to the process of high mass target diffraction ($G_{(0)}$), the diagram in fig. 5.8(b) represents the screening correction to the one cut Pomeron process ($G_{(1)}$), and the diagram in fig 5.8(c) - the cut Pomeron fusion process ($G_{(2)}$). As discussed in the preceding section, we have

$$\begin{aligned} G_{(0)} &= -1G, \\ G_{(1)} &= +4G, \\ G_{(2)} &= -2G, \end{aligned} \quad (5.56)$$

the sum being therefore equal to G , as it should be. Since G is negative, the first order contribution to the inelastic cross section is negative, so another very important property of enhanced diagrams is the suppression of the increase of the inelastic cross section with energy.

A remarkable feature of enhanced diagrams is connected to their effect on the inclusive particle spectra. In particular, if one assumes (for a qualitative discussion) that each cut Pomeron gives rise to a flat rapidity distribution of secondary hadrons, $dn/dy = \rho_0$, the sum of all three contributions gives the screening correction to the inclusive particle spectrum as

$$\frac{d\Delta n}{dy} \propto -1G \times 0\rho_0 + 4G \times 1\rho_0 - 2G \times 2\rho_0 = 0, \quad y > y_0 \quad (5.57)$$

and

$$\frac{d\Delta n}{dy} \propto -1G \times \rho_0 + 4G \times \rho_0 - 2G \times \rho_0 = G\rho_0 < 0, \quad y < y_0, \quad (5.58)$$

where y_0 is the rapidity position of the triple Pomeron vertex, see fig. 5.9. The contribution is negative, because G is negative. Thus enhanced diagrams give rise to screening corrections to

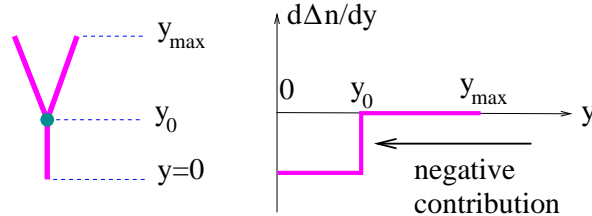


Figure 5.9: Effect on inclusive spectra.

secondary hadron spectra only in restricted regions of the kinematical phase space; contributions of different cuts exactly cancel each other in the region of rapidity space where two or more Pomerons are exchanged in parallel (in case of the diagram of fig. 5.9 for $y > y_0$) [15]. Therefore another important effect of Pomeron-Pomeron interactions is the modification of secondary hadron spectra, being mainly suppressed in the fragmentation regions of the interaction: close to $y = 0$ from the

Y-diagrams and close to y_{\max} for the inverted Y-diagrams. That explains the great importance of enhanced diagrams for the solution of the unitarity problems inherent for the pure eikonal scheme and for the construction of a consistent unitary approach to hadronic interactions at very high energies (see the discussion in chapter 3).

Another important effect is the considerable increase of fluctuations of hadronic interactions. Let us for a moment consider the indices indicating Pomeron types: $G_{3\mathbb{P}+}$ for the Y-diagram as discussed above, $G_{3\mathbb{P}-}$ for the corresponding inverted diagram, and $G_{1\mathbb{P}}(s, x^+, x^-)$ for the normal Pomeron. The full contribution (so far) is

$$G_{\mathbb{P}} = G_{1\mathbb{P}} + G_{3\mathbb{P}-} + G_{3\mathbb{P}+}. \quad (5.59)$$

Using the fact that $G_{3\mathbb{P}\pm}$ can be written as the sum of the different cut contributions $G_{3\mathbb{P}\pm(i)}$, we get

$$G_{\mathbb{P}} = G_{1\mathbb{P}} + \sum_i G_{3\mathbb{P}- (i)} + \sum_i G_{3\mathbb{P}+ (i)},$$

which may be written as

$$G_{\mathbb{P}} = \{G_{1\mathbb{P}} + G_{3\mathbb{P}- (1)} + G_{3\mathbb{P}+ (1)}\} + \{G_{3\mathbb{P}- (0)} + G_{3\mathbb{P}+ (0)}\} + \{G_{3\mathbb{P}- (2)} + G_{3\mathbb{P}+ (2)}\}. \quad (5.60)$$

This means that we have three contributions: a modified one cut Pomeron exchange, with probability w_{one} , the high mass target (see fig. 5.8(a)) and projectile diffraction, with probability w_{diff} , and the process of Pomeron fusion of fig. 5.8(c), with probability w_{fusion} , where the probabilities are given as

$$w_{\text{one}} = \frac{G_{1\mathbb{P}} + G_{3\mathbb{P}- (1)} + G_{3\mathbb{P}+ (1)}}{G_{\mathbb{P}}}, \quad w_{\text{diff}} = \frac{G_{3\mathbb{P}- (0)} + G_{3\mathbb{P}+ (0)}}{G_{\mathbb{P}}}, \quad w_{\text{fusion}} = \frac{G_{3\mathbb{P}- (2)} + G_{3\mathbb{P}+ (2)}}{G_{\mathbb{P}}}. \quad (5.61)$$

The two latter processes result in correspondingly much smaller and much larger values of the hadron multiplicity than for the one Pomeron process.

The problem of consistent treatment of Pomeron-Pomeron interactions was addressed already in [23, 19]. The number of diagrams which contribute essentially to the interaction characteristics increases fast with the energy. Therefore, one has to develop a suitable method to take into account the necessary contributions to the forward scattering amplitude, the latter one being related via the optical theorem to the total cross section of the reaction and to the weights for particular configurations of the interaction (via the “cutting” procedure). Such a scheme is still under development and our current goal was the proper treatment of some lowest order enhanced diagrams. Thus we proposed a minimal modification of the standard eikonal scheme, which allowed us to obtain a consistent description of hadronic interactions in the range of c.m. energies from some ten GeV till few thousand TeV. Already this minimal scheme allows to achieve partly the goals mentioned above: the slowing down of the energy increase of the interaction cross section and the non-AGK-type modification of particle spectra, as well as the improvement of the description of the multiplicity and inelasticity fluctuations in hadron-hadron interaction.

An important question exists concerning the nature of the triple-Pomeron coupling. As discussed above, we used the perturbative treatment for the part of a parton cascade developing in the region of parton virtualities bigger than some cutoff Q_0^2 , whereas the region of smaller virtualities is treated phenomenologically, based on the soft Pomeron. There was an argumentation in [24] that the triple Pomeron coupling is perturbative and therefore can be described on the basis of the QCD techniques. At the same time, it was shown in [25] that such perturbative coupling, corresponding to non-small parton virtualities, would result in negligible contribution to the basic interaction characteristics, in particular, to the proton structure function F_2 . The latter result

was confirmed experimentally by HERA measurements, where no real shoulder in the behavior of $F_2(x, Q^2)$ (predicted in [24]) was found in the limit $x \rightarrow 0$. Another argument in favor of the smallness of the perturbative Pomeron-Pomeron coupling comes from the HERA diffractive data, where the proportion of diffractive type events (with a large rapidity gap in secondary hadron spectra) appeared to be nearly independent on the virtuality of the virtual photon probe. This implies that the Pomeron self-interaction is rather inherent to the non-perturbative initial condition for the QCD evolution than to the dynamical evolution itself. Therefore we assumed that the Pomerons interact with each other in the non-perturbative region of parton virtualities $Q^2 < Q_0^2$ and considered it as the interaction **between soft Pomerons**. In our scheme the relatively big value of the soft triple-Pomeron coupling results in the screening corrections which finally prevent the large increase of parton densities in the small x limit and restore the unitarity, thus leaving a little room for higher twist effects in the perturbative part of the interaction.

Chapter 6

Parton Configurations

In this section, we consider the generation of parton configurations in nucleus-nucleus (including proton-proton) scattering for a given interaction configuration, which has already been determined, as discussed above. So, the numbers m_k of elementary interactions per nucleon-nucleon pair k are known, as well as the light cone momentum fractions $x_{k\mu}^+$ and $x_{k\mu}^-$ of each elementary interaction of the pair k . A parton configuration is specified by the number of partons, their types and momenta.

6.1 General Procedure of Parton Generation

We showed earlier that the inelastic cross section may be written as

$$\sigma_{\text{inel}} = \int d^2b \sum_m \int dX^+ dX^- \Omega(m, X^+, X^-), \quad (6.1)$$

where $\{m, X^+, X^-\}$ represents an interaction configuration. The function Ω is known (see eq. (2.72)) and is interpreted as the probability distribution for interaction configurations. For each individual elementary interaction a term $G_{1\text{P}}^{h_1 h_2}$ appears in the formula for Ω , where the function $G_{1\text{P}}^{h_1 h_2}$ itself can be expressed in terms of contributions of different parton configurations. Namely the QCD evolution function E_{QCD}^{ij} , which enters into the formula for the elementary interaction contribution $G_{1\text{P}}^{h_1 h_2}$, is the solution of a ladder equation, where adding a ladder rung corresponds to an integration over the momenta of the corresponding resolvable parton emitted. The complete evolution function is therefore a sum over n -rung ladder contributions, where the latter one can be written as an integration over n parton momenta. So we have

$$\Omega(m, X^+, X^-) = \prod_{k=1}^{AB} \prod_{\mu=1}^{m_k} \sum_{\tau=1}^t \sum_{\nu=1}^{n_{k\mu\tau}} \int d^3p_{k\mu\tau\nu} \Psi(\{p_{k\mu\tau\nu}\}), \quad (6.2)$$

where t is the number of Pomeron types (soft, sea-sea, ...), and $n_{k\mu\tau}$ the number of partons for the μ^{th} interaction of the pair k in case of Pomeron type τ . We interpret

$$\frac{\Psi(\{p_{k\mu\tau\nu}\})}{\Omega(m, X^+, X^-)} \quad (6.3)$$

as the probability distribution for parton configurations for a given interaction configuration $\{m, X^+, X^-\}$. The Monte Carlo method provides a convenient tool for treating such multidimensional distributions: with Θ being known (see chapter 2 and the discussion below), one generates parton configurations according to this distribution.

We want to stress that the parton generation is also based on the master formula eq. (2.72), no new elements enter.

In the following, we want to sketch the generation of parton configurations, technical details are provided in the next section. Let us consider a particular elementary interaction with given light cone momentum fractions x^+ and x^- and given impact parameter difference b between the corresponding pair of interacting nucleons, for a fixed primary energy squared s .

For the sake of simplicity, we discuss here the procedure without the triple-Pomeron contribution, with the corresponding generalization being done in appendix C.4. We have to start with specifying the type of elementary interaction (soft, semi-hard, or valence type). The corresponding probabilities are

$$\begin{aligned} & G_{\text{soft}}^{h_1 h_2}(x^+, x^-, s, b) / G_{\text{1P}}^{h_1 h_2}(x^+, x^-, s, b), \\ & G_{\text{sea-sea}}^{h_1 h_2}(x^+, x^-, s, b) / G_{\text{1P}}^{h_1 h_2}(x^+, x^-, s, b), \\ & G_{\text{val-val}}^{h_1 h_2}(x^+, x^-, s, b) / G_{\text{1P}}^{h_1 h_2}(x^+, x^-, s, b), \\ & G_{\text{val-sea}}^{h_1 h_2}(x^+, x^-, s, b) / G_{\text{1P}}^{h_1 h_2}(x^+, x^-, s, b), \\ & G_{\text{sea-val}}^{h_1 h_2}(x^+, x^-, s, b) / G_{\text{1P}}^{h_1 h_2}(x^+, x^-, s, b). \end{aligned} \quad (6.4)$$

In the case of a soft elementary interaction, no perturbative parton emission takes place. Therefore we are left with the trivial parton configuration, consisting from the initial active partons – hadron constituents – to which the Pomeron is attached.

Let us now consider a semi-hard contribution. We obtain the desired probability distributions from the explicit expressions for $G_{\text{sea-sea}}^{h_1 h_2}$. For given x^+ , x^- , and b we have

$$\begin{aligned} G_{\text{sea-sea}}^{h_1 h_2}(x^+, x^-, s, b) & \propto \int_0^1 dz^+ \int_0^1 dz^- \sum_{ij} E_{\text{soft}}^i(z^+) E_{\text{soft}}^j(z^-) \sigma_{\text{hard}}^{ij}(z^+ z^- \hat{s}, Q_0^2) \\ & \times \frac{1}{4\pi \lambda_{\text{soft}}^{h_1 h_2}(1/(z^+ z^-))} \exp\left(-\frac{b^2}{4\lambda_{\text{soft}}^{h_1 h_2}(1/(z^+ z^-))}\right) F_{\text{part}}^{h_1}(x^+) F_{\text{part}}^{h_2}(x^-) \end{aligned} \quad (6.5)$$

with $\hat{s} = x^+ x^- s$, $\lambda_{\text{soft}}^{h_1 h_2}(\xi) = R_{h_1}^2 + R_{h_2}^2 + \alpha'_{\text{soft}} \ln \xi$, and

$$\begin{aligned} \sigma_{\text{hard}}^{ij}(\hat{s}, Q_0^2) & = K \sum_{kl} \int dx_B^+ dx_B^- dp_{\perp}^2 \frac{d\sigma_{\text{Born}}^{kl}}{dp_{\perp}^2}(x_B^+ x_B^- \hat{s}, p_{\perp}^2) \\ & \times E_{\text{QCD}}^{ik}(x_B^+, Q_0^2, M_F^2) E_{\text{QCD}}^{jl}(x_B^-, Q_0^2, M_F^2) \theta(M_F^2 - Q_0^2), \end{aligned} \quad (6.6)$$

representing the perturbative parton-parton cross section, where both initial partons are taken at the virtuality scale Q_0^2 ; we choose the factorization scale as $M_F^2 = p_{\perp}^2/4$. The integrand of eq. (6.5) serves as the probability distribution to generate the momentum fractions $x_1^{\pm} = x^{\pm} z^{\pm}$ and the flavors i and j of the initial partons for the parton ladder.

The knowledge of the initial conditions – the momentum fractions x_1^{\pm} and the starting virtuality Q_0^2 for the “first partons” as well as the flavors i and j – allows us to reconstruct the complete ladder, based on the eq. (6.6) and on the evolution equations (B.28-B.29) for E_{QCD}^{ij} . To do so, we generalize the definition of the parton-parton cross section $\sigma_{\text{hard}}^{ij}$ to arbitrary virtualities of the initial partons, defining

$$\begin{aligned} \sigma_{\text{hard}}^{ij}(\hat{s}, Q_1^2, Q_2^2) & = K \sum_{kl} \int dx_B^+ dx_B^- dp_{\perp}^2 \frac{d\sigma_{\text{Born}}^{kl}}{dp_{\perp}^2}(x_B^+ x_B^- \hat{s}, p_{\perp}^2) \\ & \times E_{\text{QCD}}^{ik}(x_B^+, Q_1^2, M_F^2) E_{\text{QCD}}^{jl}(x_B^-, Q_2^2, M_F^2) \Theta(M_F^2 - \max[Q_1^2, Q_2^2]) \end{aligned} \quad (6.7)$$

and

$$\sigma_{\text{ord}}^{ij}(\hat{s}, Q_1^2, Q_2^2) = K \sum_k \int dx_B^+ dx_B^- dp_{\perp}^2 \frac{d\sigma_{\text{Born}}^{kj}}{dp_{\perp}^2}(x_B^+ x_B^- \hat{s}, p_{\perp}^2) \quad (6.8)$$

$$\times E_{\text{QCD}}^{ik}(x_B^+, Q_1^2, M_F^2, w^+) \Delta^j(Q_2^2, M_F^2) \Theta(M_F^2 - \max[Q_1^2, Q_2^2])$$

representing the full ladder contribution (σ_{hard}) and the contribution, corresponding to the ordering of parton virtualities towards the end of the ladder, i.e. to the case of parton j , involved into the highest virtuality Born process (σ_{ord}). We calculate and tabulate σ_{hard} and σ_{ord} initially, so that we can use them via interpolation to generate partons. The generation of partons is done in an iterative fashion based on the following equations:

$$\begin{aligned} \sigma_{\text{hard}}^{ij}(\hat{s}, Q_1^2, Q_2^2) &= \sum_k \int \frac{dQ^2}{Q^2} \int d\xi \Delta^i(Q_1^2, Q^2) \frac{\alpha_s}{2\pi} P_i^k(\xi) \sigma_{\text{hard}}^{kj}(\xi \hat{s}, Q^2, Q_2^2) \\ &+ \sigma_{\text{ord}}^{ji}(\hat{s}, Q_2^2, Q_1^2) \end{aligned} \quad (6.9)$$

and

$$\begin{aligned} \sigma_{\text{ord}}^{ij}(\hat{s}, Q_1^2, Q_2^2) &= \sum_k \int \frac{dQ^2}{Q^2} \int d\xi \Delta^i(Q_1^2, Q^2) \frac{\alpha_s}{2\pi} P_i^k(\xi) \sigma_{\text{ord}}^{kj}(\xi \hat{s}, Q^2, Q_2^2) \\ &+ \sigma_{\text{Born}}^{ij}(\hat{s}, Q_1^2, Q_2^2) \end{aligned} \quad (6.10)$$

Here, $\sigma_{\text{Born}}^{ij}$ gives the contribution of the configuration without any resolvable emission before the highest virtuality Born process:

$$\begin{aligned} \sigma_{\text{Born}}^{ij}(\hat{s}, Q_1^2, Q_2^2) &= K \int dp_{\perp}^2 \frac{d\sigma_{\text{Born}}^{ij}}{dp_{\perp}^2}(\hat{s}, p_{\perp}^2) \\ &\times \Delta^i(Q_1^2, M_F^2) \Delta^j(Q_2^2, M_F^2) \Theta(M_F^2 - \max[Q_1^2, Q_2^2]) \end{aligned} \quad (6.11)$$

The procedure is described in detail in the next section.

In the case of elementary interactions involving valence quarks, the method is almost identical. In that case, the corresponding momentum fractions x_1^{\pm} are the ones of valence quarks, $x_1^{\pm} = x_q^{\pm}$, to be determined according to the corresponding integrands in the expressions for $G_{\text{val}}^{h_1 h_2}$, $G_{\text{val-sea}}^{h_1 h_2}$, see eqs. (2.48-2.50). For example, in the case of both hadron constituents being valence quarks, one generates momentum fractions x_1^{\pm} and valence quark flavors i, j with the distribution (up to a normalization constant)

$$D_{\text{val-val}}^{h_1 h_2, ij}(x_{qv}^+, x_{qv}^- s, b) \bar{F}_{\text{part}}^{h_1, i}(x_{qv}^+, x^+ - x_{qv}^+) \bar{F}_{\text{part}}^{h_2, j}(x_{qv}^-, x^- - x_{qv}^-), \quad (6.12)$$

see eqs. (2.48), (2.18). One then proceeds to generate parton emissions as discussed above.

6.2 Generating the Parton Ladder

We now discuss in detail the generation of the partons in a ladder, starting from the initial partons (“leg partons”) with flavors i and j and light cone momentum fractions x_1^+ and x_1^- . To simplify the discussion, we will neglect the effects of finite virtualities and transverse momenta of initial partons in the kinematical formulas so that the 4-momenta k_1 and k_1' of the two leg partons are purely longitudinal. In the hadron-hadron (nucleus-nucleus) center of mass frame we have:

$$\begin{aligned} k_1^+ &= x_1^+ \sqrt{s}/2, & k_1^- &= 0, & k_{1\perp} &= 0, \\ k_1'^- &= x_1^- \sqrt{s}/2, & k_1'^+ &= 0, & k_{1\perp}' &= 0. \end{aligned} \quad (6.13)$$

The invariant mass squared of the ladder is $\hat{s} = (k_1 + k_1')^2$.

One first generates all resolvable partons emitted at one side of the ladder before the hardest process (for the definiteness we start with the leg parton i moving in the forward direction). At

each step one decides whether there is any resolvable emission at the forward end of the ladder before the hardest process. An emission is done with the probability

$$\text{prob}(\text{forward emission}) = \left(\sigma_{\text{hard}}^{ij}(\hat{s}, Q_1^2, Q_2^2) - \sigma_{\text{ord}}^{ji}(\hat{s}, Q_2^2, Q_1^2) \right) / \sigma_{\text{hard}}^{ij}(\hat{s}, Q_1^2, Q_2^2). \quad (6.14)$$

In case of an emission, the generation of light cone momentum fraction ξ and momentum transfer squared Q^2 for the current parton branching is done – up to a normalization constant – according to the integrand of $(\sigma_{\text{hard}}^{ij} - \sigma_{\text{ord}}^{ji})$,

$$\text{prob}(\xi, Q^2) \propto \frac{1}{Q^2} \Delta^i(Q_1^2, Q^2) \frac{\alpha_s}{2\pi} \sum_{i'} P_i^{i'}(\xi) \sigma_{\text{hard}}^{i'j}(\xi \hat{s}, Q^2, Q_2^2) \quad (6.15)$$

see eq. (6.9). Here the emitted s -channel parton gets the share $1 - \xi$ of the parent (leg) parton light cone momentum k^+ and the transverse momentum squared $p_\perp^2 \equiv (1 - \xi)Q^2$. To leading logarithmic accuracy, the initial parton virtuality is neglected in the branching probability eq. (6.15), because of $Q_1^2 \ll Q^2$. Generating randomly the polar angle φ for the emission, one reconstructs the 4-vector p of the final s -channel parton as

$$p^+ = (1 - \xi)k_1^+, \quad p^- = p_\perp^2 / ((1 - \xi)k_1^+), \quad \vec{p}_\perp = \begin{pmatrix} p_\perp \cos \varphi \\ p_\perp \sin \varphi \end{pmatrix}. \quad (6.16)$$

The remaining ladder after the parton emission is now characterized by the mass squared $\hat{s}' = (k_1 + k_1' - p)^2 \simeq \xi \hat{s}$ and the initial virtualities $Q_1'^2 = Q^2$ and Q_2^2 . The flavor i' of the new leg parton is generated according to the corresponding weights in eq. (6.15), properly normalized given as

$$\text{prob}(i') = \frac{P_i^{i'}(\xi) \sigma_{\text{hard}}^{i'j}(\hat{s}', Q^2, Q_2^2)}{\sum_l P_i^l(\xi) \sigma_{\text{hard}}^{lj}(\hat{s}', Q^2, Q_2^2)}, \quad (6.17)$$

where $\sigma_{\text{hard}}^{i'j}(\xi \hat{s}, Q^2, Q_2^2)$ is the parton cross section (6.7) for the new ladder. One then renames \hat{s}' , i' , and $Q_1'^2$ into \hat{s} , i , and Q_1^2 and repeats the above procedure.

In case of no forward emission, the generation of all resolvable parton emissions at the forward side of the ladder has been completed.

One then proceeds to generate all resolvable parton emissions for the backward side of the ladder, starting from the original leg parton j of virtuality $Q_2^2 = Q_0^2$, by using a corresponding recursive algorithm, now based on eq. (6.10). On the other end of the ladder, we have (after renaming) parton i with the virtuality Q_1^2 . One decides whether there is any resolvable emission before the hardest process, where the probability of an emission is given as

$$\text{prob}(\text{backward emission}) = \left(\sigma_{\text{ord}}^{ji}(\hat{s}, Q_2^2, Q_1^2) - \sigma_{\text{Born}}^{ij}(\hat{s}, Q_1^2, Q_2^2) \right) / \sigma_{\text{ord}}^{ji}(\hat{s}, Q_2^2, Q_1^2). \quad (6.18)$$

In case of an emission, the generation of the fraction ξ of the light cone momentum $k_1'^-$, and of the momentum transfer squared Q^2 is done – up to a normalization constant – according to the integrand of $(\sigma_{\text{ord}}^{ji} - \sigma_{\text{Born}}^{ij})$,

$$\text{prob}(\xi, Q^2) \propto \frac{1}{Q^2} \Delta^j(Q_2^2, Q^2) \frac{\alpha_s}{2\pi} \sum_{j'} P_j^{j'}(\xi) \sigma_{\text{ord}}^{j'i}(\xi \hat{s}, Q^2, Q_1^2), \quad (6.19)$$

see eq. (6.10). The flavor j' of the new leg parton is defined according to the partial contributions in (6.19). The generation of resolvable parton emissions is completed when the iterative procedure stops, with the probability

$$1 - \text{prob}(\text{backward emission}).$$

Note, that all parton emissions are simulated in the original Lorentz frame, where the original leg partons (the initial partons for the perturbative evolution) are moving along the z -axis.

The final step is the generation of the hardest $2 \rightarrow 2$ parton scattering process. In the center of mass system of two partons i and j with center-of-mass energy squared \hat{s} , we simulate the transverse momentum p_\perp^2 for the scattering within the limits (given by the condition $M_F^2 = p_\perp^2/4 > \max[Q_1^2, Q_2^2]$)

$$4 \max[Q_1^2, Q_2^2] < p_\perp^2 < \hat{s}/4 \quad (6.20)$$

according to

$$\text{prob}(p_\perp^2) \propto \frac{d\sigma_{\text{Born}}^{ij}}{dp_\perp^2}(\hat{s}, p_\perp^2) \Delta^i(Q_1^2, p_\perp^2/4) \Delta^j(Q_2^2, p_\perp^2), \quad (6.21)$$

where the differential parton-parton cross section is

$$\frac{d\sigma_{\text{Born}}^{ij}}{dp_\perp^2}(\hat{s}, p_\perp^2) = \frac{1}{16\pi\hat{s}^2\sqrt{1-4p_\perp^2/\hat{s}}} \sum_{k,l} |M^{ij \rightarrow kl}(\hat{s}, p_\perp^2)|^2 \quad (6.22)$$

with $|M^{ij \rightarrow kl}(\hat{s}, p_\perp^2)|^2$ being the squared matrix elements of the parton subprocesses [26].

Then we choose a particular subprocess $ij \rightarrow kl$ according to its contribution to the differential cross section (6.22), and reconstruct the 4-momenta p_1 and p_2 of the final partons in their center of mass system as

$$\begin{aligned} p_1^+ &= z\sqrt{\hat{s}}, & p_1^- &= p_\perp^2/(z\sqrt{\hat{s}}), & \vec{p}_{1\perp} &= \begin{pmatrix} p_\perp \cos \varphi \\ p_\perp \sin \varphi \end{pmatrix}, \\ p_2^+ &= (1-z)\sqrt{\hat{s}}, & p_2^- &= p_\perp^2/((1-z)\sqrt{\hat{s}}), & \vec{p}_{2\perp} &= \begin{pmatrix} -p_\perp \cos \varphi \\ -p_\perp \sin \varphi \end{pmatrix}, \end{aligned} \quad (6.23)$$

with

$$z = \frac{1}{2} \left(1 + \sqrt{1 - 4p_\perp^2/\hat{s}} \right) \quad (6.24)$$

and a random polar angle φ . We finally boost the momenta to the original Lorentz frame.

6.3 The Time-like Parton Cascade

The above discussion of how to generate parton configurations is not yet complete: the emitted partons are in general off-shell and can therefore radiate further partons. This so-called time-like radiation is taken into account using standard techniques [27], to be discussed in the following.

The parton emission from an off-shell parton is done using the so-called DGLAP evolution equations, which describes the process with the leading logarithmic accuracy. The splitting probability for the initial parton of type j is then given as

$$\frac{dP}{P} = -\frac{dQ^2}{Q^2} \int dz \sum_k \frac{\alpha_s(p_\perp^2)}{2\pi} P_j^k(z), \quad (6.25)$$

with the usual Altarelli-Parisi splitting functions $P_j^k(z)$. Here $Q^2 = Q_j^2$ is the virtuality of the parent parton j and z is interpreted as the energy fraction carried away by the daughter parton k . The maximum possible virtuality $q_{j\text{max}}^2$ of the parton j is given by the virtuality of the parent of j . One imagines now to decrease the virtuality of j , starting from the maximum value, such that the DGLAP evolution equations give then the probability dP that during a change dQ^2 of the virtuality, a parton splits into two daughter partons k and l – see fig. 9.1. For the energies of the daughter partons one has

$$E_k = zE_j, \quad E_l = (1-z)E_j. \quad (6.26)$$

Choosing a frame where $p_{j\perp} = 0$, we have

$$p_{k\perp} = -p_{l\perp} = p_\perp, \quad (6.27)$$

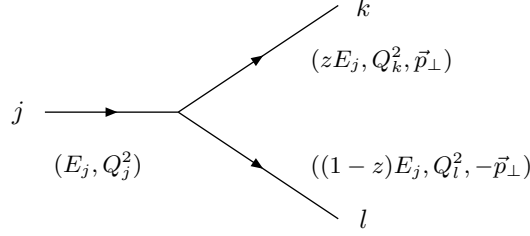


Figure 6.1: A branching of a parton j into two partons k and l . The kinematical variables used to describe the branching are the energies E_i , the virtualities Q_i^2 , and the transverse momenta $p_{i\perp}$.

with

$$p_\perp^2 = \frac{E_j^2 (z(1-z)Q_j^2 - zQ_l^2 - (1-z)Q_k^2) - \frac{1}{4}(Q_l^2 - Q_j^2 - Q_k^2)^2 + Q_j^2 Q_k^2}{E_j^2 - Q_j^2}. \quad (6.28)$$

As usual, a cutoff parameter terminates the cascade of parton emissions. We introduce a parameter $p_{\perp\text{fin}}^2$, which represents the lower limit for p_\perp^2 during the evolution, from which we obtain the lower limit for the virtualities as $Q_{\text{min}}^2 = 4p_{\perp\text{fin}}^2$.

Let us provide some technical details on the splitting procedure. Using eq. (6.25) and applying the rejection method proposed in [27] we determine the variables Q_j^2 and z as well as the flavors k, l of the daughter partons – see appendix B.3. To determine the 4-momentum p_j of the parent parton we have to distinguish between three different modes of branching (see figure 6.2):

1. If j is the initial parton for the time-like cascade, the energy E_j is given, and with the obtained value Q_j^2 , we can calculate $|\vec{p}_j| = \sqrt{E_j^2 - Q_j^2}$. The direction of \vec{p}_j is obtained from the momentum conservation constraint for the summary momentum of all partons produced in the current time-like cascade.
2. If j is the initial parton for the time-like cascade resulted from the Born process, together with a partner parton j' , then we know the total energy $E_j + E_{j'}$ for the two partons. After obtaining the virtualities Q_j^2 and $Q_{j'}^2$ from the secondary splittings $j \rightarrow k, l$ and $j' \rightarrow k', l'$ we can use the momentum conservation constraint in the parton-parton center of mass frame, which gives $\vec{p}_j = -\vec{p}_{j'} = \vec{p}$ and allows to determine $|\vec{p}|$. The direction of \vec{p} can be chosen randomly.
3. If parton j is produced in a secondary time-like branching, its energy $E_j = zE_{\text{parent}}$ as well as the energy of the second “daughter” $E_{j'} = (1-z)E_{\text{parent}}$ are known from the previous branching, as well as Q_j^2 and $Q_{j'}^2$ – from the splittings $j \rightarrow k, l$ and $j' \rightarrow k', l'$, which allows to determine $\vec{p}_{j\perp} = -\vec{p}_{j'\perp} = \vec{p}_\perp$ using eq. (6.28) in the frame where the parent parton moves along the z -axis. In some cases one gets $p_\perp^2 < 0$; then the current splitting of the parton j is rejected and its evolution continues.

The described leading order algorithm is known to be not accurate enough for secondary hadron production, in particular it gives too high multiplicities of secondaries in e^+e^- -annihilation. The method can be corrected if one takes into account the phenomenon of color coherence. The latter one appears if one considers some higher order corrections to the simplest leading logarithmic contributions, the latter ones being the basis for the usual Altarelli-Parisi evolution equations. In the corresponding treatment [28] – so-called modified leading logarithmic approach – one essentially recovers the original scheme for the time-like parton cascading supplemented by the additional condition, the strict ordering of the emission angles in successive parton branchings. The appearance of the angular ordering can be explained in a qualitative way: (see [29]): if a transverse wavelength

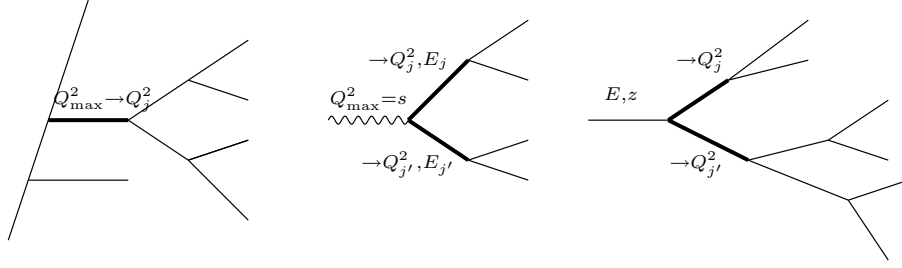


Figure 6.2: The three branching modes as explained in the text. The arrows indicate the variables to be determined.

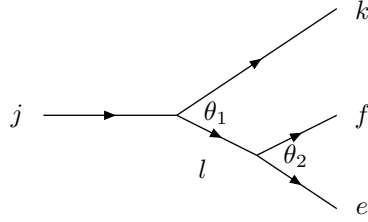


Figure 6.3: Angular ordering in successive branchings.

of an emitted gluon (f or e on figure 6.3) is larger than the separation between the two, this gluon cannot see the color charge of the parent (l) but only the total (much smaller) charge of the two partons ($k + l = j$) and the radiation is suppressed. In a Monte-Carlo model this can be easily realized by imposing the angular ordering condition via rejection [30]. Thus, for each branching we check whether the angular ordering $\theta_2 < \theta_1$ is valid, where θ_1 is the angle of the previous branching, and reject the current splitting otherwise.

Chapter 7

Hadronization

Till now, our discussion concerned exclusively partons, whereas “in the real world” one observes finally hadrons. It is the purpose of this chapter, to provide the link, i.e. to discuss how to calculate hadron production starting from partonic configurations, discussed in the previous chapters.

Hadron production is related to the structure of cut Pomerons. A cut Pomeron is in principle a sum over squared amplitudes of the type $a + b \rightarrow \text{hadrons}$, integrated over phase space, with a and b being the nucleon constituents involved in the interaction. So far there was no need to talk about the details of the hadron production, which could be considered to be “integrated out”. In case of soft Pomerons, we used a parameterization of the whole object, based on general asymptotic considerations, which means that all the hadron production is hidden in the few parameters characterizing the soft Pomeron. In case of hard Pomerons, we discussed the explicit partonic structure of the corresponding diagram without talking about hadrons. This is justified based on the assumption that summing over hadronic final states is identical to summing over partonic final states, both representing complete sets of states. But although our ignorance of hadronic states so far was well justified, we finally have to be specific about the hadronic structure of the cut Pomerons, because these are hadronic spectra which are measured experimentally, and not parton configurations.

Lacking a rigorous theoretical treatment, we are going to use the same strategy as we used already for treating the soft Pomeron: we are going to present a “parameterization” of the hadronic structure of the cut Pomerons, as simple as possible with no unnecessary details, in agreement with basic laws of physics and basic experimental observations. We do not claim at all to understand the microscopic mechanism, so our parameterization, called “string model”, should not be considered as a microscopic hadronization model.

7.1 Hadronic Structure of Cut Pomerons

In order to develop our multiple scattering theory, we used a simple graphical representation of a cut Pomeron, namely a thick vertical line connecting the external legs representing nucleon components, as shown in fig. 7.1. This simple diagram hides somewhat the fact that there is a

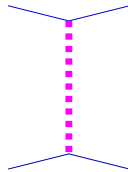


Figure 7.1: Symbol representing a cut Pomeron.

complicated structure hidden in this Pomeron, and the purpose of this section is to discuss in particular the hadronic content of the Pomeron.

Let us start our discussion with the soft Pomeron. Based on Veneziano's topological expansion one may consider a soft Pomeron as a "cylinder" i.e. the sum of all possible QCD diagrams having a cylindrical topology, see fig. 7.2. As discussed in detail in chapter 2.2, the "nucleon components"

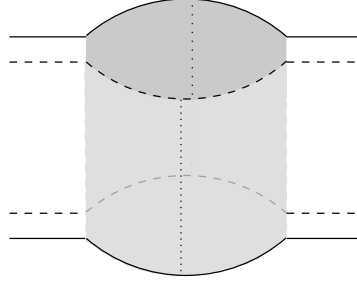


Figure 7.2: Cut soft Pomeron represented as a cut cylinder. The grey areas represent unresolved partons.

mentioned earlier, representing the external legs of the diagram, are always quark-anti-quark pairs, indicated by a dashed line (anti-quark) and a full line (quark) in fig. 7.2. Important for the discussion of particle production are of course cut diagrams, therefore we show in fig. 7.2 a cut cylinder representing a cut Pomeron: the cut plane is shown as two vertical dotted lines. Let us consider the half-cylinder, for example, the one to the right of the cut, representing an inelastic amplitude.



Figure 7.3: Planar representation of a half-cylinder obtained from cutting a cylinder diagram (see fig. 7.2).

We can unfold this object in order to have a planar representation, as shown in fig.7.3. Here, the dotted vertical lines indicate the cuts of the previous figure, and it is here where the hadronic final state hadrons appear. Lacking a theoretical understanding of this hadronic structure, we simply apply a phenomenological procedure, essentially a parameterization. We require the method to be as simple as possible, with a minimum of necessary parameters. A solution coming close to these demands is the so-called string model: each cut line is identified with a classical relativistic string, a Lorentz invariant string breaking procedure provides the transformation into a hadronic final state, see fig. 7.4.

The phenomenological microscopic picture which stays behind this procedure was discussed in a number of reviews [21, 20, 31]: the string end-point partons resulted from the interaction appear to be connected by a color field. With the partons flying apart, this color field is stretched into a tube, which finally breaks up giving rise to the production of hadrons and to the neutralization of the color field.

We now consider a semi-hard Pomeron of the "sea-sea" type, where we have a hard pQCD

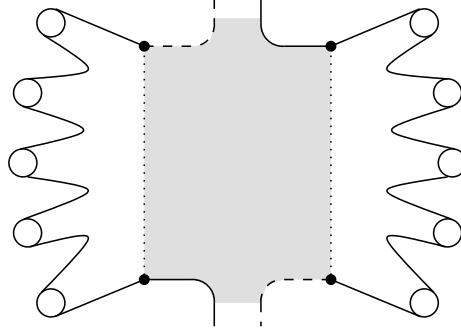


Figure 7.4: The string model: each cut line (dotted vertical lines) represents a string, which decays into final state hadrons (circles).

process in the middle and a soft evolution at the end, see fig. 7.5. We generalize the picture

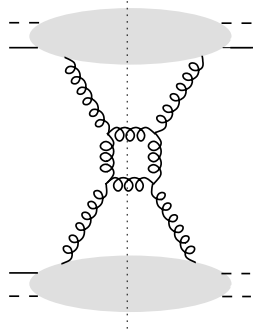


Figure 7.5: A simple diagram contributing to the semi-hard Pomeron of the “sea-sea” type.

introduced above for the soft Pomeron. Again, we assume a cylindrical structure. For the example of fig. 7.5, we have the picture shown in fig. 7.6: the shaded areas on the cylinder ends represent

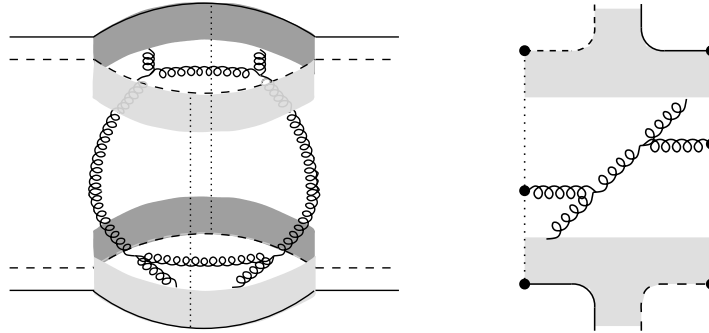


Figure 7.6: Cylindrical representation of a contribution to the semi-hard Pomeron (left figure) and planar diagram representing the corresponding half-cylinder (right figure).

the soft Pomerons, whereas in the middle part we draw explicitly the gluon lines on the cylinder surface. We apply the same procedure as for the soft Pomeron: we cut the diagram and present a half-cylinder in a planar fashion, see fig. 7.6. We observe one difference compared to the soft case: there are three partons (dots) on each cut line: apart from the quark and the anti-quark at the end, we have a gluon in the middle. We again apply the string picture, but here we identify

a cut line with a so-called kinky string, where the internal gluons correspond to internal kinks. The underlying microscopic picture will be presented by three color-connected partons - the gluon connected by the color field to the quark and to the anti-quark. The string model provides then a “parameterization” of hadron production, see fig. 7.7. The procedure described above can be

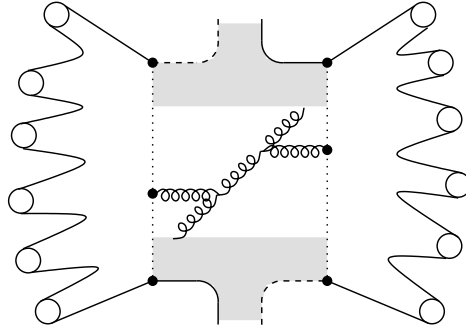


Figure 7.7: The “kinky” string model: the cut line (vertical dotted line) corresponds to a kinky string, which decays into hadrons (circles).

easily generalized to the case of complicated parton ladders involving many gluons and quark-anti-quark pairs. One should note that the treatment of semi-hard Pomeron is just a straightforward generalization of the string model for soft Pomeron, or one might see it the other way round: the soft string model is a natural limiting case of the kinky string procedure for semi-hard Pomeron.

We now need to discuss Pomeron of valence type. In case of “valence-valence” the first partons of the parton ladder are valence quarks, there is no soft Pomeron between the parton ladder and

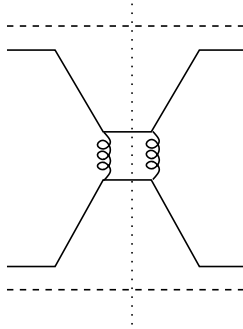


Figure 7.8: The simplest contribution to the “valence-valence” Pomeron.

the nucleon. The nucleon components representing the external legs are, as usual, quark-anti-quark pairs, but the anti-quark plays in fact just the role of a spectator. The simplest possible interaction is the exchange of two gluons, as shown in fig.7.8. We follow the scheme used for soft Pomeron and “sea-sea” type semi-hard Pomeron: we draw the diagram on a cylinder, see fig. 7.9. There is no soft region, the gluons couple directly to the external partons. We cut the cylinder, one gluon being to the right and one gluon to the left of the cut, and then we consider the corresponding half-cylinder presented in a planar fashion, see fig. 7.9 (right). Here, we have only internal gluons, on the cut line we observe just the external partons, the corresponding string is therefore just an ordinary quark-anti-quark string without internal kinks, as in the case of the soft Pomeron. We apply the usual string breaking procedure to obtain hadrons, see fig. 7.10.

Let us consider a more complicated valence-type diagram, as shown in fig. 7.11. It is again a contribution to the Pomeron of the “valence-valence” type: the external partons of the parton ladders are the valence quarks of the nucleons. In contrast to the previous example, we have here an

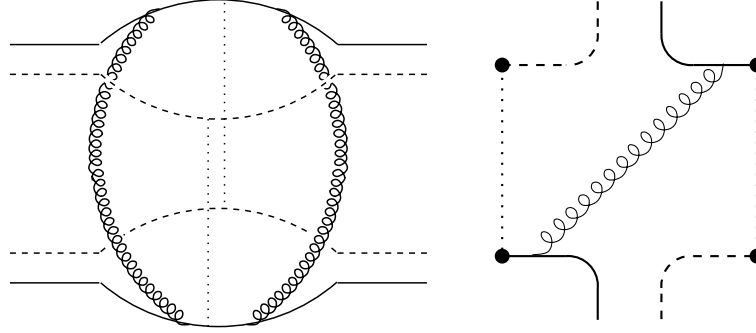


Figure 7.9: Cylindrical representation of the diagram of fig. 7.8 (left figure) and planar diagram representing the corresponding half-cylinder (right figure).

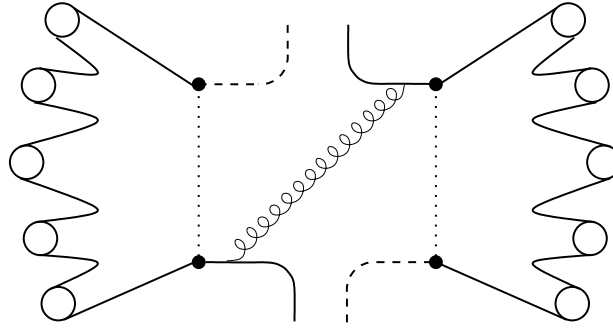


Figure 7.10: The string model: the cut line (vertical dotted line) corresponds to a string, which decays into hadrons (circles).

emission of s-channel gluons, traversing the cut. As usual, we present the diagram on the cylinder, as shown in fig. 7.12, where we also show the corresponding planar half-cylinder. In addition to internal gluons, we now observe also external ones, presented as dots on the cut line. As usual, we identify the cut line with a relativistic kinky string, where each external (s-channel) gluon represents a kink. We then employ the usual string procedure to produce hadrons, as sketched in fig. 7.13.

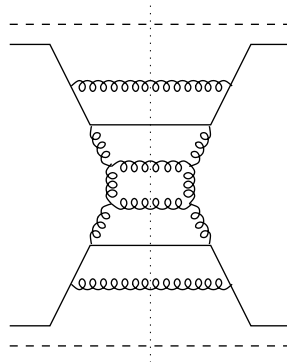


Figure 7.11: A more complicated contribution to the valence type Pomeron.

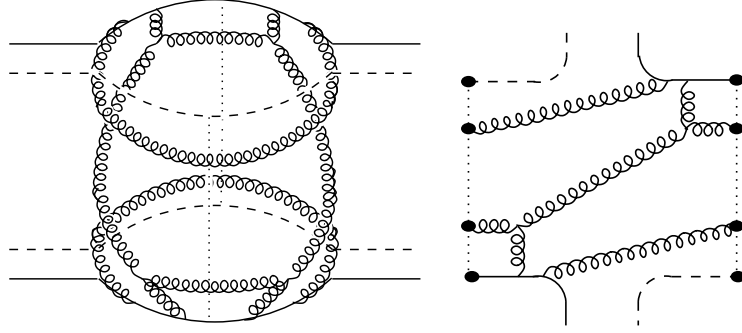


Figure 7.12: Cylindrical representation of the diagram of fig. 7.11 (left figure) and planar diagram representing the corresponding half-cylinder (right figure).

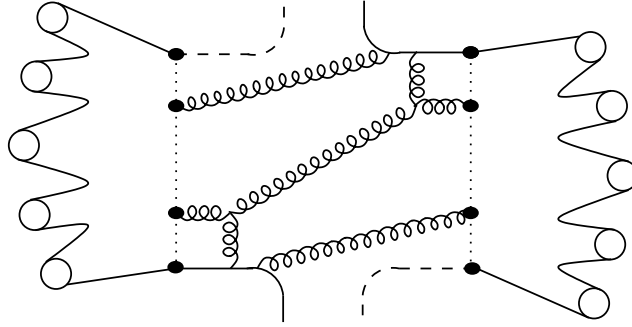


Figure 7.13: The string model: the cut line (vertical dotted line) corresponds to a string, which decays into hadrons (circles).

The general procedure should be clear from the above examples: in any case, no matter what type of Pomeron, we have the following procedure:

1. drawing of a cylinder diagram;
2. cutting the cylinder;
3. planar presentation of the half-cylinder;
4. identification of a cut line with a kinky string;
5. kinky string hadronization

The last point, the string hadronization procedure, will be discussed in detail in the following. This work is basically inspired by [32, 33] and further developed in [34]. The main differences to [33] are that hadrons are directly obtained from strings instead from low mass clusters, and an intrinsic transverse momentum is added to a string break-up. The main difference to the Lund-model is to use the area-law instead of a fragmentation function.

7.2 Lagrange Formalism for Strings

A string can be considered as a point particle with one additional space-like dimension. The trajectory in Minkowski space depends on two parameters:

$$x^\mu = x^\mu(\sigma, \tau), \quad \sigma = 0 \dots \pi, \quad (7.1)$$

with σ being a space-like and τ a time-like parameter. In order to obtain the equation of motion, we need a Lagrangian. It is obtained by demanding the invariance of the trajectory with respect to gauge transformations of the parameters σ and τ . This way we find [1] the Lagrangian of Nambu-Goto:

$$\mathcal{L} = -\kappa \sqrt{(x' \dot{x})^2 - x'^2 \dot{x}^2}, \quad (7.2)$$

with $\dot{x}^\mu = dx^\mu/d\tau$, $x'^\mu = dx^\mu/d\sigma$ and κ being the energy density or string tension. With this Lagrangian we write down the action

$$S = \int_0^\pi d\sigma \int_{\tau_0}^{\tau_1} d\tau \mathcal{L}, \quad (7.3)$$

which leads to the Euler-Lagrange equation:

$$\frac{\partial}{\partial \tau} \frac{\partial \mathcal{L}}{\partial \dot{x}_\mu} + \frac{\partial}{\partial \sigma} \frac{\partial \mathcal{L}}{\partial x'_\mu} = 0, \quad (7.4)$$

with the initial conditions

$$\frac{\partial \mathcal{L}}{\partial x'_\mu} = 0, \quad \sigma = 0, \pi, \quad (7.5)$$

since we have $\delta x = 0$ for $\tau = \tau_0$ and $\tau = \tau_1$. This equation can be solved most easily by a partial gauge fixing. We have this freedom, since the result is independent on the choice of the parameters. This is done indirectly by imposing the following conditions:

$$\dot{x}^2 + x'^2 = 0, \quad \dot{x}x' = 0. \quad (7.6)$$

The Euler-Lagrange equation gives us a simple solution, the wave equation:

$$\frac{\partial^2 x_\mu}{\partial \tau^2} - \frac{\partial^2 x_\mu}{\partial \sigma^2} = 0, \quad (7.7)$$

with the following boundary conditions:

$$\frac{\partial x_\mu}{\partial \sigma} = 0, \quad \sigma = 0, \pi. \quad (7.8)$$

The total momentum of a string is given by [1]

$$p_{\text{string}}^\mu = - \int_C \frac{\partial \mathcal{L}}{\partial \dot{x}_\mu} d\sigma + \frac{\partial \mathcal{L}}{\partial x'_\mu} d\tau \quad (7.9)$$

with C being a curve between the two ends of the string ($\sigma = 0$ and $\sigma = \pi$). This gives for (7.6) and for $d\tau = 0$

$$p_{\text{string}}^\mu = \int_0^\pi \kappa \dot{x}^\mu d\sigma. \quad (7.10)$$

We still have to fix completely the gauge since it has been fixed partially only. This can be done with the following conditions for the parameter τ :

$$n^\mu x_\mu = \lambda \tau \quad (7.11)$$

Different choices for n and λ are possible, like $n = (1, -1, 0, 0)$ which is called the transverse gauge. We will use $n = (1, 0, 0, 0)$ which leads to $\lambda = E/\pi\kappa$ and another choice $\pi = E/\kappa$ will identify τ with the time x_0 , whereas $E = \int_0^\pi \kappa \dot{x}_0 d\sigma$ is the total energy of the string. We define “string units” via $\kappa = 1$; σ and τ have thereby the dimension of energy and $\pi = E$. In “ordinary” units, one has $\kappa = \tilde{\kappa}$ GeV/fm, with $\tilde{\kappa}$ being approximately 1, so a length of 1 GeV corresponds to $1 \text{ fm}/\tilde{\kappa} \approx 1 \text{ fm}$.

The solution of a wave equation is a function which depends on the sum or the difference of the two parameters σ and τ . As the second derivative shows up, we have two degrees of freedom to impose the initial conditions on the space-like extension and the speed of the string at $\tau = 0$. One can easily verify that the following Ansatz [32, 33] fulfills the wave equation (7.7):

$$x^\mu(\sigma, \tau) = \frac{1}{2} \left[f^\mu(\sigma + \tau) + f^\mu(\sigma - \tau) + \int_{\sigma - \tau}^{\sigma + \tau} g^\mu(\xi) d\xi \right] \quad (7.12)$$

$$f(\sigma) = x^\mu(\sigma, \tau)|_{\tau=0} \quad (7.13)$$

$$g(\sigma) = \dot{x}^\mu(\sigma, \tau)|_{\tau=0} \quad (7.14)$$

We identify the function $f(\sigma)$ with the initial spatial extension and $g(\sigma)$ with the initial speed of the string at the time $\tau = 0$.

We will consider here a special class of strings, namely those with $f = 0$ (initially point-like) and with a piecewise constant function g ,

$$g(\sigma) = v_k \quad \text{for } E_{k-1} \leq \sigma \leq E_k, \quad 1 \leq k \leq n \quad (7.15)$$

with some integer n . The set $\{E_k\}$ is a partition of the σ -range $[0, E]$,

$$0 = E_0 < E_1 < \dots < E_{n-1} < E_n = E, \quad (7.16)$$

and $\{v_k\}$ represents n constant 4-vectors. Such strings are called kinky strings, with n being the number of kinks, and the n vectors v_k being called kink velocities.

In order to use eq. (7.12), we have to extend the function g beyond the physical range between 0 and π . This can be done by using the boundary conditions, which gives

$$g(\tau) = g(-\tau), \quad (7.17)$$

$$g(\tau + 2\pi) = g(\tau), \quad (7.18)$$

So g is a symmetric periodic function, with the period 2π . This defines g everywhere, and the eq. (7.12) is the complete solution of the string equation, expressed in terms of the initial condition g (f is taken to be zero). In case of kinky strings the latter is expressed in terms of the kink velocities $\{v_k\}$ and the energy partition $\{E_k\}$.

7.3 Identifying Partons and Kinks

We discussed earlier that a cut Pomeron may be identified with two sequences of partons of the type

$$q - g - g - \dots - g - \bar{q}, \quad (7.19)$$

representing all the partons on a cut line. We identify such a sequence with a kinky string, by requiring

$$\text{parton} = \text{kink}, \quad (7.20)$$

which means that we identify the partons of the above sequence with the kinks of a kinky string, such that the partition of the energy is given by the parton energies,

$$E_k = \text{energy of parton } k \quad (7.21)$$

and the kink velocities are just the parton velocities,

$$v_k = \frac{\text{momentum of parton } k}{E_k}. \quad (7.22)$$

We consider massless partons, so that the energy is equal to the absolute value of the parton momentum. Fig. 7.14 shows as an example the evolution of a kinky string representing three

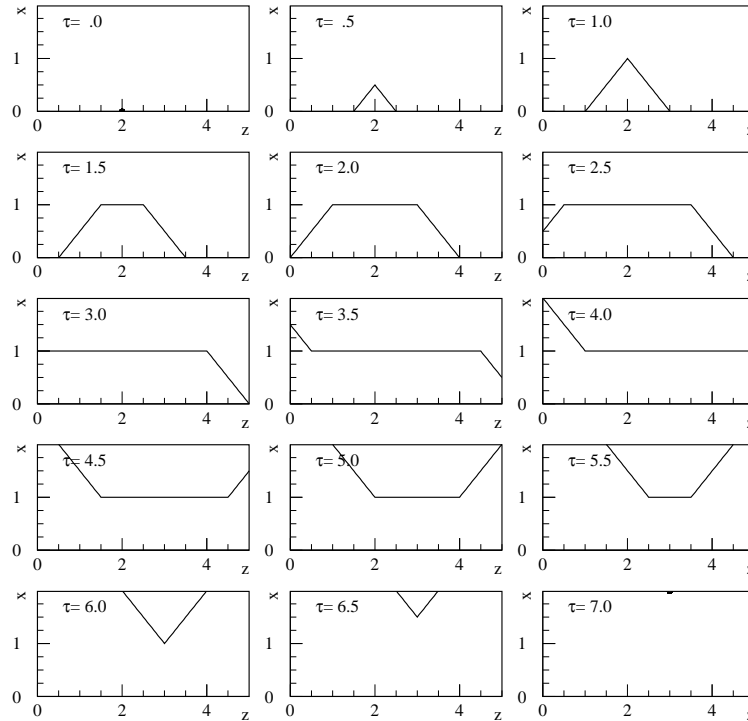


Figure 7.14: Movement of a string with 3 partons on the $z - x$ plane: The partons have momenta of $p_q = (p_x, p_y, p_z) = (0, 0, -2)$ GeV/c, $p_g = (2, 0, 0)$ GeV/c and $p_{\bar{q}} = (0, 0, 3)$ GeV/c. The first half-cycle is finished after $\tau = 7$ GeV.

partons: a quark, an anti-quark, and a gluon, as a function of the time τ . One sees that the partons start to move along their original direction with the speed of light. After some time which corresponds to their energy they take the direction of the gluon. One could say that they lose energy to the string itself. The gluon loses energy in two directions, to the quark and to the anti-quark and therefore in half the time. The ends of the string move continuously with the speed of each of the partons until the whole string is contracted again in one point. The cycle starts over.

Another example is shown on fig. 7.15, where realistic partons coming from a simulation of a e^+e^- annihilation process at 14 GeV c.m.s. energy are considered. We will see later how to generate these partons. We observe 6 partons, 2 quarks and 4 gluons, symbolically displayed in the first sub-figure. As the total energy is 14 GeV the cycle has a periodicity of 28 GeV. But one sees that the perturbative gluons play an important role in the beginning of the movement, and later from 2 GeV on, the longitudinal character dominates. As we will see later, a string breaks typically after $1 \text{ GeV}/\kappa$ which gives much importance to the perturbative gluons.

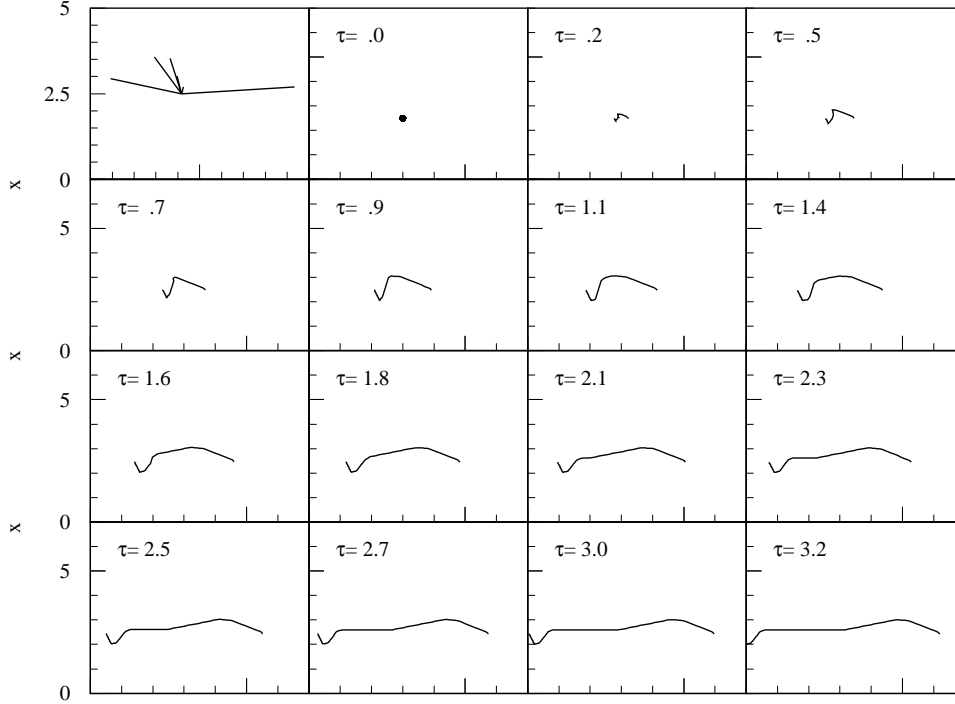


Figure 7.15: Partons in an e^+e^- annihilation event with $\sqrt{s} = 14$ GeV in the $z-x$ plane. The first figure shows the momenta in the $p_z - p_x$ plane.

7.4 Momentum Bands in Parameter Space

As we will see later, it is not necessary for a fragmentation model to know the spatial extension at each instant. Therefore, we concentrate on a description in momentum space which simplifies the model even more. By using formula (7.12) we can express the derivatives of $x(\sigma, \tau)$ in terms of the initial conditions $g(\sigma)$ as

$$\dot{x}(\sigma, \tau) = \frac{1}{2} [g(\sigma + \tau) + g(\sigma - \tau)] \quad (7.23)$$

$$x'(\sigma, \tau) = \frac{1}{2} [g(\sigma + \tau) - g(\sigma - \tau)] . \quad (7.24)$$

Since the function g is stepwise constant, we easily identify regions in the parameter space (σ, τ) , where $g(\sigma + \tau)$ is constant or where $g(\sigma - \tau)$ is constant, as shown in fig. 7.16, 7.17.

These regions are called momentum bands, more precisely R-bands and L-bands, being of great importance for the string breaking. If we overlay the two figures of 7.16, 7.17, we get fig. 7.18, which allows us to identify regions, where $g(\sigma + \tau)$ and $g(\sigma - \tau)$ are constant at the same time, namely the intersections of R-bands and L-bands. In these areas \dot{x} and x' are constant, given as

$$\dot{x}(\sigma, \tau) = \frac{1}{2} [v^- + v^+] \quad (7.25)$$

$$x'(\sigma, \tau) = \frac{1}{2} [v^- - v^+] , \quad (7.26)$$

with v^+ and v^- being the velocities of the partons corresponding to the two intersecting bands.

Rather than considering a σ -range between $-\infty$ and $+\infty$, one may simply consider the physical range from 0 to π , and construct the bands via reflection. As an example, let us follow the L-band

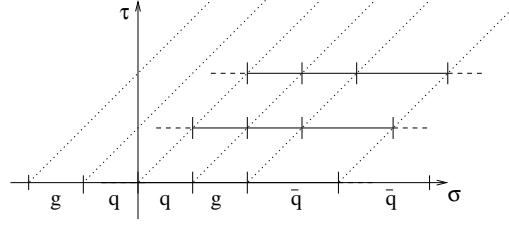


Figure 7.16: Construction of bands where $g(\sigma - \tau)$ is constant, being referred to as R-bands (“right moving bands”).

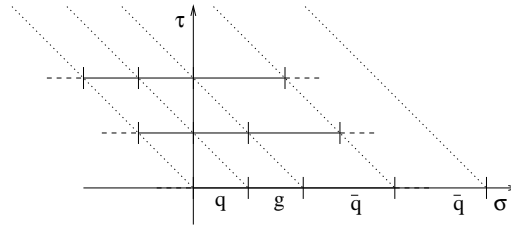


Figure 7.17: Construction of bands where $g(\sigma + \tau)$ is constant, being referred to as L-bands (“left moving bands”).

corresponding to the parton i , starting at $\tau = 0$. With increasing τ one reaches at some stage the border $\sigma = 0$. Here, we have an intersection with the R-band, corresponding to the same parton i , coming from the unphysical region $\sigma < 0$. We now follow this R-band, which corresponds to a reflection of the above-mentioned L-band, till we hit the border $\sigma = \pi$,

In the regions where $g(\sigma + \tau)$ and $g(\sigma - \tau)$ have the same value, corresponding to collinear partons or to an overlap of the momentum bands of one and the same parton, one finds $x' = 0$, i.e. there is no spatial extension in the dependence of the parameter σ . Therefore the coordinates x^μ stay unchanged and we recover the speed of the original partons. In particular, this is the case for the whole string at $\tau = 0$, due to $f = 0$. With the string evolving in time, more and more bands of non collinear partons overlap, which gives $x' \neq 0$; the string is extending as we have seen in fig. 7.14 until $\tau = 7$.

7.5 Area Law

In order to consider string breaking, we are going to extend the model in a covariant fashion. We use the method proposed by Artru and Menessier [35], which is based on a simple extension of the decay law of unstable particles, where the probability dP to decay within a time interval dt is given as

$$dP = \lambda dt, \quad (7.27)$$

with some decay constant λ . For strings, we use the same formula by replacing the proper time by proper surface in Minkowski space,

$$dP = \lambda dA. \quad (7.28)$$

By construction, this method is covariant. Since we work in parameter space it is useful to express this dependence as a function of σ and τ ,

$$dA = \sqrt{(\dot{x}x')^2 - x'^2 \dot{x}^2} d\sigma d\tau. \quad (7.29)$$

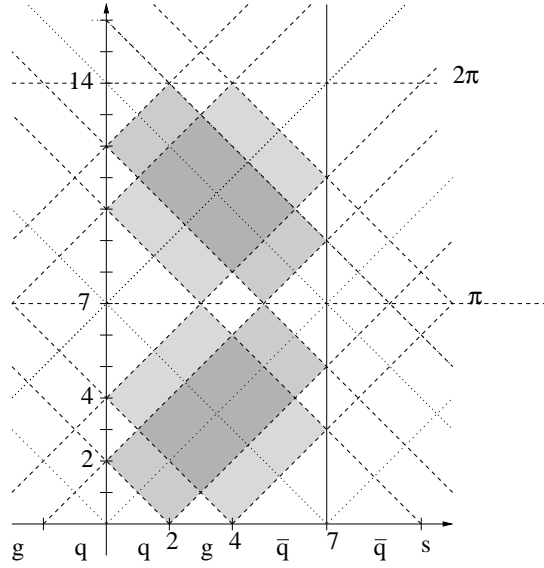


Figure 7.18: The superposition of bands where $g(\sigma + \tau)$ and $g(\sigma - \tau)$ are constant (see fig. 7.16, 7.17) gives regions of constant x' and \dot{x} .

By using the expressions for \dot{x} and x' and $\dot{x}x' = 0$ and $g^2 = 0$, we find

$$dA = \sqrt{-\frac{1}{4}(-2g(\sigma + \tau)g(\sigma - \tau))\frac{1}{4}(2g(\sigma + \tau)g(\sigma - \tau))}d\sigma d\tau \quad (7.30)$$

$$= \left[\frac{1}{2}g(\sigma + \tau)g(\sigma - \tau) \right] d\sigma d\tau \quad (7.31)$$

$$= \frac{1}{2}(1 - \cos \phi) d\sigma d\tau, \quad (7.32)$$

with ϕ being the angle between the partons. Consequently, a string cannot break at a point where the momentum bands of the same parton overlap, because in this case the angle ϕ is zero, which leads to $dA = 0$. The maximal contribution is obtained for partons moving in opposite directions.

We still have to define how a string breaks and how the sub-strings evolve. At each instant, one knows exactly the momenta of the string by eq. (7.25) and (7.26). The configuration of $g(\sigma + \tau)$ and $g(\sigma - \tau)$ at the time τ_1 of the break point is used as initial condition for the two substrings. The function $g(\sigma + \tau)$ is cut into two pieces between 0 and σ_1 and between σ_1 and π . The two resulting functions are continued beyond their physical ranges $[0, \sigma_1]$ and $[\sigma_1, \pi]$ by taking them to be symmetric and periodic with periods $2\sigma_1$ and $2(\pi - \sigma_1)$. Fig. 7.19 shows this for a breaking at (σ_1, τ_1) and a second break point at (σ_2, τ_2) . In principle, the cycle starts over with the two sub-strings breaking each until the resulting pieces are light enough to form hadrons. However, it is easier to look for many break-points at once. If they are space-like separated, they do not interfere with each other. For the coordinates in the parameter space this translates into the condition

$$|\sigma_1 - \sigma_2| > |\tau_1 - \tau_2|. \quad (7.33)$$

7.6 Generating Break Points

Having assumed that string breaking occurs according to the area law,

$$dP = \lambda dA, \quad (7.34)$$

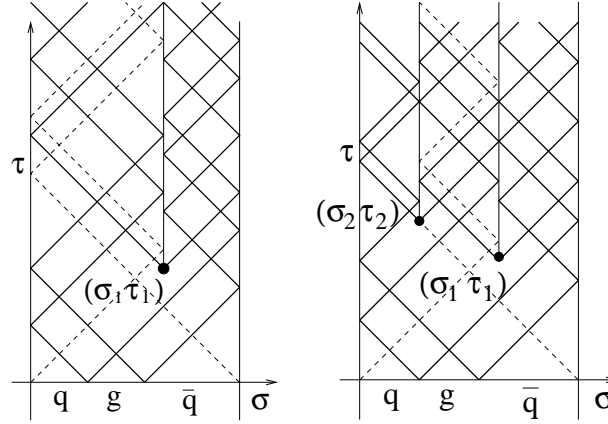


Figure 7.19: The breaking of a string. The functions g are found by imposing the symmetry and periodicity conditions.

we now need an algorithm to accomplish this in the framework of the Monte-Carlo method. The most simple way is to sub-divide a given surface into sufficiently small pieces and then to decide according to formula (7.34) if there is a break point or not. This is what we refer to as the naive method, which is of course not efficient. We will therefore construct another algorithm (the direct one) which is based on

$$P_0(A) = e^{-\lambda A} \quad (7.35)$$

being the probability of having no break point within the area A . One generates surfaces A_1, A_2, \dots according to $P_0(A)$ as

$$A_i = -\log(r_i)/\lambda, \quad (7.36)$$

with random numbers r_i between 0 and 1. The formula does not say anything about the form of the surfaces A_i . Actually, several choices are possible as long as they do not violate causality. In the case of a simple string without any gluons, it is easiest to place the surfaces A_i from left to right such that the break points P_i are the left upper corners of A_{i+1} , as shown in fig. 7.20: one first takes A_1 , which defines the line L_1 . The first break point P_1 is generated randomly on this line. The next surface A_2 has to be placed in a way that does not violate causality. The first break point is therefore used as a constraint for the next one, etc. Finally, if the last surface obtained is too large to be placed on the rest of the string, the procedure is finished. The advantage of this method is that no break-points are rejected because the causality principle is obeyed constantly throughout the whole procedure.

We generalize the method to work for any number of perturbative gluons in the following way. Since the elementary invariant area dA is proportional to the scalar product of the momenta of two partons, we can easily calculate the area A_{ij} corresponding to a sub-region S_{ij} of the (σ, τ) -space, representing the intersection of the momentum bands of the partons i and j . We find

$$A_{ij} = \int_{S_{ij}} \left(\frac{1}{2} g(\sigma + \tau) g(\sigma - \tau) \right) d\sigma d\tau = \frac{1}{4} p_i \cdot p_j, \quad (7.37)$$

with p_i and p_j being the 4-momenta of the two partons. We now construct the break points in the parameter space rather than in Minkowski space. One first defines the area in the parameter space of allowed breakpoints as

$$S_{\text{break}} = \bigcup S_{ij}, \quad (7.38)$$

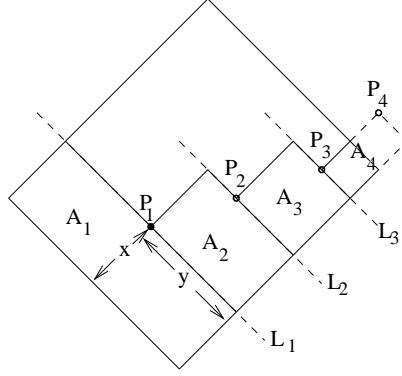


Figure 7.20: The direct method of searching break points (see text).

with the indices running as indicated in fig. 7.21. To obtain a unique way of counting the regions, we mark bands which come from a left-moving band at $\tau = 0$ with a '. We further observe that the outer bands 1 and 1' as well as 5 and 5', which come from the (anti-)quark-momenta, are neighboring. It is therefore useful to redefine them as one band 1 and 5' (with double momentum), see fig. 7.21. For each of these sub-areas S_{ij} the corresponding area in Minkowski space A_{ij} is

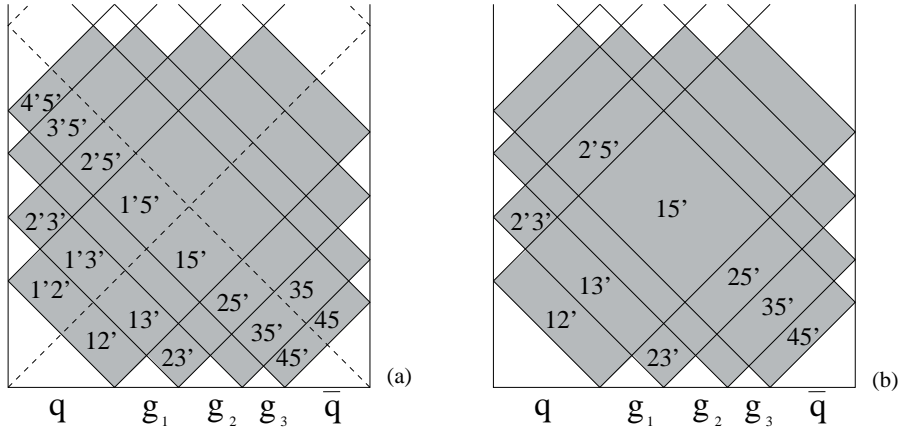


Figure 7.21: The area S_{break} in parameter (σ, τ) space, before and after the redefinition of the outer bands.

known ($= p_i p_j / 4$). One then generates areas A_1, A_2, A_3, \dots (in Minkowski space) according to eq. (7.36), and places the corresponding areas S_1, S_2, S_3, \dots (in parameter space) into S_{break} from left to right such that the break points P_i are the left upper corners of S_{i+1} .

Let us consider an example of five partons (1,2,3,4,5), see fig. 7.22. Suppose that we have sampled a surface A_1 . If it is smaller than the first region $A_{12'}$, we determine $S_1 = S_{12'} \cdot A_1 / A_{12'}$ and we place S_1 into the left side of $S_{12'}$ and generate the break point P_1 randomly on the right upper border of $S_{12'}$, see fig. 7.22. If A_1 is greater than $A_{12'}$, we subtract $A_{12'}$ from A_1 :

$$A'_1 = A_1 - A_{12'}. \quad (7.39)$$

In the case of the sum of the three areas $A_s = A_{2'3'} + A_{13'} + A_{23'}$ being greater than A'_1 , the first coordinate x of the break point P_1 (see fig. 7.23) is determined by

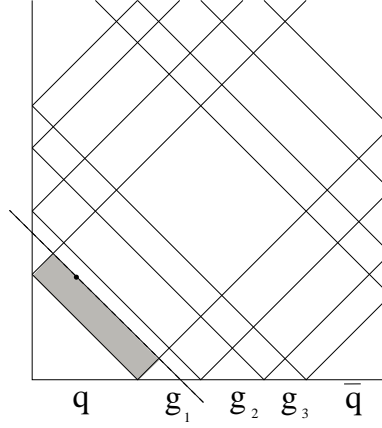


Figure 7.22: Placing S_1 into $S_{12'}$ in case of $A_1 < A_{12'}$.

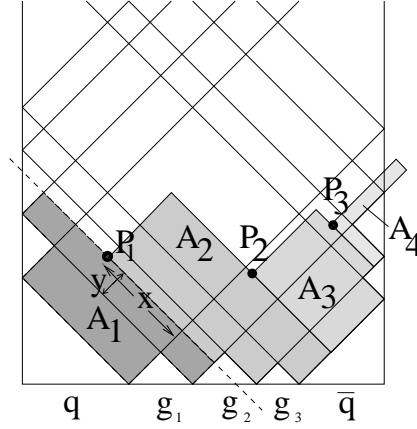


Figure 7.23: The determination of the break point for the case of a string with kinks. The regions are weighted according to the scalar product of their momenta.

$$x = \frac{A'_1}{A_s}. \quad (7.40)$$

Otherwise we continue the procedure correspondingly. The y coordinate is determined as

$$y = \begin{cases} r \frac{A_s}{A_{2'3'}} & \text{if } 0 < r < \frac{A_{2'3'}}{A_s} & (\text{region } S_{2'3'}) \\ \left(r - \frac{A_{2'3'}}{A_s}\right) \left(\frac{A_s}{A_{13'}}\right) & \text{if } \frac{A_{2'3'}}{A_s} < r < \frac{A_{2'3'} + A_{13'}}{A_s} & (\text{region } S_{13'}) \\ \left(r - \frac{A_{2'3'} + A_{13'}}{A_s}\right) \left(\frac{A_s}{A_{23'}}\right) & \text{if } \frac{A_{2'3'} + A_{13'}}{A_s} < r < 1 & (\text{region } S_{23'}) \end{cases}, \quad (7.41)$$

with r being a random number between 0 and 1. This means that after having determined in which of the regions we find the break point, it is placed randomly on the world-line which points to the future. After having obtained the break point P_1 we continue the procedure in the same way by obeying to the principle of causality. The area to sweep over is then limited by the first break point as shown on fig. 7.23.

In fig. 7.24, we apply our hadronization procedure, referred to as *direct method*, as discussed above, to calculate the distributions of xy , x , $\eta = \frac{1}{2} \log \left(\frac{x}{y} \right)$, and the multiplicity n of break points

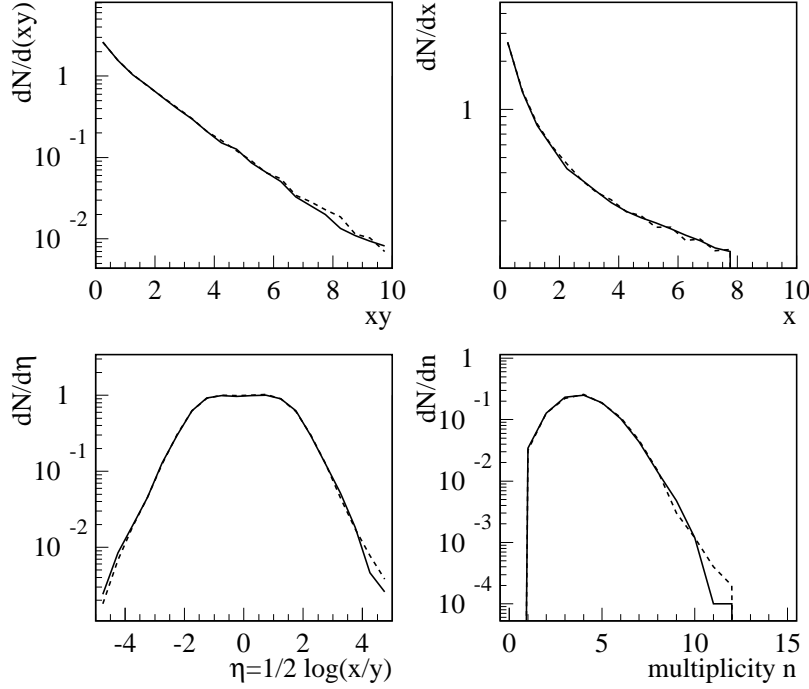


Figure 7.24: Distributions in (xy) , x , $\frac{1}{2} \log \left(\frac{x}{y} \right)$, and the multiplicity n of break points. The full line represents the naive method, the dashed one the direct one. The coordinates of the break points are as defined on fig. 7.20.

for a quark-anti-quark string of $E_q = E_{\bar{q}} = 8\text{GeV}$. We compare our results with the *the naive method*, where the area of the string is divided into small elements $\Delta A = 8 \cdot 8 \text{ GeV}^2/N^2$, with N sufficiently large to not change the results any more. In each of these elements, a break point is found with the probability $\lambda \Delta A$. The points which are in the future of another one are rejected. The latter method is a literal realization of the area-law. As one can easily see in fig. 7.24, the two methods agree within statistical errors.

7.7 From String Fragments to Hadrons

So far, we discussed how to break a string into small pieces, i.e. string fragments with invariant masses between 0 and about two GeV. In order to identify string fragments and hadrons, we first have to define the flavors (= quark content) of the fragments, and then we have to discuss the question of fragment masses.

Flavors of String Fragments

A string as a whole has some flavor, carried by the partons at its two extremities. Additional flavor is created (by definition) at each break point in the form of a quark-anti-quark or a diquark-anti-diquark pair of a certain flavor. The corresponding probabilities are free parameters of the model. In case of quark-anti-quark formation, we introduce the parameter p_{ud} , which gives the probability of flavor u or d . The probability to get an s -quark is therefore $1 - 2p_{ud}$ which is smaller than p_{ud} because of the larger mass of the s quark. For diquark-anti-diquark production, we introduce the corresponding probability p_{diquark} .

Masses of String Fragments

In the following, we show how to determine the masses of string fragments, characterized by break points in the parameter space.

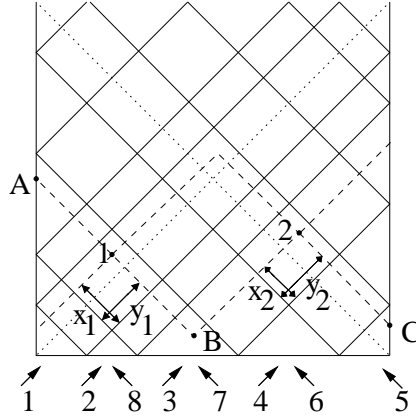


Figure 7.25: How to calculate the mass of a sub-string.

Fig. 7.25 shows an example of two break points for a string with 3 inner kinks. The momentum bands and the regions of their overlaps are shown: in case of the inner bands, we have three R-bands (2,3,4) and three L-bands (6,7,8). The bands at the extremities play a special role, since we may have the corresponding R- and L-band as just one band, due to the fact that one of the bands is reflected immediately. So, we consider two “double bands” (1 and 5).

The string momentum is given as

$$p_{\text{string}} = \int_C [\dot{x}d\sigma + x'd\tau], \quad (7.42)$$

where C is an arbitrary curve from one border ($\sigma = 0$) to the other ($\sigma = \pi$) in the parameter space. This leads to

$$p_{\text{string}} = \frac{1}{2} \int_C (g(\sigma + \tau) + g(\sigma - \tau)) d\sigma + \frac{1}{2} \int_C (g(\sigma + \tau) - g(\sigma - \tau)) d\tau \quad (7.43)$$

The momenta of the bands are by definition

$$p_{(i)} = \begin{cases} \frac{1}{2} \int_{\text{band } i} g(\sigma - \tau) d\sigma - \frac{1}{2} \int_{\text{band } i} g(\sigma - \tau) d\tau & \text{if R-band} \\ \frac{1}{2} \int_{\text{band } i} g(\sigma + \tau) d\sigma + \frac{1}{2} \int_{\text{band } i} g(\sigma + \tau) d\tau & \text{if L-band} \end{cases}, \quad (7.44)$$

where one integrates along an arbitrary curve from one border of the band to the other. An important property: an integration path parallel to a band provides zero contribution. One has to pay attention for the bands at the extremities: integrating only along $\tau = 0$ represents only half the band. We have

$$\sum_i p_{(i)} = p_{\text{string}}. \quad (7.45)$$

The momenta of the bands are related to the corresponding parton momenta as

$$p_{(i)} = \begin{cases} \frac{1}{2} p_{\text{parton}} & \text{if inner band} \\ p_{\text{parton}} & \text{if outer band} \end{cases}, \quad (7.46)$$

which one verifies easily by expressing g in terms of the parton momenta. The difference between inner and outer bands is due to the fact that the outer ones (at the extremities) represent in reality two bands. For the example of fig. 7.25, we have

$$\begin{aligned}
 p_{(1)} &= p_q \\
 p_{(2)} = p_{(8)} &= \frac{1}{2}p_{g_1} \\
 p_{(3)} = p_{(7)} &= \frac{1}{2}p_{g_2} \\
 p_{(4)} = p_{(6)} &= \frac{1}{2}p_{g_3} \\
 p_{(5)} &= p_{\bar{q}}
 \end{aligned} \tag{7.47}$$

Summing over the bands, we get

$$\sum_{i=1}^8 p_{(i)} = p_q + p_{g_1} + p_{g_2} + p_{g_3} + p_{\bar{q}} = p_{\text{string}}, \tag{7.48}$$

which is the total momentum of the string.

For a fragment of the string, the momentum is given as

$$p_{\text{fragm}} = \frac{1}{2} \int_{C'} (g(\sigma + \tau) + g(\sigma - \tau)) d\sigma + \frac{1}{2} \int_{C'} (g(\sigma + \tau) - g(\sigma - \tau)) d\tau, \tag{7.49}$$

where the path of the integration C' is an arbitrary curve between two breakpoints, or between one break point and a boundary. One may write

$$p_{\text{fragm}} = p_R + p_L, \tag{7.50}$$

with

$$p_R = \frac{1}{2} \int_{C'} g(\sigma - \tau) d\sigma - \frac{1}{2} \int_{C'} g(\sigma - \tau) d\tau, \tag{7.51}$$

$$p_L = \frac{1}{2} \int_{C'} g(\sigma + \tau) d\sigma + \frac{1}{2} \int_{C'} g(\sigma + \tau) d\tau, \tag{7.52}$$

where p_R and p_L represent sums of momenta of R-bands and L-bands. For the example of fig. 7.25, we can choose the path $(1 \rightarrow B)$, $(B \rightarrow 2)$ for the string fragment between the break points 1 and 2. Since the first path is parallel to all L-bands (only R-bands contribute) and the second one is parallel to all R-bands (only L-bands contribute), we find

$$p_{\text{fragm } 1-2} = p_{1 \rightarrow B} + p_{B \rightarrow 2} \tag{7.53}$$

with

$$p_{1 \rightarrow B} = x_1 p_{(1)} + p_{(2)} + (1 - x_1) p_{(3)}, \tag{7.54}$$

$$p_{B \rightarrow 2} = (1 - y_1) p_{(7)}^\mu + p_{(6)}^\mu + y_2 p_{(5)}^\mu, \tag{7.55}$$

where the factors x_1 , $(1 - x_1)$, y_1 , $(1 - y_1)$ represent the fact that the bands at the extremities are only partially integrated over. The other string fragments are treated correspondingly. For the left string fragment, we may chose the integration path $(A \rightarrow 1)$, for the right one $(2 \rightarrow C)$. So we find for the three string fragments (referred to as a , b , c) of fig. 7.25 the momenta

$$p_a = y_1 p_{(7)} + p_{(8)} + (1 - x_1) p_{(1)} \tag{7.56}$$

$$p_b = x_1 p_{(1)} + p_{(2)} + (1 - x_2) p_{(3)} + y_2 p_{(5)} + p_{(6)} + (1 - y_1) p_{(7)} \tag{7.57}$$

$$p_c = x_2 p_{(3)} + p_{(4)} + (1 - y_2) p_{(5)}. \tag{7.58}$$

It is easy to verify that the sum of the three sub-strings gives the total momentum of the string,

$$p_a + p_b + p_c = \sum_{i=1}^8 p_{(i)} = P_{\text{string}}. \quad (7.59)$$

The mass squared of the string fragments is finally given as

$$m_{\text{fragm}}^2 = p_{\text{fragm}}^2, \quad (7.60)$$

for example

$$m_a^2 = 2 (p_{(1)}p_{(8)} - x_1 p_{(8)}p_{(1)} + y_1 (p_{(7)}p_{(8)} + p_{(7)}p_{(1)}) - x_1 y_1 p_{(7)}p_{(1)}) , \quad (7.61)$$

where we took advantage of the light-cone character of the momenta of the bands ($p_{(i)}^2 = 0$).

Determination of Hadrons

So far, we have determined the flavor f and the mass m of each string fragment. In order to identify string fragments with hadrons, we construct a mass table, which defines the hadron type as a function of the mass and the flavor of the fragment. For a given flavor f of the fragment, we introduce a sequence $m_1^f < m_2^f < \dots$ of masses, such that in case of a fragment mass being within an interval $[m_{i-1}^f, m_i^f]$, one assigns a certain hadron h_i . The masses m_i^f are determined by the masses of the neighboring particles. So we decide for a $u - \bar{u}$ pair to be a pion if its mass is between 0 and $(140 + 770)/2 = 455$ MeV. So the particle masses give a natural parameterization. This works, however, only up to strange flavor. For charm and bottom flavor we choose with a fraction 1 : 3 between pseudo-scalar and vector-mesons.

Mass Corrections

An unrealistic feature of our approach, so far, is the fact that stable particles are in general off-mass-shell. In order to correct for this, we employ a slight modification of the break point such that the on-shell mass is imposed.

Let us again consider the example of fig. 7.25. For a given mass, the parameters x_1 and y_1 describe hyperbolas in the regions of overlapping bands (different ones in different regions). Fig. 7.26 shows for our example some curves of constant mass for the left sub-string (between the

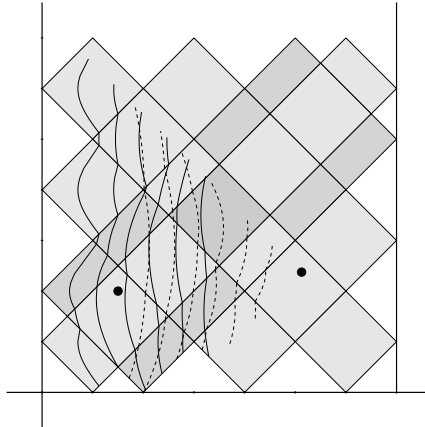


Figure 7.26: The hyperbolas of constant mass for the two sub-strings if one moves the break-point on the left side. The solutions of the mass conditions are the crossing of the hyperbolas.

left side and the first break point). In the same way we find hyperbolas of constant mass for the right sub-string (between the break points 1 and 2).

If two neighboring substrings are stable particles, one needs to impose on-shell masses to both fragments, which amounts to find the intersection of the two corresponding hyperbolas.

If one has to modify the break point according to only one mass condition, with the mass of the second sub-string being still large enough not to represent a stable hadron, a possible break point must lie on the corresponding hyperbola. To completely determine the point, we need a second condition. Apart from the squared mass, another Lorentz invariant variable available is the squared proper time of the break point, defined as

$$\Gamma^2 = (x(\sigma_{\text{break}}, \tau_{\text{break}}))^2. \quad (7.62)$$

So the second condition is the requirement that the proper time of the new break point should coincide with the proper time of the original one. To calculate the proper time, we use eq. (7.12), to obtain

$$\Gamma^2 = \left(\frac{1}{2} \int_{\sigma-\tau}^{\sigma+\tau} g(\xi) d\xi \right)^2. \quad (7.63)$$

The integration is done in the same way as for the masses, it is a summation of the momenta of the bands or of fractions of them. In the case of our example, we find in the region (1, 7)

$$\Gamma^2 = \frac{1}{4} (x_1 p_{(1)} + p_{(2)} + y_1 p_{(3)})^2 \quad (7.64)$$

$$= \frac{1}{2} (x_1 p_{(1)} p_{(2)} + y_1 p_{(2)} p_{(3)} + x_1 y_1 p_{(1)} p_{(3)}) , \quad (7.65)$$

which represents again a hyperbola in the parameter space, as shown in fig. 7.27. So finding a

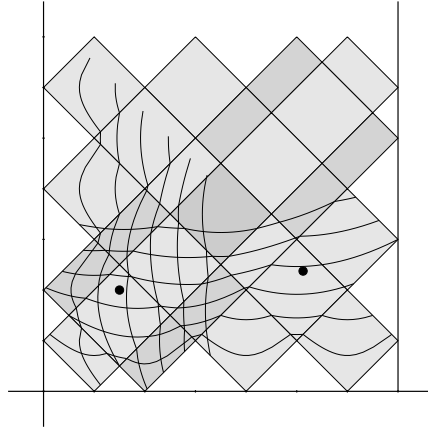


Figure 7.27: Lines of constant masses (vertical lines) and constant proper time (horizontal lines).

new break point amounts to finding the intersection of the two curves (hyperbolas) representing constant mass and proper time.

7.8 Transverse Momentum

Inspired by the uncertainty principle, a transverse momentum is generated at each breaking, which means that 4-vectors p_{\perp} and $-p_{\perp}$ are assigned to the string ends at both sides of the break

point. First we choose the absolute value $k = |\vec{p}_\perp|$ of the transverse momentum according to the distribution

$$f(k) \propto e^{-\frac{k}{2p_\perp^{\text{break}}}}, \quad (7.66)$$

with the parameter p_\perp^{break} to be fixed. We require p_\perp to be orthogonal to the momenta $p_{(i)}$ and $p_{(j)}$ of the two intersecting bands where the break point is located. So we have

$$p_\perp p_{(i)} = 0 \quad (7.67)$$

$$p_\perp p_{(j)} = 0 \quad (7.68)$$

$$p_\perp^2 = -k^2. \quad (7.69)$$

Technically this is most easily done, if we perform a Lorentz-boost into the center of mass system of the two momenta $p_{(i)}$ and $p_{(j)}$ followed by a rotation such that $p_{(i)}$ is oriented along the z-axis. One defines a vector p'_\perp , having the components

$$(p'_\perp)_o = 0 \quad (7.70)$$

$$(p'_\perp)_x = k \cos \alpha \quad (7.71)$$

$$(p'_\perp)_y = k \sin \alpha \quad (7.72)$$

$$(p'_\perp)_z = 0, \quad (7.73)$$

α being a random angle between 0 and 2π . The transformation back to the original system gives the 4-vector p_\perp .

This operation modifies, however, the mass of the string. In order to account for this, we consider the transverse momentum as an additional band of the string. It is treated in the same way as the others with the only exception that we do not look for break points in this region. For our example of fig. 7.25, we obtain for the left string fragment the momentum

$$p_a = p_\perp + y_1 p_{(7)} + p_{(8)} + (1 - x_1) p_{(1)}, \quad (7.74)$$

rather than eq. (7.56). The modification of the coefficients of the corresponding hyperbola for the mass correction procedure is obvious. In the case where we have to pass to another region to find a modified break point for the mass correction, we have to perform a rotation such that the vector p_\perp is transverse to the two momenta of the new region.

7.9 The Fragmentation Algorithm

In the following, we describe the fragmentation algorithm which is used to obtain a complete set of particles from one string.

1. For a given string, we look for break points. Let n be the number of break points.
2. For each break point, we generate a flavor and a transverse momentum.
3. We choose one break point by random and calculate the masses of the two neighboring substrings.
4. If there is at least one mass in the region of the resonances, we try to modify the break point as discussed to get exactly this mass. If this is not possible, we reject (delete) this break point and go to step 3.
5. If the mass of a sub-string is bigger than the upper limit in the mass table, we fragment this sub-string (go to step 1).

In this way, we can deal in an elegant manner with the kinematical constraints. Often, break points are rejected when a sampled transverse momentum is too high, which results in a negative mass squared for a final particle. In this case we look for another break point with another transverse momentum until a valid configuration is found.

Chapter 8

Parameters

We discuss in this chapter the parameters of the model, how they are determined, and also their values. Parameter fixing is done in a systematic way, starting with the hadronization parameters and the ones determining the time-like cascade, before considering parton-parton-scattering and hadron-hadron scattering.

8.1 Hadronization

The breaking probability p_{break} is the essential parameter in the hadronization model to determine the multiplicity and the form of the rapidity distribution. For γp , pp , pA , AA , we use a fixed value, fitted to reproduce the pion multiplicity in γp scattering. For e^+e^- annihilation, this parameter is considered to be Q dependent as

$$p_{\text{break}}(Q) = 0.14 + \frac{7.16\text{GeV}}{Q} - \frac{111.1\text{GeV}^2}{Q^2} + \frac{855\text{GeV}^3}{Q^3} \quad (8.1)$$

in the region $14 \leq Q \leq 91.2$ GeV, and to be constant outside this interval. Figure 8.1 shows

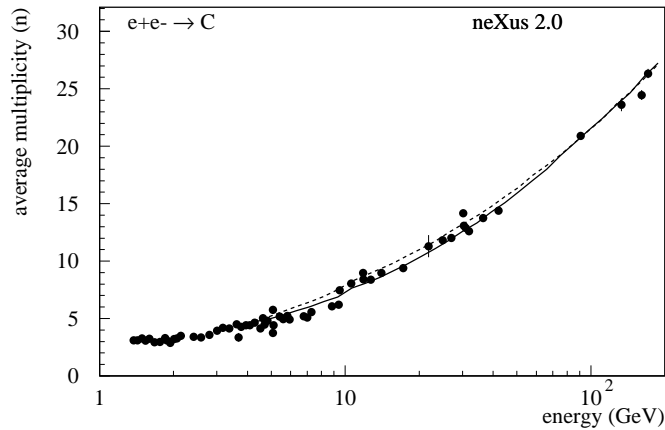


Figure 8.1: Charged particles multiplicity as a function of energy. The full line is for p_{break} parameterized, the dashed one for $p_{\text{break}} = 0.21$.

the total multiplicity of charged particles in e^+e^- annihilation as a function of energy. The solid line corresponds to the Q^2 dependent p_{break} , the dashed line is for $p_{\text{break}} = 0.21$ (the value for $Q = 91\text{GeV}$). In fig. 8.2, we show the corresponding rapidity distributions. The effect of making

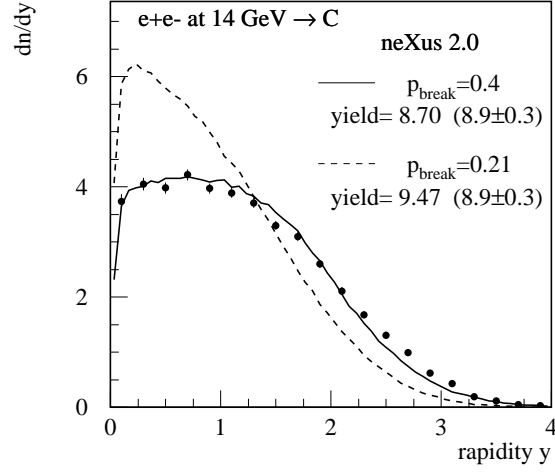


Figure 8.2: Rapidity distributions for the parameters $p_{\text{break}} = 0.4$ (full line) and $p_{\text{break}} = 0.21$ (dashed).

p_{break} Q-dependent shows up more in the shape of the rapidity distribution, not in the total multiplicity. The parameter p_{\perp}^{break} , which determines the transverse momenta of the partons at a string break, is determined by investigating transverse momentum spectra of charged particles. A value of 0.50 GeV provides the best fit to data concerning γp , pp , pA , AA , whereas for e^+e^- a value of 0.35 GeV is more favorable. The parameter p_{ud} affects strongly kaon production, we use $p_{\text{ud}} = 0.44$ adjusted to the multiplicity of kaons. Baryon production is determined by p_{diquark} , we use 0.08 adjusted to proton production in e^+e^- -annihilation. In table 8.4, we give the complete list of hadronization parameters, with their default values. So we use absolutely the same

name	value	meaning
p_{break}	eq. (8.1) for e^+e^- 0.40 for γp , pp , pA , AA	break probability
p_{\perp}^{break}	0.35 GeV for e^+e^- 0.50 GeV for γp , pp , pA , AA	mean transverse momentum at break
p_{ud}	0.44	probability of $u-\bar{u}$ or $d-\bar{d}$
p_{diquark}	0.08	probability of $qq-\bar{q}q$

Table 8.1: Hadronization parameters.

parameters for all the reactions γp , pp , pA , AA . A perfect fit for e^+e^- requires a modification of two parameters, p_{break} and p_{\perp}^{break} .

8.2 Time-Like Cascade

Let us discuss the parameters which determine the time-like cascade, all fixed via studying e^+e^- annihilation. For the pQCD parameter, we use the usual leading order value $\Lambda = 0.2$ GeV. We have also a technical parameter q_{fin}^2 , which determines the lower mass limit of partons in the time-like cascade. In figure 8.3, we analyze how certain spectra depend on this parameter. We show rapidity, transverse momentum and multiplicity distributions for partons and for charged particles for an e^+e^- annihilation at 34 GeV. We show results for different values of q_{fin}^2 , namely 0.25 GeV², 1.0 GeV² and 4.0 GeV², which means a lower mass limit of 1 GeV, 2 GeV or 4 GeV, respectively. One sees that only parton distributions are sensitive to the choice of this parameter,

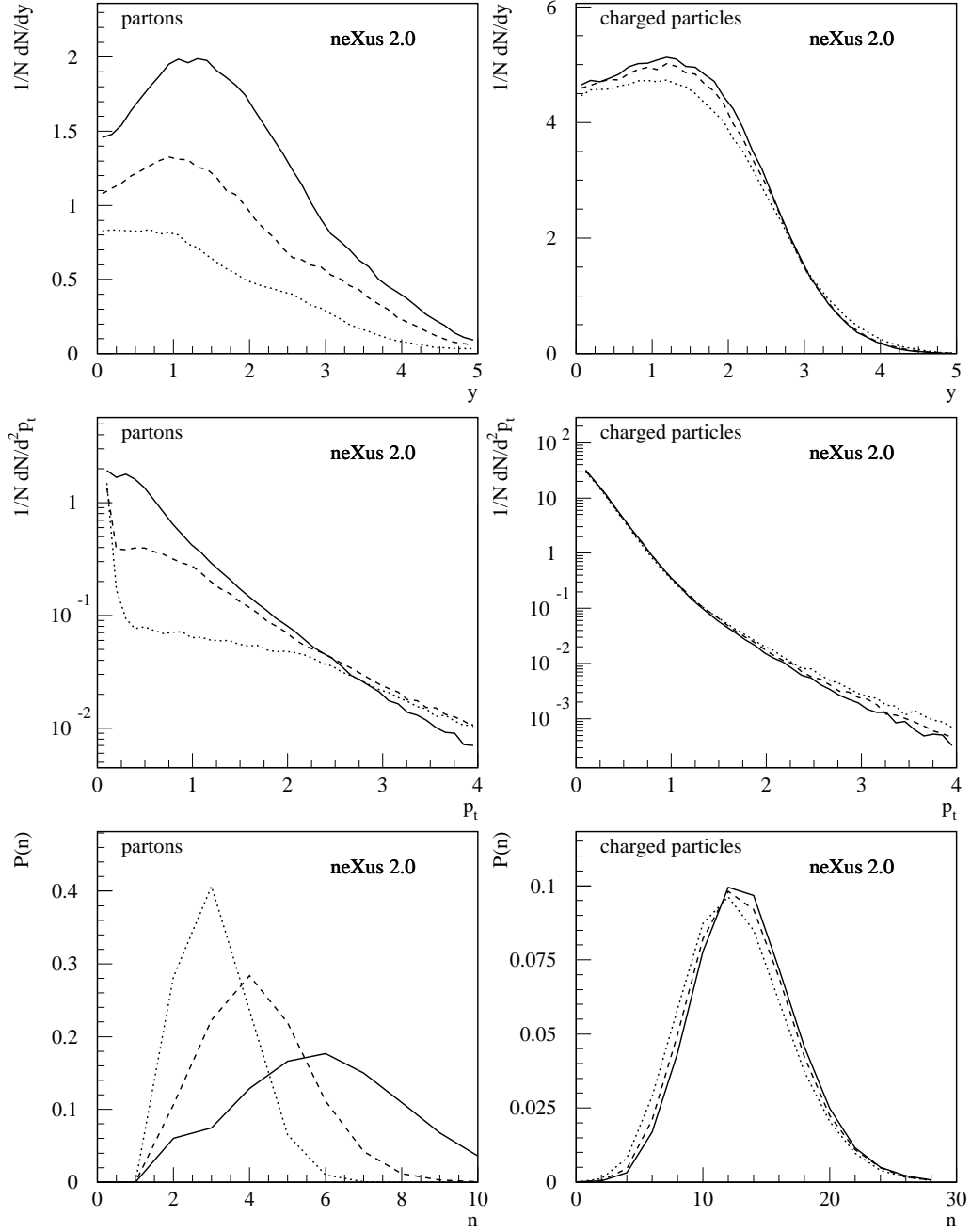


Figure 8.3: Rapidity, transverse momentum and multiplicity distributions for partons (left column) and for charged particles (right column). The curves correspond to the parameters $q_{\text{fin}}^2 = 0.25, 1.0, 2.0$ (full, dashed, dotted). Only parton distributions exhibit strong sensitivity to the value of q_{fin}^2 .

whereas the corresponding charged particle spectra exhibit rather weak dependence on it. This can be explained from the fact that decreasing q_{fin}^2 mainly results in production of additional partons with transverse momenta $p_{\perp}^2 \sim q_{\text{fin}}^2$ and such soft collinear partons hardly affect the fragmentation procedure, which is in this sense “infrared stable”. The number N_f of active flavors is taken to be

5 for e^+e^- annihilation, whereas for γp , pp , pA , AA we use for the moment $N_f = 3$. In table 8.2 we show the cascade parameters and their default values.

name	value	meaning
Λ	0.2 GeV	pQCD parameter
q_{fin}^2	0.25 GeV ²	transverse momentum cutoff
N_f	5 for e^+e^- 3 for γp , pp , pA , AA	active flavors

Table 8.2: Time-like cascade parameters.

8.3 Parton-Parton Scattering

There is first of all the parameter Q_0 which defines the borderline between soft and hard processes, where one has to choose a reasonable value (say between 1 and 2 GeV²).

Then we have a couple of parameters characterizing the soft Pomeron: the intercept $\alpha_{\text{soft}}(0)$ and the slope α'_{soft} of the Pomeron trajectory, the vertex value γ_{part} and the slope R_{part} for the Pomeron-parton coupling, and the characteristic hadronic mass scale s_0 . We have two parameters, β_g and w_{split} , characterizing the coupling between the soft Pomeron and the parton ladder. Whereas for s_0 one just chooses some “reasonable” value and R_{part} is taken to be zero, one fixes the other parameters by trying to get a good fit for the total cross section and the slope parameter for proton-proton scattering as a function of the energy as well as the structure function F_2 of deep inelastic lepton-proton scattering.

Concerning the hard scattering part, the resolutions scale $p_{\perp \text{res}}^2$ and the K-factor K are fixed such that the standard parton evolution is reproduced.

Finally, we have the triple Pomeron coupling weight $r_{3\text{P}}$, which is fixed by as well checking the energy dependence of the proton-proton total cross section.

name	value	meaning
Q_0^2	1.5 GeV ²	soft virtuality cutoff
s_0	1 GeV ²	soft mass scale
$\alpha_{\text{soft}}(0)$	1.054	Pomeron intercept
α'_{soft}	0.21 GeV ⁻²	Pomeron slope
γ_{part}	1.11 GeV ⁻¹	Pomeron-parton coupling vertex
R_{part}	0	Pomeron-parton coupling slope
β_g	0.5	Pomeron-ladder coupling parameter
w_{split}	0.15	Pomeron-ladder coupling parameter
$p_{\perp \text{res}}^2$	0.25 GeV ²	resolutions scale
K	1.5	K-factor
$r_{3\text{P}}$	0.0096 GeV ⁻¹	triple Pomeron coupling constant

Table 8.3: Parton-parton scattering parameters.

The values of these parameters are shown in table 8.3.

8.4 Hadron-Hadron Scattering

Let us first discuss the parameters related to the partonic wave function of the hadron h (for numerical applications we only consider nucleons: $h = N$). The transverse momentum distribution is characterized by the hadronic Regge radius squared R_N^2 , the longitudinal momentum distributions

are given in terms of two exponents, α_{remn}^N and α_{part} . The latter one is taken to be independent of the hadron type as $2\alpha_{\mathbb{R}}(0) - 1$, with the usual Reggeon intercept $\alpha_{\mathbb{R}}(0) = 1/2$. The parameter R_N also affects the proton-proton total cross sections, whereas α_{remn}^N can be determined by investigating baryon spectra (but it also influences the total cross section).

There are several more parameters, which have not been mentioned so far: the remnant excitation probability $p_{\text{remn.ex}}$ and the exponent $\alpha_{\text{remn.ex}}$, which gives a remnant mass distribution as

$$(M^2)^{-\alpha_{\text{remn.ex}}} . \quad (8.2)$$

The minimum string mass $m_{\text{string min}}$ assures that Pomerons with string masses less than this minimal mass are ignored. The partons defining the string ends are assumed to have transverse momenta according to a Gaussian distribution with a mean value $p_{\perp \text{SE}}$. Diffractive scattering is assumed to transfer transverse momentum according to a Gaussian distribution, with a mean value $p_{\perp \text{diff}}$. The parameter $m_{\text{string min}}$ is taken to be just slightly bigger than two times the pion mass to allow at least string fragmentation into two pions. The other parameters can be fixed by comparing with experimental inclusive spectra.

name	value	meaning
R_N^2	2 GeV^{-2}	parton-hadron coupling slope
α_{part}	0	participant exponent
α_{remn}^N	1.5	remnant exponent
$p_{\text{remn.ex}}$	0.45	remnant excitation probability
$\alpha_{\text{remn.ex}}$	1.4	remnant excitation exponent
$m_{\text{string min}}$	0.29 GeV	minimal string mass
$p_{\perp \text{SE}}$	0.21 GeV	mean p_{\perp} for string ends
$p_{\perp \text{diff}}$	0.35 GeV	mean p_{\perp} for diffractive scattering

Table 8.4: hadron-hadron scattering parameters (for the case of nucleons).

In table 8.4, we show the numerical values of the parameters.

Chapter 9

Testing Time-like Cascade and Hadronization: Electron-Positron Annihilation

Electron-positron annihilation is the simplest possible system to test the time-like cascade as well as the model of fragmentation, since the decay of a virtual photon in electron-positron annihilation gives a quark and an anti-quark, both emitting a cascade of time-like partons, which finally hadronize.

Electron-positron annihilation is therefore used to test both the time-like cascade and the hadronization model, and in particular to fix parameters.

The simulation of an electron-positron annihilation event can be divided into three different stages:

1. The annihilation into a virtual photon or a Z boson and its subsequent decay into a quark-anti-quark pair (the basic diagram).
2. The evolution of the quark and the anti-quark into on-shell partons by radiation of perturbative partons (time-like cascade).
3. The transition of the partonic system into hadrons via a fragmentation model (hadronization).

These stages are discussed in the following sections.

After having described the three stages of electron-positron annihilation, we will be able to test the model against numerous data available. We will show comparisons with experimental results at low energies at PETRA (DESY), by the TASSO collaboration [36]. The center-of-mass energies are 14, 22 and 34 GeV. Higher energies are reached at LEP, where we compare especially with results for 91.2 GeV, the Z^0 mass, where a big number of events has been measured.

By comparing with data, we will be able to fix the essential parameters of the hadronization model, namely p_{break} , p_{ud} , p_{diquark} and p_{\perp}^{break} . The free parameters in the parton cascade are the pQCD scaling parameter Λ and q_{fin}^2 , representing the minimum transverse momentum for a branching in the cascade. For the pQCD parameter, we use the usual leading order value $\Lambda = 0.2$ GeV. The influence of the technical parameter q_{fin}^2 has been investigated in detail.

9.1 The Basic Diagram

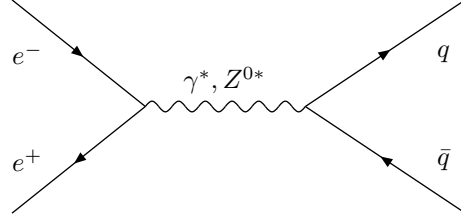


Figure 9.1: Electron-positron annihilation.

The first order differential cross section for the process

$$e^+ e^- \rightarrow \gamma^* \text{ or } Z \rightarrow q \bar{q} \quad (9.1)$$

is given as [29]

$$\begin{aligned} \frac{d\sigma}{d\cos\theta} = \frac{\pi\alpha^2}{2s} \left[(1 + \cos^2\theta) \{q_f^2 - 2q_f V_e V_f \chi_1(s) + (A_e^2 + V_e^2)(A_f^2 + V_f^2) \chi_2(s)\} \right. \\ \left. + \cos\theta \{-4q_f A_e A_f \chi_1(s) + 8A_e V_e A_f V_f \chi_2(s)\} \right] \end{aligned} \quad (9.2)$$

with

$$\chi_1(s) = \kappa \frac{s(s - M_Z^2)}{(s - M_Z^2)^2 + \Gamma_Z^2 M_Z^2}, \quad (9.3)$$

$$\chi_2(s) = \kappa^2 \frac{s^2}{(s - M_Z^2)^2 + \Gamma_Z^2 M_Z^2}, \quad (9.4)$$

where κ is given as

$$\kappa = \frac{\sqrt{2}G_F M_Z^2}{16\pi\alpha}.$$

Here, α is the fine structure constant, q_f the quark flavor, M_z the mass of the Z boson, Γ_Z its decay width. The vector and axial coupling factors are

$$V_f = T_f^3 - 2q_f \sin^2 \theta_W, \quad A_f = T_f^3 \quad (9.5)$$

and

$$T_f^3 = \begin{cases} \frac{1}{2} & \text{if } f = \nu, u, c \\ -\frac{1}{2} & \text{if } f = e, d, s, b \end{cases}. \quad (9.6)$$

θ_W is the Weinberg mixing angle. The Fermi constant

$$G_F = \frac{\sqrt{2}g_W^2}{8M_W^2} \quad (9.7)$$

is expressed via the weak coupling $g_W^2 = 4\pi\alpha/\sin^2 \theta_W$ and the W-boson mass M_w . At low energies, $s \ll M_Z^2$, we recover the well known formula

$$\sigma = \frac{4\pi\alpha^2}{3s} q_f^2. \quad (9.8)$$

The factors $\chi_1(s)$ and $\chi_2(s)$ correspond to the intermediate Z -boson state and to the photon- Z -boson interference, respectively. Formula (9.2) can now be used to generate an initial quark-anti-quark pair.

9.2 The Time-like Parton Cascade and String Formation

If one considers a quark and an anti-quark coming from the decay of a virtual photon or Z-boson to be on-shell, this amounts to a lowest order treatment. At high energies, a perturbative correction has to be done. Since it is difficult to calculate the higher order Feynman diagrams exactly, one uses the so-called DGLAP evolution equations, which describes the evolution of a parton system with leading logarithmic accuracy. This amounts to successively emitting partons (time-like parton cascade, see fig. 9.2). This has been discussed in detail in connection with the parton production

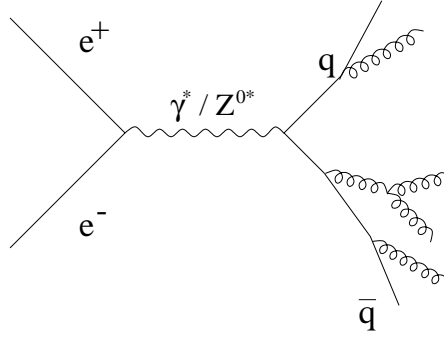


Figure 9.2: Time-like parton cascade.

in proton-proton or nucleus-nucleus collisions. We use exactly the same method here. Even for determining three momenta of the primary quark and anti-quark, we do not need any new input, since this corresponds exactly to the case of the time-like cascade of the two partons involved in the Born scattering in hadronic collisions.

The fact that we use one and the same procedure for the time-like parton cascade in all the different reactions, allows us to test elements of hadronic interactions in a much simpler context of elementary electron-positron interactions.

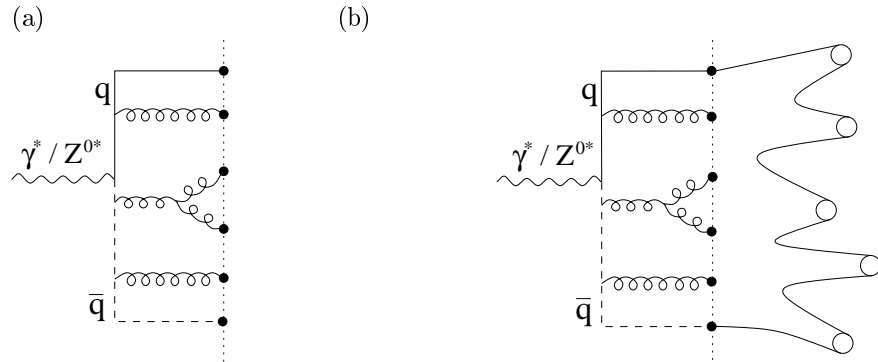


Figure 9.3: Forming strings for an e^+e^- event.

The final step is the hadronization of the above-mentioned parton configuration. Here we use the string model, as in case of pp or γp scattering. The string formation in e^+e^- is much simpler than in proton-proton scattering, where the cut Pomeron is represented as a cylinder. The structure of an e^+e^- event is planar in the sense that the whole event can be represented on a plane. So we simply plot the diagram on a plane with only one cut line. In fig. 9.3(a), we present a half-plane (on one side of the cut) for the amplitude shown in fig. 9.2. The dotted line represents the cut. There are a couple of partons crossing the cut, indicated by dots. As in the case of proton-proton or photon-proton scattering, we identify the cut line as a kinky relativistic string, with the partons

representing the kinks. So in our example, we have a kinky string with six kinks, two external ones and four internal ones. We then apply the usual hadronization procedure, discussed earlier in detail, in order to calculate hadron production from a fragmenting string, see fig. 9.3(b).

9.3 Event Shape Variables

We start our presentation of results by considering the so-called event-shape variables, which describe the form of an e^+e^- event in general. For example, one is interested in knowing whether the particle momenta are essentially aligned along a certain axis, distributed isotropically over the phase space, or lying more or less in a plane. In the figs. 9.4 to 9.8, we are going to compare our calculated distributions of several event-variables with data. Let us first discuss the different event-shape variables, one after the other.

Sphericity

The sphericity is defined by the eigenvalues of the sphericity tensor,

$$S^{\alpha\beta} = \sum_i (p_i)^\alpha (p_i)^\beta, \quad (9.9)$$

where i sums all particles and p^α is the particle four-momentum. One finds three eigenvalues λ_i with $\lambda_1 < \lambda_2 < \lambda_3$ and $\lambda_1 + \lambda_2 + \lambda_3 = 1$. The sphericity is then defined as

$$S = \frac{3}{2}(\lambda_1 + \lambda_2). \quad (9.10)$$

For a perfectly isotropic event, one finds $\lambda_1 = \lambda_2 = \lambda_3 = 1/3$ and therefore $S = 1$. An event oriented along one axis gives $S = 3/2(0 + 0) = 0$.

To test whether an event has planar geometry, one defines the aplanarity

$$A = \frac{3}{2}\lambda_1. \quad (9.11)$$

For events in a plane we will find $\lambda_1 = A = 0$. The maximum of this value is $A = 3/2 \cdot 1/3 = 1/2$ for an isotropic event, since the eigenvalues are ordered.

The three eigenvectors $\vec{v}_{1,2,3}$ of the matrix $S^{\alpha\beta}$ can be used to define a coordinate system.

C and D Parameters

The C-parameter is defined by

$$C = 3(\lambda_1\lambda_2 + \lambda_1\lambda_3 + \lambda_2\lambda_3), \quad (9.12)$$

with $\lambda_{1,2,3}$ being the eigenvalues of the tensor

$$M^{\alpha\beta} = \frac{\sum_i \frac{p_i^\alpha p_i^\beta}{|p_i|}}{\sum_i |p_i|}. \quad (9.13)$$

The D -parameter is

$$D = 27\lambda_1\lambda_2\lambda_3. \quad (9.14)$$

These values measure the multiple jet-structure of events. For small values of C two of the eigenvalues are close to zero, we have a two-jet event. If one of the three eigenvalues is close to zero, the D -parameter is approaching zero as well, we have at least a planar event.

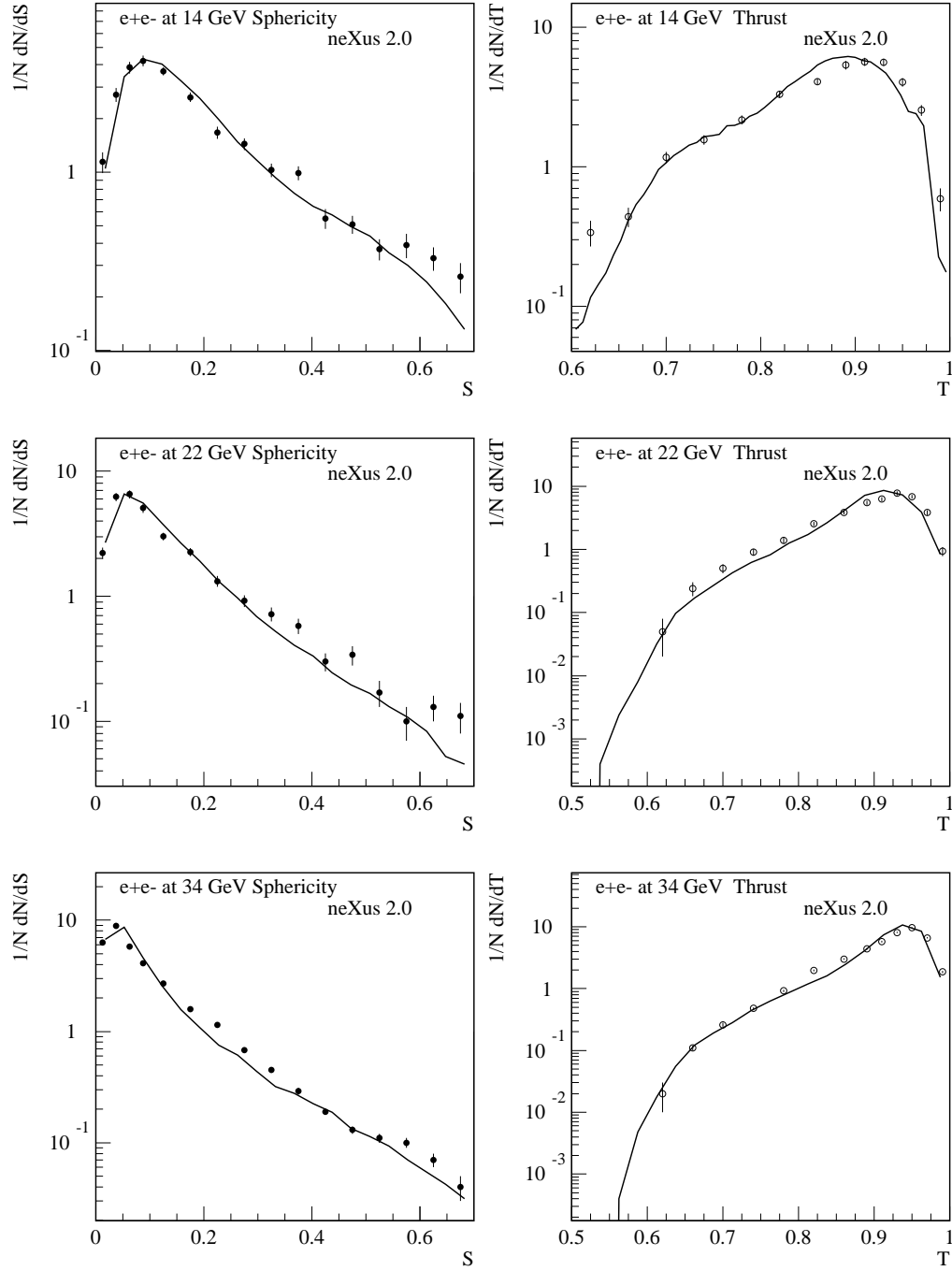


Figure 9.4: The sphericity and thrust for the energies 14 GeV, 22 GeV and 34 GeV.

Thrust

The thrust of an event is defined as

$$T = \max_{\vec{n}} \frac{\sum_j |\vec{n} \cdot \vec{p}_j|}{\sum_j |\vec{p}_j|}. \quad (9.15)$$

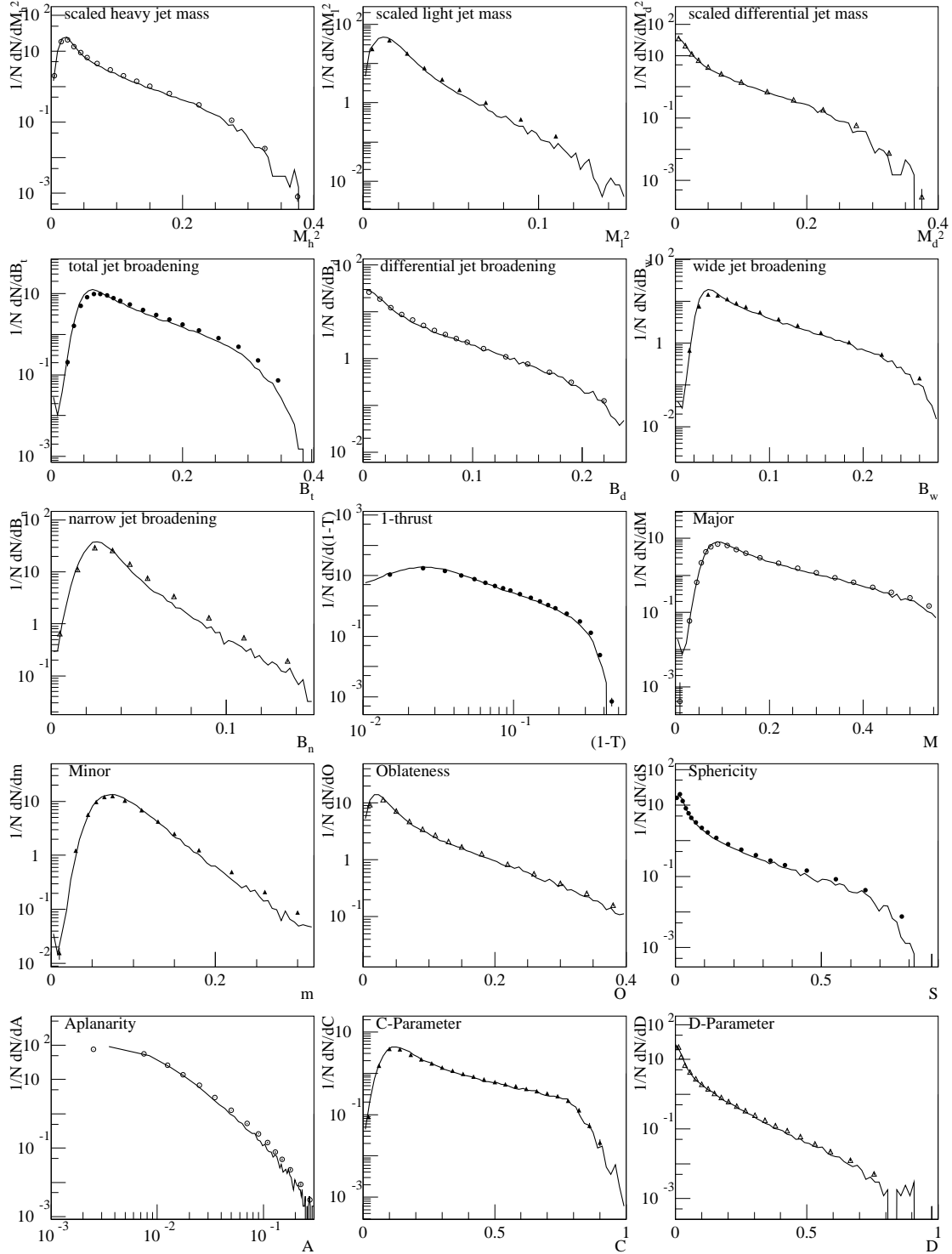


Figure 9.5: Event shape variables at 91.2 GeV. The data (dots) are from the DELPHI collaboration [37].

The vector \vec{n}_{thrust} , which maximizes this expression, defines the thrust axis. A two-jet event will give a thrust value of 1 and a thrust axis along the two jets. An isotropic event gives $T \sim 1/2$.

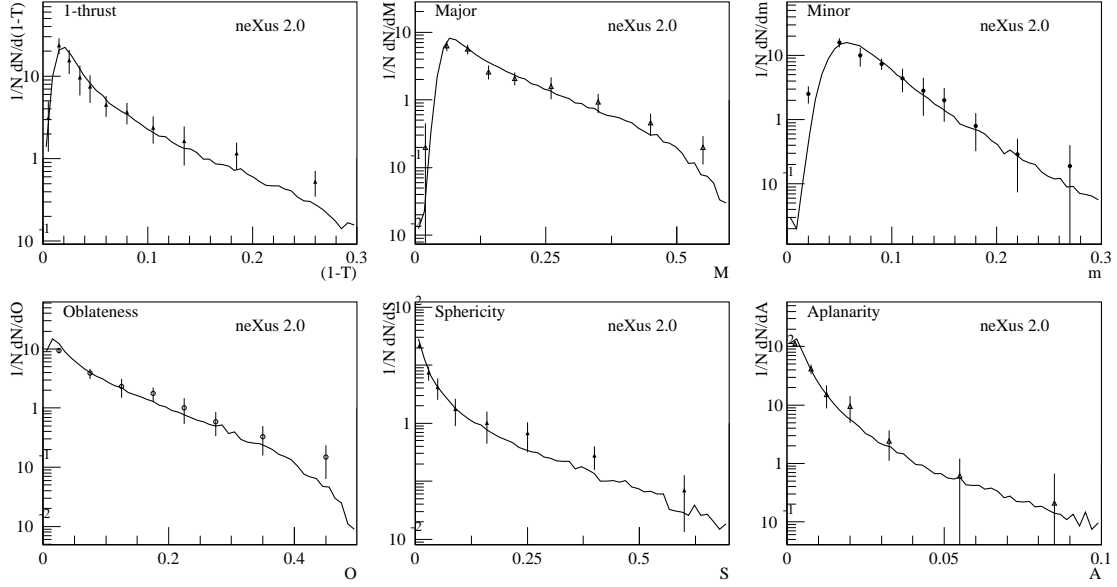


Figure 9.6: Event shape variables for 133 GeV. The data (dots) are from OPAL collaboration [38].

One can repeat the same algorithm with the imposed condition $\vec{n} \perp \vec{n}_{\text{thrust}}$; this gives an expression for the major M with the axis \vec{n}_{Major} .

A third variable, the minor m , is obtained by evaluating the above expression with $\vec{n} \perp \vec{n}_{\text{thrust}}$ and $\vec{n} \perp \vec{n}_{\text{Major}}$, the axis being already given. Each of these values describes the extension of the event perpendicular to the thrust axis. Similar values for M and m describe therefore a cylindrical event. For this, the oblateness is defined as $O = M - m$ which, as the aplanarity, describes a cylindrical event for $O = 0$ and a planar event for higher values.

Jet Broadening

In each hemisphere, the sum of the transverse momenta of the particles relative to the thrust axis is divided by the sum of the absolute values of the momenta.

$$B_{\pm} = \frac{\sum_{\pm \vec{p} \cdot \vec{n}_{\text{thrust}} > 0} |\vec{p}_i \times \vec{n}_{\text{thrust}}|}{2 \sum_i |\vec{p}_i|} \quad (9.16)$$

The greater B_+ is, the greater is the mean transverse momentum. One defines in addition the following variables,

$$B_{\text{wide}} = \max(B_+, B_-), \quad B_{\text{narrow}} = \min(B_+, B_-), \quad (9.17)$$

$$B_{\text{total}} = B_+ + B_-, \quad B_{\text{diff}} = |B_+ - B_-|, \quad (9.18)$$

to compare jet broadening in both hemispheres. For small B_{wide} , one finds a longitudinal event, B_{diff} measures the asymmetry between the two hemispheres.

Heavy Jet or Hemisphere Mass

The variable M_h^2 is defined as

$$M_h^2 = \max \left(\left(\sum_{\vec{p}_i \cdot \vec{n}_{\text{thrust}} > 0} p_i \right)^2, \left(\sum_{\vec{p}_i \cdot \vec{n}_{\text{thrust}} < 0} p_i \right)^2 \right). \quad (9.19)$$

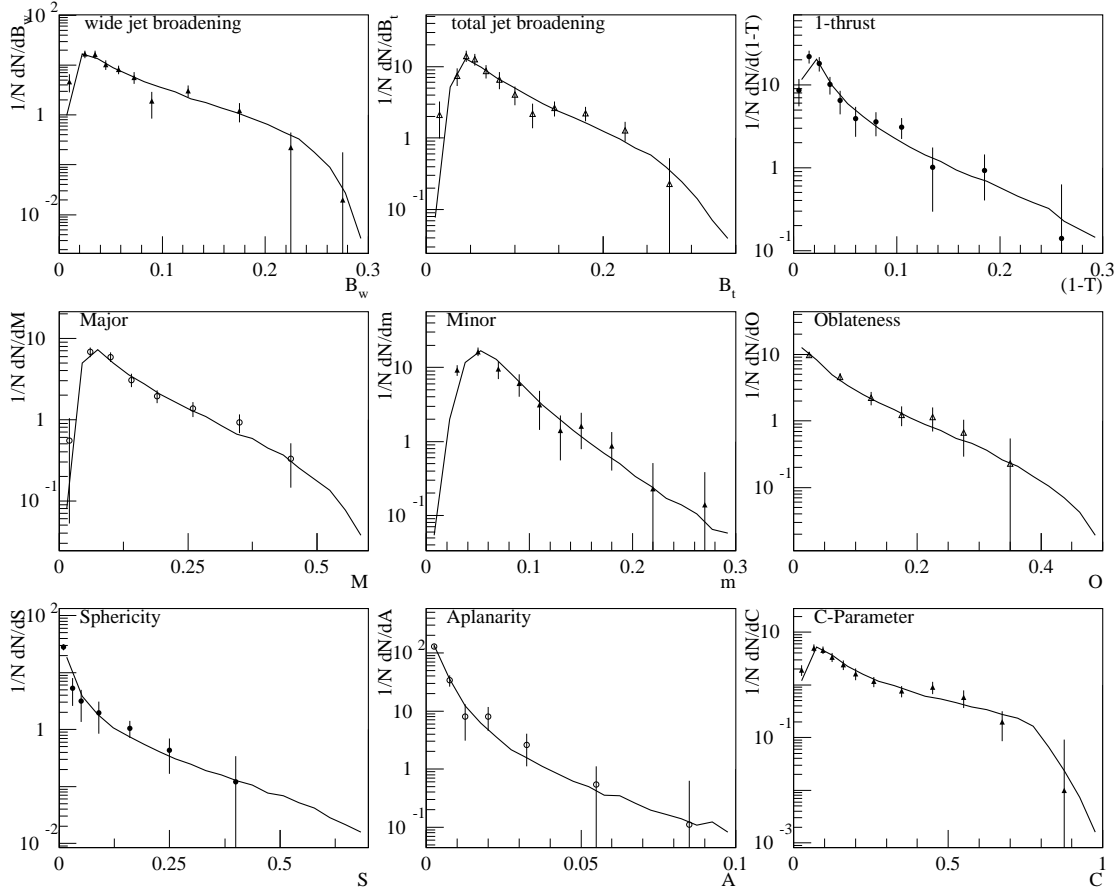


Figure 9.7: Event shape variables for 161 GeV. The data (dots) are from OPAL collaboration [38].

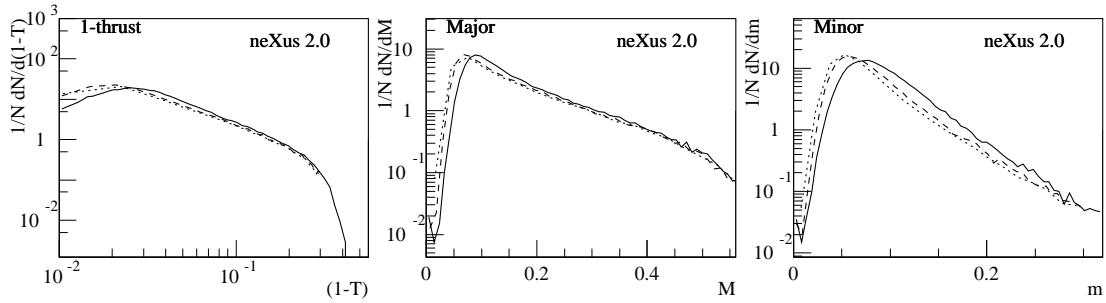


Figure 9.8: Thrust, minor and major for 91 GeV (full line), 133 GeV (dashed) and 161 GeV (dotted).

and corresponds to the maximal invariant mass squared of the hemispheres. The corresponding formula with “min” instead of “max” defines the variable M_l . One defines as well $M_{\text{diff}} = M_h - M_l$. Usually one analyzes distributions of $\frac{M_h^2}{E_{\text{vis}}^2}$, $\frac{M_l^2}{E_{\text{vis}}^2}$ or $\frac{M_{\text{diff}}^2}{E_{\text{vis}}^2}$, which describe the squared masses normalized to the visible energy.

Some Comments

Fig. 9.4 shows the distributions of sphericity and thrust for the lower energies 14, 22 et 34 GeV. Even though one expects an increasing contribution of perturbative gluons, which is confirmed by the inclusive hadron distributions (see next section), the events are more longitudinal at higher energies, corresponding to the values of thrust close to 1 and to the sphericity $S \simeq 0$. This can be explained by the fact that the leading quarks dominate the event shape. The results for higher energies (figs. 9.5, 9.6, 9.7) confirm the above statements.

In figs. 9.5, 9.6, 9.7, we show also the distributions of other event variables, like heavy jet mass, Major, etc. In general, our model describes quite well all these event shape variables.

9.4 The Charged Particle Distributions

We will now consider the distributions of charged particles, which by definition contain all the particles with a decay time smaller than 10^{-9} s, i.e. the spectra contain, for example, products of decay of K_{short}^0 , while K^\pm are considered stable. The decay products of strange baryons are also included in the distributions.

In fig. 9.9, we plot multiplicity distributions of charged particles for three different energies, where one observes an obvious increase of the multiplicity with energy. In fig. 9.10, we show the distributions of the absolute value of the rapidity for the energies 14 GeV, 22 GeV, 34 GeV, 91.2 GeV, 133 GeV and 161 GeV. The rapidity is defined as $y = 0.5 \ln((E + p_z)/(E - p_z))$, where the variable p_z may be defined along the thrust axis or along the sphericity axis. For both, multiplicity and rapidity distributions, the theoretical curves agree well with the data.

The multiplicity increases faster than $\langle n_{\text{ch}} \rangle = a + b \ln s$ as a function of s [39], which is due to the fact that the maximal height of the rapidity distribution increases with energy, as seen in fig. 9.10. This comes from radiated gluons, leading to kinky strings, since a flat string without gluons shows an increasing width but a constant height, as one can see in fig. 9.11. Here, the rapidity distributions of charged particles are plotted for the fragmentation of a flat $d - \bar{d}$ string for the energies 14, 22 and 34 GeV. One observes that the width of the distributions increases whereas its height does not change, giving rise to a proportionality to $\ln s$. Additional hard gluons with non-collinear momenta increase the multiplicity in the mid-rapidity region.

Rather than the rapidity, one may consider the scaled momentum $x_p = 2|\vec{p}_i|/E$ or the scaled energy $x_E = 2E_i/E$, as well as the “rapidity-like” variable $\xi = -\ln x_p$. Concerning the ξ distributions shown in fig. 9.12, one sees that the value ξ_{max} corresponding to the maximum of the curves increases with energy. The x_p distributions (see fig. 9.13) show the development of a more and more pronounced peak at x_p close to zero, with increasing energy.

Having discussed in detail the variables describing the longitudinal phase space, we now turn to transverse momentum, which can be defined according to the sphericity axis or to the thrust axis. One writes

$$p_\perp^{\text{in}} = \begin{cases} |\vec{v}_2 \cdot \vec{p}| & \text{for sphericity} \\ |\vec{n}_{\text{major}} \cdot \vec{p}| & \text{for thrust} \end{cases}, \quad (9.20)$$

and

$$p_\perp^{\text{out}} = \begin{cases} |\vec{v}_3 \cdot \vec{p}| & \text{for sphericity} \\ |\vec{n}_{\text{minor}} \cdot \vec{p}| & \text{for thrust} \end{cases}, \quad (9.21)$$

There are mainly two “sources” of transverse momentum. The first one is the transverse momentum created at each string break. The second one is the transverse momentum from hard gluon radiation, which can be much larger than the first one. So we find large values of p_\perp in the event plane, and smaller ones out of the event plane. Here the event plane is essentially defined by the direction of the hardest gluon emitted.

Let us have a look at transverse momenta of charged particles coming from a string decay for different energies (see fig. 9.14). As expected, the curves show the same behavior. In the same

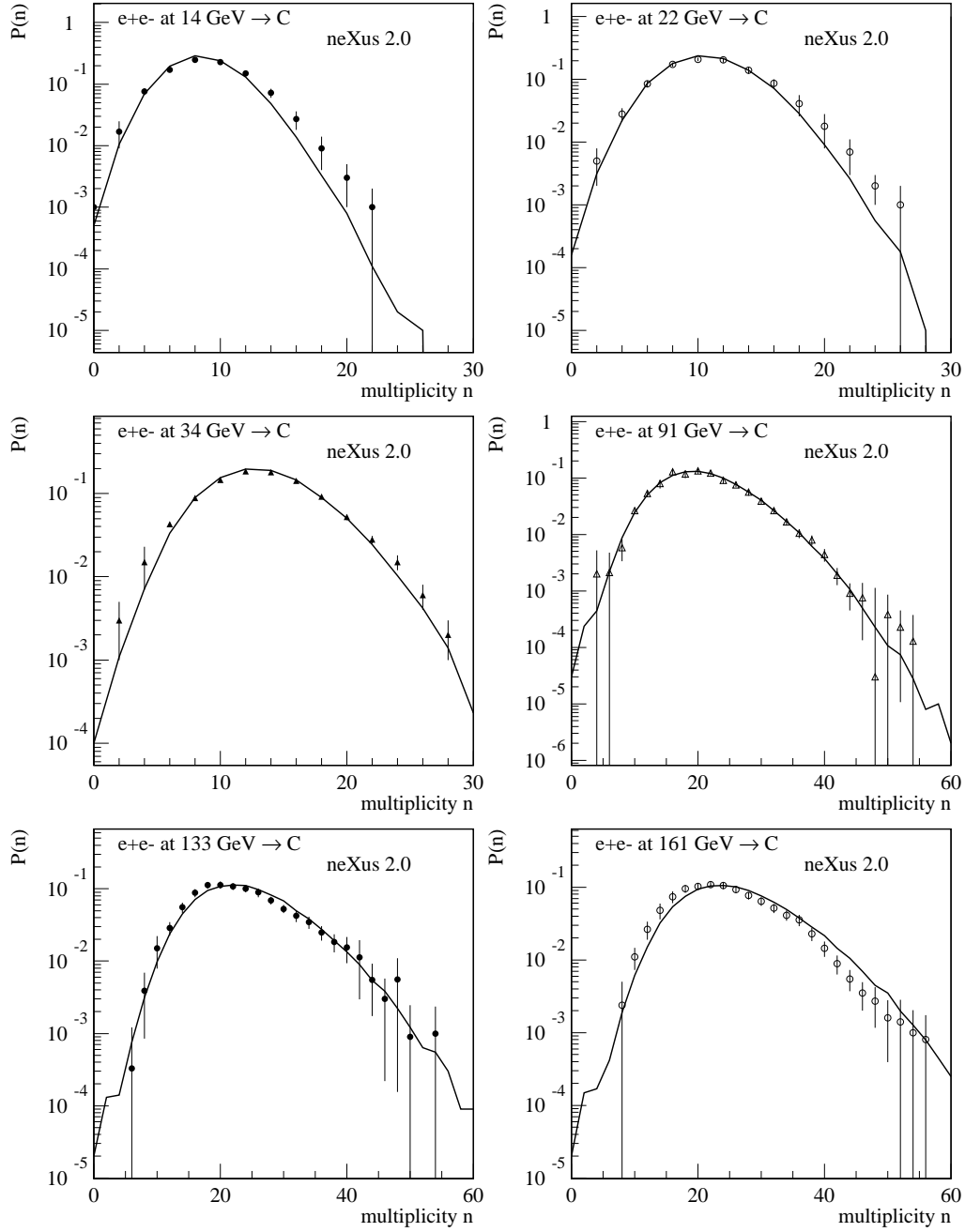


Figure 9.9: Multiplicity distributions for charged particles.

figure, we show the results for an e^+e^- annihilation at 14 GeV. Already at 14 GeV the influence of parton radiation is important. Fig. 9.15 shows the results for 14-34 GeV. Our results agree well with data from the TASSO collaboration [36]. One can see how transverse momenta increase with the energy as an indication of more hard gluon radiation: the p_{\perp}^{out} distributions change little, whereas the p_{\perp}^{in} distributions get much harder at high energies as compared to lower ones.

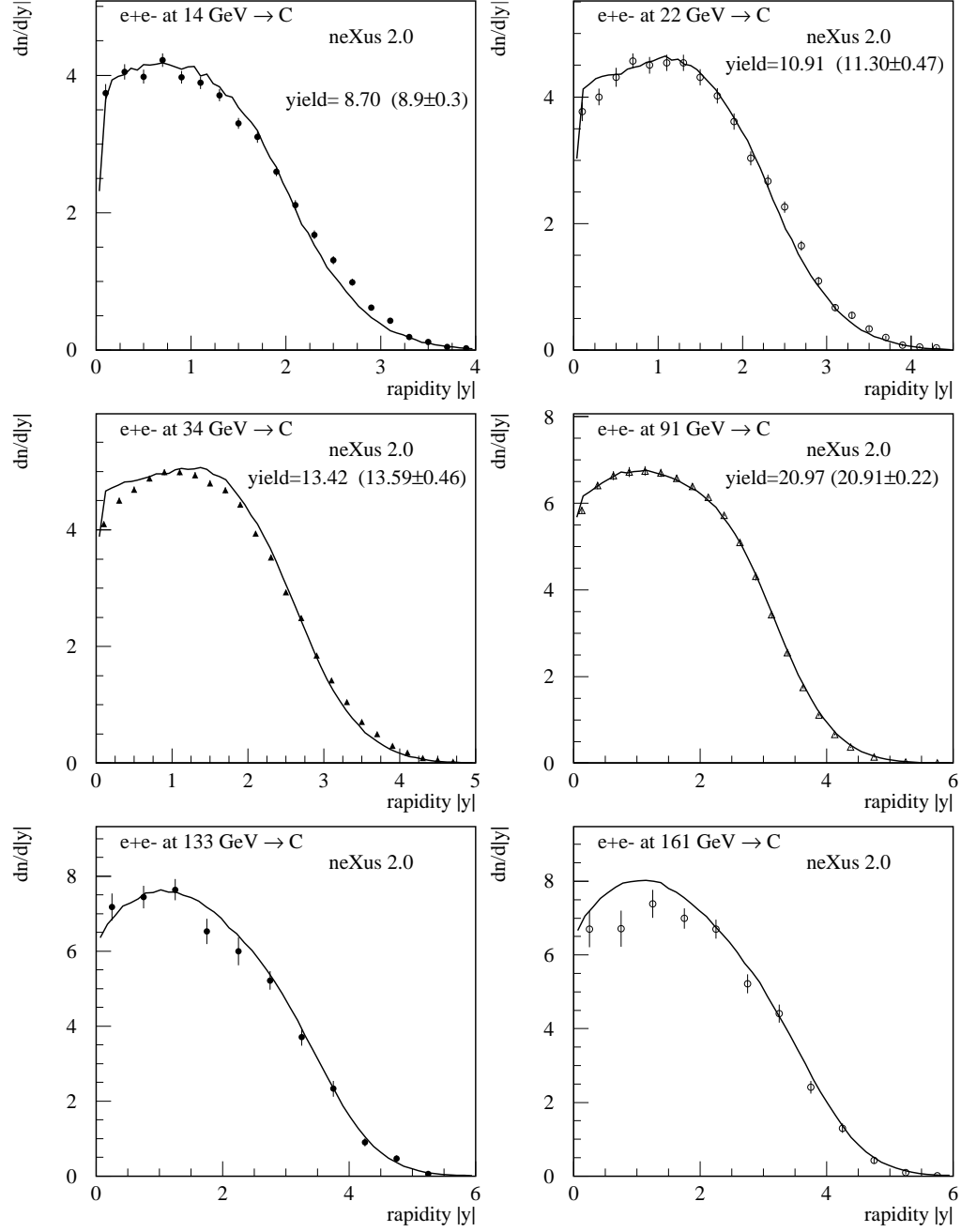


Figure 9.10: Rapidity distributions for charged particles.

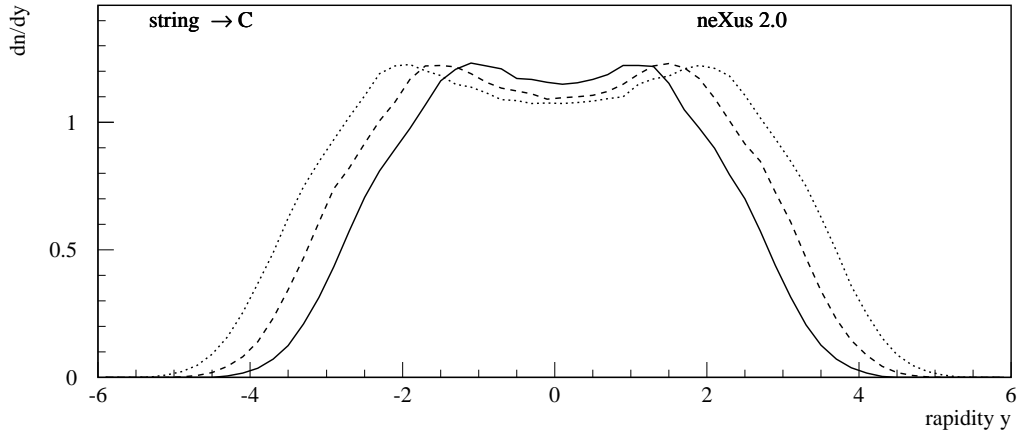


Figure 9.11: Rapidity distribution of charged particles for flat strings at 14 GeV (full), 22 GeV (dashed) and 34 GeV (dotted). The height of the distribution does not change, but its width does.

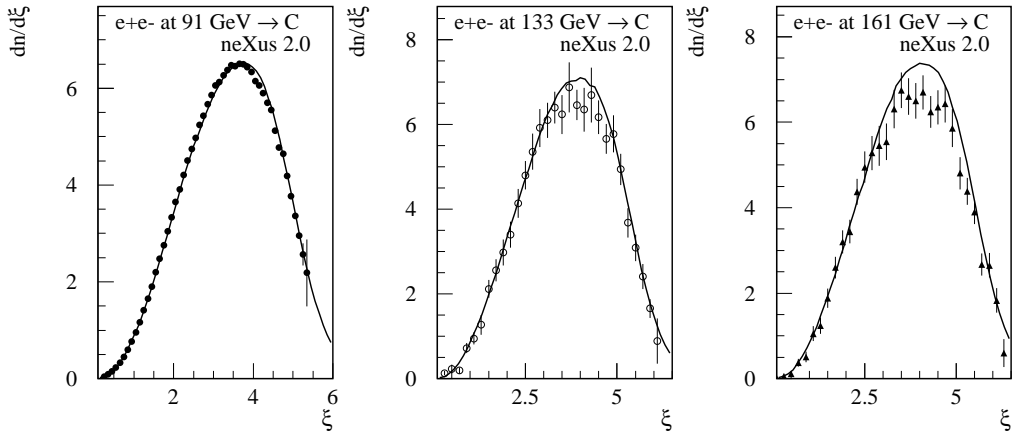
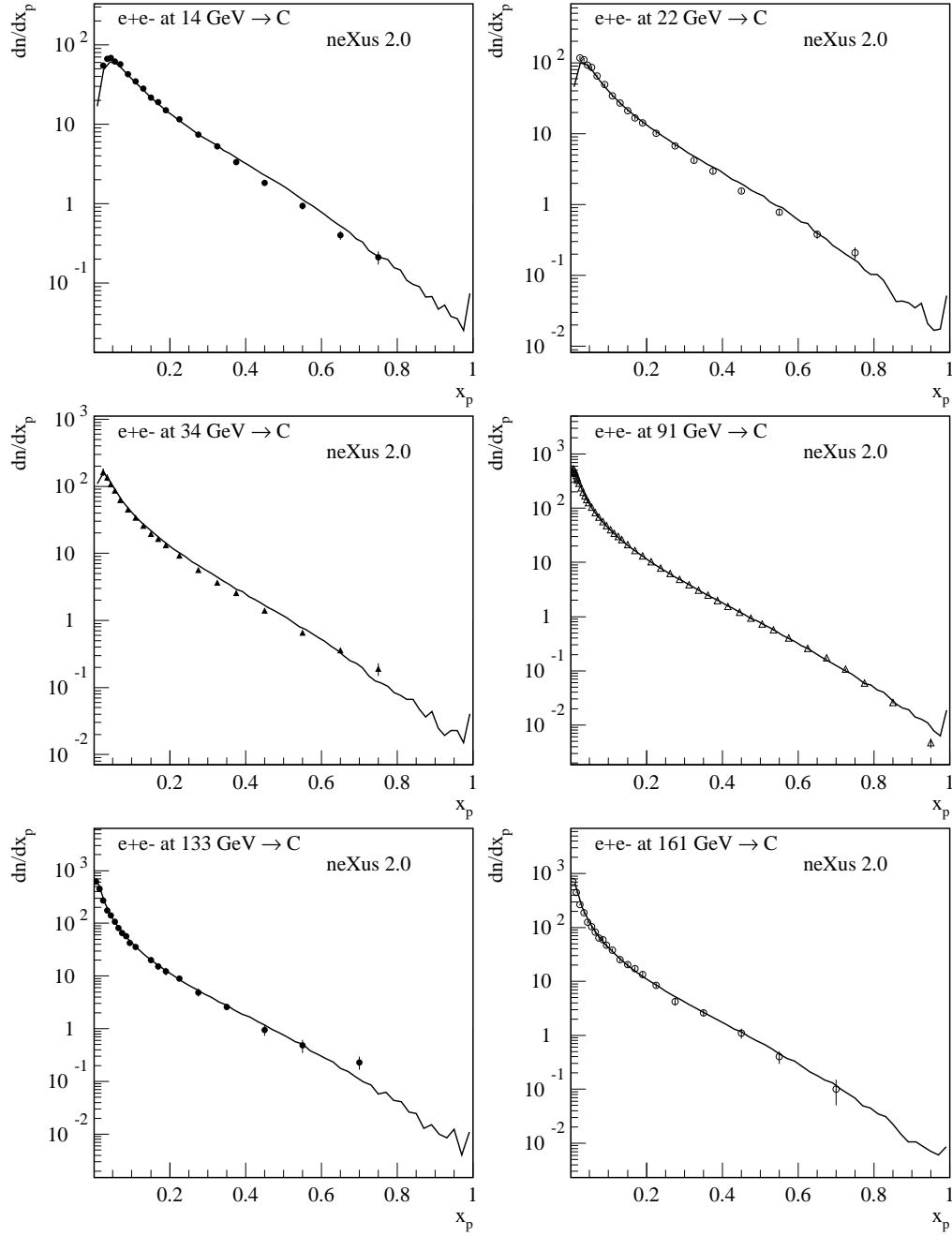


Figure 9.12: $\xi = -\ln x_p$ distributions of charged particles at the energies 91 GeV, 133 GeV and 161 GeV.

Figure 9.13: x_p distributions of charged particles.

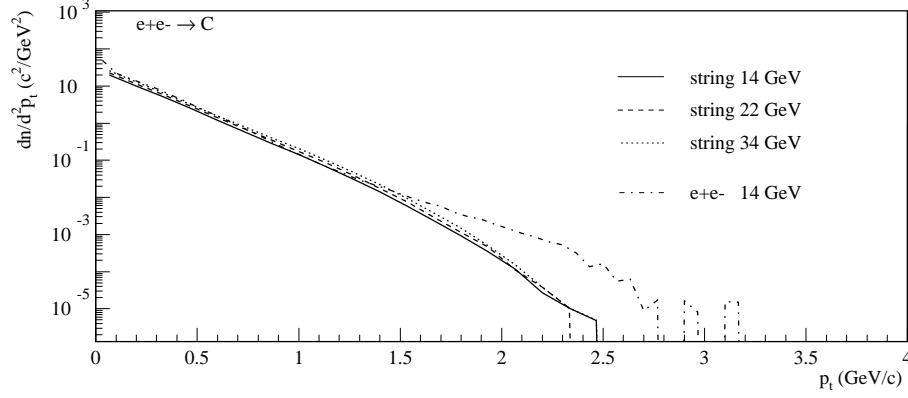


Figure 9.14: Transverse momentum spectra of charged particles for a flat string at energies 14, 22 and 34 GeV together with a simulation for e^+e^- at 14 GeV.

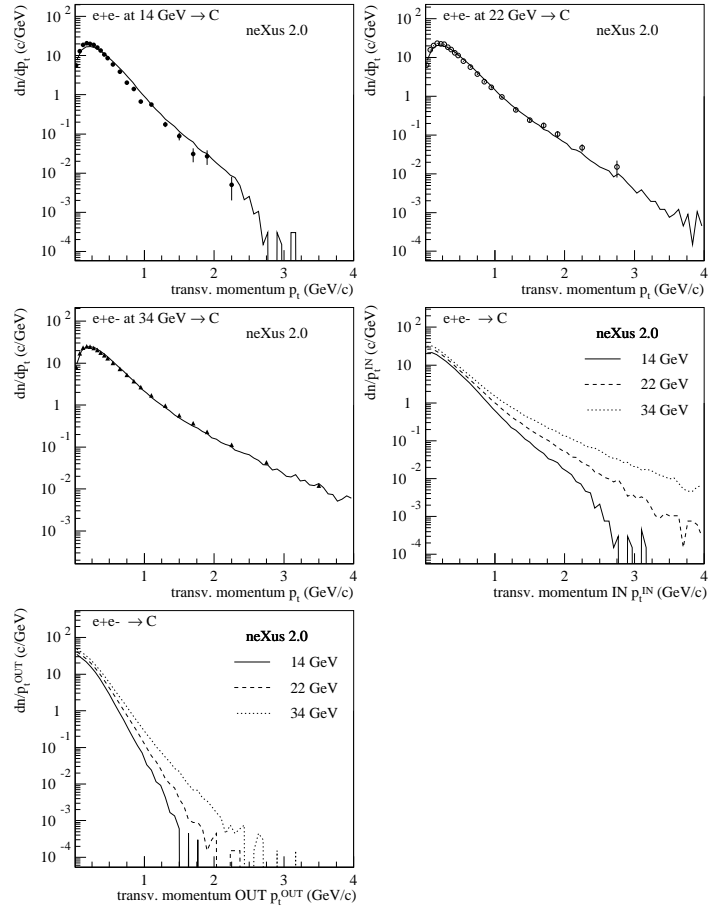


Figure 9.15: Transverse momentum spectra of charged particles at 14, 22 and 34 GeV. The spectra of p_{\perp}^{out} are steeper than the ones of p_{\perp}^{in} .

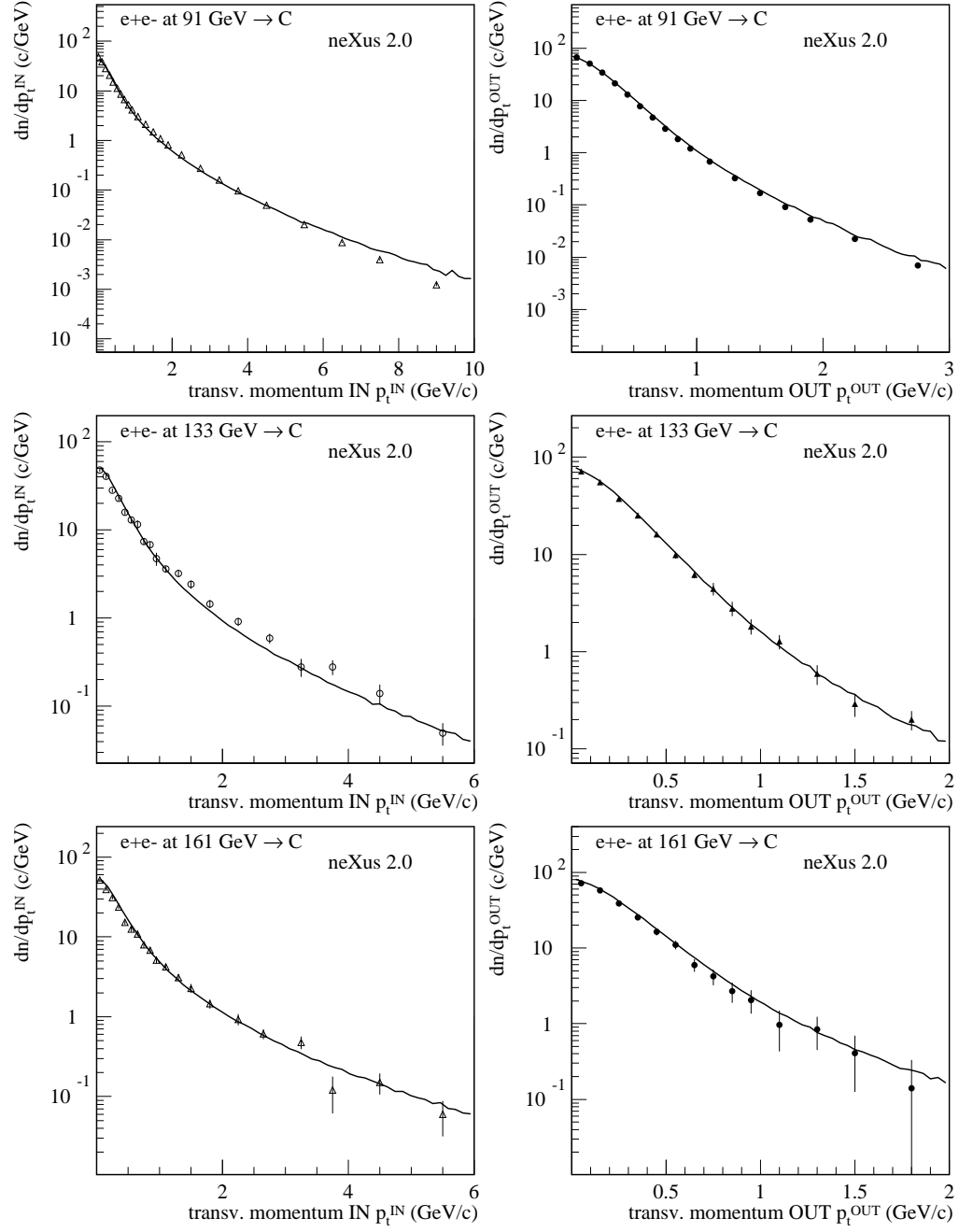


Figure 9.16: Transverse momentum spectra of charged particles at 91, 133 and 161 GeV.

9.5 Identified Particles

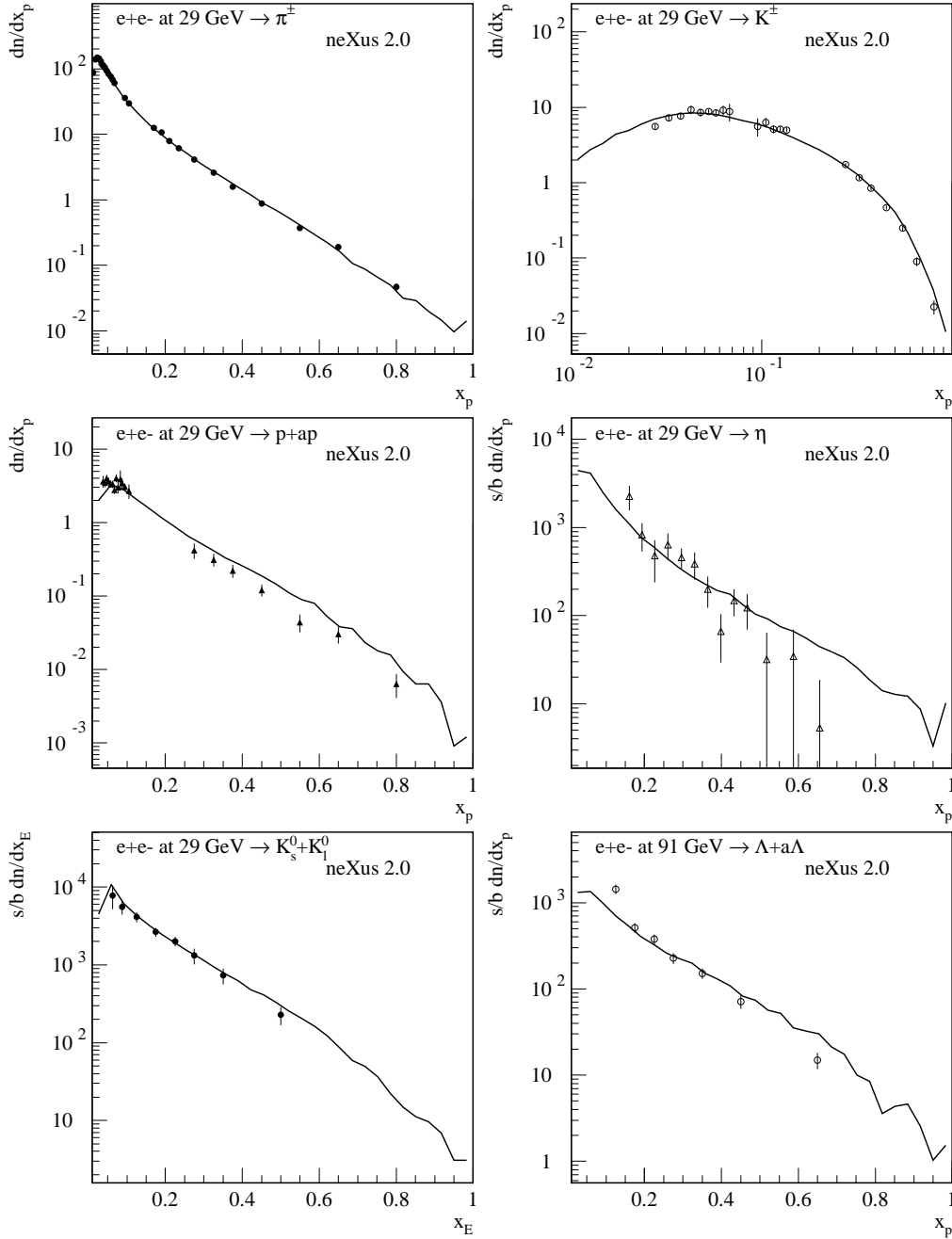


Figure 9.17: Longitudinal momentum fraction distributions for different identified hadrons at $\sqrt{s} = 29$ GeV.

In this section we consider inclusive spectra of identified hadrons. This provides a crucial test of the fragmentation model and allows to fix the two hadronization parameters p_{ud} et $p_{diquark}$. The first one gives the probability to find a pair $u - \bar{u}$ or $d - \bar{d}$, fixing so the strangeness probability to be $(1 - 2p_{ud})$. The parameter $p_{diquark}$ determines the multiplicity of baryons.

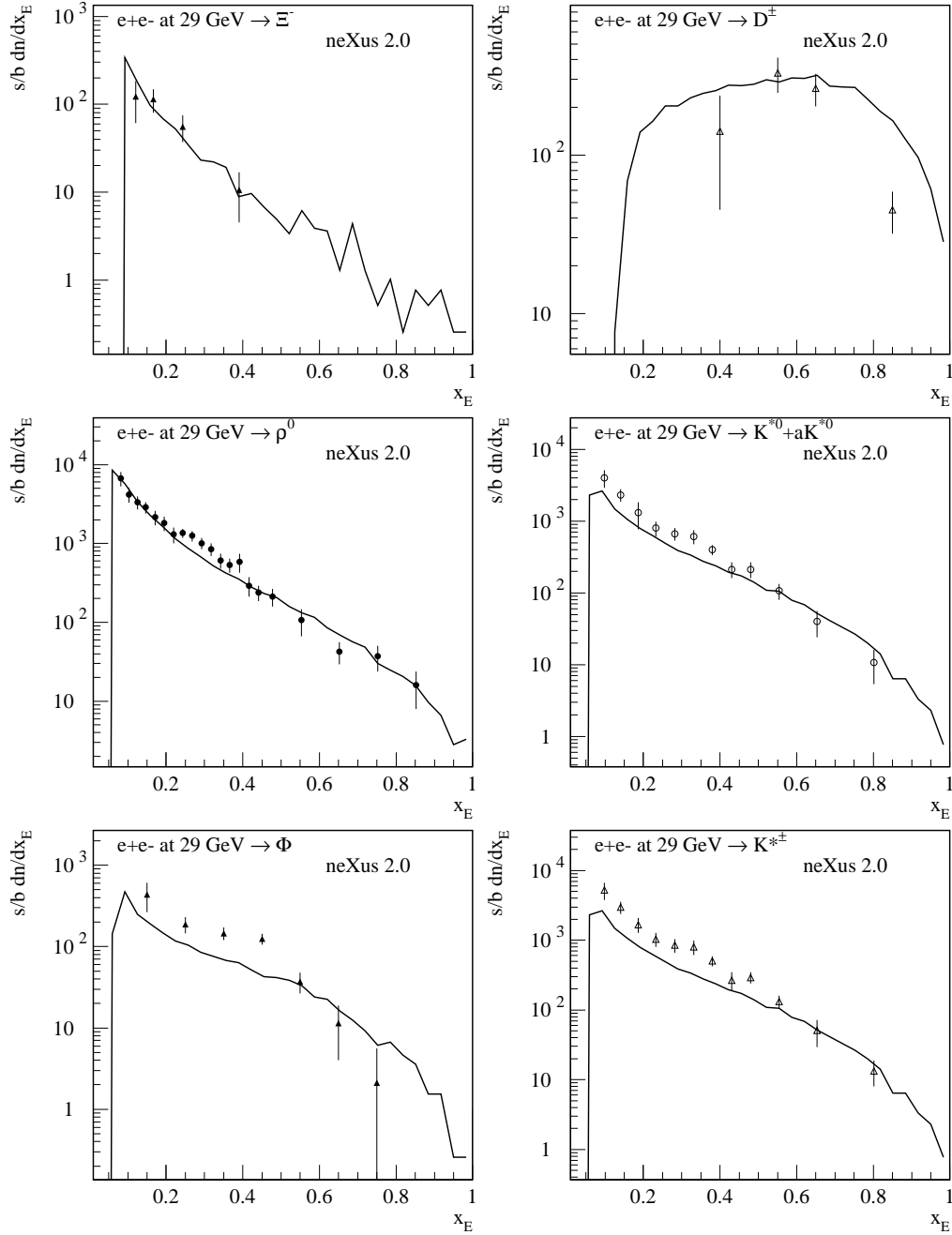


Figure 9.18: Longitudinal momentum fraction distributions for different identified hadrons at $\sqrt{s} = 29$ GeV.

Let us look at spectra at 29 GeV obtained at SLAC ([40], [41]) (figs. 9.17, 9.18) and at 91 GeV at LEP (figs. 9.19, 9.20, 9.21). Since the total multiplicity is dominated by small x -values, we show this regions separately for some figures. The results are in general quite good, however, K^{*} 's are underestimated.

For charmed particles, there is no production from the string decay due to the large mass of the $c - \bar{c}$ pair. The corresponding probability p_{charm} is taken to be zero. Charmed quarks come

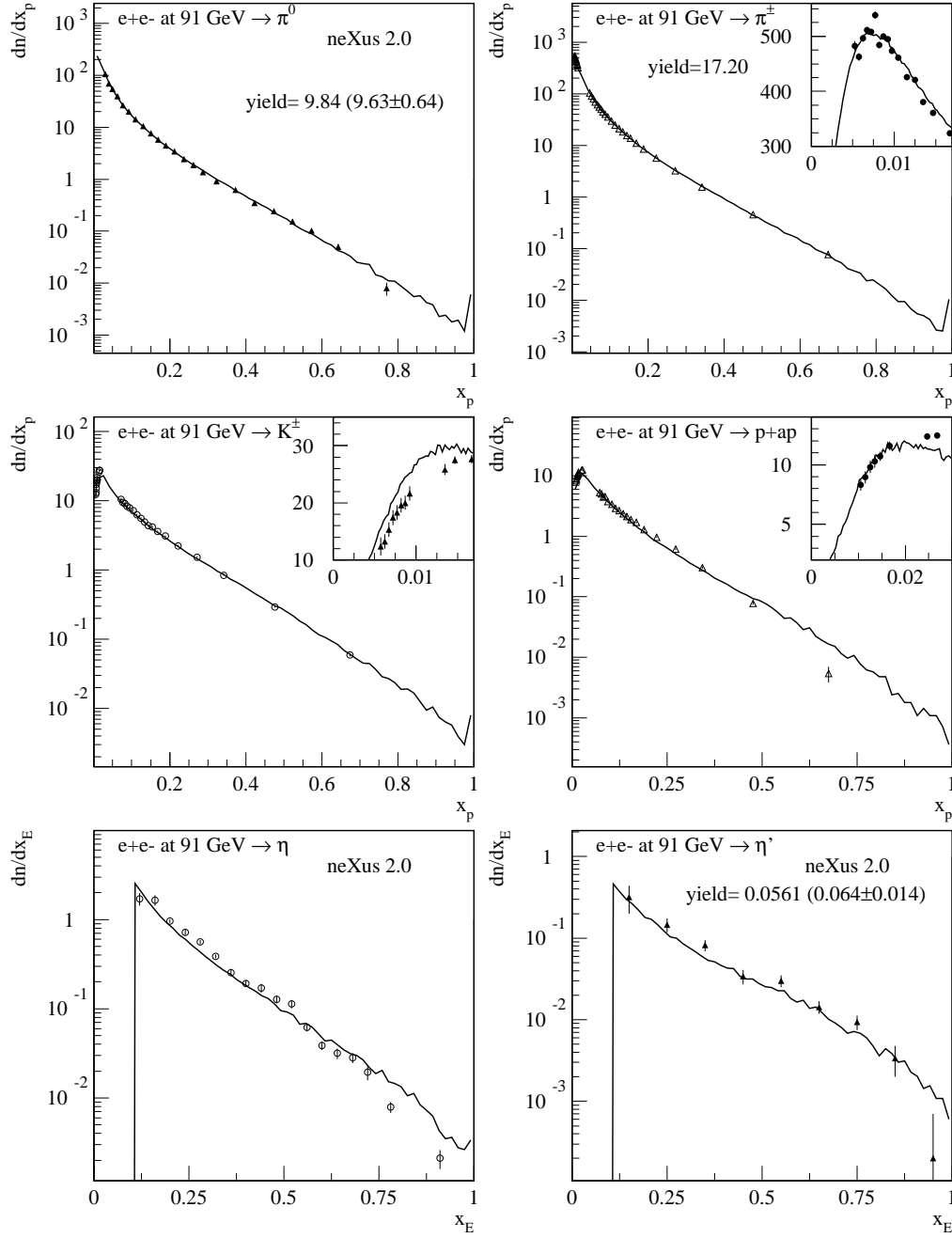


Figure 9.19: Longitudinal momentum fraction distributions for different identified hadrons at $\sqrt{s} = 91$ GeV.

therefore directly from the decay of the virtual photon as well as from perturbative parton cascade. This explains as well the drop of D spectrum at small x_p .

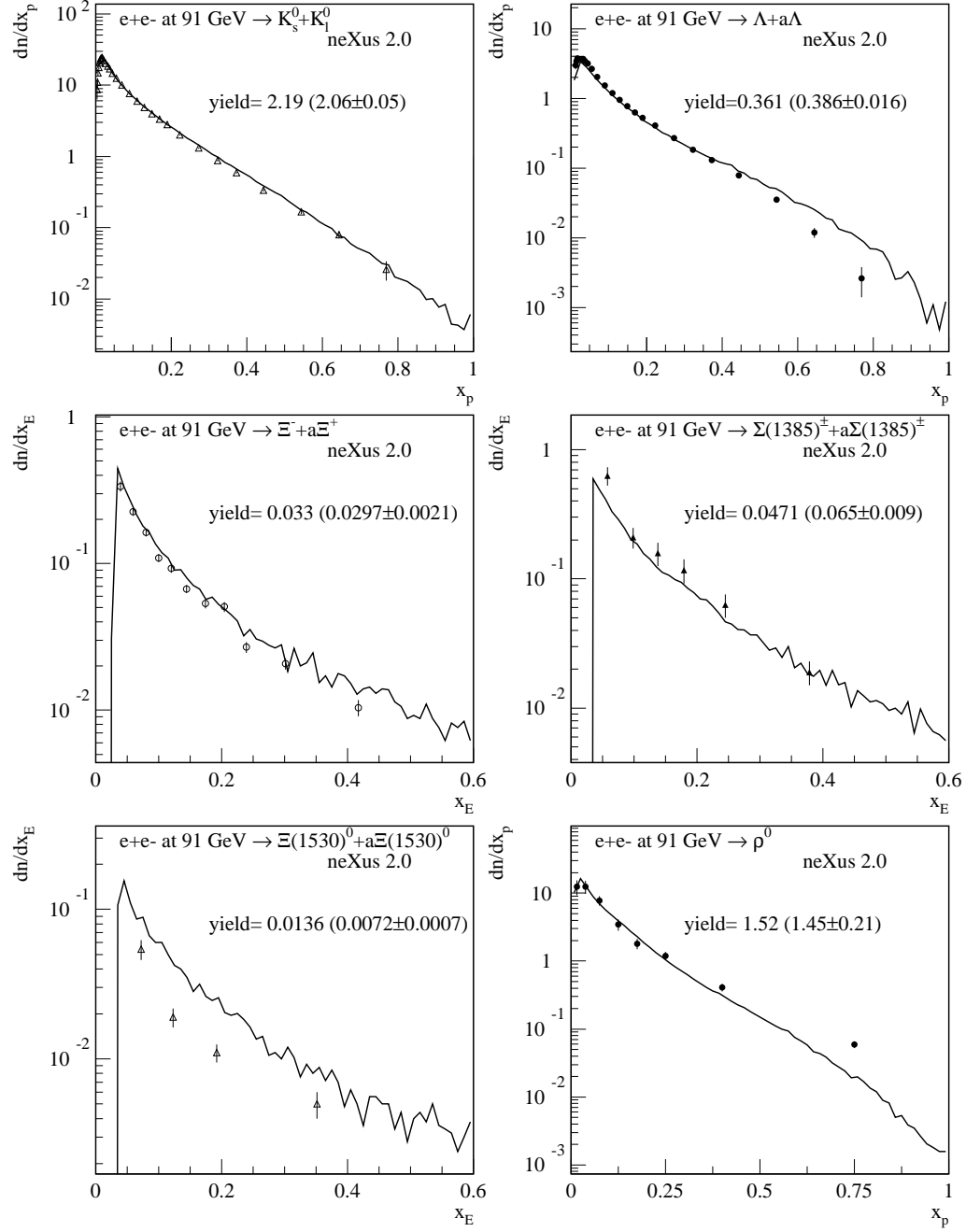


Figure 9.20: Longitudinal momentum fraction distributions for different identified hadrons at $\sqrt{s} = 91$ GeV.

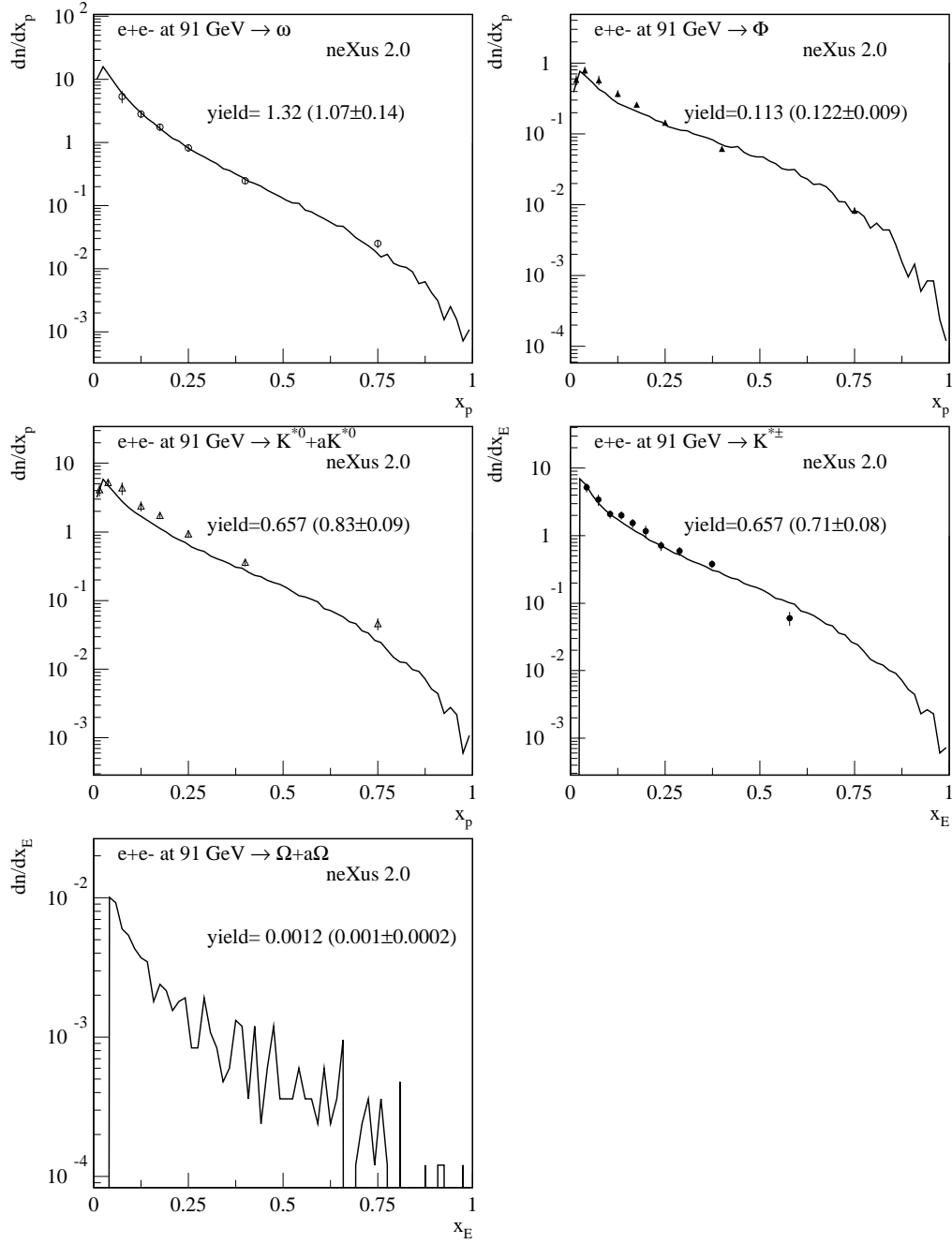


Figure 9.21: Longitudinal momentum fraction distributions for different identified hadrons at $\sqrt{s} = 91$ GeV.

9.6 Jet Rates

Jet multiplicities play an important role in e^+e^- physics since their measurements proved the validity of perturbative QCD. The first 3-jet event was found in 1979. Fig. 9.22 shows this

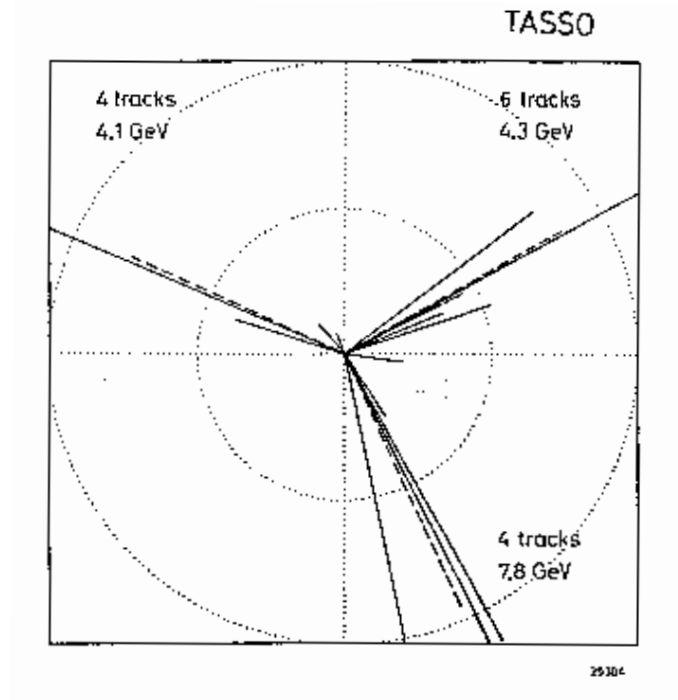


Figure 9.22: The first 3-jet event [39].

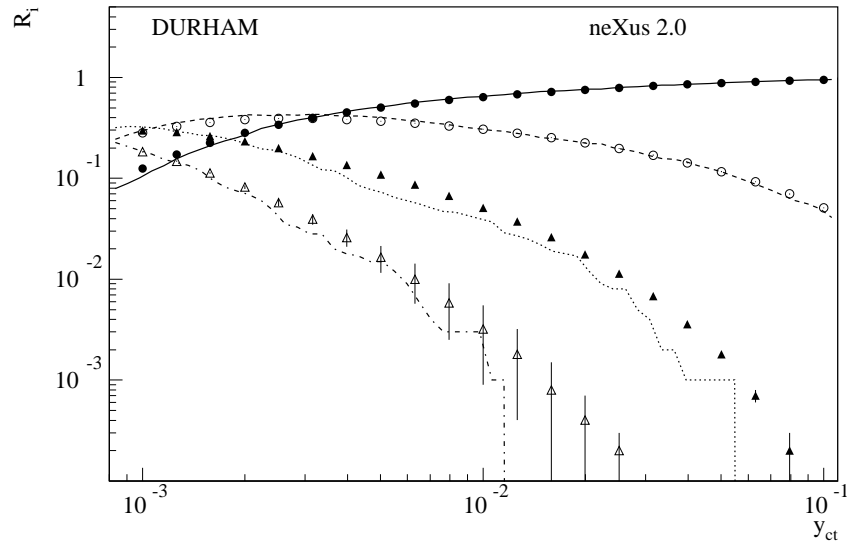


Figure 9.23: Jet rates at 91.2 GeV calculated with the DURHAM algorithm as a function of y_{cut} . The rates for 2, 3, 4 and 5 jets are shown.

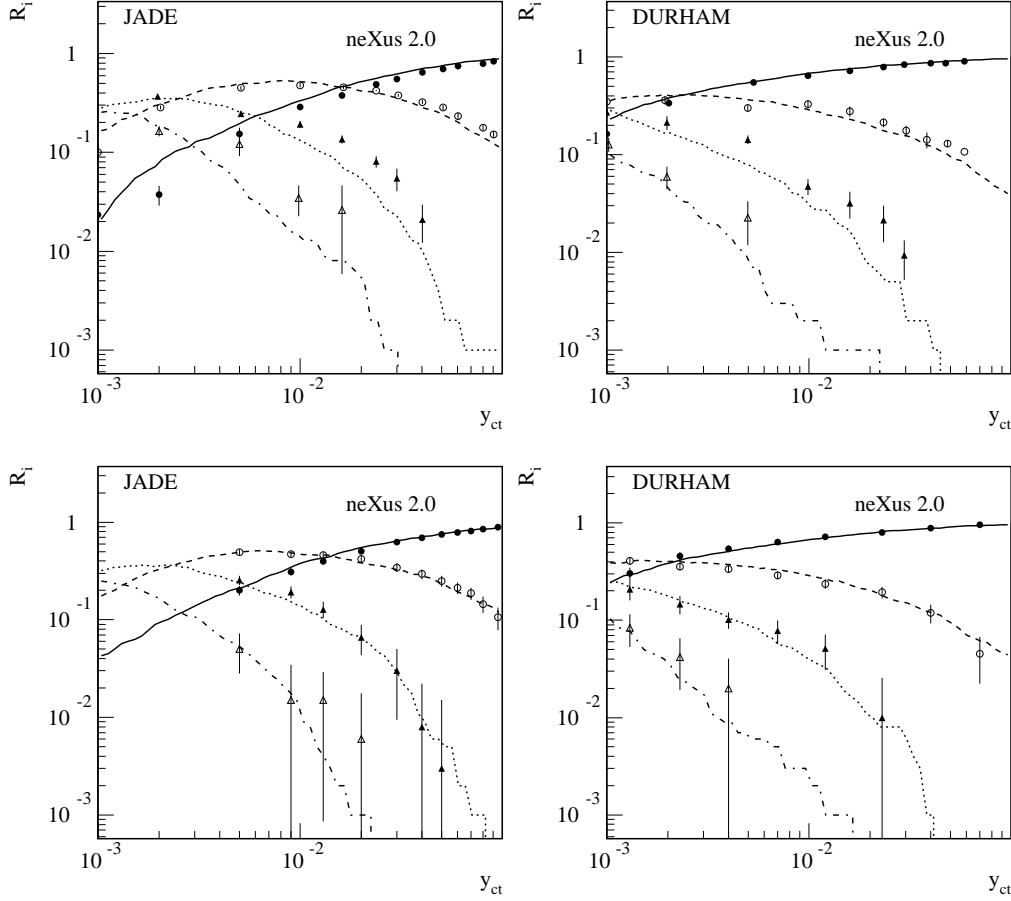


Figure 9.24: Jet rates at 133 GeV (top) et 161 GeV (bottom) for the two algorithms DURHAM and JADE.

historical event.

There are several methods to determine the number of jets in an event, but they are all based on some distance y_{ij} between two particles i and j in momentum space, something like an invariant mass. For the JADE algorithm one defines [42]

$$y_{ij} = \frac{2E_i E_j (1 - \cos \theta_{ij})}{E_{vis}^2}, \quad (9.22)$$

θ_{ij} being the angle between the two particles, and for the algorithm DURHAM one has [43]

$$y_{ij} = \frac{2 \min(E_i^2, E_j^2) (1 - \cos \theta_{ij})}{E_{vis}^2}. \quad (9.23)$$

E_{vis} is the total visible energy of all the particles which contribute to the jet finding. The algorithm works as follows: one determines the pair with the lowest distance y and replaces it with one pseudo-particle having the sum of the momenta of the two particles i and j : $p^\mu = p_i^\mu + p_j^\mu$. One repeats this until all pairs of pseudo-particles have a distance greater than y_{cut} . The number of jets is then the total number of pseudo-particles. Of course, this depends on the choice of y_{cut} . Therefore one displays often the jet multiplicity distribution as a function of y_{cut} .

Let us compare the jet rates for different energies. Fig. 9.23 shows the jet rates for 91.2 GeV, fig. 9.24 for 133 and 161 GeV. The greater is y_{cut} the smaller is the number of jets.

Chapter 10

Testing the Semi-hard Pomeron: Photon-Proton Scattering

It is well known that both photon-proton (γ^*p) scattering and hard processes in proton-proton (pp) collisions can be treated on the basis of perturbative QCD, using the same evolution equations. In both cases, the perturbative partons are finally coupled softly to the proton(s). This provides a very useful consistency check: any model for (semi)hard proton-proton collisions should be applied to photon-proton scattering, where a wealth of data exists, mainly from deep inelastic electron-proton scattering (DIS). In particular the soft coupling to the protons is not calculable from first principles, so photon-proton scattering provides a nice opportunity to test the scheme.

Let us discuss the relation between γ^*p and pp scattering. In figure 10.1, we show the cut

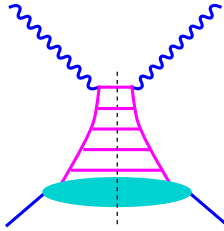


Figure 10.1: The cut diagram representing photon-proton (γ^*p) scattering.

diagram (integrated squared amplitude), representing a contribution to photon-proton scattering: a photon couples to a quark of the proton, where this quark represents the last one in a “cascade” of partons emitted from the nucleon. In the leading logarithmic approximation (LLA) the virtualities of the partons are ordered such that the largest one is close to the photon [9, 8]. Comparing the cut diagram for γ^*p (figure 10.1) with the cut diagram representing a semi-hard elementary proton-proton scattering (figure 10.2), we see immediately that the latter one is essentially made of two γ^*p diagrams, glued together by a Born process. So, understanding γ^*p implies understanding an elementary nucleon-nucleon interaction as well. Actually, probably everybody agrees with this statement, which is nothing but the factorization hypothesis, proved in QCD [44], and the standard procedure to calculate inclusive cross sections in proton-proton scattering amounts to using input from the DIS structure functions. But one can profit much more from studying γ^*p , for example, concerning the production of hadrons. Not being calculable from first principles, the hadronization of parton configurations is a delicate issue in any model for proton-proton (or nucleus-nucleus) scattering. So studying γ^*p provides an excellent possibility to “gauge” the hadronization procedure, such that there is no freedom left on the level of nucleon-nucleon (or nucleus-nucleus)

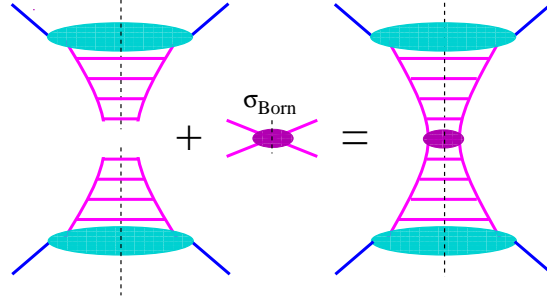


Figure 10.2: The universality hypothesis implies that the upper and the lower part of the Pomeron diagram are identical to the photon-proton diagram.

scattering.

The simple picture, depicted at the fig. 10.1, is correct for large virtualities, but it fails when the photon virtuality becomes small. In that case a virtual photon behaves to a large extent as a hadron and is characterized by some parton content instead of interacting with a proton just as a point-like object. Then the contribution of so-called resolved photon interactions - see fig. 10.3 -

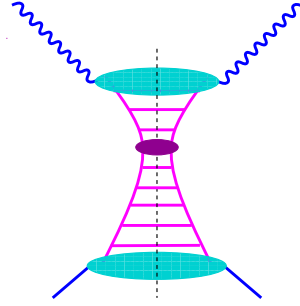


Figure 10.3: The cut diagram representing resolved photon-proton (γ^*p) scattering.

is important and has to be taken into account properly for the description of hadron production in DIS. Only then one may deduce the parton momentum distributions of the proton from the measured virtual photon-proton cross section σ^{γ^*p} .

10.1 Kinematics

In the following, we consider photon-proton collisions in the context of electron-proton scattering. We first recall the basic kinematic variables, see fig. 10.4. We use standard conventions: k , k' , and p are the four-momenta of incoming and outgoing lepton and the target nucleon, $q = k - k'$ is the four-momentum of the photon. Then the photon virtuality is $Q^2 = -q^2$, and one defines the Bjorken x -variable as

$$x_B = \frac{Q^2}{2(pq)}. \quad (10.1)$$

The y -variable is defined as

$$y = \frac{(pq)}{(pk)} = \frac{2(pq)}{s} = \frac{Q^2}{x_B s}, \quad (10.2)$$

which gives the energy fraction of the photon relative to the incident electron in the proton rest frame. In the above formula we used

$$s = (k + p)^2, \quad (10.3)$$

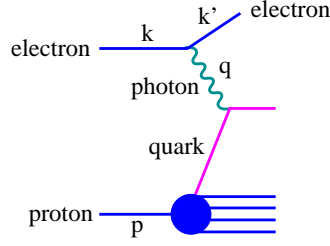


Figure 10.4: Kinematics of electron-proton scattering.

being the total center-of-mass squared energy and neglected the proton and electron masses, $p^2 \simeq 0$, $k^2 \simeq 0$. For the center-of-mass squared energy of photon-proton interaction, we use

$$\hat{s} = (p + q)^2, \quad (10.4)$$

and we finally define the variable

$$\tilde{s} = \hat{s} + Q^2 = 2(pq) = ys, \quad (10.5)$$

which allows to write

$$x_B = \frac{Q^2}{\tilde{s}}. \quad (10.6)$$

It is often convenient to take \tilde{s} and Q^2 as the basic kinematical variables instead of x_B and Q^2 .

10.2 Cross Sections

The differential cross section for deep inelastic electron-proton scattering in the one-photon approximation can be written as [29]

$$\frac{d\sigma^{ep}(s, x_B, Q^2)}{dQ^2 dx_B} = \frac{\alpha}{\pi Q^2 x_B} \left[L_T^\gamma(y) \sigma_T^{\gamma^*p}(\tilde{s}, Q^2) + L_L^\gamma(y) \sigma_L^{\gamma^*p}(\tilde{s}, Q^2) \right], \quad (10.7)$$

where $\sigma_{T(L)}^{\gamma^*p}(\tilde{s}, Q^2)$ are the cross sections for interactions of transversely (longitudinally) polarized photons of virtuality Q^2 with a proton, α is the fine structure constant and factors $L_{T(L)}^\gamma(y)$ define the flux of transversely (longitudinally) polarized photons,

$$L_T^\gamma(y) = \frac{1 + (1 - y)^2}{2} \quad L_L^\gamma(y) = (1 - y). \quad (10.8)$$

The cross sections $\sigma_{T(L)}^{\gamma^*p}(\tilde{s}, Q^2)$ are related to the proton structure functions F_2 , F_L , describing the proton structure as seen by a virtual photon probe, as

$$F_2(x_B, Q^2) = \frac{Q^2}{4\pi^2\alpha} \left[\sigma_T^{\gamma^*p}(\tilde{s}, Q^2) + \sigma_L^{\gamma^*p}(\tilde{s}, Q^2) \right] \quad (10.9)$$

$$F_L(x_B, Q^2) = \frac{Q^2}{4\pi^2\alpha} \sigma_L^{\gamma^*p}(\tilde{s}, Q^2) \quad (10.10)$$

To the leading logarithmic accuracy one has to take into account a number of processes, contributing to $\sigma_{T(L)}^{\gamma^*p}(\tilde{s}, Q^2)$. In the case of transverse polarization of the photon, we have three contributions: the direct coupling of the virtual photon γ^* to a light quark from the proton (“light”), the direct coupling to a charm quark (“charm”), and finally we have a “resolved” contribution, i.e.

$$\sigma_T^{\gamma^*p}(\tilde{s}, Q^2) = \sigma_{T(\text{light})}^{\gamma^*p}(\tilde{s}, Q^2) + \sigma_{T(\text{charm})}^{\gamma^*p}(\tilde{s}, Q^2) + \sigma_{T(\text{resolved})}^{\gamma^*p}(\tilde{s}, Q^2). \quad (10.11)$$

The latter one is becoming essential at small Q^2 and large \tilde{s} . For our study, contributions of beauty and top quarks can be neglected. The longitudinal photon cross section receives leading order contributions only from the direct γ^* -coupling to a charm quark. So we have

$$\sigma_L^{\gamma^* p}(\tilde{s}, Q^2) = \sigma_{L(\text{charm})}^{\gamma^* p}(\tilde{s}, Q^2). \quad (10.12)$$

Again, contributions of beauty and top quarks can be neglected.

Let us list the different contributions. The leading order light quark- γ^* coupling contribution (“light”) can be expressed via the quark momentum distributions in the proton $f_{q/p}(x_B, Q^2)$ as

$$\sigma_{T(\text{light})}^{\gamma^* p}(\tilde{s}, Q^2) = \frac{4\pi^2\alpha}{Q^2} \sum_{i \in \{u, d, s, \bar{u}, \bar{d}, \bar{s}\}} e_i^2 x_B f_{i/p}(x_B, Q^2), \quad (10.13)$$

where e_q^2 is the quark q electric charge squared.

The contributions of heavy quarks can be taken into account via photon-gluon fusion (PGF) process [45],

$$\sigma_{T/L(\text{charm})}^{\gamma^* p}(\tilde{s}, Q^2) = e_c^2 \int dx^- dp_\perp^2 \frac{d\sigma_{T/L}^{\gamma^* g \rightarrow c\bar{c}}(x^- \tilde{s}, Q^2, p_\perp^2)}{dp_\perp^2} f_{g/p}(x^-, M_F^2), \quad (10.14)$$

where $f_{g/p}(x^-, M_F^2)$ is the gluon momentum distribution in the proton at the factorization scale M_F^2 , and where the photon-gluon cross section in lowest order is given as

$$\frac{d\sigma_{T/L}^{\gamma^* g \rightarrow c\bar{c}}(\tilde{s}, Q^2, p_\perp^2)}{dp_\perp^2} = \frac{1}{16\pi\tilde{s}\hat{s}\sqrt{1-4(p_\perp^2+m_c^2)/\hat{s}}} \left| M_{T/L}^{\gamma^* g \rightarrow c\bar{c}}(\tilde{s}, Q^2, p_\perp^2) \right|^2 \quad (10.15)$$

with $\hat{s} = \tilde{s} - Q^2$, and with the corresponding matrix elements squared given as

$$\begin{aligned} \left| M_T^{\gamma^* g \rightarrow c\bar{c}}(\tilde{s}, Q^2, p_\perp^2) \right|^2 &= \pi\alpha\alpha_s \left[\left(\frac{t'}{u'} + \frac{u'}{t'} \right) \frac{Q^4 + \hat{s}^2}{\hat{s}^2} \right. \\ &\quad \left. + \frac{2m_c^2\hat{s}^2}{t'^2u'^2} (Q^2 - 2m_c^2) + \frac{4m_c^2}{t'u'} (\tilde{s} - 2Q^2) \right] \end{aligned} \quad (10.16)$$

$$\left| M_L^{\gamma^* g \rightarrow c\bar{c}}(\tilde{s}, Q^2, p_\perp^2) \right|^2 = 8\pi\alpha\alpha_s \left(\frac{\hat{s}Q^2}{\hat{s}^2} - \frac{m_c^2Q^2}{t'u'} \right) \quad (10.17)$$

Here, the variables t', u' are expressed via standard Mandelstam variables for parton-parton scattering as $t' = t - m_c^2$, $u' = u - m_c^2$. According to [45], the factorization scale M_F^2 has to be chosen irrespectively to the photon virtuality Q^2 to assure the perturbative stability of the result; we use $M_F^2 = p_\perp^2 + m_c^2$, which coincides at large \hat{s} with the virtuality (off-shellness) of the intermediate t -channel c -quark $|t'|$, with $m_c = 1.6$ GeV being the c -quark mass.

In addition, at small Q^2 and large \tilde{s} , the contribution of resolved photon processes becomes important for the production of parton jets of transverse momenta $p_\perp^2 > Q^2$. Here,

$$\begin{aligned} \sigma_{T(\text{resolved})}^{\gamma^* p}(\tilde{s}, Q^2) &= \int dx^+ dx^- dp_\perp^2 \sum_{i,j} \frac{d\sigma_{\text{Born}}^{ij}(x^+ x^- \hat{s}, p_\perp^2)}{dp_\perp^2} \\ &\quad \times f_{i/\gamma^*}(x^+, M_\gamma^2, Q^2) f_{j/p}(x^-, M_p^2) \theta(p_\perp^2 - Q^2) \end{aligned} \quad (10.18)$$

where $\hat{s} = \tilde{s} - Q^2$ is the c.m. energy squared for γ^* -proton interaction, $d\sigma_{\text{Born}}^{ij}/dp_\perp^2$ is the differential partonic cross section, f_{i/γ^*} is the parton momentum distribution in the photon, M_p^2 , M_γ^2 are the factorization scales for the proton and photon correspondingly. As in hadron-hadron scattering, we use $M_p^2 = p_\perp^2/4$, whereas for the photon we take $M_\gamma^2 = 4p_\perp^2$. This requires some more explanation.

To the leading order accuracy, the factorization scales are rather undefined as the difference between the results, obtained for different scale choices, is due to higher order corrections. The scheme would be scale independent only after summing up all order contributions both in the structure functions and in the partonic cross section. High p_\perp jet production in γ^* -proton interaction is known to obtain essential contributions from next to leading order (NLO) direct processes [46]. As it was shown in [46], the sum of the leading order resolved γ^* -proton cross section and the NLO direct one exhibits a remarkable independence on the scale M_γ^2 for the production of parton jets with $p_\perp > Q$, where Q is the photon virtuality. So our strategy is to choose M_γ^2 such that it allows to represent effectively the full contribution by the leading order resolved cross section.

10.3 Parton Momentum Distributions

The cross sections mentioned in the preceding section are all expressed via the so-called parton distribution functions $f_{i/a}$, representing the momentum fraction distribution of parton i inside particle a (proton or photon). In this section, we are going to discuss these distribution functions.

We are first discussing parton distribution functions of the proton. They are represented by the hadronic part of the photon-proton diagram, i.e. the diagram without the external photon line. As mentioned before, this diagram is also a building block of one of the elementary diagrams of pp scattering, and one can therefore repeat literally the argumentation of the chapter 2. In pp scattering, we have (apart of the soft one) four contributions, since on each side the parton ladder couples to the nucleon either via a soft Pomeron or it connects directly to a valence quark. In addition, there is a triple Pomeron diagram. Corresponding we have here three contributions, referred to as “sea”, “triple Pomeron”, and “valence”.

The Sea Contribution

The sea contribution contains the perturbative parton cascade, described as a parton ladder with strictly ordered virtualities, and the non-perturbative soft block, dominated by the soft Pomeron asymptotics, see fig. 10.5. We obtain the momentum distribution $f_{i/p(\text{sea})}^{1\text{P}}(x, M_F^2)$ of the parton

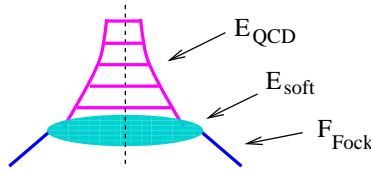


Figure 10.5: The diagram corresponding to the parton distribution functions.

i at the virtuality scale M_F^2 in the proton as the convolution of three distributions (see fig. 10.5): the inclusive parton Fock state distribution in the proton $\tilde{F}_p^{(1)}(x_0)$ (see eq. (C.18)),

$$\tilde{F}_p^{(1)}(x_0) = F_{\text{remn}}^p(1 - x_0) F_{\text{part}}^p(x_0), \quad (10.19)$$

the distribution for the parton momentum share in the soft Pomeron $E_{\text{soft}}^j(z)$ (see eqs. (B.21-B.22)), and the QCD evolution function $E_{\text{QCD}}^{ji}(z, Q_0^2, M_F^2)$:

$$f_{i/p(\text{sea})}^{1\text{P}}(x, M_F^2) = \sum_j \int_x^1 \frac{dx_0}{x_0} \int_x^{x_0} \frac{dx_1}{x_1} \times \tilde{F}_p^{(1)}(x_0) E_{\text{soft}}^j\left(\frac{x_1}{x_0}\right) E_{\text{QCD}}^{ji}\left(\frac{x}{x_1}, Q_0^2, M_F^2\right), \quad (10.20)$$

see fig. 10.5. This equation may be written as

$$f_{i/p(\text{sea})}^{1\text{IP}}(x, M_F^2) = \sum_j \int_x^1 \frac{dx_1}{x_1} \varphi_{j/p(\text{sea})}^{1\text{IP}}(x_1) E_{\text{QCD}}^{ji}\left(\frac{x}{x_1}, Q_0^2, M_F^2\right), \quad (10.21)$$

where $\varphi_{j/p(\text{sea})}^{1\text{IP}}(x_1)$ by construction corresponds to the distribution at the initial scale Q_0^2 ,

$$\varphi_{j/p(\text{sea})}^{1\text{IP}}(x_1) = \int_{x_1}^1 \frac{dx_0}{x_0} \tilde{F}_p^{(1)}(x_0) E_{\text{soft}}^j\left(\frac{x_1}{x_0}\right) \quad (10.22)$$

Here we use the same expressions for $F_{\text{remn}}^p(x)$, $F_{\text{part}}^p(x)$, and $E_{\text{soft}}^j(z)$ as in the case of proton-proton or nucleus-nucleus scattering, see eqs. (C.20-C.21), (B.21-B.22).

The Triple Pomeron Contribution

We have to take also into account triple-Pomeron contributions $f_{i/p(\text{sea})}^{3\text{IP}}(x, M_F^2)$ to gluon and sea quark momentum distributions. The latter ones are defined by the diagrams of fig. 5.6 with the upper cut Pomeron being replaced by the “half” of the sea-sea type semihard Pomeron which consists from a soft Pomeron coupled to the triple-Pomeron vertex and the parton ladder describing the perturbative parton evolution from the initial scale Q_0^2 to the final scale M_F^2 , see fig. 10.6. The lower legs are (un)cut Pomerons.

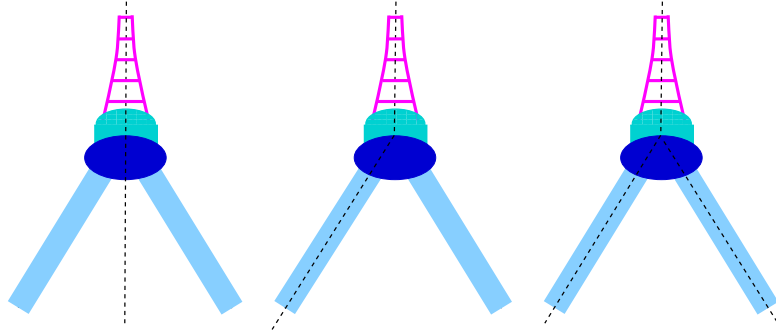


Figure 10.6: The triple Pomeron contribution.

Let us consider the part $\Delta\sigma_{pp(\text{sea-sea})}^{3\text{IP}-}(s)$ of the contribution of cut triple-Pomeron diagram

$$\Delta\sigma_{pp}^{3\text{IP}-}(s) = \frac{1}{2s} 2\text{Im} T_{pp}^{3\text{IP}-}(s, t=0),$$

corresponding to the semihard sea-sea type parton-parton scattering in the upper Pomeron, which is according to eqs. (5.5-5.6) given as

$$\begin{aligned} \Delta\sigma_{pp(\text{sea-sea})}^{3\text{IP}-}(s) &= -\frac{r_{3\text{IP}}}{2} \text{Im} \left[\int_0^1 dx^+ \int_0^1 dx_1^- \int_0^{1-x_1^-} dx_2^- F_{\text{remn}}^p(1-x^+) F_{\text{remn}}^p(1-x_1^- - x_2^-) \right. \\ &\quad \times 8\pi^2 \int \frac{dx_{12}^-}{x_{12}^-} \left[\frac{1}{2s^+} \text{Im} T_{\text{sea-sea}}^p(x^+, s^+, 0) \right] \\ &\quad \times \left. \int dz^+ \int d^2 q_{1\perp} \prod_{l=1}^2 \left[\frac{1}{8\pi^2 \hat{s}_l} iT^p(x_l^-, \hat{s}_l, -q_{1\perp}^2) \right] \right], \end{aligned} \quad (10.23)$$

where we used $x_{12}^- = s_0/(x_{12}^+ s)$, $s^+ = x^+ x_{12}^- s$, $\hat{s}_1 = z^+ s_0 x_1^- / x_{12}^-$, $\hat{s}_2 = (1 - z^+) s_0 x_2^- / x_{12}^-$, and T^p , $T_{\text{sea-sea}}^p$ are defined in (5.15-5.17). Applying the AGK cutting rules, the contribution (10.23) can be written as a sum of three terms,

$$\Delta\sigma_{pp(\text{sea-sea})}^{3\text{IP}-}(s) = \Delta\sigma_{pp(\text{sea-sea})}^{3\text{IP}-(0)}(s) + \Delta\sigma_{pp(\text{sea-sea})}^{3\text{IP}-(1)}(s) + \Delta\sigma_{pp(\text{sea-sea})}^{3\text{IP}-(2)}(s), \quad (10.24)$$

corresponding to the diffractive type semihard interaction, screening correction to the usual semihard interaction, and double cut Pomeron contribution, with the weights

$$\Delta\sigma_{pp(\text{sea-sea})}^{3\text{IP}-(0)}(s) = -1 \times \Delta\sigma_{pp(\text{sea-sea})}^{3\text{IP}-}(s) \quad (10.25)$$

$$\Delta\sigma_{pp(\text{sea-sea})}^{3\text{IP}-(1)}(s) = +4 \times \Delta\sigma_{pp(\text{sea-sea})}^{3\text{IP}-}(s) \quad (10.26)$$

$$\Delta\sigma_{pp(\text{sea-sea})}^{3\text{IP}-(2)}(s) = -2 \times \Delta\sigma_{pp(\text{sea-sea})}^{3\text{IP}-}(s) \quad (10.27)$$

Making use of (5.16), (B.20), (2.15), we have

$$\begin{aligned} \frac{1}{2s^+} \text{Im } T_{\text{sea-sea}}^p(x^+, s^+, 0) &= \frac{1}{2} F_{\text{part}}^p(x^+) \sum_{jk} \int_0^1 \frac{dz_1^+}{z_1^+} \frac{dz_1^-}{z_1^-} E_{\text{soft}}^j(z_1^+) E_{\text{soft}}^k(z_1^-) \\ &\times \sum_{ml} \int_{z_1^+}^1 dz_B^+ \int_{z_1^-}^1 dz_B^- \int dp_{\perp}^2 E_{\text{QCD}}^{jm}(z_B^+/z_1^+, Q_0^2, M_F^2) E_{\text{QCD}}^{kl}(z_B^-/z_1^-, Q_0^2, M_F^2) \\ &\times K \frac{d\sigma_{\text{Born}}^{ml}}{dp_{\perp}^2}(z_B^+ z_B^- s^+, p_{\perp}^2) \theta(M_F^2 - Q_0^2) \end{aligned} \quad (10.28)$$

Now, using (10.19-10.20), we can rewrite (10.23) as

$$\begin{aligned} \Delta\sigma_{pp(\text{sea-sea})}^{3\text{IP}-}(s) &= \sum_{ml} \int dx_B^+ dx_B^- dp_{\perp}^2 f_{m/p(\text{sea})}^{1\text{IP}}(x_B^+, M_F^2) f_{l/p(\text{sea})}^{3\text{IP}}(x_B^-, M_F^2) \\ &\times K \frac{d\sigma_{\text{Born}}^{ml}}{dp_{\perp}^2}(x_B^+ x_B^- s, p_{\perp}^2) \theta(M_F^2 - Q_0^2), \end{aligned} \quad (10.29)$$

where we denoted

$$x_B^+ = x^+ z_B^+, \quad x_B^- = z_B^- \frac{s_0}{x_{12}^+ s},$$

and defined

$$f_{i/p(\text{sea})}^{3\text{IP}}(x, M_F^2) = \sum_j \int_x^1 \frac{dx_1}{x_1} \varphi_{j/p(\text{sea})}^{3\text{IP}}(x_1) E_{\text{QCD}}^{ji}\left(\frac{x}{x_1}, Q_0^2, M_F^2\right), \quad (10.30)$$

with

$$\begin{aligned} \varphi_{j/p(\text{sea})}^{3\text{IP}}(x) &= -\frac{r_{3\text{IP}}}{2} \int_x^1 \frac{dx_{12}}{x_{12}} E_{\text{soft}}^j\left(\frac{x}{x_{12}}\right) \int dx_1 dx_2 F_{\text{remn}}^p(1 - x_1 - x_2) \\ &\times 4\pi^2 \int dz \int d^2 q_{\perp} \text{Im} \left[\prod_{l=1}^2 \left[\frac{1}{8\pi^2 \hat{s}_l} iT^p(x_l, \hat{s}_l, -q_{\perp}^2) \right] \right] \\ &= -\frac{r_{3\text{IP}}}{8} \int_x^1 \frac{dx_{12}}{x_{12}} E_{\text{soft}}^j\left(\frac{x}{x_{12}}\right) \int dx_1 dx_2 F_{\text{remn}}^p(1 - x_1^- - x_2^-) \\ &\times \int d^2 b \int dz G^p(x_1, \hat{s}_1, b) G^p(x_2, \hat{s}_2, b), \end{aligned} \quad (10.31)$$

with $\hat{s}_1 = z s_0 x_1 / x_{12}$, $\hat{s}_2 = (1 - z) s_0 x_2 / x_{12}$, where $G^p(x, \hat{s}, b)$ is given in (5.33-5.36).

Now, replacing in (10.29) the interaction with the projectile parton m by the interaction with a virtual photon probe of virtuality M_F^2 or by the interaction with a hypothetical probe which couples directly to a gluon, we immediately see that $f_{i/p(\text{sea})}^{3\text{IP}}(x, M_F^2)$ defines the (negative) contribution of the triple-Pomeron diagram to parton structure functions.

The Valence Contribution

The third contribution, referred to as “valence”, amounts to the case where a valence quark is the first parton of the ladder, see fig. 10.7. Here, the soft pre-evolution, governed by the sec-

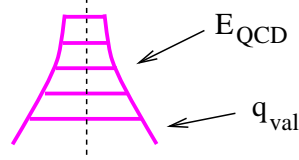


Figure 10.7: The diagram corresponding to the “valence” contribution to the parton distribution functions.

ondary Reggeon, is typically short and therefore not considered explicitly. One simply uses the parameterized input for valence quark momentum distributions at the initial scale Q_0^2 ,

$$\varphi_{i/p(\text{val})}(x_1) = q_{\text{val}}^i(x_1, Q_0^2) \quad (10.32)$$

with the Gluck-Reya-Vogt parameterization for $q_{\text{val}}^i(x, Q_0^2)$ [47].

The Complete Proton Distribution Function

The total parton distribution in the proton at the initial scale Q_0^2 is then defined as

$$\varphi_{i/p}(x_1) = \varphi_{i/p(\text{sea})}(x_1) + \varphi_{i/p(\text{val})}(x_1), \quad (10.33)$$

with

$$\varphi_{i/p(\text{sea})}(x_1) = \varphi_{i/p(\text{sea})}^{\text{1P}}(x_1) + \varphi_{i/p(\text{sea})}^{\text{3P}}(x_1) \quad (10.34)$$

which results for an arbitrary scale M_F^2 in

$$f_{i/p}(x, M_F^2) = \sum_j \int \frac{dx_1}{x_1} \varphi_{i/p}(x_1) E_{\text{QCD}}^{ji} \left(\frac{x}{x_1}, Q_0^2, M_F^2 \right). \quad (10.35)$$

For $M_F^2 = Q_0^2$, the semi-hard contribution is a function which peaks at very small values of x and then decreases monotonically towards zero for $x = 1$. The valence contribution, on the other hand, has a maximum at large values of x and goes towards zero for small values of x . For moderate values of M_F^2 , the precise form of f depends crucially on the exponent for the Pomeron-nucleon coupling α_{part} , whereas for large M_F^2 it is mainly defined by the QCD evolution and depends weakly on the initial conditions at the scale Q_0^2 .

The Photon Distribution Functions

To calculate the resolved photon cross section (10.18), one needs also to know parton momentum distributions of a virtual photon $f_{i/\gamma^*}(x, M_\gamma^2, Q^2)$. According to [48], f_{i/γ^*} gets contributions both from vector meson states of the photon and from perturbative point-like photon splitting into a quark-anti-quark pair,

$$f_{i/\gamma}(x, M_\gamma^2, Q^2) = f_{i/\gamma}^{\text{VDM}}(x, M_\gamma^2, Q^2) + f_{i/\gamma}^{\text{point}}(x, M_\gamma^2, Q^2). \quad (10.36)$$

For the former one, one has [48]

$$f_{i/\gamma}^{\text{VDM}}(x, M_\gamma^2, Q^2) = \eta(Q^2) \alpha \left[G_i^2 f_{i/\pi^0}(x, M_\gamma^2) + \frac{1}{2} \delta_i (G_u^2 - G_d^2) f_{s/\pi^0}(x, M_\gamma^2) \right], \quad (10.37)$$

where the function η is given as

$$\eta(Q^2) = (1 + Q^2/m_\rho^2)^{-2}, \quad (10.38)$$

with $m_\rho^2 = 0.59 \text{ GeV}^2$ and with

$$\begin{aligned} \delta_u &= -1, & \delta_d &= 1, & \delta_s &= 0, & \delta_g &= 0, \\ G_u^2 &= 0.836, & G_d^2 &= 0.250, & G_s^2 &= 0.543, & G_g^2 &= 0.543. \end{aligned} \quad (10.39)$$

Pion structure functions f_{i/π^0} are defined in the same way as proton ones, namely

$$f_{i/\pi^0}(x, M_F^2) = \sum_j \int \frac{dx_1}{x_1} \varphi_{i/\pi^0}(x_1) E_{\text{QCD}}^{ji} \left(\frac{x}{x_1}, Q_0^2, M_F^2 \right), \quad (10.40)$$

with

$$\varphi_{i/\pi^0}(x_1) = \varphi_{i/\pi(\text{sea})}(x_1) + \varphi_{i/\pi^0(\text{val})}(x_1), \quad (10.41)$$

Here $\varphi_{i/\pi^0(\text{val})}$ is a parameterized initial distribution for the valence component from [49]

$$\varphi_{i/\pi^0(\text{val})}(x_1) = q_{\text{val}/\pi^0}^i(x_1, Q_0^2), \quad (10.42)$$

and the sea component $\varphi_{j/\pi(\text{sea})}$ is given by the formulas (10.33-10.34), (10.22), (10.31), (10.32) with the subscript p being replaced by π and using the appropriate parameters α_{remn}^π , γ_π in F_{part}^π , F_{remn}^π , but keeping all other parameters, characterizing the Pomeron trajectory, unchanged compared to proton case.

The point-like contribution $f_{i/\gamma}^{\text{point}}$ is given as a convolution of the photon splitting into a quark-anti-quark pair (with the Altarelli-Parisi splitting function $P^{\gamma \rightarrow q\bar{q}}(z) = N_c/2 (z^2 + (1-z)^2)$, $N_c = 3$ being the number of colors), followed by the QCD evolution of a (anti-)quark from the initial virtuality q^2 of the splitting till the scale M_γ^2

$$\begin{aligned} f_{i/\gamma}^{\text{point}}(x, M_\gamma^2, Q^2) &= \langle e_q^2 \rangle \int \frac{dq^2}{q^2} \int_x^1 \frac{dx_\gamma}{x_\gamma} \frac{\alpha}{2\pi} P^{\gamma \rightarrow q\bar{q}}(x_\gamma) \\ &\times \sum_{j \in \{u, d, s, \bar{u}, \bar{d}, \bar{s}\}} E_{\text{QCD}}^{ji} \left(\frac{x}{x_\gamma}, q^2, M_\gamma^2 \right) \Theta(q^2 - \max[Q_0^2, x_\gamma Q^2]) \end{aligned} \quad (10.43)$$

with x_γ being the share of the virtual photon light cone momentum taken by the (anti-)quark and with

$$\langle e_q^2 \rangle = \frac{1}{3} (e_u^2 + e_d^2 + e_s^2) \quad (10.44)$$

being the average light quark charge squared. Here we have chosen the initial scale for the QCD evolution of a t -channel (anti-)quark to be equal to its initial virtuality $q^2 = x_\gamma Q^2 + p_\perp^2/(1-x_\gamma)$, with p_\perp^2 being the transverse momentum squared for the splitting in the γ^*p center of mass system [50].

10.4 The Structure Function F_2

We have now all elements to calculate the structure function F_2 , based on the formula (10.9), with all leading order contributions to $\sigma_{T(L)}^{\gamma^*p}$ as given in eqs. (10.11-10.18) and with the parton momentum distributions in the proton and photon as discussed in the preceding section. The results for $F_2(x, Q^2)$ are shown in fig. 10.8 together with experimental data from H1 [51], ZEUS [52] and NMC [53]. The parameters affecting the results for F_2 are actually the same ones which affect parton-parton and hadron-hadron scattering. So we fix them in order to have an overall

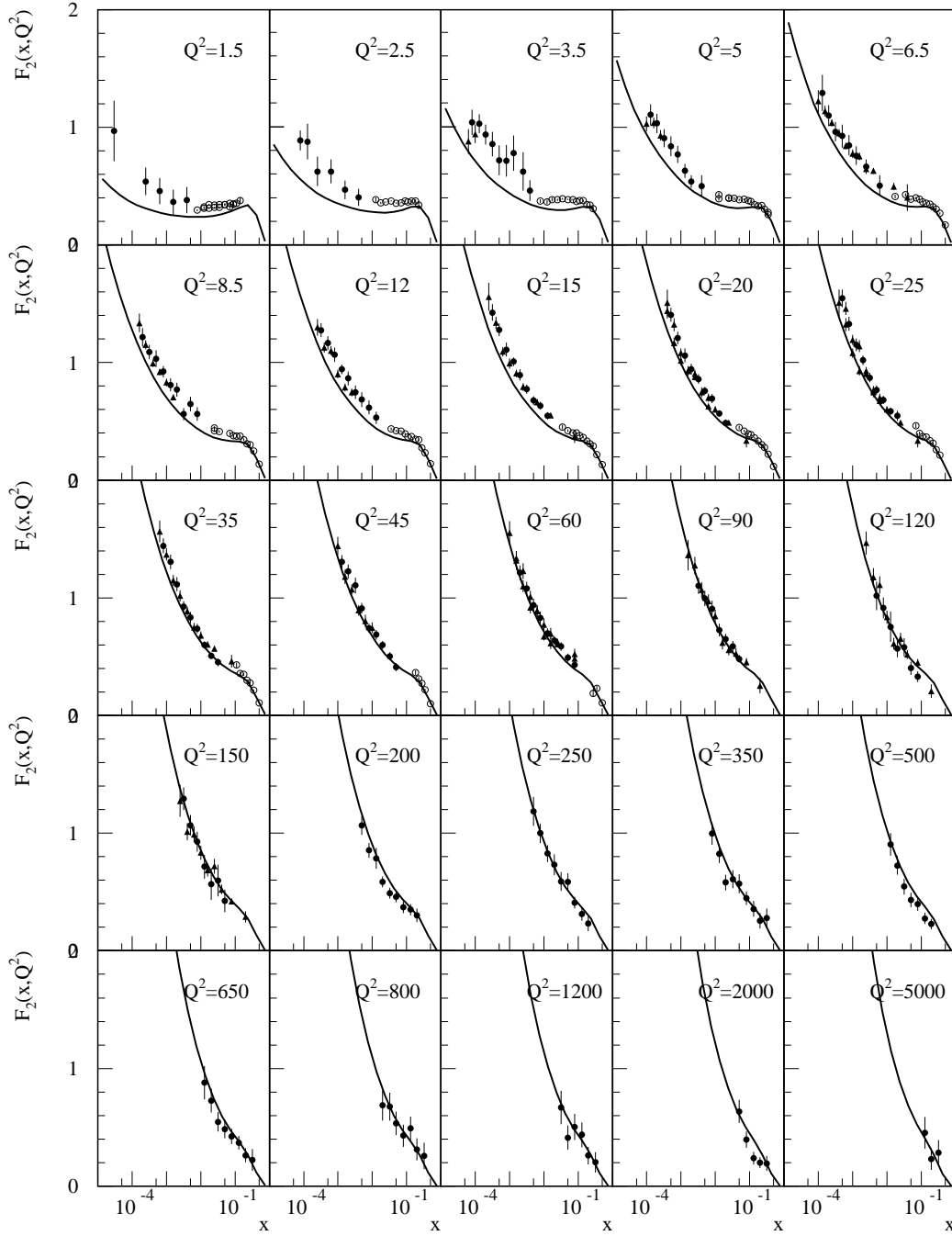


Figure 10.8: The structure function F_2 for different values of Q^2 together with experimental data from H1 [51], ZEUS [52] and NMC [53].

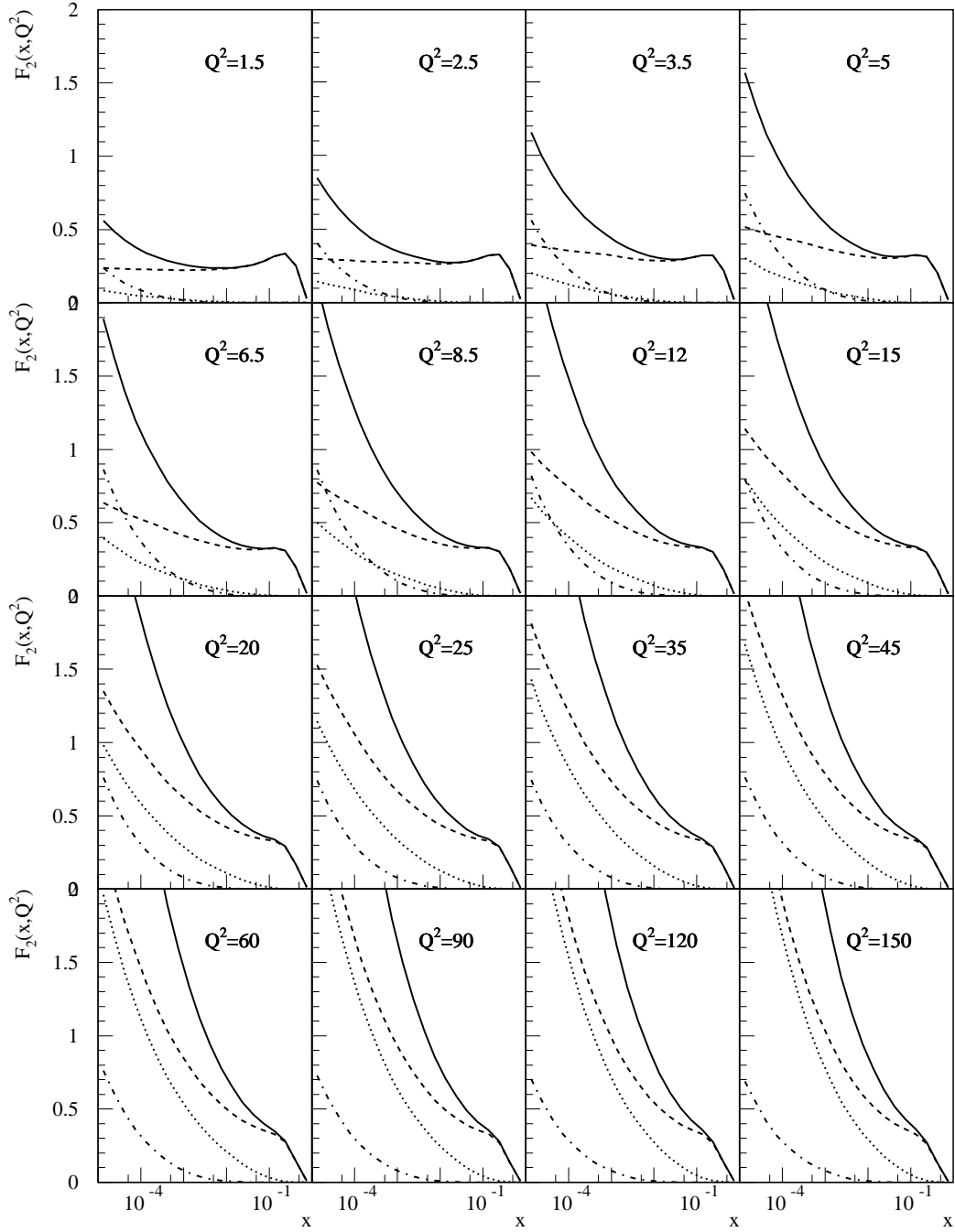


Figure 10.9: Same as fig. 10.8, but here we show separately the “direct-light” contribution (dashed), the “direct-charm” contribution (dotted), and the “resolved” contribution (dashed-dotted).

good fit for F_2 and at the same time the energy dependence of the total cross section and of the slope parameter. It is possible to get a reasonable agreement, which is of course not perfect due to the fact that enhanced diagrams are only treated to lowest order. In fig. 10.9, we show separately the direct light quarks contribution (10.13), as well as the ones of charm quarks (10.14) and of resolved photons (10.18), for $Q^2 = 1.5 \text{ GeV}^2$, 5 GeV^2 , and 25 GeV^2 . It is easy to see that the resolved photon cross section contributes significantly to $F_2(x, Q^2)$ for small photon virtualities Q^2 .

10.5 Parton Configurations: Basic Formulas

In order to have a coherent approach, we base our treatment of particle production on exactly the same formulas as derived earlier for the cross sections. To be more precise, we take the formulas for $d\sigma/dx_B dQ^2$ as a basis for treating particle production, which means first of all parton production.

The differential cross section for lepton-nucleon scattering is given in eq. (10.7). Using (B.28), (B.30), the QCD evolution function E_{QCD}^{ij} , which enters into the formulas for the cross sections $\sigma_{T(L)}^{\gamma^* p}(\bar{s}, Q^2)$, can be expanded as a sum over n -rung ladder contributions, where the latter ones can be written as an integration over the momenta p_1, p_2, \dots, p_n of n resolvable final partons. Introducing a multidimensional variable

$$P = \{p_1, p_2, \dots, p_n\}, \quad (10.45)$$

and considering the symbol \sum_P representing $\sum_n \int dP_n$, with dP_n being the invariant phase space volume for n -parton state, we may write

$$\frac{d\sigma_{lp}}{dx_B dQ^2} = \sum_P \sigma(x_B, Q^2, P). \quad (10.46)$$

After normalization, $\sigma(x_B, Q^2, P)$ may be interpreted as the probability distribution for a parton configuration P for given values of x_B and Q^2 . The Monte Carlo method provides a convenient tool for treating such multidimensional distributions: with $\sigma(x_B, Q^2, P)$ being known (see preceding sections), one generates parton configurations P according to this distribution. In addition to x_B , Q^2 , and P , additional variables occur, specifying a particular contribution to the DIS cross section. One essentially follows the structure of the formula for the cross section. Let us discuss the procedure to generate parton configurations in detail.

We start with some useful definitions. Using the relation (B.28) for the evolution function E_{QCD}^{ij} , any parton momentum distribution at the scale Q^2 can be decomposed into two contributions, corresponding to the case of no resolvable emission in the range of virtualities between Q_0^2 and Q^2 and to at least one resolvable emission:

$$f_j(x, Q^2) = f_j(x, Q_0^2) \Delta^j(Q_0^2, Q^2) + \sum_i \int_x^{1-\epsilon} \frac{dz}{z} \bar{E}_{QCD}^{ij}(z, Q_0^2, Q^2) f_i\left(\frac{x}{z}, Q_0^2\right) \quad (10.47)$$

In case of “ i ” and “ j ” being quarks, we split the sum $\sum_j \bar{E}_{QCD}^{ij}$ into two components,

$$\sum_j \bar{E}_{QCD}^{ij} = \bar{E}_{NS} + \bar{E}_S \quad (i, j = \text{quarks}), \quad (10.48)$$

with the so-called non-singlet evolution \bar{E}_{NS} , where only gluons are emitted as final s -channel partons, and the singlet evolution \bar{E}_S representing all the other contributions, see fig. 10.10a,c. The non-singlet evolution (compare with eq. (B.29)) satisfies the evolution equation

$$\begin{aligned} \bar{E}_{NS}(x, Q_0^2, Q^2) = & \quad (10.49) \\ & \int_{Q_0^2}^{Q^2} \frac{dQ_1^2}{Q_1^2} \left[\int_x^{1-\epsilon} \frac{dz}{z} \frac{\alpha_s}{2\pi} P_q^q(z) \bar{E}_{NS}\left(\frac{x}{z}, Q_0^2, Q_1^2\right) \Delta^q(Q_1^2, Q^2) + \frac{\alpha_s}{2\pi} P_q^q(x) \Delta^q(Q_0^2, Q^2) \right], \end{aligned}$$

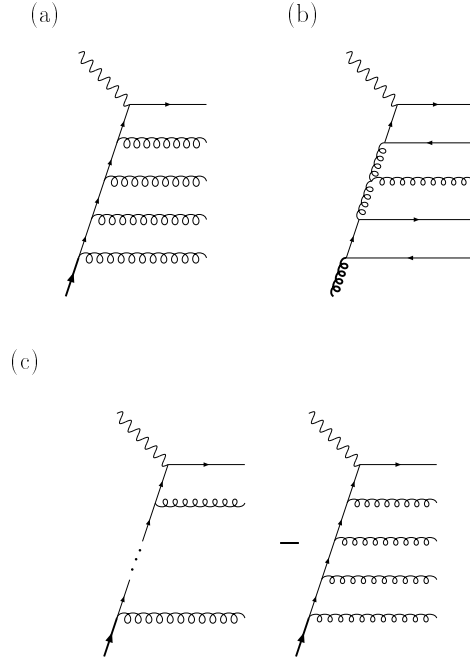


Figure 10.10: The non-singlet contribution (a), the gluon contribution (b), and the singlet contribution (c).

and the singlet one

$$\bar{E}_S(x, Q_0^2, Q^2) = \int_{Q_0^2}^{Q^2} \frac{dQ_1^2}{Q_1^2} \int_x^{1-\epsilon} \frac{dz}{z} \frac{\alpha_s}{2\pi} \left[P_q^q(z) \bar{E}_S\left(\frac{x}{z}, Q_0^2, Q_1^2\right) + 2n_f P_g^q(z) \bar{E}_{\text{QCD}}^{qg}\left(\frac{x}{z}, Q_0^2, Q_1^2\right) \right] \Delta^q(Q_1^2, Q^2), \quad (10.50)$$

with $n_f = 3$ being the number of active quark flavors.

Now it is convenient to define parton level cross sections, corresponding to different contributions to the deep inelastic scattering process and to different partons, entering the perturbative evolution at the initial scale Q_0^2 , see fig. 10.10. Essentially, we include into the cross sections the perturbative part of parton evolution, whereas the initial conditions, given by parton momentum densities at the initial scale Q_0^2 , are factorized out. The non-singlet and singlet contributions to the direct (light) photon-quark interaction are defined as

$$\sigma_{T(\text{NS})}^{\gamma^* q}(\tilde{s}, Q^2, Q_0^2) = \frac{4\pi^2\alpha}{\tilde{s}} \bar{E}_{\text{NS}}\left(\frac{Q^2}{\tilde{s}}, Q_0^2, Q^2\right) \quad (10.51)$$

$$\sigma_{T(\text{S})}^{\gamma^* q}(\tilde{s}, Q^2, Q_0^2) = \frac{4\pi^2\alpha}{\tilde{s}} \bar{E}_S\left(\frac{Q^2}{\tilde{s}}, Q_0^2, Q^2\right) \quad (10.52)$$

For the direct (light) photon-gluon interaction, we define

$$\sigma_{T(\text{light})}^{\gamma^* g}(\tilde{s}, Q^2, Q_0^2) = \frac{4\pi^2\alpha}{\tilde{s}} \bar{E}_{\text{QCD}}^{gq}\left(\frac{Q^2}{\tilde{s}}, Q_0^2, Q^2\right) \quad (10.53)$$

The photon-parton charm production cross section is defined as

$$\sigma_{T/L(\text{charm})}^{\gamma^* i}(\tilde{s}, Q^2, Q_0^2) = \int dx^- \int dp_\perp^2 E_{\text{QCD}}^{ig}(x^-, Q_0^2, M_F^2) \frac{d\sigma_{T/L}^{\gamma^* g \rightarrow c\bar{c}}(x^- \tilde{s}, Q^2, p_\perp^2)}{dp_\perp^2}, \quad (10.54)$$

where the parton (i) may be a quark or a gluon. Finally, we define the parton-parton cross section for resolved processes similarly to (6.7) as

$$\begin{aligned} \sigma_{T(\text{resolved})}^{ij}(\hat{s}, Q^2, q^2, Q_0^2) &= \int dx^+ dx^- \int dp_\perp^2 \sum_{k,l} \frac{d\sigma_{\text{Born}}^{kl}(x^+ x^- \hat{s}, p_\perp^2)}{dp_\perp^2} \\ &\times E_{\text{QCD}}^{ik}(x^+, q^2, M_\gamma^2) E_{\text{QCD}}^{jl}(x^-, Q_0^2, M_p^2) \theta(p_\perp^2 - Q^2). \end{aligned} \quad (10.55)$$

Based on the above partial photon-parton cross sections, we define now the total photon-parton cross sections, summed over the quark flavors of the quark coupling to the photon with the appropriate squared charge (e^2) factor. We obtain for the photon-gluon cross section

$$\begin{aligned} \sigma_T^{\gamma^*g}(\tilde{s}, Q^2, Q_0^2) &= \langle e_q^2 \rangle \sigma_{T(\text{light})}^{\gamma^*g}(\tilde{s}, Q^2, Q_0^2) + e_c^2 \sigma_{T(\text{charm})}^{\gamma^*g}(\tilde{s}, Q^2, Q_0^2) \\ &+ \sum_j \int dx_\gamma f_{j/\gamma}^{\text{VDM}}(x_\gamma, Q_0^2, Q^2) \sigma_{T(\text{resolved})}^{jg}(x_\gamma(\tilde{s} - Q^2), Q^2, Q_0^2, Q_0^2) \\ &+ \langle e_q^2 \rangle \int \frac{dq^2}{q^2} \int dx_\gamma \frac{\alpha}{2\pi} P^{\gamma \rightarrow q\bar{q}}(x_\gamma) \\ &\times \sum_{j \in \{u, d, s, \bar{u}, \bar{d}, \bar{s}\}} \sigma_{T(\text{resolved})}^{jg}(x_\gamma \tilde{s} - q^2, Q^2, q^2, Q_0^2) \Theta(q^2 - \max[Q_0^2, x_\gamma Q^2]). \end{aligned} \quad (10.56)$$

The photon-quark cross section for a quark with flavor “ i ” is given as

$$\begin{aligned} \sigma_T^{\gamma^*i}(\tilde{s}, Q^2, Q_0^2) &= e_i^2 \sigma_{T(\text{NS})}^{\gamma^*q}(\tilde{s}, Q^2, Q_0^2) + \langle e_q^2 \rangle \sigma_{T(\text{S})}^{\gamma^*q}(\tilde{s}, Q^2, Q_0^2) \\ &+ e_c^2 \sigma_{T(\text{charm})}^{\gamma^*g}(\tilde{s}, Q^2, Q_0^2) \\ &+ \sum_j \int dx_\gamma f_{j/\gamma}^{\text{VDM}}(x_\gamma, Q_0^2, Q^2) \sigma_{T(\text{resolved})}^{ji}(x_\gamma(\tilde{s} - Q^2), Q^2, Q_0^2, Q_0^2) \\ &+ \langle e_q^2 \rangle \int \frac{dq^2}{q^2} \int dx_\gamma \frac{\alpha}{2\pi} P^{\gamma \rightarrow q\bar{q}}(x_\gamma) \\ &\times \sum_{j \in \{u, d, s, \bar{u}, \bar{d}, \bar{s}\}} \sigma_{T(\text{resolved})}^{ji}(x_\gamma \tilde{s} - q^2, Q^2, q^2, Q_0^2) \Theta(q^2 - \max[Q_0^2, x_\gamma Q^2]) \end{aligned} \quad (10.57)$$

The longitudinal photon-parton cross section for a parton of flavor i (quark or gluon) is finally given as

$$\sigma_L^{\gamma^*i}(\tilde{s}, Q^2, Q_0^2) = e_c^2 \sigma_{L(\text{charm})}^{\gamma^*i}(\tilde{s}, Q^2, Q_0^2). \quad (10.58)$$

Finally, we may express the photon-proton cross sections in terms of the above photon-parton cross sections and the parton distribution functions $\varphi(x) = f(x, Q_0^2)$ at the scale Q_0^2 . The transverse cross section is given as

$$\begin{aligned} \sigma_T^{\gamma^*p}(\tilde{s}, Q^2) &= \int dx_1 \varphi_{g/p}(x_1) \sigma_T^{\gamma^*g}(x_1 \tilde{s}, Q^2, Q_0^2) \\ &+ \sum_{i \in \{u, d, s, \bar{u}, \bar{d}, \bar{s}\}} \left(\frac{4\pi^2 \alpha}{Q^2} e_i^2 x_B \varphi_{i/p}(x_B) \Delta^q(Q_0^2, Q^2) + \int dx_1 \varphi_{i/p}(x_1) \sigma_T^{\gamma^*i}(x_1 \tilde{s}, Q^2, Q_0^2) \right), \end{aligned} \quad (10.59)$$

the longitudinal cross section is given as

$$\begin{aligned} \sigma_L^{\gamma^*p}(\tilde{s}, Q^2) &= \int dx_1 \varphi_{g/p}(x_1) \sigma_L^{\gamma^*g}(x_1 \tilde{s}, Q^2, Q_0^2) \\ &+ \sum_{i \in \{u, d, s, \bar{u}, \bar{d}, \bar{s}\}} \int dx_1 \varphi_{i/p}(x_1) \sigma_L^{\gamma^*i}(x_1 \tilde{s}, Q^2, Q_0^2), \end{aligned} \quad (10.60)$$

with the quark momentum distributions being a sum of two terms,

$$\varphi_{i/p}(x_1) = \varphi_{i/p(\text{sea})}(x_1) + \varphi_{i/p(\text{val})}(x_1), \quad (10.61)$$

see eqs. (10.22-10.33).

The above formulas together with eq. (10.7) serve as the basis to generate all main variables for the description of deep inelastic scattering. After modeling Q^2 and x_B we simulate types (a valence quark, a sea quark, or a gluon) and kinematical characteristics for first partons, entering the perturbative evolution (at the initial scale Q_0^2), and then, for given initial conditions, generate corresponding parton configurations, based on the particular structure of perturbative cross sections (10.51-10.55). The detailed description of this procedure is given in the next sections.

The triple Pomeron contributions are included here in the definition of the parton distribution $\varphi_{i/p(\text{sea})}$. At HERA energies, the triple Pomeron contribution is dominated by the process where the two Pomerons exchanged in parallel are soft ones, and therefore no additional parton production needs to be considered in that case.

10.6 Generating Initial Conditions for the Perturbative Evolution

We start with the generation of the kinematical variables x_B and Q^2 according to the differential cross section eq. (10.7) together with the explicit form for the photon-proton cross sections eqs. (10.59-10.60). Then we choose an interaction with the transverse or with the longitudinal polarization component of the photon, with the corresponding weights

$$L_{T/L}^{\gamma^*}(y) \sigma_{T/L}^{\gamma^*p}(\tilde{s}, Q^2) / \left(L_T^{\gamma^*}(y) \sigma_T^{\gamma^*p}(\tilde{s}, Q^2) + L_L^{\gamma^*}(y) \sigma_L^{\gamma^*p}(\tilde{s}, Q^2) \right). \quad (10.62)$$

After that, we consider virtual photon-proton interaction for given photon virtuality Q^2 and polarization (T , L), and for given c.m. energy squared $\hat{s} = \tilde{s} - Q^2$ for the interaction; we use the photon-proton center of mass system.

Let us first consider the case of transverse photon polarization. We have to choose between “sea” and “valence” contribution, where the latter one is chosen with the probability

$$\begin{aligned} \text{prob(val)} = \frac{1}{\sigma_T^{\gamma^*p}(\tilde{s}, Q^2)} & \left\{ \frac{4\pi^2\alpha}{Q^2} \sum_{i \in \{u,d\}} e_i^2 x_B \varphi_{i/p(\text{val})}(x_B) \Delta^q(Q_0^2, Q^2) + \right. \\ & \left. + \sum_{i \in \{u,d\}} \int dx_1 \varphi_{i/p(\text{val})}(x_1) \sigma_T^{\gamma^*i}(x_1 \tilde{s}, Q^2, Q_0^2) \right\} \end{aligned} \quad (10.63)$$

and the former one with the probability $1 - \text{prob(val)}$, which is the sum of the contributions, corresponding to a gluon or a sea quark from the proton being the first ladder parton,

$$\begin{aligned} \text{prob(sea)} = \frac{1}{\sigma_T^{\gamma^*p}(\tilde{s}, Q^2)} & \left\{ \frac{4\pi^2\alpha}{Q^2} \sum_{i \in \{u,d,s,\bar{u},\bar{d},\bar{s}\}} e_i^2 x_B \varphi_{i/p(\text{sea})}(x_B) \Delta^q(Q_0^2, Q^2) + \right. \\ & \left. + \sum_{i \in \{g,u,d,s,\bar{u},\bar{d},\bar{s}\}} \int dx_1 \varphi_{i/p(\text{sea})}(x_1) \sigma_T^{\gamma^*i}(x_1 \tilde{s}, Q^2, Q_0^2) \right\}. \end{aligned} \quad (10.64)$$

The next step consists of defining the type (flavor) of the first ladder parton and its momentum share x_1 in the proton. Here one has to distinguish two possible parton configurations for the interaction: parton cascading without any resolvable parton emission in the ladder (corresponding

to a valence or a sea quark of the proton scattered back in the Breit frame), with the relative weights given by the first term in the curly brackets in eqs. (10.63, 10.64), i.e.

$$\text{prob}(\text{no emission}) = \frac{\frac{4\pi^2\alpha}{Q^2} \sum_i e_i^2 x_B \varphi_{i/p(\text{val/sea})}(x_B) \Delta^q(Q_0^2, Q^2)}{\text{prob}(\text{val/sea}) \sigma_T^{\gamma^*p}(\tilde{s}, Q^2)}, \quad (10.65)$$

and the configurations with at least one resolvable parton emission, with the weight $1 - \text{prob}(\text{no emission})$. In the case of no resolvable emission we have $x_1 = x_B = Q^2/\tilde{s}$ and the flavor of the quark is generated according to the weights

$$\begin{cases} e_i^2 \varphi_{i/p(\text{val})}(x_B) & \text{if } \text{val} \\ e_i^2 \varphi_{i/p(\text{sea})}(x_B) & \text{if } \text{sea} \end{cases} \quad (10.66)$$

Then we are left with a trivial parton configuration. For a valence quark contribution it consists of an anti-quark, moving along the original proton direction, and the quark, scattered back.

In the case of at least one resolvable emission, one generates the type (flavor) i and the light cone momentum fraction x_1 of the first parton of the QCD cascade according to the distributions, given by the expressions in the curly brackets in (10.63), (10.64),

$$\text{prob}(i, x_1) = \begin{cases} \delta_q^i \varphi_{i/p(\text{val})}(x_1) \sigma_T^{\gamma^*i}(x_1 \tilde{s}, Q^2, Q_0^2) & \text{if } \text{val} \\ \varphi_{i/p(\text{sea})}(x_1) \sigma_T^{\gamma^*i}(x_1 \tilde{s}, Q^2, Q_0^2) & \text{if } \text{sea} \end{cases}, \quad (10.67)$$

where δ_q^i is zero if $i = g$ and otherwise one.

Then one chooses between different types of interactions, contributing to the photon-parton cross section, according to their partial weights in eqs. (10.56, 10.57). The direct photon-parton contribution is chosen with the weight

$$\text{prob}(\text{direct}) = \begin{cases} \left[e_i^2 \sigma_{T(\text{NS})}^{\gamma^*q} + \langle e_q^2 \rangle \sigma_{T(\text{S})}^{\gamma^*q} + e_c^2 \sigma_{T(\text{charm})}^{\gamma^*q} \right] / \sigma_T^{\gamma^*i} & \text{if } i = \text{quark} \\ \left[\langle e_q^2 \rangle \sigma_{T(\text{light})}^{\gamma^*g} + e_c^2 \sigma_{T(\text{charm})}^{\gamma^*g} \right] / \sigma_T^{\gamma^*g} & \text{if } i = \text{gluon} \end{cases} \quad (10.68)$$

For the resolved photon contributions, the weight is given by the last two terms in eqs. (10.56, 10.57). The probability for the VDM part is

$$\text{prob}(\text{VDM}) = \sum_j \int dx_\gamma f_{j/\gamma}^{\text{VDM}}(x_\gamma, Q_0^2, Q^2) \sigma_{T(\text{resolved})}^{ji}(x_\gamma(x_1 \tilde{s} - Q^2), Q^2, Q_0^2, Q_0^2) / \sigma_T^{\gamma^*i}, \quad (10.69)$$

where x_1 is the light cone momentum share and i is the type (flavor) of the first ladder parton on the proton side (already determined), whereas the probability for the point-like resolved contribution is

$$\begin{aligned} \text{prob}(\text{point}) &= \langle e_q^2 \rangle \int \frac{dq^2}{q^2} \int dx_\gamma \frac{\alpha}{2\pi} P^{\gamma \rightarrow q\bar{q}}(x_\gamma) \\ &\times \sum_{j \in \{u, d, s, \bar{u}, \bar{d}, \bar{s}\}} \sigma_{T(\text{resolved})}^{ji}(x_\gamma x_1 \tilde{s} - q^2, Q^2, q^2, Q_0^2) \Theta(q^2 - \max[Q_0^2, x_\gamma Q^2]) / \sigma_T^{\gamma^*i}. \end{aligned} \quad (10.70)$$

In case of a direct light contribution, one has to generate the configuration for a parton ladder, strictly ordered in parton virtualities towards the virtual photon. The method is quite analogous to the one of section 2 in chapter 5 and is described in the next section.

In case of a resolved contribution, we need to define the initial conditions for the other end of the parton ladder, on the photon side, as well as the parton type (a quark of some flavor or a gluon) and the share of the light cone momentum fraction x_γ , taken by the parton from the

photon. For the direct resolved contribution, corresponding to the point-like photon splitting into a quark-anti-quark pair, the flavor j , the share x_γ , and the virtuality q^2 of the (anti-)quark, being the first ladder parton, are generated according to

$$\text{prob}(j, x_\gamma, q^2) \sim \frac{1}{q^2} \frac{\alpha}{2\pi} P^{\gamma \rightarrow q\bar{q}}(x_\gamma) \sigma_{T(\text{resolved})}^{ji}(x_\gamma x_1 \tilde{s} - q^2, Q^2, q^2, Q_0^2) \Theta(q^2 - \max[Q_0^2, x_\gamma Q^2]) \delta_q^j \quad (10.71)$$

For the VDM contribution, the first ladder parton is taken at the initial virtuality Q_0^2 and its type j and momentum share x_γ are chosen according to the distribution

$$\text{prob}(j, x_\gamma) \sim f_{j/\gamma}^{\text{VDM}}(x_\gamma, Q_0^2, Q^2) \sigma_{T(\text{resolved})}^{ji}(x_\gamma(x_1 \tilde{s} - Q^2), Q^2, Q_0^2, Q_0^2), \quad (10.72)$$

with the VDM parton momentum distributions in the photon defined in (10.37). In both cases for resolved photon interactions, the simulation of parton configurations, corresponding to the ladder of given mass squared \hat{s}' ($\hat{s}' = x_\gamma x_1 \tilde{s} - q^2$ for the direct resolved contribution and $\hat{s}' = x_\gamma(x_1 \tilde{s} - Q^2)$ for the VDM one), and of given types and virtualities of the leg partons, is done exactly in the same way as for proton-proton (nucleus-nucleus) interactions, as described in the chapter 5. The only difference comes from the presence of two different scales M_p^2 , M_γ^2 and the cutoff $p_\perp^2 > Q^2$ in the parton-parton cross section $\sigma_{T(\text{resolved})}^{ij}$ for resolved DIS processes as given in eq. (10.55), when compared to the cross section in eq. (6.7).

In the case of interaction with the longitudinal photon component, the procedure simplifies considerably, as one only has to consider direct photon-parton interactions via the parton-gluon fusion process. One starts by choosing between the coupling of the parton ladder to a valence quark (“val”) or to a soft Pomeron (“sea”), the weights are

$$\text{prob}(\text{val}) = \frac{\int dx_1 \sum_i \varphi_{i/p(\text{val})}(x_1) \sigma_L^{\gamma^* i}(x_1 \tilde{s}, Q^2, Q_0^2)}{\sigma_L^{\gamma^* p}(\tilde{s}, Q^2)}, \quad (10.73)$$

$$\text{prob}(\text{sea}) = \frac{\int dx_1 \sum_i \varphi_{i/p(\text{sea})}(x_1) \sigma_L^{\gamma^* i}(x_1 \tilde{s}, Q^2, Q_0^2)}{\sigma_L^{\gamma^* p}(\tilde{s}, Q^2)}. \quad (10.74)$$

The weight for the parton type (flavor) i and the distribution for the light cone momentum fraction x_1 of the first parton of the QCD cascade is given by the integrands of (10.73-10.74). The final step amounts to generating the configuration for the parton ladder, strictly ordered in parton virtualities towards the virtual photon, with the largest momentum transfer parton process of parton-gluon fusion type, as discussed in the next section.

10.7 Generating the Ladder Partons

In this section we describe the procedure to generate parton configurations, corresponding to direct photon-parton interaction with at least one resolvable emission in the parton cascade. In that case, a parton ladder is strictly ordered in parton virtualities towards the virtual photon and the ladder cross section is given as a sum of the contributions eqs. (10.51-10.54) in the case of transverse photon polarization,

$$\sigma_{T(\text{direct})}^{\gamma^* i}(\tilde{s}, Q^2, Q_0^2) = \begin{cases} e_i^2 \sigma_{T(\text{NS})}^{\gamma^* q}(\tilde{s}, Q^2, Q_0^2) + \langle e_q^2 \rangle \sigma_{T(\text{S})}^{\gamma^* q}(\tilde{s}, Q^2, Q_0^2) \\ + e_c^2 \sigma_{T(\text{charm})}^{\gamma^* q}(\tilde{s}, Q^2, Q_0^2) & i = q, \\ \langle e_q^2 \rangle \sigma_{T(\text{NS})}^{\gamma^* g}(\tilde{s}, Q^2, Q_0^2) + e_c^2 \sigma_{T(\text{charm})}^{\gamma^* g}(\tilde{s}, Q^2, Q_0^2) & i = g, \end{cases} \quad (10.75)$$

or by the cross section eq. (10.54) for the longitudinal one,

$$\sigma_{L(\text{direct})}^{\gamma^* i}(\tilde{s}, Q^2, Q_0^2) = e_c^2 \sigma_{T(\text{charm})}^{\gamma^* i}(\tilde{s}, Q^2, Q_0^2). \quad (10.76)$$

All the photon-parton cross sections are expressed in terms of the QCD evolution functions \bar{E}_{QCD} . Using the explicit representation eqs. (B.30-B.32) for \bar{E}_{QCD} , one can rewrite the recursive relations eqs. (B.29), (10.50-10.50) in a form, such that the first (lowest virtuality) emission in the ladder is treated explicitly, multiplied by a weight factor, given by the contribution of the rest of the ladder (the sum of any number of additional resolvable emissions),

$$\begin{aligned}\bar{E}_{\text{QCD}}^{ij}(x, Q_0^2, Q^2) &= \int_{Q_0^2}^{Q^2} \frac{dQ_1^2}{Q_1^2} \sum_k \int_x^{1-\epsilon} \frac{dz}{z} \frac{\alpha_s}{2\pi} P_i^k(z) \Delta^i(Q_0^2, Q_1^2) \bar{E}_{\text{QCD}}^{kj}\left(\frac{x}{z}, Q_1^2, Q^2\right) \\ &+ \int_{Q_0^2}^{Q^2} \frac{dQ_1^2}{Q_1^2} \Delta^i(Q_0^2, Q_1^2) \Delta^j(Q_1^2, Q^2) \frac{\alpha_s}{2\pi} P_i^j(x)\end{aligned}\quad (10.77)$$

$$\begin{aligned}\bar{E}_{NS}(x, Q_0^2, Q^2) &= \int_{Q_0^2}^{Q^2} \frac{dQ_1^2}{Q_1^2} \int_x^{1-\epsilon} \frac{dz}{z} \frac{\alpha_s}{2\pi} P_q^q(z) \Delta^q(Q_0^2, Q_1^2) \bar{E}_{NS}\left(\frac{x}{z}, Q_1^2, Q^2\right) \\ &+ \Delta^q(Q_0^2, Q^2) \int_{Q_0^2}^{Q^2} \frac{dQ_1^2}{Q_1^2} \frac{\alpha_s}{2\pi} P_q^q(x)\end{aligned}\quad (10.78)$$

$$\begin{aligned}\bar{E}_S(x, Q_0^2, Q^2) &= \int_{Q_0^2}^{Q^2} \frac{dQ_1^2}{Q_1^2} \sum_k \int_x^{1-\epsilon} \frac{dz}{z} \Delta^q(Q_0^2, Q_1^2) \frac{\alpha_s}{2\pi} \left[P_q^q(z) \bar{E}_S\left(\frac{x}{z}, Q_1^2, Q^2\right) \right. \\ &+ \left. P_q^g(z) \bar{E}_{\text{QCD}}^{gq}\left(\frac{x}{z}, Q_1^2, Q^2\right) \right]\end{aligned}\quad (10.79)$$

With the help of eqs. (10.77-10.79), (10.51-10.54), one can obtain the recursive relations for the cross sections eqs. (10.75, 10.76) for an arbitrary virtuality Q_1^2 of the initial parton i ,

$$\begin{aligned}\sigma_{T/L(\text{direct})}^{\gamma^* i}(\tilde{s}, Q^2, Q_1^2) &= \sum_j \int_{Q_1^2}^{Q^2} \frac{d\tilde{Q}^2}{\tilde{Q}^2} \Delta^i(Q_1^2, \tilde{Q}^2) \int dz \frac{\alpha_s}{2\pi} P_i^j(z) \sigma_{T/L(\text{direct})}^{\gamma^* j}(z\tilde{s}, Q^2, \tilde{Q}^2) + \\ &+ \sigma_{T/L(\text{direct } 2 \rightarrow 2)}^{\gamma^* i}(\tilde{s}, Q^2, Q_1^2),\end{aligned}\quad (10.80)$$

where $\sigma_{T/L(\text{direct } 2 \rightarrow 2)}^{\gamma^* i}$ represents the contribution of parton configurations with only one resolvable parton emission in the ladder, or with the photon-gluon fusion process without any additional resolvable parton emissions,

$$\sigma_{T(\text{direct } 2 \rightarrow 2)}^{\gamma^* i}(\tilde{s}, Q^2, Q_1^2) = \frac{4\pi^2 \alpha e_i^2}{\tilde{s}} E_{\text{QCD}}^{(1)qq}\left(\frac{Q^2}{\tilde{s}}, Q_1^2, Q^2\right) \Theta(Q^2 - Q_1^2) \quad (i = \text{quark}) \quad (10.81)$$

$$\begin{aligned}\sigma_{T(\text{direct } 2 \rightarrow 2)}^{\gamma^* g}(\tilde{s}, Q^2, Q_1^2) &= \frac{4\pi^2 \alpha \langle e_q^2 \rangle}{\tilde{s}} E_{\text{QCD}}^{(1)gq}\left(\frac{Q^2}{\tilde{s}}, Q_1^2, Q^2\right) \Theta(Q^2 - Q_1^2) \\ &+ e_c^2 \int dp_\perp^2 \frac{d\sigma_T^{\gamma^* g \rightarrow c\bar{c}}(\tilde{s}, Q^2, p_\perp^2)}{dp_\perp^2} \Delta^g(Q_1^2, M_F^2)\end{aligned}\quad (10.82)$$

$$\sigma_{L(\text{direct } 2 \rightarrow 2)}^{\gamma^* i}(\tilde{s}, Q^2, Q_1^2) = \delta_i^g e_c^2 \int dp_\perp^2 \frac{d\sigma_L^{\gamma^* g \rightarrow c\bar{c}}(\tilde{s}, Q^2, p_\perp^2)}{dp_\perp^2} \Delta^g(Q_1^2, M_F^2) \quad (10.83)$$

It is noteworthy that to the leading logarithmic accuracy one should not use in $\sigma_{T(\text{direct } 2 \rightarrow 2)}^{\gamma^* i}$ the Born process matrix elements $d\sigma_T^{\gamma^* g \rightarrow q\bar{q}}/dp_\perp^2$ and $d\sigma_T^{\gamma^* q \rightarrow gq}/dp_\perp^2$; the contribution of just one resolvable parton emission is proportional to $E_{\text{QCD}}^{(1)iq}$, eq. (B.32), defined by the corresponding Altarelli-Parisi kernel $P_i^q(z)$.

The formulas (10.80-10.83) allow us to generate the cascade of partons, corresponding to the direct γ^* -quark (gluon) interaction of energy squared $\hat{s} = \tilde{s} - Q^2$ and photon virtuality Q^2 , starting

from an initial parton with a flavor i , taken at a scale $Q_1^2 = Q_0^2$. We use an iterative procedure, similar to the one of chapter 5. At each step one checks whether there is any additional resolvable parton emission before the last one, with the probability

$$\text{prob}(\text{forward emission}) = \frac{\sigma_{T/L(\text{direct})}^{\gamma^* i}(\tilde{s}, Q^2, Q_1^2) - \sigma_{T/L(\text{direct } 2 \rightarrow 2)}^{\gamma^* i(2 \rightarrow 2)}(\tilde{s}, Q^2, Q_1^2)}{\sigma_{T/L(\text{direct})}^{\gamma^* i}(\tilde{s}, Q^2, Q_1^2)} \quad (10.84)$$

In case of an emission, the flavor j of the new ladder leg parton, the light cone momentum fraction z , taken from the parent parton, and the virtuality \tilde{Q}^2 are generated according to the integrand of $\sigma_{T/L(\text{direct})}^{\gamma^* i} - \sigma_{T/L(\text{direct } 2 \rightarrow 2)}^{\gamma^* i}$ in (10.80),

$$\text{prob}(j, z, \tilde{Q}^2) \sim \frac{1}{\tilde{Q}^2} \Delta^i(Q_1^2, \tilde{Q}^2) \frac{\alpha_s}{2\pi} P_i^j(z) \sigma_{T/L(\text{direct})}^{\gamma^* j}(z\tilde{s}, Q^2, \tilde{Q}^2). \quad (10.85)$$

The process is repeated for the new ladder of energy squared $\hat{s}' = z\tilde{s} - Q^2$, with the initial parton $i' = j$, and with virtuality $Q_1'^2 = \tilde{Q}^2$ and so on. At each step one decides about emission or not, which finally terminates the iteration.

Having done the iterative parton emission, we finally generate the last (highest virtuality) resolvable parton emission or the photon-gluon fusion process (if $i' = g$) in the photon-parton center-of-mass system. The photon-gluon fusion (PGF) process is chosen for $i' = g$ with the probability

$$\text{prob}(\text{PGF}) = \frac{1}{\sigma_{T(\text{direct } 2 \rightarrow 2)}^{\gamma^* g}(\tilde{s}', Q^2, \tilde{Q}^2)} e_c^2 \int dp_\perp^2 \frac{d\sigma_T^{\gamma^* g \rightarrow c\bar{c}}(\tilde{s}', Q^2, p_\perp^2)}{dp_\perp^2} \Delta^g(\tilde{Q}^2, M_F^2) \quad (10.86)$$

for the transverse photon polarization and always for the longitudinal photon polarization. For $i' = q$, we have $\text{prob}(\text{PGF}) = 0$. In case of PGF, with our choice $M_F^2 = m_c^2 + p_\perp^2$, we generate the transverse momentum squared of final charm quarks in the region $\tilde{Q}^2 - m_c^2 < p_\perp^2 < \frac{1}{4}\hat{s} - m_c^2$ according to

$$\text{prob}(p_\perp^2) \sim \frac{d\sigma_T^{\gamma^* g \rightarrow c\bar{c}}(\tilde{s}', Q^2, p_\perp^2)}{dp_\perp^2} \Delta^g(\tilde{Q}^2, M_F^2) \quad (10.87)$$

In case of no PGF, we generate the momentum transfer squared for the last resolvable parton emission in the range $\tilde{Q}^2 < Q'^2 < Q^2$ according to

$$\text{prob}(Q'^2) \sim \frac{1}{Q'^2} \Delta^i(\tilde{Q}^2, Q'^2) \Delta^q(Q'^2, Q^2) \frac{\alpha_s}{2\pi} P_i^q(z'), \quad (10.88)$$

with

$$z' = 1 - \left(1 - \frac{Q'^2}{\tilde{s}}\right) \left(1 - \frac{Q^2}{\tilde{s}}\right), \quad (10.89)$$

and find the parton transverse momentum squared as $p_\perp^2 = Q'^2(1 - z')$.

We then reconstruct final parton 4-momenta in their center of mass system with a random polar angle for the transverse momentum vector \vec{p}_\perp and boost them to the original Lorentz frame. This completed the description of the algorithm to generate parton configurations, based on exactly the same formulas as for calculations of F_2 before.

The above discussion of how to generate parton configurations is not yet complete: the emitted partons are in general off-shell and can therefore radiate further partons. This so called time-like radiation is taken into account using standard techniques [27], as discussed already in chapter 5.

10.8 Hadron Production

For the hadronization, we use exactly the same philosophy and even the same procedure as in case of proton-proton (pp) scattering. Hadronization is not considered as a dynamical procedure, rather we consider the hadronic states as being integrated out in the considerations of cross section calculations of the preceding sections. Hadronization means simply a phenomenological procedure to explicitly reintroduce these hadronic states. The procedure employed for pp scattering and to be used here as well is as follows:

1. drawing a cylinder diagram;
2. cutting the cylinder;
3. planar presentation of half-cylinder;
4. identification of cut line with kinky string;
5. kinky string hadronization (as explained in chapter 6).

We are going to explain the steps (1-4) for a concrete example of a diagram contributing to photon-proton scattering, where the photon interacts directly with a light quark (contribution “light”), and where the first parton of the ladder on the proton side couples to the proton via a soft Pomeron (contribution “sea”), as shown in fig. 10.11. The external legs on the lower (proton) side are a quark

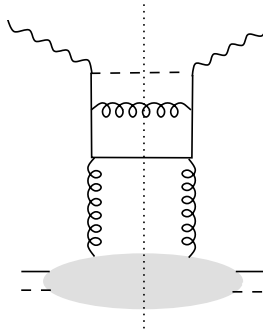


Figure 10.11: A diagram contributing to the photon-proton cross section.

(full line) and an anti-quark (dashed), representing together the proton constituent participating in the interaction. In fig. 10.12(left), we show the result of plotting the diagram on a cylinder. The shaded area on the lower part of the cylinder indicates the soft Pomeron, a complicated non-resolved structure, where we do not specify the microscopic content. The two space-like gluons emerge out of this soft structure. The cut is represented by the two vertical dotted lines on the cylinder. We now consider one of the two half-cylinders, say the left one, and we plot it in a planar fashion, as shown in fig. 10.12(right). We observe one internal gluon, and one external one, appearing on the cut line. We now identify the two cut lines with kinky strings such that a parton on the cut line corresponds to a kink: we have one kinky string with one internal kink (gluon) in addition to the two end kinks, and we have one flat string with just two end kinks, but no internal one. The strings are then hadronized according to the methods explained in chapter 6, see fig. 10.13.

In principle, we have also triple Pomerons contributing to the event topology. However, due to AGK cancellations, such contributions to the inclusive spectra cancel each other in the kinematical region where the two Pomerons are in parallel. Therefore, the average characteristics are correctly described by considering the simple cylinder-type topology corresponding to one Pomeron exchange.

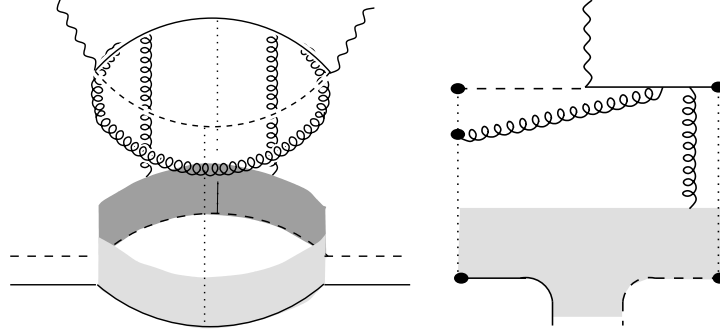


Figure 10.12: Cylindrical representation of the diagram of fig. 10.11 (left figure) and planar diagram representing the corresponding half-cylinder (right figure).

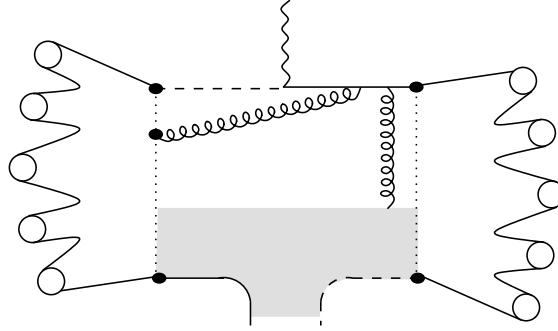


Figure 10.13: The string model: the cut line (vertical dotted line) corresponds to a string, which decays into hadrons (circles).

10.9 Results

We are now capable to simulate events from deep inelastic scattering. When fixing the parameters, we found that all the ones found in e^+e^- can be kept with the exception of the mean transverse momentum of string breaking p_\perp^f and the break probability p_{break} , see the discussion in chapter 8.

We show results from ep scattering and compare to the data of the experiments accomplished at HERA. Electrons of an energy 26.7 GeV collide with protons of 820 GeV, which gives a center of mass energy 296 GeV. We made the analysis for the kinematical region $10^{-4} < x < 10^{-2}$ and $10 < Q^2 < 100 \text{ GeV}^2$. The distribution of the events calculated using our model is shown on figure 10.14.

We recall the principal variables

$$x \equiv x_B = \frac{Q^2}{2(pq)} = \frac{Q^2}{ys}; \quad y = \frac{Q^2}{xs}, \quad (10.90)$$

which gives straight lines for $y = \text{const.}$ in fig. 10.14. The sharp borders are due to imposing the experimental cuts $0.03 < y$, $E' > 12 \text{ GeV}$ and $\theta_e > 7.5$. On figure 10.15, we plot charged particle distributions for different values of $W = \hat{s} = 2(pq) - Q^2$. The particle spectra look very similar for different W values; the distributions decrease rapidly with x_F . The dependence of the average p_\perp^2 on x_F shows an overall good agreement with the data from H1 collaboration [54].

In table 10.1 the bins in x and Q^2 are given for the experimental data points on figures 10.15-10.20 (see [55]). The bin 0 is the sum of all the others. First, we compare the p_\perp distribution in the photon-proton center of mass system for the different bins - fig. 10.16. Fig. 10.16(a) shows the comparison of the results for low and high x values for the values of $Q^2 \simeq 10 - 20 \text{ GeV}^2$ (bins 6 and

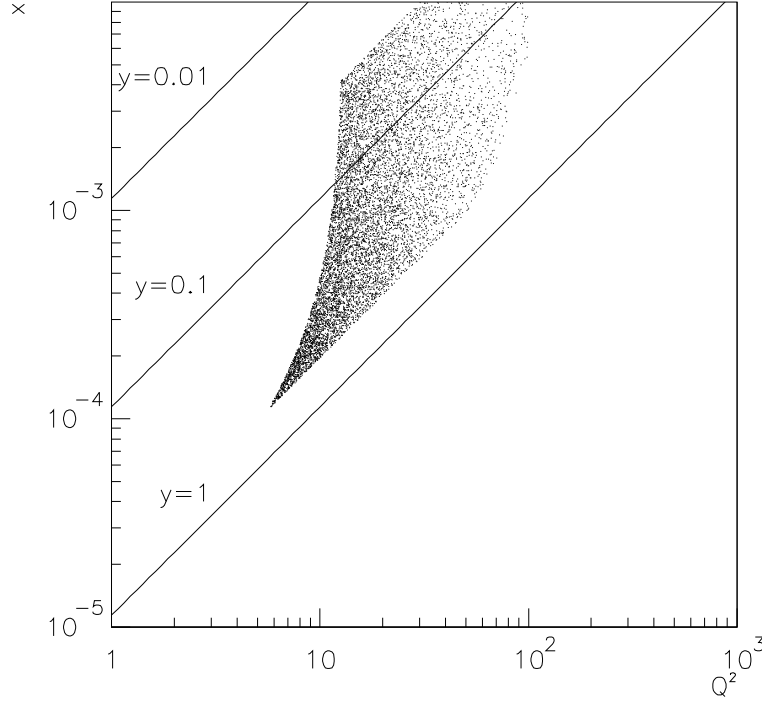


Figure 10.14: Distribution of the simulated events in the $Q^2 - x$ plane.

bin	$x/10^{-3}$	Q^2/GeV^2	$\langle x \rangle /10^{-3}$	$\langle Q^2 \rangle / \text{GeV}^2$	$\langle W^2 \rangle / \text{GeV}^2$
0	0.1-10	5-50	1.14	18.3	24975
1	0.1-0.2	5-10	0.16	7.7	45296
2	0.2-0.5	6-10	0.29	8.8	31686
3	0.2-0.5	10-20	0.37	13.1	36893
4	0.5-0.8	10-20	0.64	14.0	22401
5	0.8-1.5	10-20	1.1	14.3	13498
6	1.5-4.0	10-20	2.1	15.3	7543
7	0.5-1.4	20-50	0.93	28.6	32390
8	1.4-3.0	20-50	2.1	31.6	16025
9	3.0-10	20-50	4.4	34.7	8225

Table 10.1: Bins in x and Q^2 for the figures 10.15-10.20.

3). We find harder spectra for smaller x , which is the consequence of the larger kinematical space (in x) for the initial state radiation. Next, on figures 10.16(b,c), the spectra are compared for two different values of Q^2 and either the energy $W \sim Q^2/x$ being fixed (bins 2 and 7, fig. 10.16(b)), or for a given value of x (bins 6 and 8, figure 10.16(c)). The spectra in p_\perp are always harder for larger Q^2 , which is now the consequence of the larger kinematical space in p_\perp^2 for the initial state radiation. Two cuts in pseudo-rapidity η for bin 3 are considered on figure 10.16(d). We see a harder distribution for $1.5 < \eta < 2.5$. Around mid-rapidity, where η is maximal, one finds higher transverse momenta as this region is dominated by the contribution of the largest virtuality photon process.

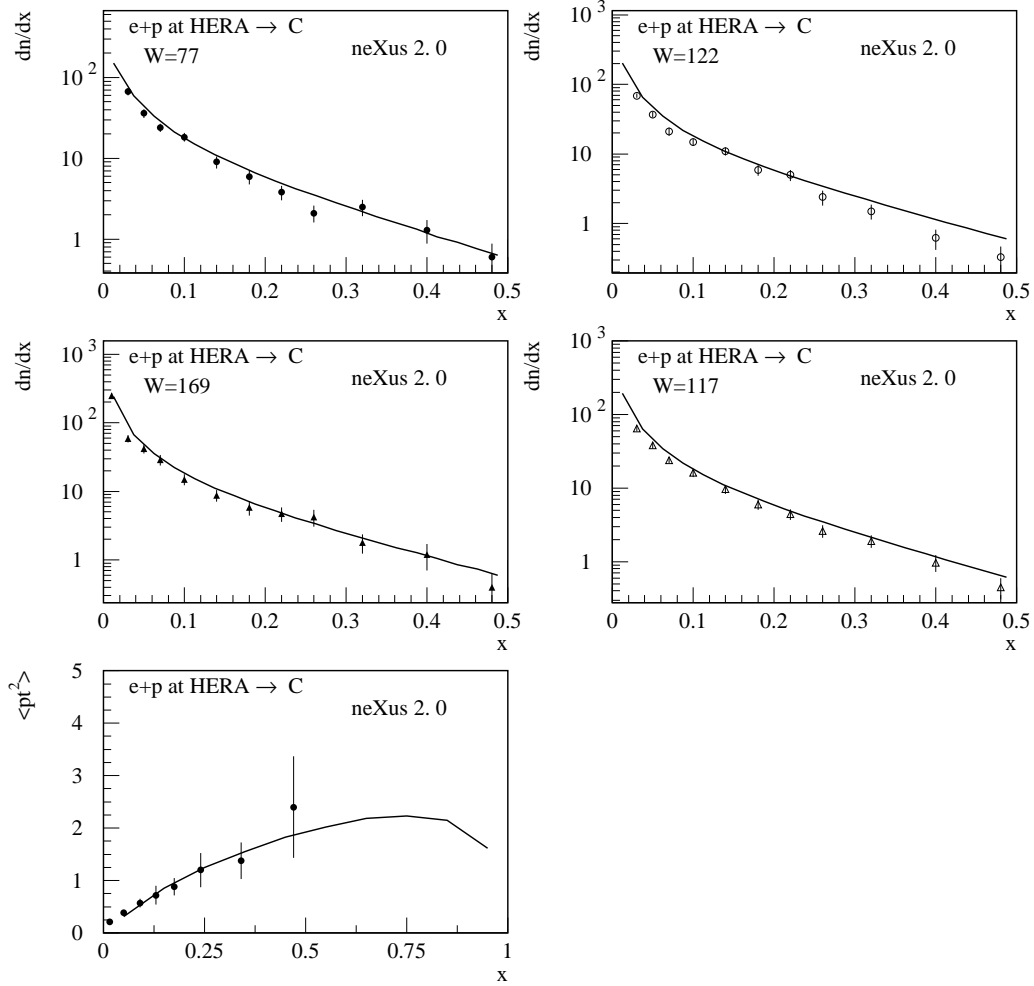


Figure 10.15: x_F distribution of charged particles for different values of W : 50-100 GeV, 100-150 GeV, 150-200 GeV and for the total W region of 50-200 GeV. The last diagram shows mean p_{\perp}^2 as a function of x_F . All the variables are defined in the hadronic center of mass system. The data are from H1 collaboration [54].

Let us now consider pseudo-rapidity distributions of charged particles. Figures 10.17, 10.18 show the η -distributions for the 9 bins of table 10.1 for different values of Q^2 and x . On figure 10.18, a cut for $p_{\perp} > 1$ GeV has been made to extract the contribution of hard processes. The latter one results in approximately 10% of the total hadron multiplicity. At fig. 10.18 we find fewer particles at small η which is the consequence of smaller kinematical space (in x) for the initial state radiation and the reduced influence of the largest virtuality photon process.

The transverse momenta for all particles are generally well described by the model - figs. 10.19, 10.20. The fact that we find harder spectra for higher Q^2 and lower x is best seen for smaller values of η - see fig. 10.20.

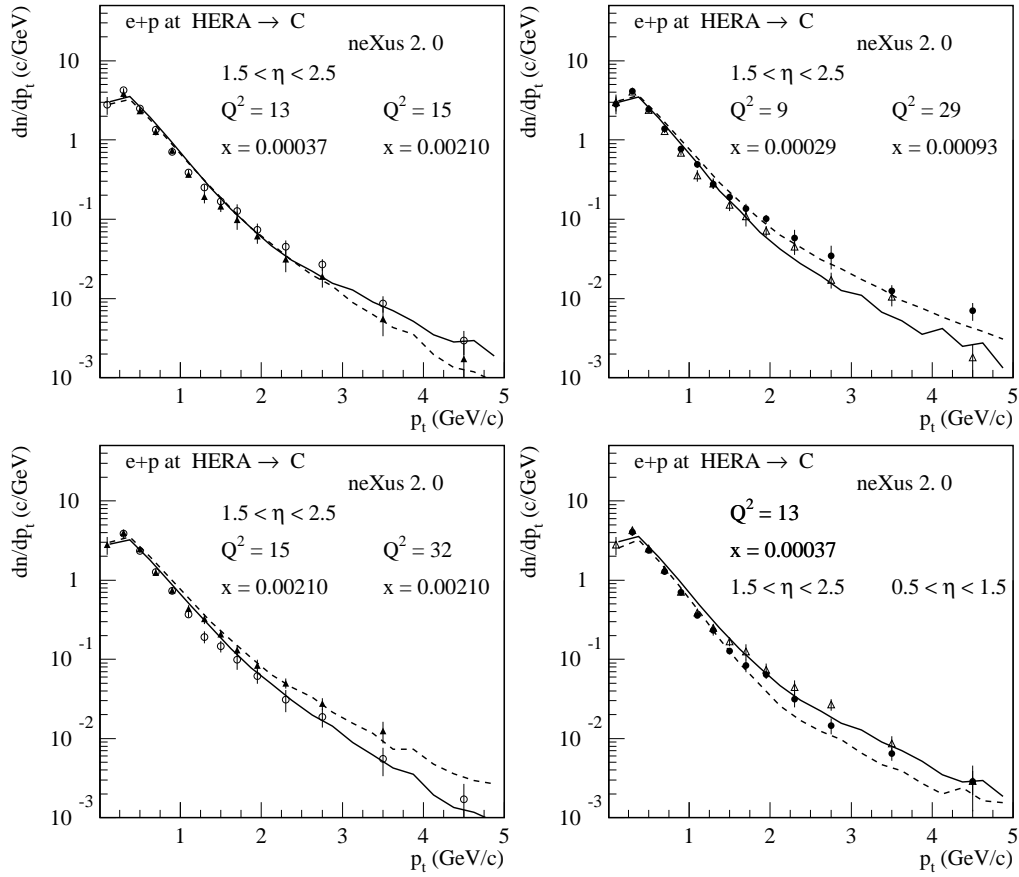


Figure 10.16: p_{\perp} distribution of charged particles for different kinematic regions. The values of the cuts are indicated on the figures (column 1 - full line, column 2 - dashed line).

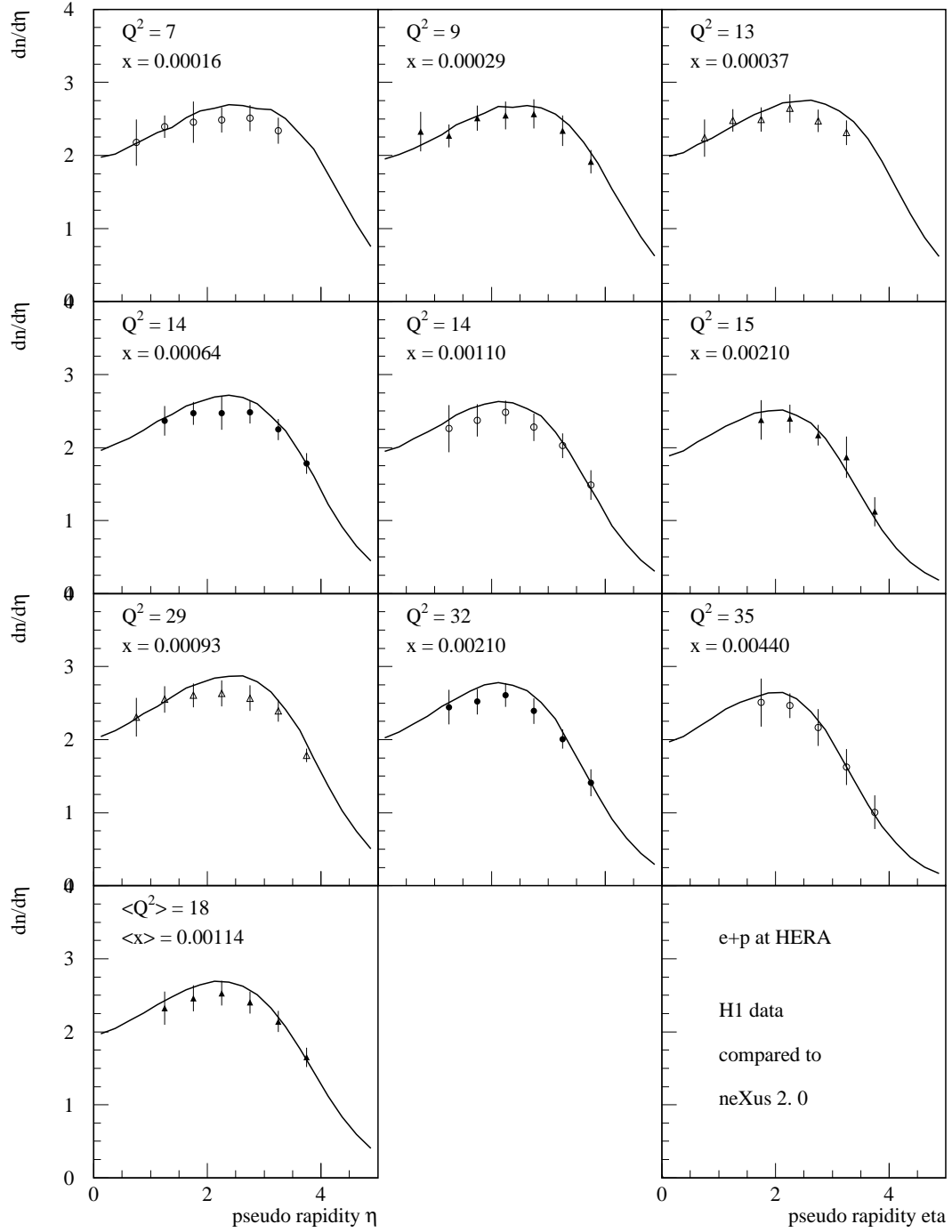


Figure 10.17: Pseudo rapidity distribution of charged particles for the bins indicated in table 10.1. The lower left diagram represents no cut results.

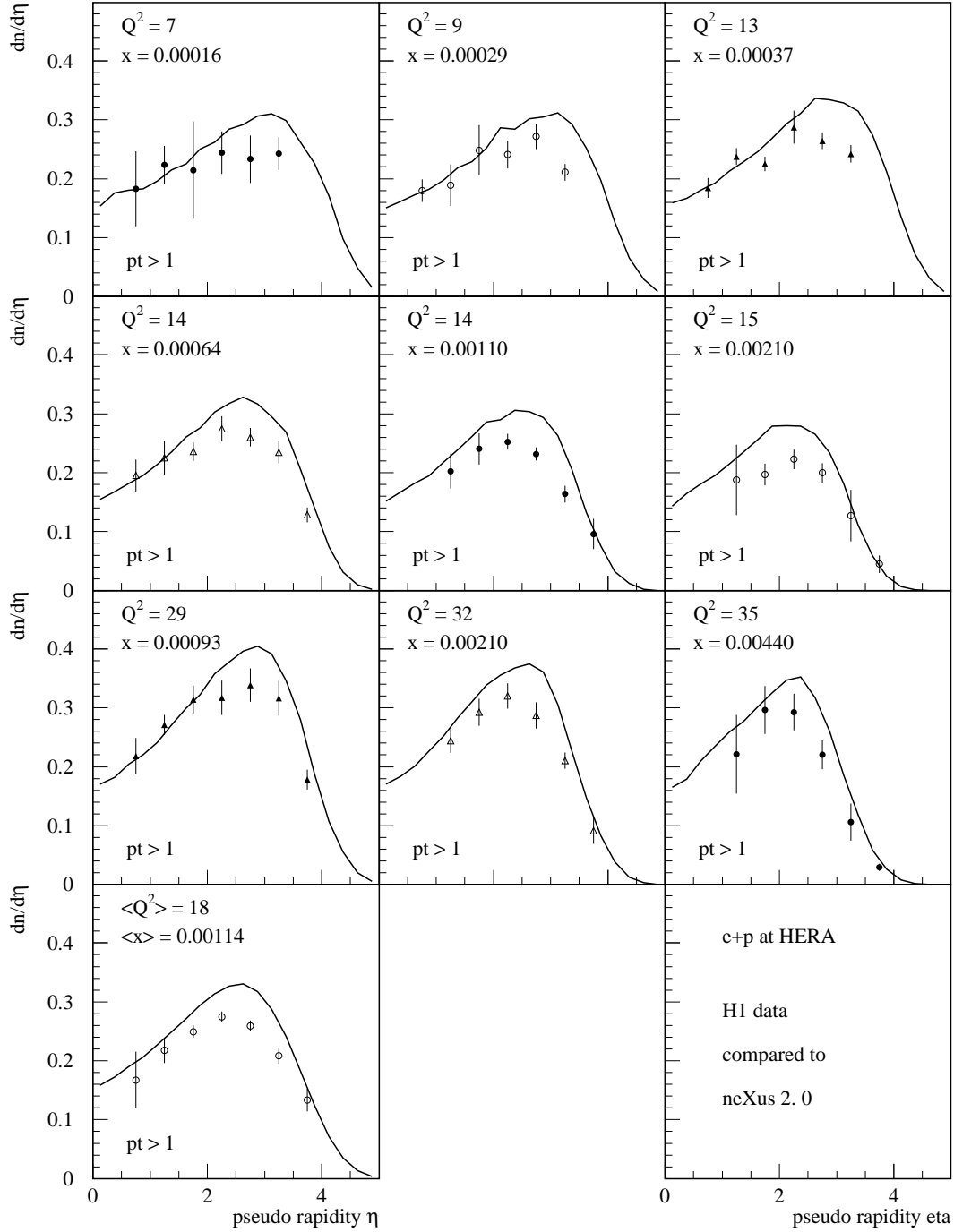


Figure 10.18: The same as on figure 10.17, but with an additional cut $p_{\perp} > 1$ GeV.

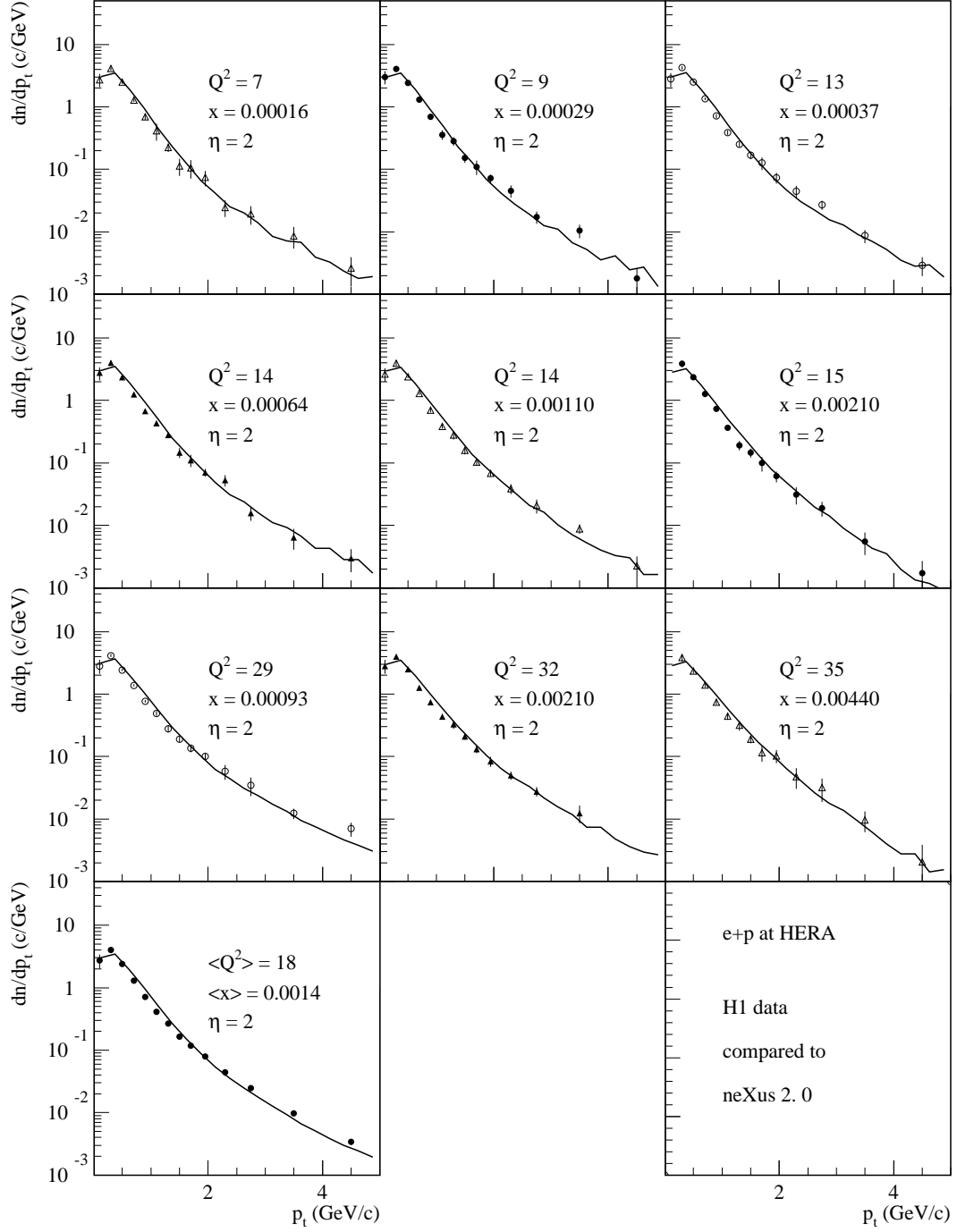


Figure 10.19: Transverse momentum of charged particles for $1.5 < \eta < 2.5$.

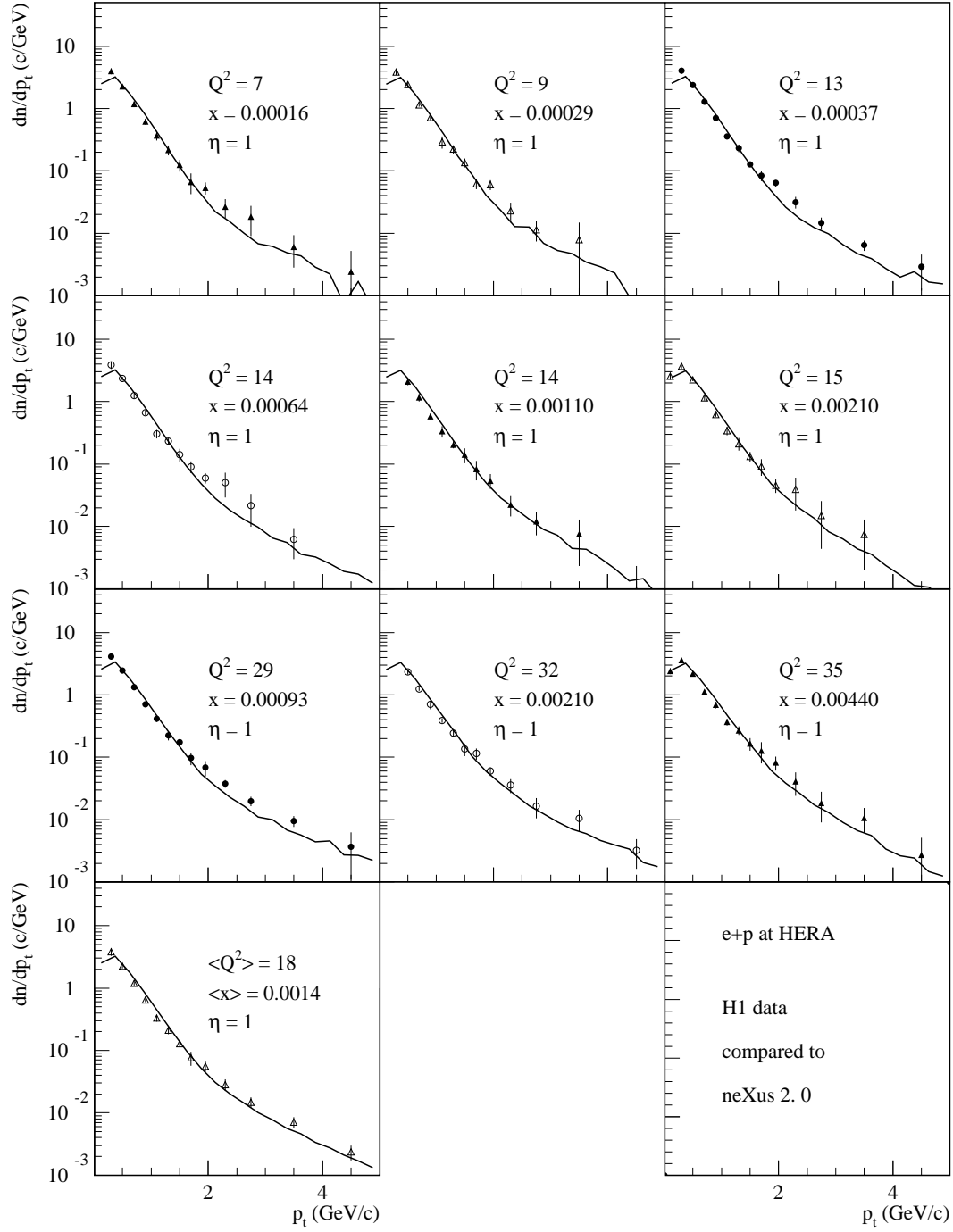


Figure 10.20: Transverse momentum of charged particles for $0.5 < \eta < 1.5$.

Chapter 11

Results for Proton-Proton Scattering

In this section we are going to discuss our results for proton-proton interactions in the energy range between roughly 10 and 2000 GeV, which represents the range of validity of our approach. The lower limit is a fundamental limitation due to the fact that our approach requires hadron production to start after the primary interactions are finished, which is no longer fulfilled at low energies. The upper limit is due to the fact that above 2000 GeV higher order screening corrections need to be taken into account.

11.1 Energy dependence

We first consider the energy dependence of some elementary quantities in pp scattering in the above mentioned energy range. In fig. 11.1, the results for the total cross section are shown. The

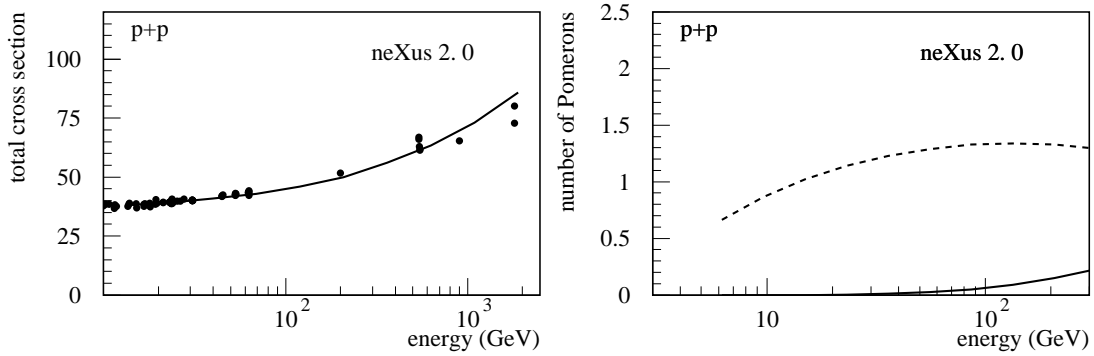


Figure 11.1: The total cross section as a function of the energy \sqrt{s} (left figure): the full line is the simulation, the points represent data. Pomeron numbers as a function of the energy \sqrt{s} (right): soft (dashed) and semi-hard (solid line) Pomeronons.

cross section is essentially used to fit the soft Pomeron parameters. Also shown in the figure is the energy dependence of the number of soft and semi-hard Pomeronons. Over the whole energy range shown in the figure, soft physics is dominating. So for example at RHIC, soft physics dominates by far.

Our results for hadron production are based on the Pomeron parameters, defined from the cross sections fitting, and on the fragmentation procedure, adjusted on the basis of e^+e^- data. In fig. 11.2, average multiplicities of different hadron species are given as a function of the energy. In fig.

11.3, we show the energy dependence of the pseudo-rapidity plateau $dn_C/d\eta(0)$ and of the mean squared transverse momentum $\langle p_t^2 \rangle$.

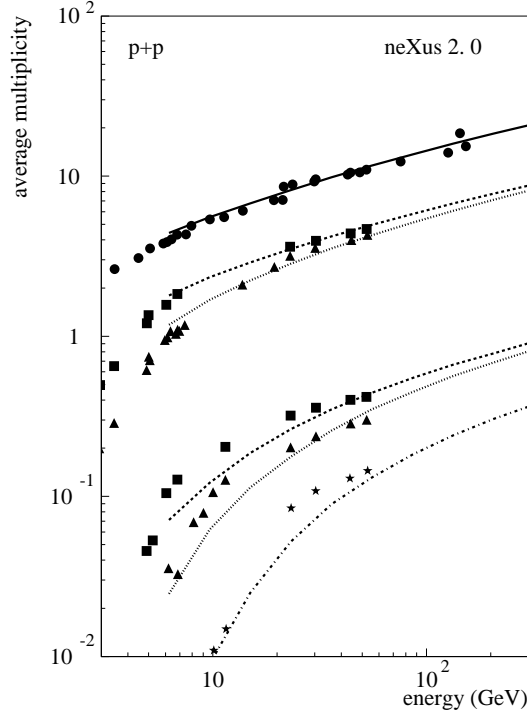


Figure 11.2: The average multiplicities of different hadron species, as a function of the energy \sqrt{s} . From top to bottom: all charged particles, π^+ , π^- , K^+ , K^- , \bar{p} . The full lines are simulations, the points represent data (from [56]).

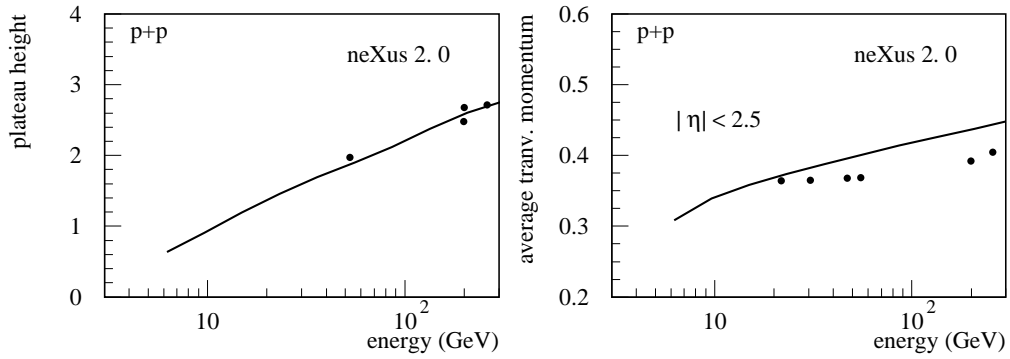


Figure 11.3: Pseudo-rapidity plateau $dn/d\eta(0)$ and mean squared transverse momentum $\langle p_t^2 \rangle$ as a function of the energy \sqrt{s} . The full lines are simulations, the points represent data.

11.2 Charged Particle and Pion Spectra

In fig. 11.4, we present rapidity distributions of pions at 100 GeV, in fig. 11.5 rapidity distributions of pions and charged particles at 200 GeV. The values following the Symbol “I=” represent the integrals, i.e. the average multiplicity. The first number is the simulation, the second number (in brackets) represents data.

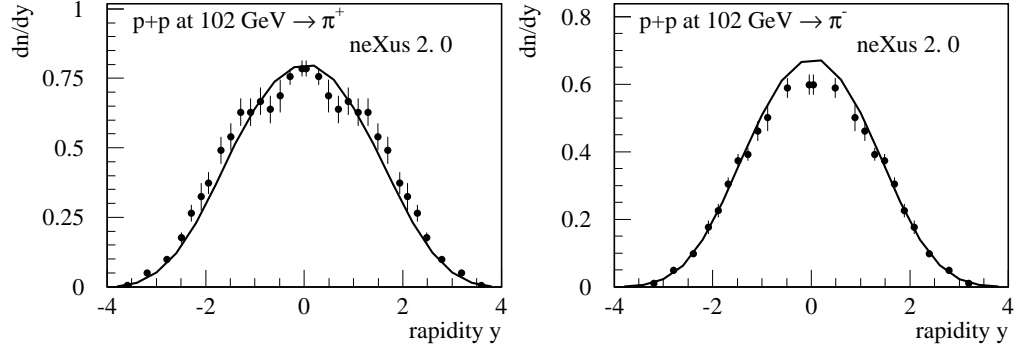


Figure 11.4: Rapidity distributions of pions at 100 GeV. The full lines are simulations, the points represent data.

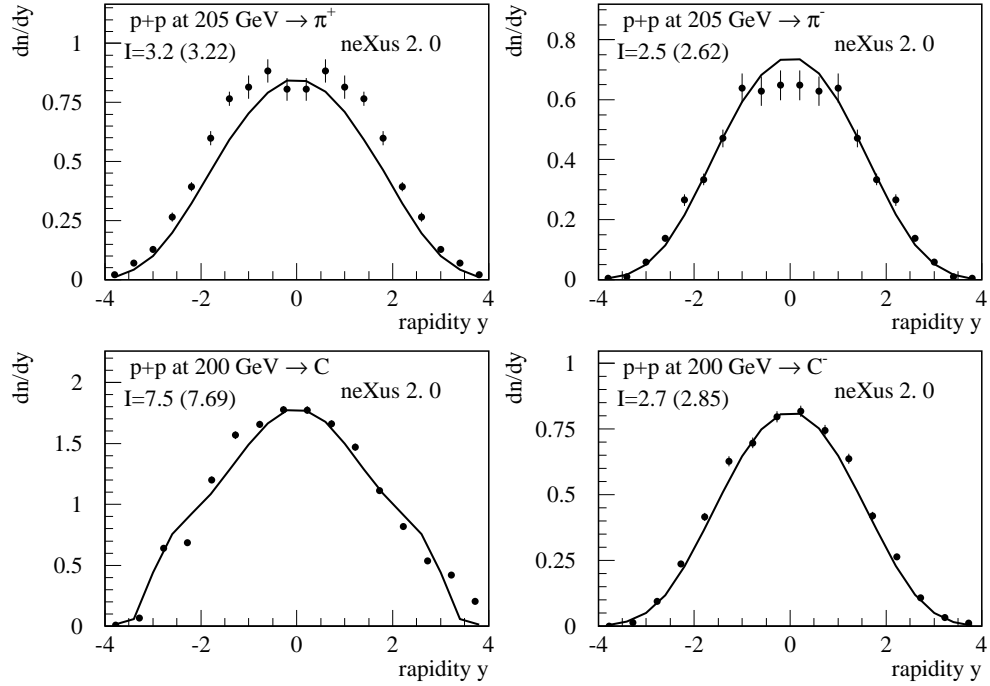


Figure 11.5: Pseudo-rapidity distributions of pions (π^+ , π^-) and charged particles (all charged and negatively charged) at 200 GeV. The full lines are simulations, the points represent data.

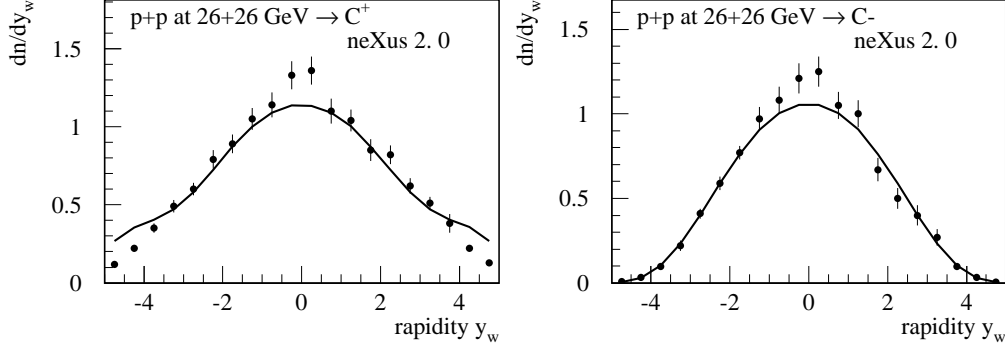


Figure 11.6: Pseudo-rapidity distributions of positively and negatively charged particles at 53 GeV (cms). The full lines are simulations, the points represent data.

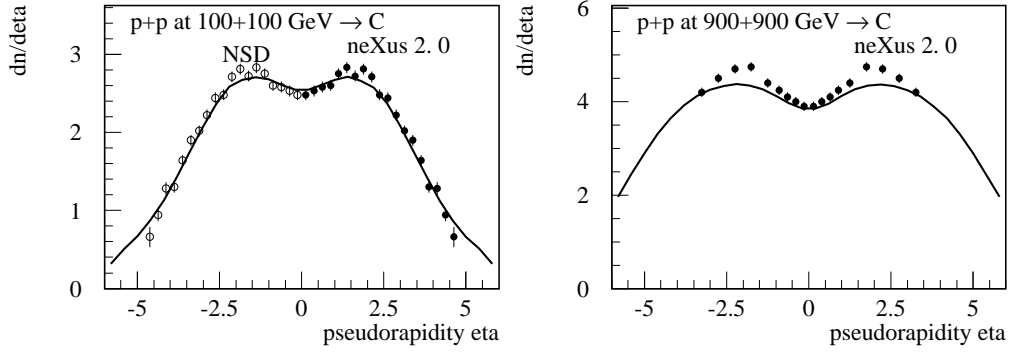


Figure 11.7: Pseudo-rapidity distributions of charged particles at 200 and 1800 GeV (cms). The full lines are simulations, the points represent data.

In fig. 11.6, we show rapidity distributions for positively and negatively charged particles at 53 GeV (cms), where we adopted also for the simulations the experimental definition of the rapidity by always taking the pion mass. In fig. 11.7, we show pseudo-rapidity distributions of charged particles at 200 and 1800 GeV (cms). In figs. 11.8 and 11.9, we finally show transverse momentum spectra at different energies between 100 GeV (lab) and 1800 GeV (cms).

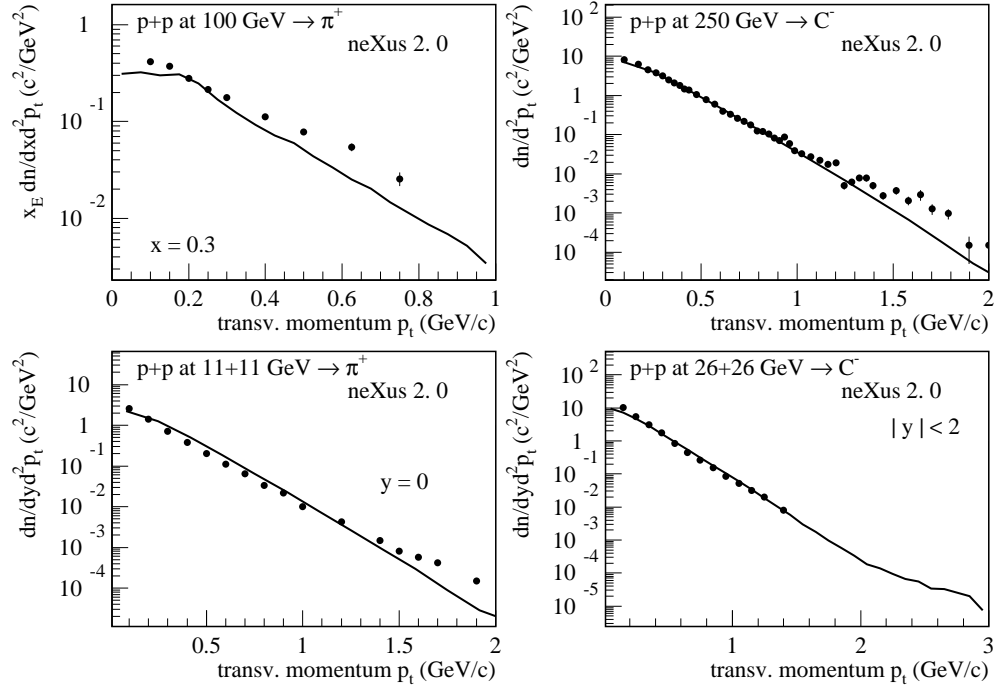


Figure 11.8: Transverse momentum distributions of pions or negatively charged particles at different energies. The full lines are simulations, the points represent data.

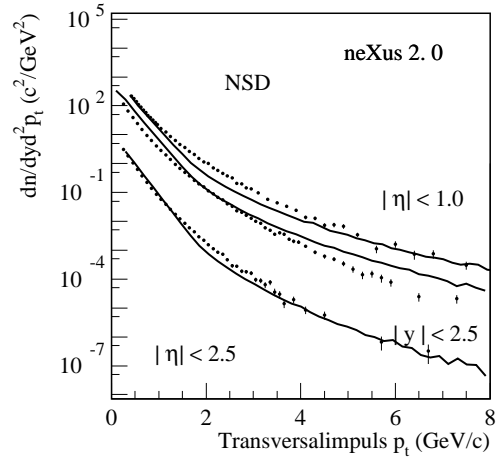


Figure 11.9: Transverse momentum distributions of charged particles at (from bottom to top) 200, 900, and 1800 GeV (cms). The full lines are simulations, the points represent data.

11.3 Proton spectra

In fig. 11.10, we plot longitudinal momentum fraction distributions of protons for different values of t at 200 GeV, in figs. 11.11 and 11.12 as well longitudinal momentum fraction distributions at 100-200 GeV, for given values of p_t or integrated over p_t . In fig. 11.13, we show transverse momentum spectra of protons for different values of the longitudinal momentum fraction x at 100 and 205 GeV.

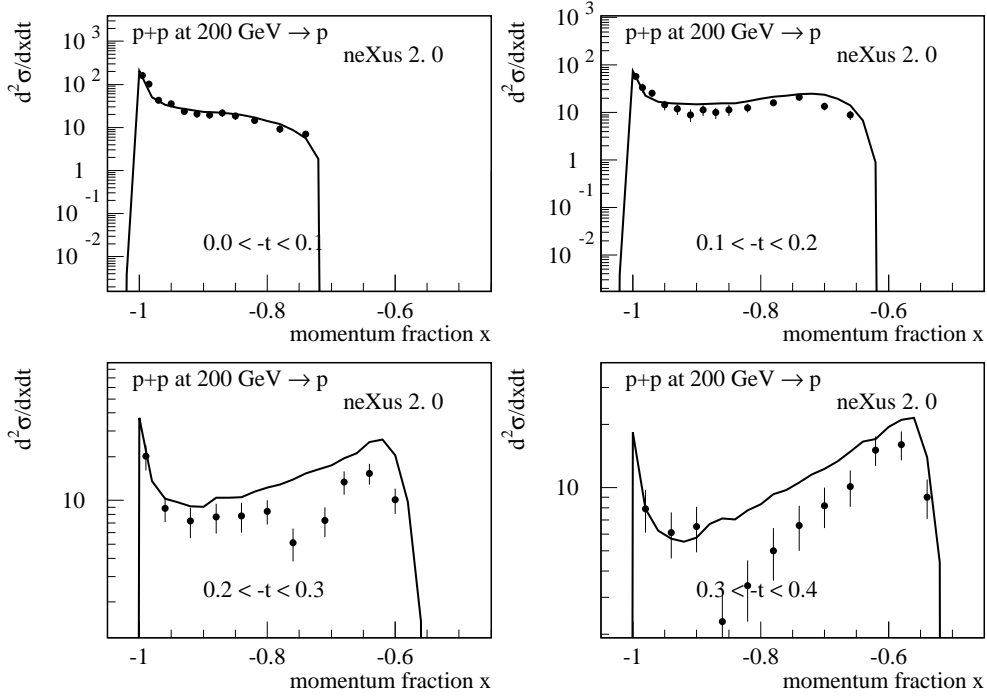


Figure 11.10: Longitudinal momentum fraction distributions of protons for different values of t at 200 GeV. The full lines are simulations, the points represent data.

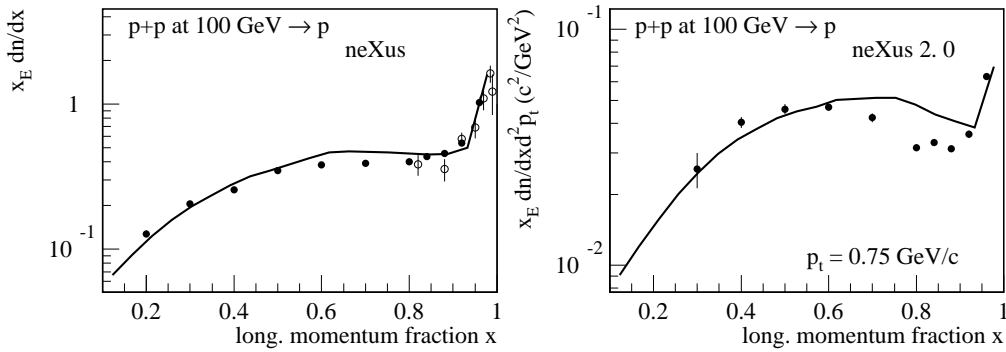


Figure 11.11: Longitudinal momentum fraction distribution of protons at 100 GeV, integrated over p_t (left) and for $p_t = 0.75$ GeV/c (right). The full lines are simulations, the points represent data.

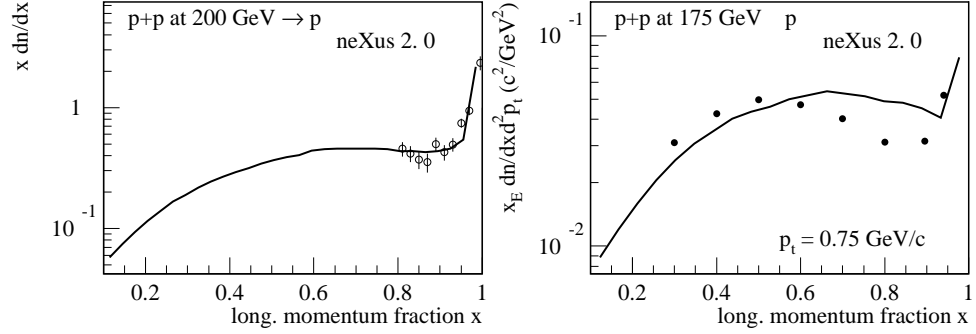


Figure 11.12: Longitudinal momentum fraction distributions of protons at 200 GeV, integrated over p_t (left) and at 175 GeV, for $p_t = 0.75 \text{ GeV}/c$ (right). The full lines are simulations, the points represent data.

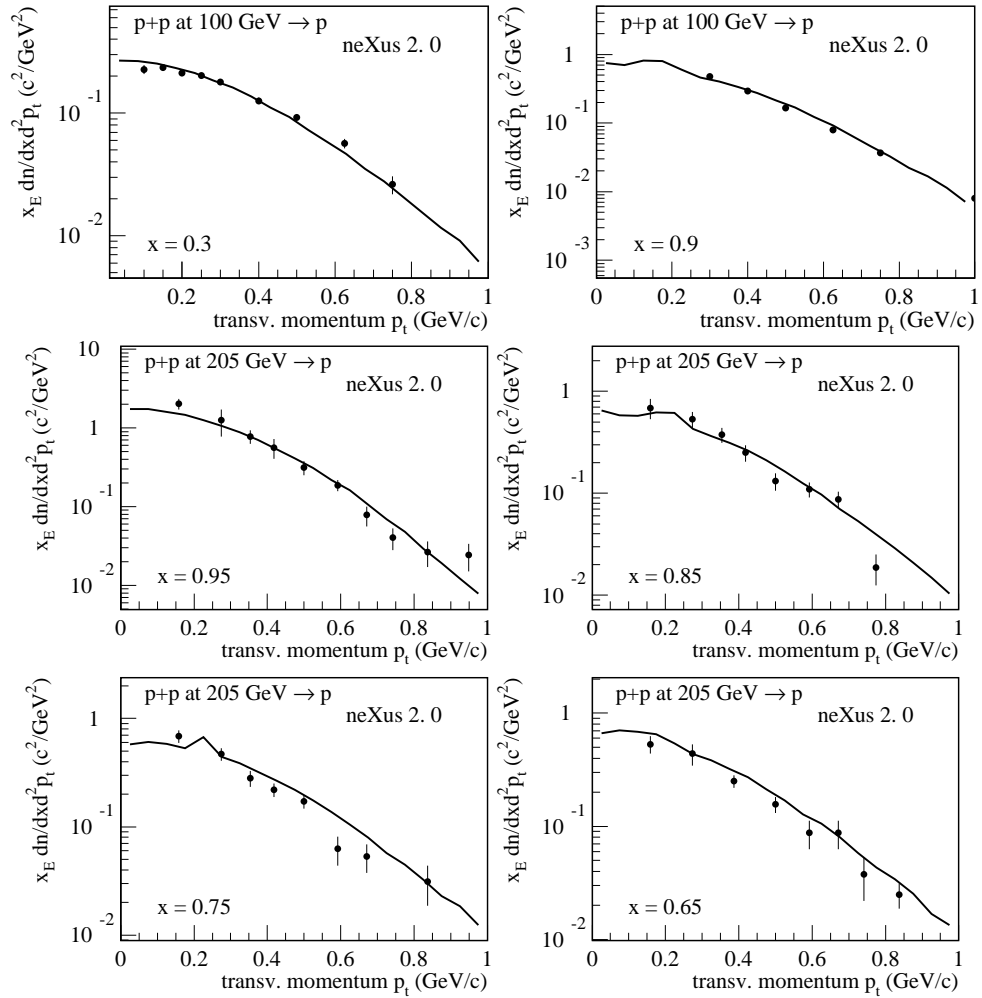


Figure 11.13: Transverse momentum spectra of protons for different values of the longitudinal momentum fraction x at 100 and 205 GeV. The full lines are simulations, the points represent data.

11.4 Strange particle spectra

In figs. 11.14 and 11.15, we show transverse momentum and rapidity spectra of lambdas (including Σ_0), anti-lambdas (including $\bar{\Sigma}_0$), and kaons. The numbers represent the integrals, i.e. the average multiplicity. The first number is the simulation, the second number (in brackets) represents data.

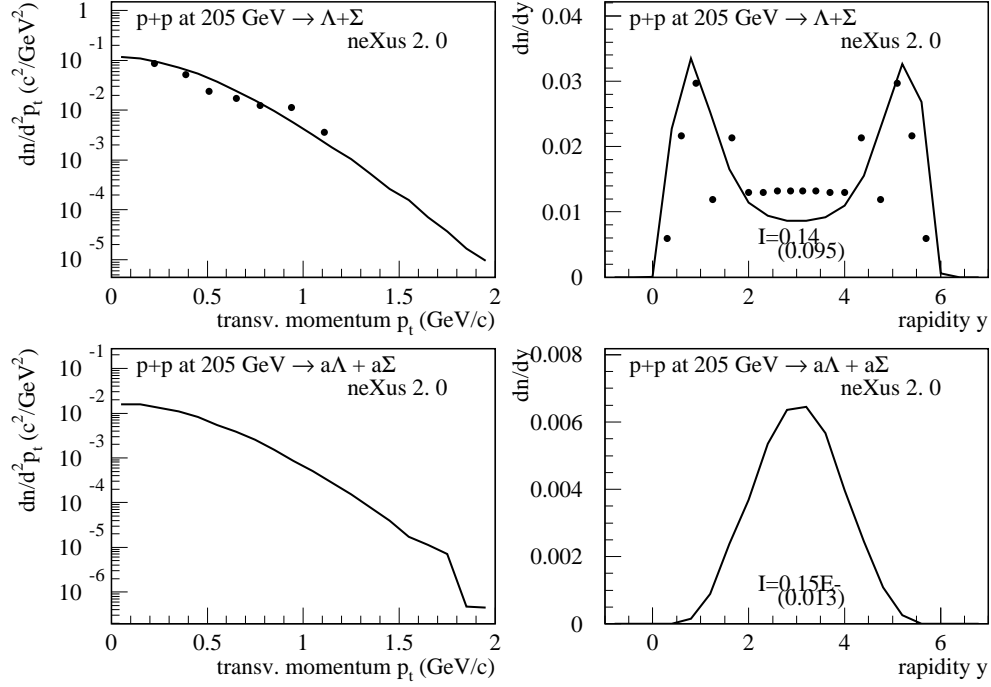


Figure 11.14: Distributions of transverse momentum (left) and rapidity (right) of lambdas plus neutral sigmas (upper) and of anti-lambdas plus neutral anti-sigmas (lower) at 205 GeV. The full lines are simulations, the points represent data.

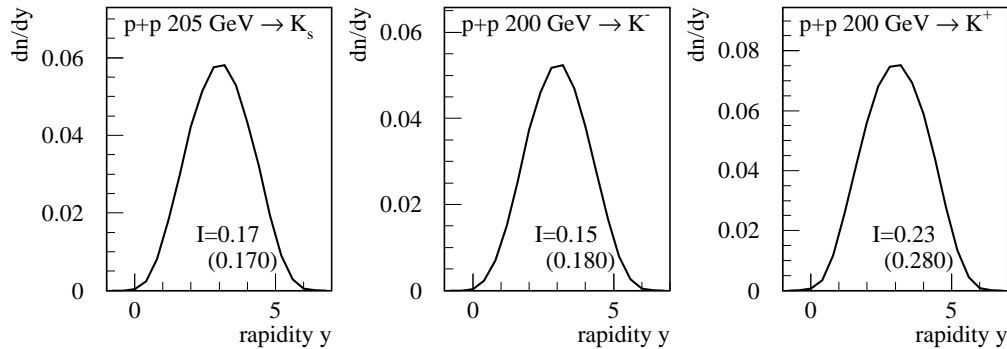


Figure 11.15: Rapidity distributions of kaons (K_s , K^- , K^+) at 205 GeV. The numbers represent y -integrated results: the first number is the simulated one, the number in brackets the experimental one.

Chapter 12

Results for Collisions Involving Nuclei

It is well known that secondary interactions play an important role in collisions involving nuclei. Nevertheless, in this report, we do not want to consider any rescattering procedure, we just present bare NEXUS simulations. This seems to us the most honest way to present results.

12.1 Proton-Nucleus Scattering

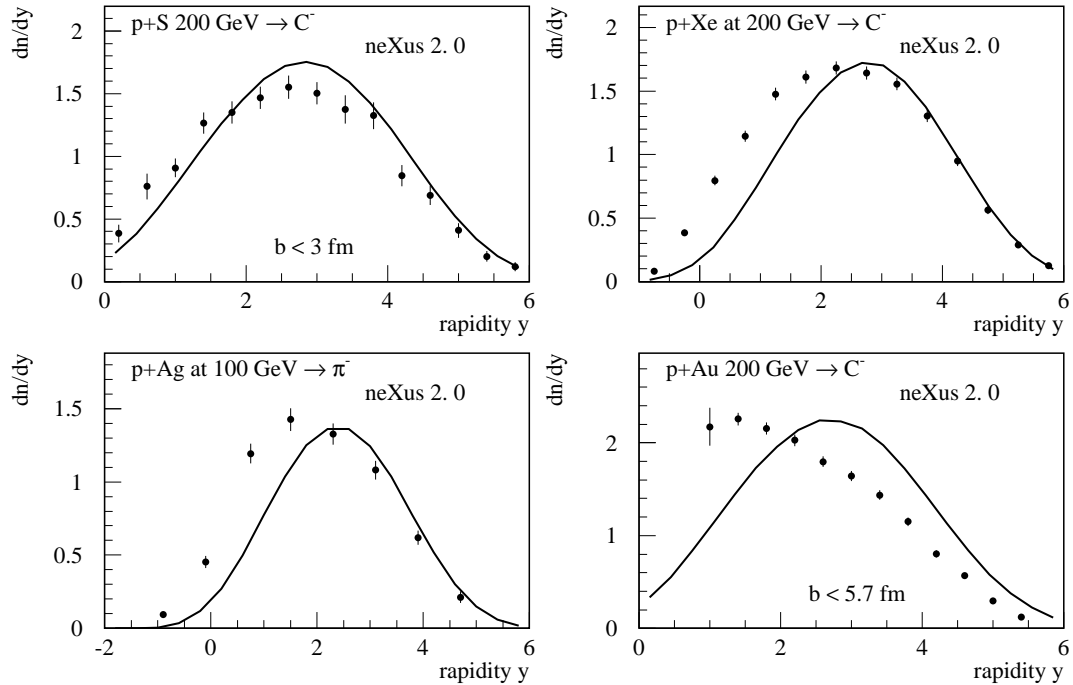


Figure 12.1: Rapidity distributions of charged particles or negative pions for different $p + A$ collisions at 200 GeV (lab).

In fig. 12.1, we show rapidity spectra of negatively charged particles for different target nuclei. Missing particles in the backward region are certainly due to rescattering. In the forward region, the model works well, except for $p+Au$, which represents the heaviest target, but in addition one has here a centrality trigger, in contrast to the other reactions. Here, we expect some reduction due to nuclear screening effects. The transverse momentum spectra are well reproduced in case of $p+S$, as shown in fig. 12.2, whereas for $p+Au$ one sees some deviations for small values of p_t , see fig. 12.3.

Let us turn to proton spectra. In fig. 12.4, we show rapidity spectra of net protons (protons minus anti-protons) for different target nuclei. Since secondary interactions are not considered, we are missing the pronounced peak around rapidity zero (not visible in the figure, since we have chosen the range for the y-axis to be $[0,1]$). Apart of the target fragmentation region, the model works well. The transverse momentum spectra shown in fig. 12.5 refer to the target fragmentation region, and therefore the absolute number is too small, whereas the shape of the spectra is quite good.

Strange particle spectra are shown in figs. 12.6 and 12.7. Whereas the simulations agree with the data for the kaons, the spectra are largely underestimated in case of lambdas, in particular in the backward region, where rescattering plays a dominant role.

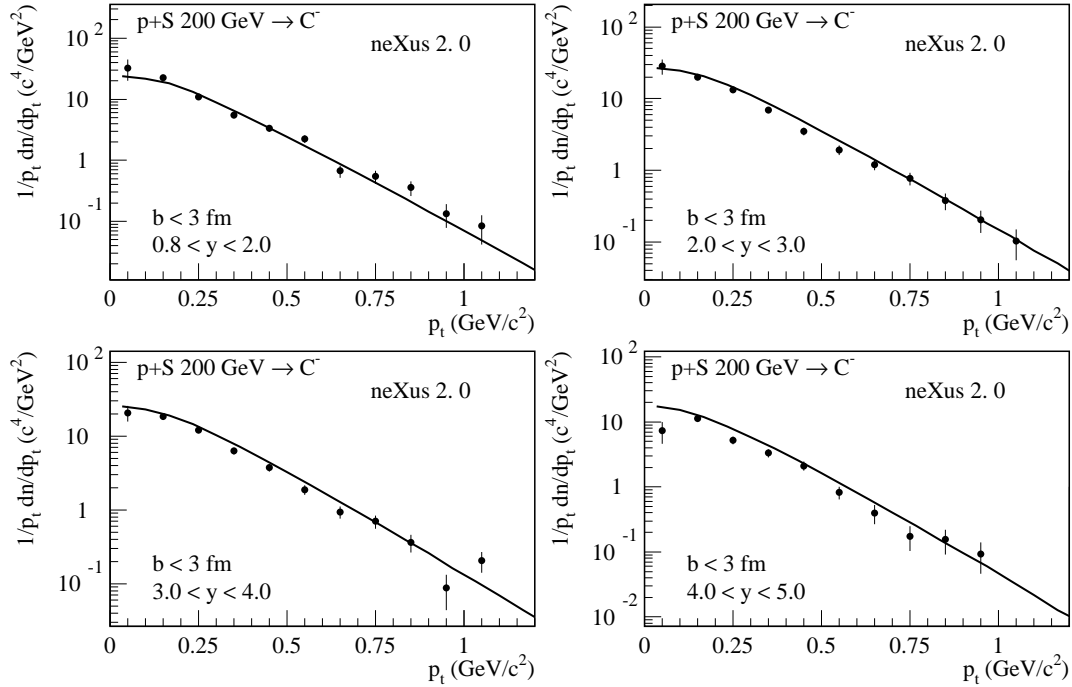


Figure 12.2: Transverse momentum distributions of negatively charged particles for different $p+S$ collisions at 200 GeV (lab).

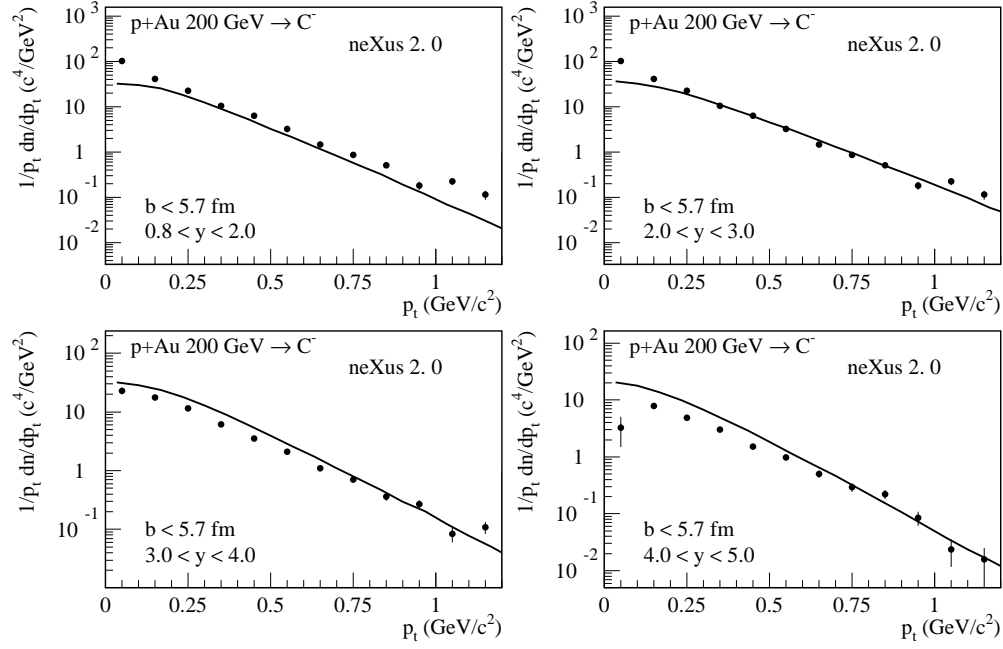


Figure 12.3: Transverse momentum distributions of negatively charged particles for different $p + Au$ collisions at 200 GeV (lab).

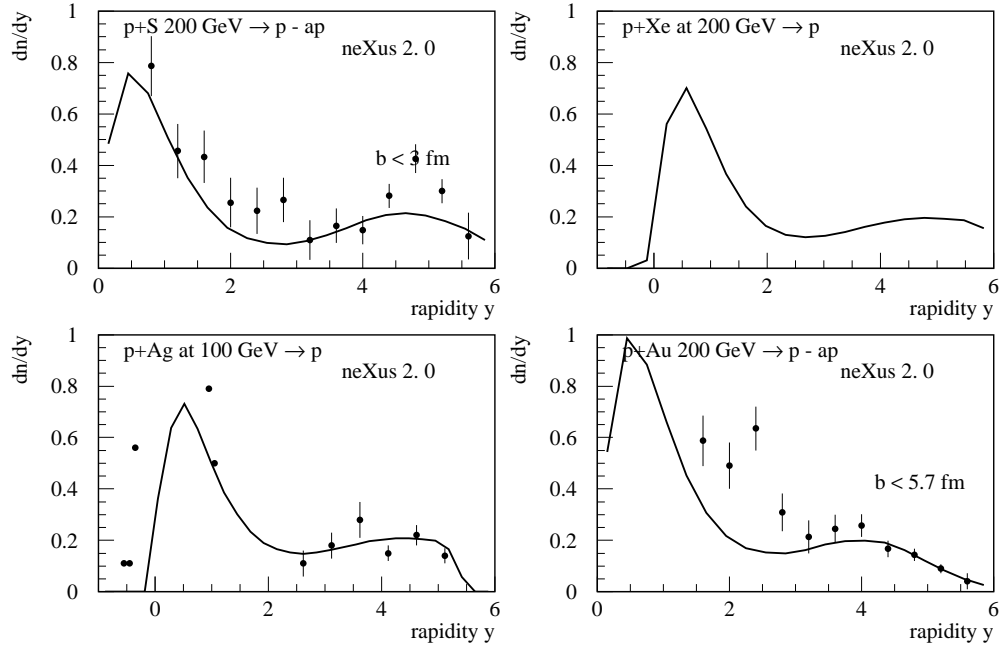


Figure 12.4: Rapidity distributions of net protons for different $p + A$ collisions at 200 GeV (lab).

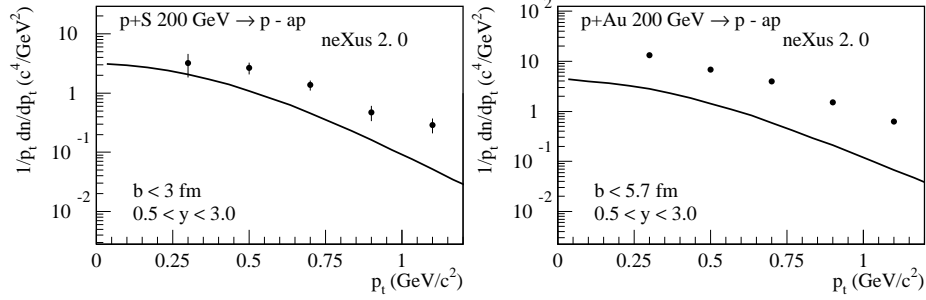


Figure 12.5: Transverse momentum spectra of net protons for different $p + A$ collisions at 200 GeV (lab).

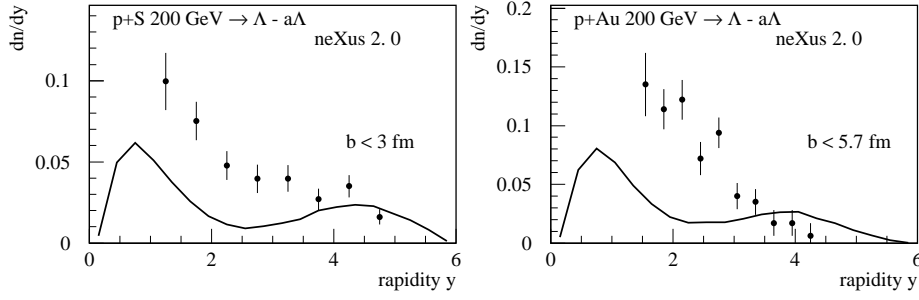


Figure 12.6: Rapidity distributions of net lambdas for different $p + A$ collisions at 200 GeV (lab).

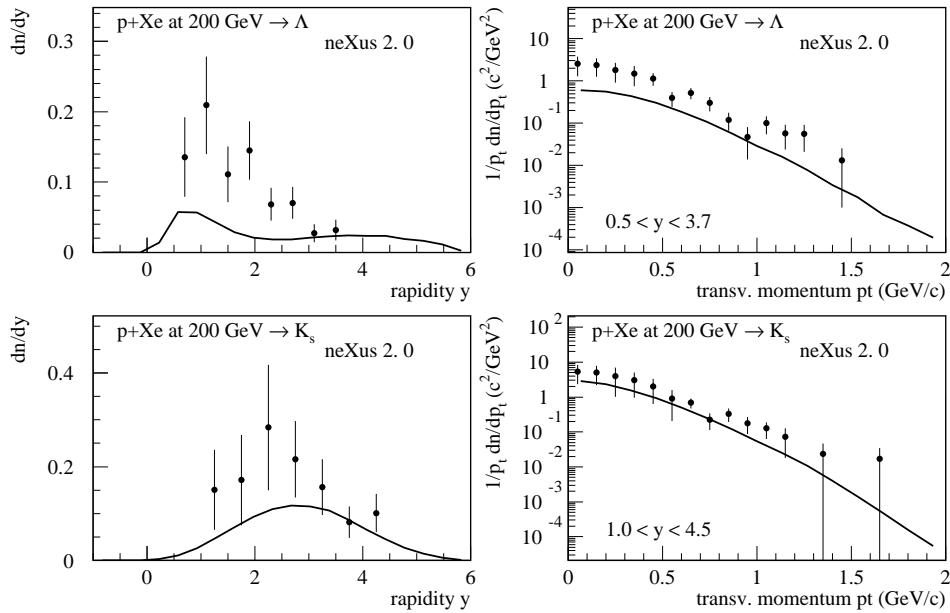


Figure 12.7: Rapidity and p_t spectra of net lambdas and K_s for $p + Xe$ collisions at 200 GeV (lab).

12.2 Nucleus-Nucleus Scattering

Again, we show results of the bare NEXUS model, without any secondary interactions. Considering rapidity distributions of negatively charged particles, as shown in fig. 12.8, we observe a strong excess at central rapidities compared to the data. Rescattering will partly cure this, but not completely. For asymmetric systems like for example S+Ag, we observe in addition a missing asymmetry in the shape of the rapidity spectrum, in other words, the simulated spectrum is too symmetric. This is not surprising, since in our approach AGK cancelations apply, which make $A + B$ spectra identical to the $p + p$ ones, up to a factor. Rescattering will not cure this, since it acts essentially at central rapidities. But we expect another important effect due to additional screening effects coming from contributions of enhanced Pomeron diagrams. In fig. 12.9, we show

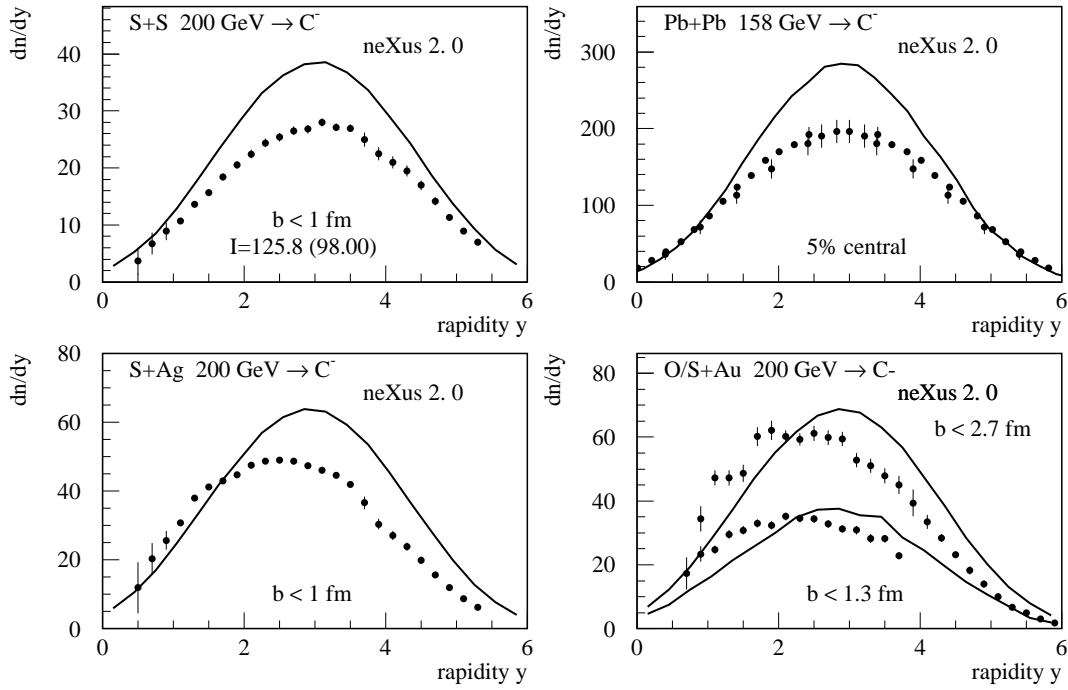


Figure 12.8: Rapidity distributions of negatively charged particles for different $A + B$ collisions at 200 GeV (lab).

transverse momentum or transverse mass spectra of negatively charged particles for different $A + B$ collisions at 200 GeV (lab). Several rapidity windows are shown; from top to bottom: 3.15-3.65, 3.65-4.15, 4.15-4.65, 4.65-5.15, 5.15-5.65 in case of Pb+Pb and 0.8-2, 2-3, 3-4, 4-4.4 for the other reactions. The lowest curves are properly normalized, the next ones are multiplied by ten, etc. We again observe an excess at certain rapidities, as already discussed above. In addition, in particular for heavy systems, the slopes are too steep, there is clearly some need of secondary interactions to “heat up” the system. This is consistent with the fact that the multiplicity is too high: collective motion should reduce the multiplicity but instead increase the transverse energy per particle.

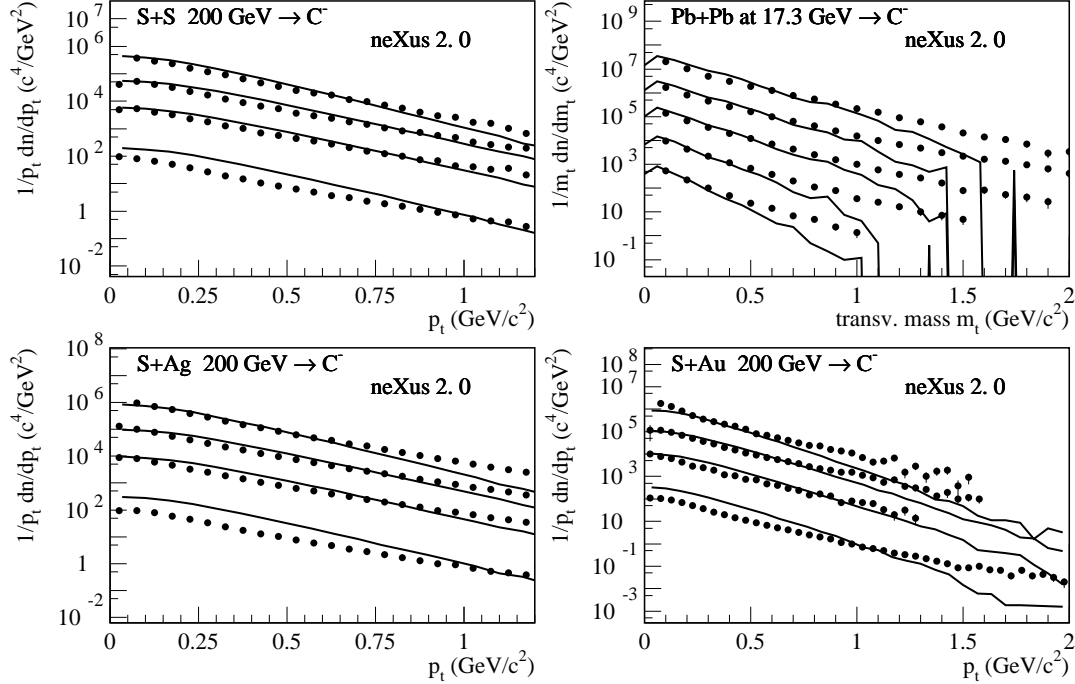


Figure 12.9: Transverse momentum or transverse mass spectra of negatively charged particles in several rapidity windows (see text) for different $A + B$ collisions at 200 GeV (lab).

In fig. 12.10, we show rapidity distributions of net protons (protons minus anti-protons) for different $A + B$ collisions at 200 GeV. For the asymmetric systems one observes clearly the effect of missing target nucleons, which should be cured by rescattering. The simulated results for symmetric systems are close to the data, rescattering does not contribute much here. But as for pion production, we expect also some changes due to screening effects. Transverse momentum spectra, as shown in fig. 12.11, show a similar behavior as for pions but even more pronounced: the theoretical spectra are much too steep, in particular for heavy systems.

In fig. 12.12-12.15, we show rapidity spectra of strange particles. K^- seem to be correct, whereas K^+ are in general somewhat too low compared to the data. Lambdas and anti-lambdas are way too low. For these particles, rescattering has to provide most of the particles which are finally observed.

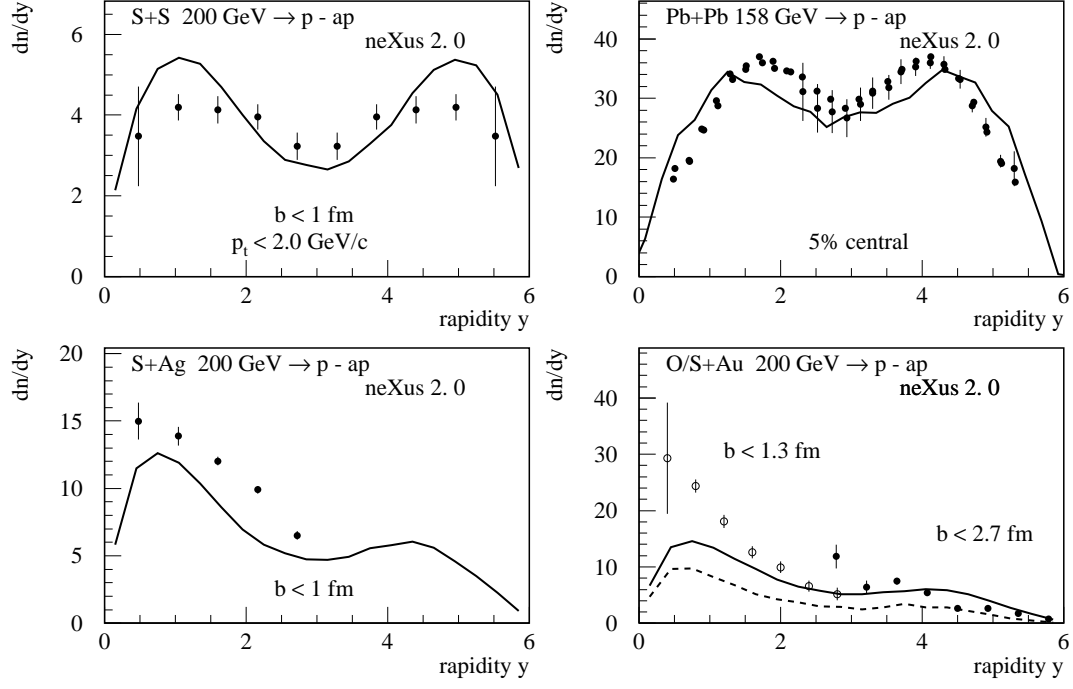


Figure 12.10: Rapidity distributions of net protons for different $A + B$ collisions at 200 GeV (lab).

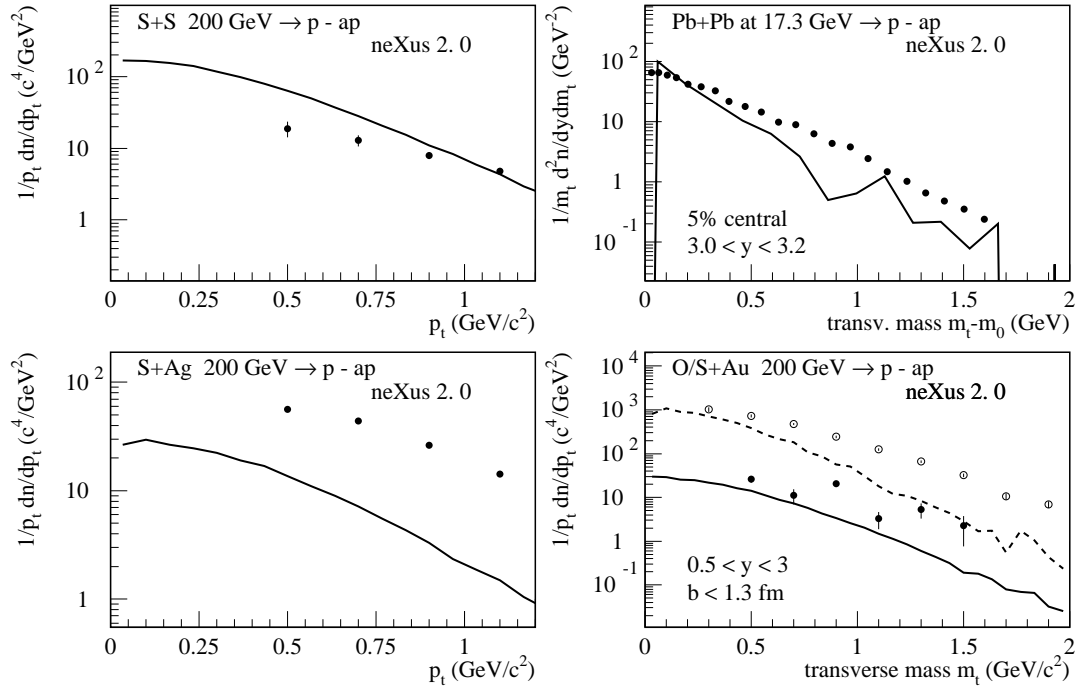


Figure 12.11: p_t distributions of net protons for different $A + B$ collisions at 200 GeV (lab).

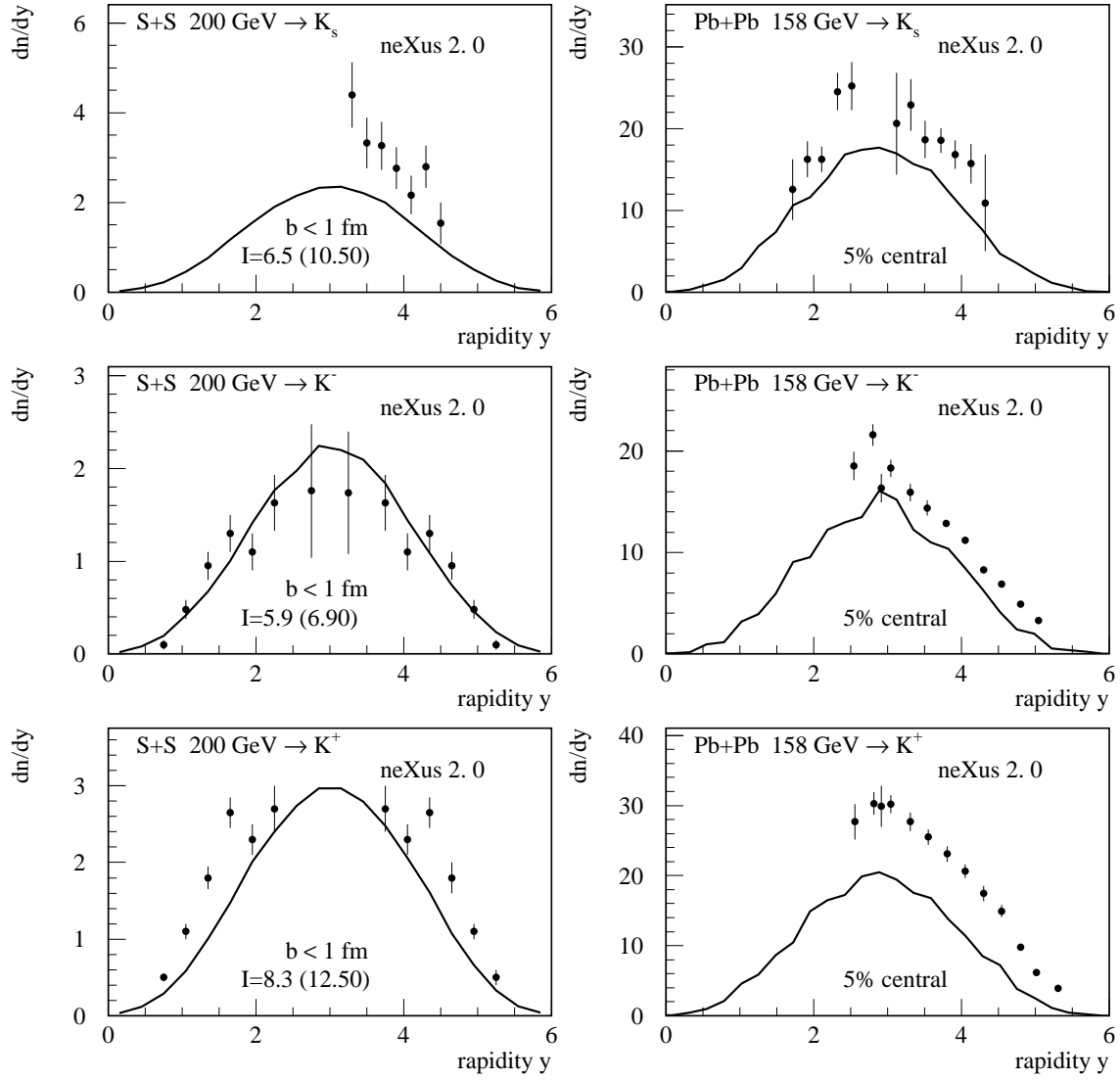


Figure 12.12: Rapidity distributions of kaons for S+S and Pb+Pb.

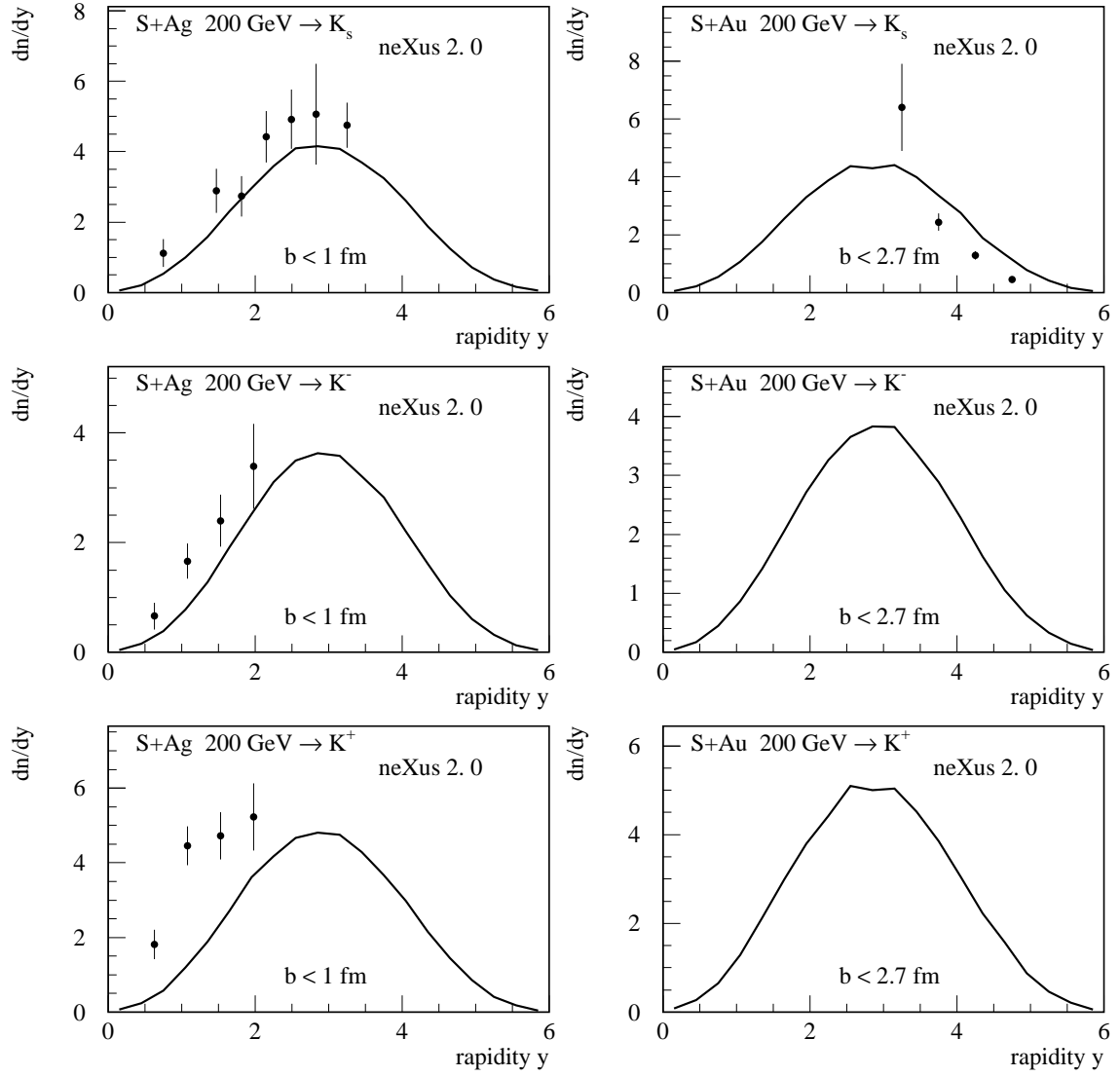


Figure 12.13: Rapidity distributions of kaons for S+Ag and S+Au.

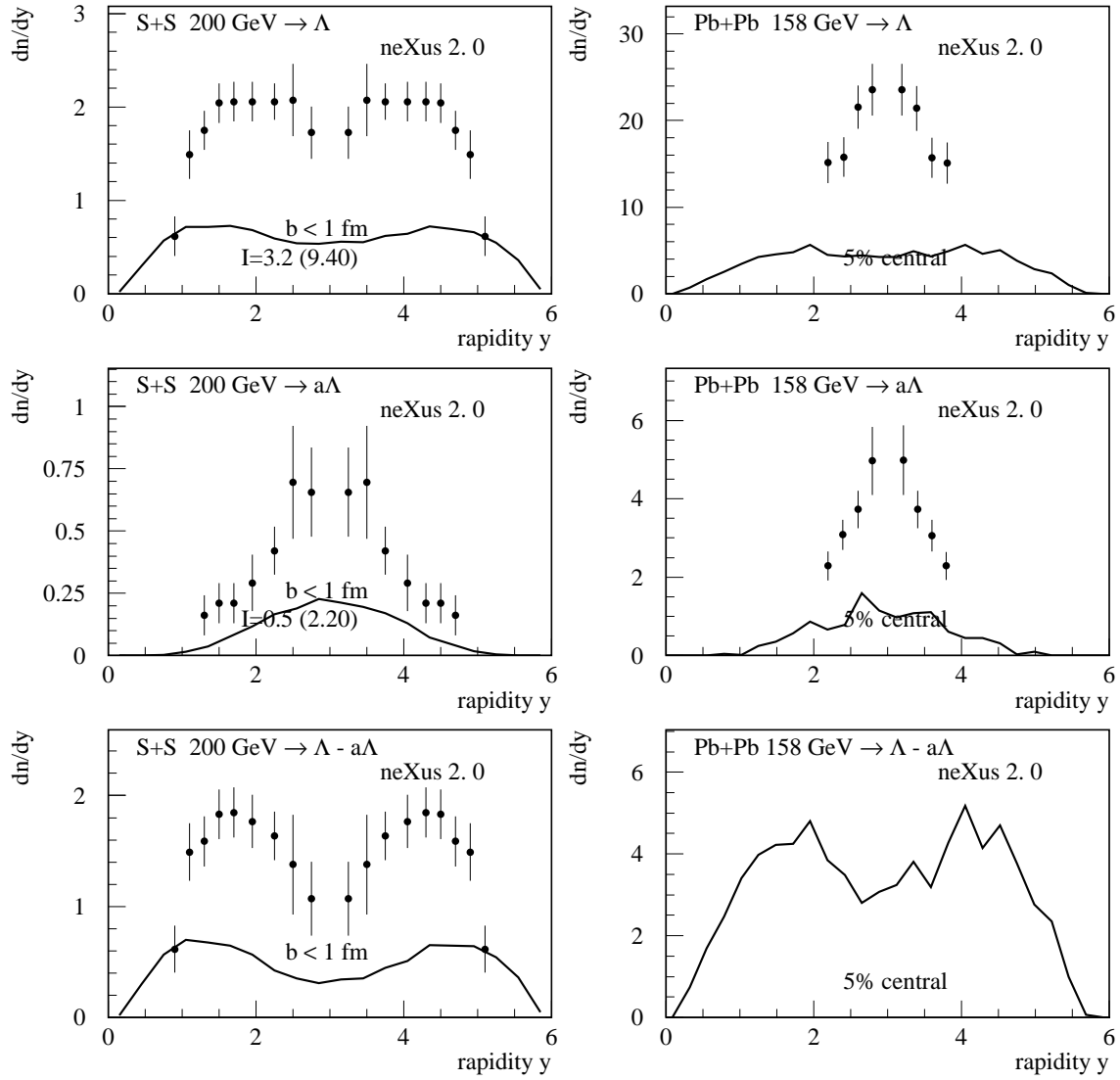


Figure 12.14: Rapidity distributions of (from top to bottom) lambdas, anti-lambdas, and net lambdas for S+S and Pb+Pb.

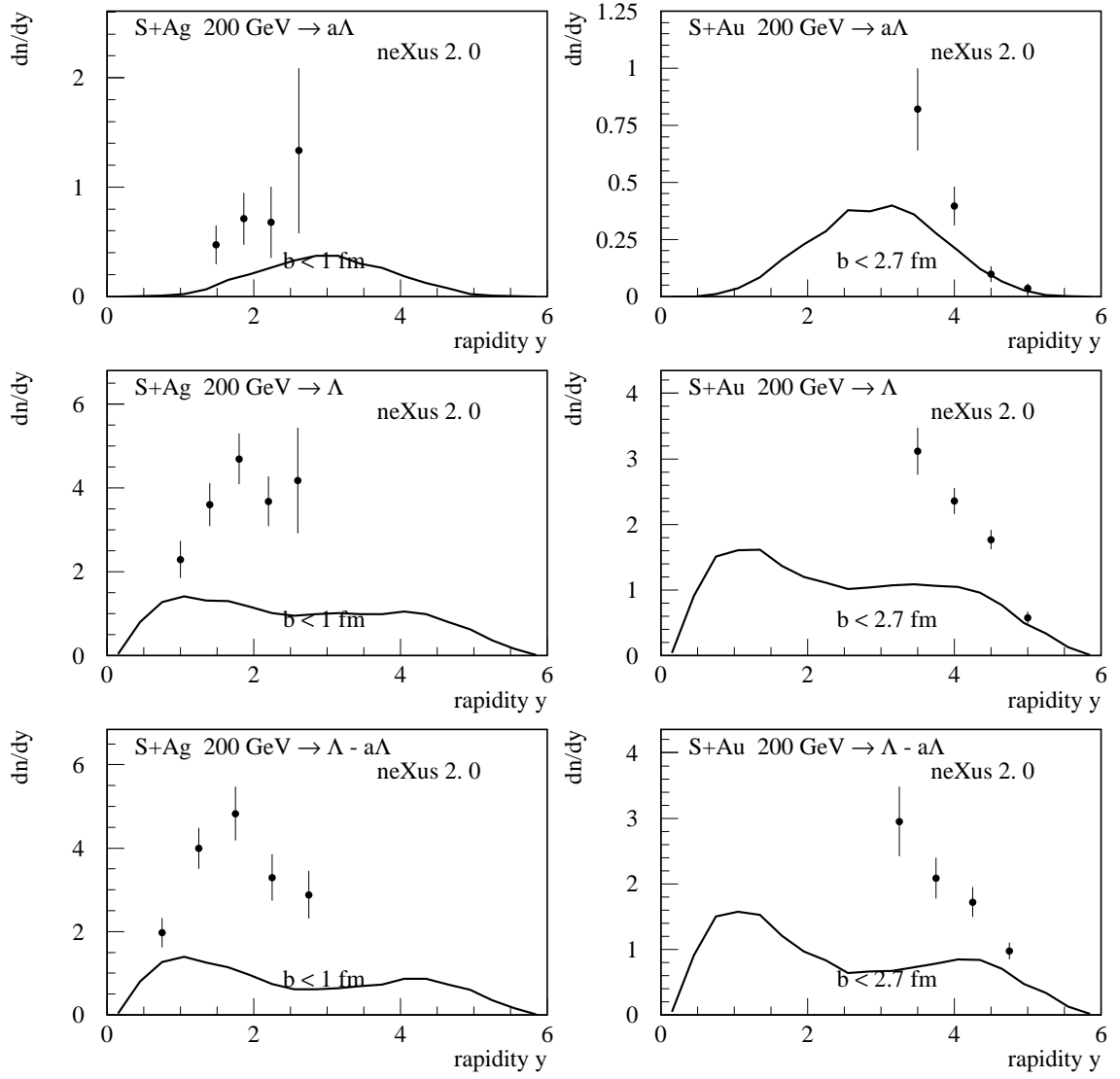


Figure 12.15: Rapidity distributions of (from top to bottom) lambdas, anti-lambdas, and net lambdas for S+Ag and S+Au.

Chapter 13

Summary

We presented a new approach for hadronic interactions and for the initial stage of nuclear collisions, which solves several conceptual problems of certain classes of models, which are presently widely used in order to understand experimental data.

The main problem of these models is the fact that energy is not conserved in a consistent fashion: the fact that energy needs to be shared between many elementary interactions in case of multiple scattering is well taken into account when calculating particle production, but energy conservation is not taken care of in cross section calculations. Related to this problem is the fact that different elementary interactions in case of multiple scattering are usually not treated equally, so the first interaction is usually considered to be quite different compared to the subsequent ones.

We provided a rigorous treatment of the multiple scattering aspect, such that questions as energy conservation are clearly determined by the rules of field theory, both for cross section and particle production calculations. In both cases, energy is properly shared between the different interactions happening in parallel. This is the most important and new aspect of our approach, which we consider to be a first necessary step to construct a consistent model for high energy nuclear scattering.

Another important aspect of our approach is the hypothesis that particle production is a universal process for all the elementary interactions, from e^+e^- annihilation to nucleus-nucleus scattering. That is why we also carefully study e^+e^- annihilation and deep inelastic scattering. This allows to control reasonably well for example the hadronization procedure, which is not treatable theoretically from first principles.

This work has been funded in part by the IN2P3/CNRS (PICS 580) and the Russian Foundation of Basic Researches (RFBR-98-02-22024).

Appendix A

Kinematics of Two Body Collisions

A.1 Conventions

We consider a scattering of a projectile P on a target T (hadron-hadron or parton-parton). We define the incident 4-momenta to be p and p' and the transferred momentum q , so that the outgoing momenta are $\tilde{p} = p + q$ and $\tilde{p}' = p' - q$, see fig. A.1. We define as usual the Mandelstam variables

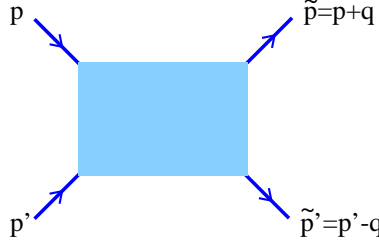


Figure A.1: Two body kinematics.

$$s = (p + p')^2, \quad t = (\tilde{p} - p)^2. \quad (\text{A.1})$$

Usually, we employ light cone momentum variables, connected to the energy and z -component of the particle momentum, as

$$p^\pm = p_0 \pm p_z, \quad (\text{A.2})$$

and we denote the particle 4-vector as

$$p = (p^+, p^-, \vec{p}_\perp). \quad (\text{A.3})$$

A.2 Proof of the Impossibility of Longitudinal Excitations

Here, we present a mathematical proof of the well known fact that longitudinal excitations are impossible at high energies. Consider a collision between two hadrons h and h' which leads to two hadrons \tilde{h} and \tilde{h}' ,

$$h(p) + h'(p') \rightarrow \tilde{h}(\tilde{p}) + \tilde{h}'(\tilde{p}') \quad (\text{A.4})$$

with four-momenta $p, p', \tilde{p}, \tilde{p}'$. As usual, we define $s = (p + p')^2$ and $t = (\tilde{p} - p)^2$. For the following, we consider always the limit $s \rightarrow \infty$ and ignore terms of the order p^2/s . We expand $q = \tilde{p} - p = p' - \tilde{p}'$ as

$$q = \alpha p + \beta p' + q_\perp, \quad (\text{A.5})$$

and obtain

$$\alpha = \frac{2qp'}{s}, \beta = \frac{2qp}{s}, \quad (\text{A.6})$$

where we used

$$p^2 = 0, p'^2 = 0, pq_{\perp} = p'q_{\perp} = 0, s = 2pp'. \quad (\text{A.7})$$

We get

$$q = \frac{q^2}{s}(p - p') + q_{\perp}, \quad (\text{A.8})$$

having used

$$q = \tilde{p} - p = p' - \tilde{p}', p^2 = p'^2 = 0, p'\tilde{p}' = p\tilde{p} = -q^2/2. \quad (\text{A.9})$$

This proves

$$q = q_{\perp} \quad (\text{A.10})$$

for $s \rightarrow \infty$ and limited q^2 . In other words, momentum transfer is purely transversal at high energies.

Appendix B

Partonic Interaction Amplitudes

B.1 Semi-hard Parton-Parton Scattering

Let us derive the mathematical expression corresponding to the contribution of so-called semi-hard parton-parton scattering, see fig. B.1. Here p, p' are the 4-momenta of the constituent partons

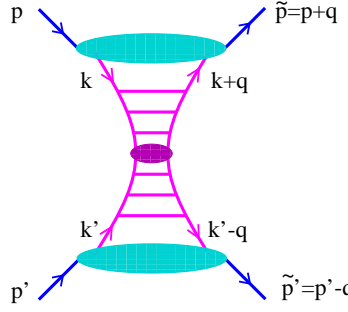


Figure B.1: Semi-hard contribution $T_{\text{sea-sea}}$.

participating in the process. We denote by k, k' the 4-momenta of the first partons entering the perturbative evolution, i.e. the initial partons for the perturbative parton cascade (characterized by parton virtualities $Q^2 > Q_0^2$). Further, we define light cone momentum fractions

$$x^+ = \frac{p^+}{p_0^+}, \quad x^- = \frac{p'^-}{p_0^-}, \quad x_1^+ = \frac{k^+}{p_0^+}, \quad x_1^- = \frac{k'^-}{p_0^-}, \quad (\text{B.1})$$

with p_0^\pm being the total light-cone momenta for the interaction.

At high energies, the dominant contribution to the process comes from the kinematical region where these partons are slow, i.e. $x_1^\pm \ll x^\pm$, so that a relatively small contribution of the perturbative parton cascade (of the ladder part of the diagram of the fig. B.1) is compensated by the large density of such partons, resulted from the soft pre-evolution [24, 57]. Since the initial partons k, k' are gluons or sea quarks (contrary to valence quarks) we talk about “sea-sea” contribution.

Let us first consider the case where the intermediate partons k, k' are gluons. Then the amplitude for the diagram of fig. B.1 can be written as

$$\begin{aligned} iT_{\text{sea-sea}}^{gg}(\hat{s}, t) &= \int \frac{d^4 k}{(2\pi)^4} \frac{d^4 k'}{(2\pi)^4} \sum_{\lambda\lambda'\gamma\gamma'\delta\delta'\tau\tau'} iM_{\text{soft}}^g(p, -k, p+q, -k-q)_{\lambda\gamma} \\ &\times D_{\lambda\delta}^g(k^2) D_{\gamma\tau}^g((k+q)^2) iM_{\text{hard}}^{gg}(k, k', k+q, k'-q, Q_0^2)_{\delta\tau\delta'\tau'} \\ &\times D_{\lambda'\delta'}^g(k'^2) D_{\gamma'\tau'}^g((k'-q)^2) iM_{\text{soft}}^g(p', -k', p'-q, -k'+q)_{\lambda'\gamma'} , \end{aligned} \quad (\text{B.2})$$

where the amplitude $M_{\text{hard}}^{gg}(k, k', k+q, k'-q, Q_0^2)_{\delta\tau\delta'\tau'}$ represents the perturbative contribution of the parton ladder with the initial partons of momenta k, k' and with the momentum transfer along the ladder q (hard parton-parton scattering), the amplitude $M_{\text{soft}}^g(p, k, p+q, k-q)_{\lambda\gamma}$ corresponds to the non-perturbative soft interaction between the constituent parton with the 4-momentum p and the gluon with the 4-momentum k , and $D_{\lambda\delta}^g(k)$ is the non-perturbative gluon propagator, $D_{\lambda\delta}^g(k) = i\tilde{D}^g(k^2) \varepsilon_{\lambda\delta}(k)$ with $\varepsilon_{\lambda\delta}(k)$ being the usual gluon polarization tensor in the axial gauge; $\lambda, \gamma, \delta, \dots$ denotes symbolically the combination of color and Lorentz indexes for the intermediate gluons.

As by construction partons of large virtualities $Q^2 > Q_0^2$ can only appear in the parton ladder part of the diagram of the fig. B.1, we assume that the integral $\int d^4k$ converges in the region of restricted virtualities $k^2 \sim -s_0$ with $s_0 \simeq 1 \text{ GeV}^2$ being the typical hadronic mass scale, i.e. the combination

$$M_{\text{soft}}^g(p, -k, p+q, -k-q)_{\lambda\gamma} D_{\lambda\delta}^g(k^2) D_{\gamma\tau}^g((k+q)^2) \quad (\text{B.3})$$

drops down fast with increasing $|k^2|$; this implies that the transverse momentum k_\perp is also restricted to the region $k_\perp \leq s_0$. Similar arguments apply for k' . Further we make the usual assumption that longitudinal polarizations in the gluon propagators $D_{\lambda\delta}^g(k^2)$ are canceled in the convolution with the soft contribution M_{soft}^g even for finite gluon virtualities k^2 [13]. Finally we assume that in the considered limit $x_1^\pm \ll x^\pm$ the amplitude $M_{\text{soft}}^g(p, k, p+q, k-q)_{\lambda\gamma}$ is governed by the non-perturbative soft Pomeron exchange between the constituent parton p and the gluon k , which implies in particular that it has the singlet structure in the color and Lorentz indexes:

$$M_{\text{soft}}^g(p, k, p+q, k-q)_{\lambda\gamma} \sim \delta_\gamma^\lambda. \quad (\text{B.4})$$

Then, for small momentum transfer q in the process of fig. B.1 the intermediate gluons of momenta $k, k', k+q, k'-q$ can be considered as real (on-shell) ones with respect to the perturbative parton evolution in the ladder, characterized by large momentum transfers $Q^2 > Q_0^2$. Then we obtain

$$\begin{aligned} \frac{1}{K_g^2} \sum_{\lambda\lambda'\delta\delta'\tau\tau'} M_{\text{hard}}^{gg}(k, k', k+q, k'-q, Q_0^2)_{\delta\tau\delta'\tau'} \\ \times \varepsilon_{\lambda\delta}(k) \varepsilon_{\delta\tau}(k+q) \varepsilon_{\lambda'\delta'}(k') \varepsilon_{\delta'\tau'}(k'-q) \simeq T_{\text{hard}}^{gg}(\hat{s}_{\text{hard}}, q^2, Q_0^2), \end{aligned} \quad (\text{B.5})$$

where the averaging over the spins and the colors of the initial gluons k, k' is incorporated in the factor K_g^2 , $T_{\text{hard}}^{gg}(\hat{s}_{\text{hard}}, t, Q_0^2)$ is defined in (2.16), and $\hat{s}_{\text{hard}} = (k+k')^2 \simeq k^+k'^- = x_1^+x_1^-s$.

Now, using (B.4-B.5) we can rewrite (B.2) as

$$\begin{aligned} iT_{\text{sea-sea}}^{gg}(\hat{s}, t) &= \int \frac{dk^+ dk^- d^2k_\perp}{2(2\pi)^4} \frac{dk'^+ dk'^- d^2k'_\perp}{2(2\pi)^4} iT_{\text{hard}}^{gg}(\hat{s}_{\text{hard}}, q^2, Q_0^2) \\ &\times \left[-i \sum_{\lambda} M_{\text{soft}}^g(p, -k, p+q, -k-q)_{\lambda\lambda} \tilde{D}^g(k^2) \tilde{D}^g((k+q)^2) \right] \\ &\times \left[-i \sum_{\lambda'} M_{\text{soft}}^g(p', -k', p'-q, -k'+q)_{\lambda'\lambda'} \tilde{D}^g(k'^2) \tilde{D}^g((k'-q)^2) \right]. \end{aligned} \quad (\text{B.6})$$

It is convenient to perform separately the integrations over $k^-, k'^+, k_\perp, k'_\perp$ keeping in mind that the only dependence on those variables in the eq. (B.6) appears in the non-perturbative contributions in the square brackets. Let us consider the first of those contributions, corresponding to the upper soft blob at fig. B.1 together with the intermediate gluon propagators (for the lower blob the derivation is identical). Being described by the soft Pomeron exchange, the amplitude $M_{\text{soft}}^g(p, -k, p+q, -k-q)_{\lambda\lambda}$ is an analytical function of the energy invariants $\hat{s}_{\text{soft}} = (p-k)^2 \simeq -p^+k^-$ and $\hat{u}_{\text{soft}} = (p+k+q)^2 \simeq p^+k^-$ with the singularities in the complex k^- -plane, corresponding to the values $\hat{s}_{\text{soft}} = s' - i0$ for all real s' which are greater than some threshold value s_{thr} for the Pomeron asymptotics to be applied, as well as for $\hat{u}_{\text{soft}} = u' - i0$, where $u' > u_{\text{thr}}$

with some threshold value u_{thr} [14]. Thus one has the singularities in the variable k^- in the upper half of the complex plane at $k^- \simeq (-s' - i0)/p^+$ and in the lower half of the complex plane at $k^- \simeq (u' - i0)/p^+$. Then one can use the standard trick to rotate the integration contour C in the variable k^- such that the new contour C' encloses the left-hand singularities in k^- , corresponding to the right-hand singularities in the variable \hat{s}_{soft} [14]. Then one ends up with the integral over the discontinuity of the amplitude M_{soft}^g on the left-hand cut in the variable k^- , which is up to a minus sign equal to the discontinuity on the right-hand cut in \hat{s}_{soft} :

$$\begin{aligned} & \int_{-\infty}^{+\infty} dk^- \left[\sum_{\lambda} M_{\text{soft}}^g(p, -k, p+q, -k-q)_{\lambda\lambda} \tilde{D}^g(k^2) \tilde{D}^g((k+q)^2) \right] \\ &= \int_{-\infty}^{-s_{\text{thr}}/k^+} dk^- \text{disc}_{\hat{s}_{\text{soft}}} \left[\sum_{\lambda} M_{\text{soft}}^g(p, -k, p+q, -k-q)_{\lambda\lambda} \tilde{D}^g(k^2) \tilde{D}^g((k+q)^2) \right] \quad (\text{B.7}) \end{aligned}$$

$$= \int_{-\infty}^{-s_{\text{thr}}/k^+} dk^- 2i \text{Im} \left[\sum_{\lambda} M_{\text{soft}}^g(p, -k, p+q, -k-q)_{\lambda\lambda} \tilde{D}^g(k^2) \tilde{D}^g((k+q)^2) \right]. \quad (\text{B.8})$$

Now, using $\int dk^- = \int dk^2/k^+$ and recalling our assumption that the integral over k^2 gets dominant contribution from the region $k^2 \sim -s_0$, we may write

$$\begin{aligned} & \int \frac{dk^- d^2 k_{\perp}}{(2\pi)^4} \text{Im} \left[\sum_{\lambda} M_{\text{soft}}^g(p, -k, p+q, -k-q)_{\lambda\lambda} \tilde{D}^g(k^2) \tilde{D}^g((k+q)^2) \right] \\ &= \frac{1}{k^+} \text{Im} T_{\text{soft}}^g(\hat{s}_{\text{soft}}, q^2) \end{aligned} \quad (\text{B.9})$$

with

$$\hat{s}_{\text{soft}} = s_0 \frac{p^+}{k^+} = s_0 \frac{x^+}{x_1^+}. \quad (\text{B.10})$$

The integrations over k^2 in the vicinity of $k^2 = -s_0$ and over $k_{\perp} \leq s_0$ are supposed to just contribute to the redetermination of the Pomeron-gluon coupling of the usual soft Pomeron amplitude, and therefore we parameterize the amplitude T_{soft}^g as (compare with eq. (2.5))

$$T_{\text{soft}}^g(\hat{s}, t) = 8\pi s_0 \eta(t) \gamma_{\text{part}} \gamma_g \left(\frac{\hat{s}}{s_0} \right)^{\alpha_{\text{P}}(0)} \exp\left(\lambda_{\text{soft}}^{(1)}(\hat{s}/s_0) t\right) \left(1 - \frac{s_0}{\hat{s}}\right)^{\beta_g}, \quad (\text{B.11})$$

with

$$\lambda_{\text{soft}}^{(1)}(z) = R_{\text{part}}^2 + \alpha'_{\text{soft}} \ln z, \quad (\text{B.12})$$

where we used γ_g for the Pomeron-gluon coupling and we neglected the radius of the Pomeron-gluon vertex assuming that the coupling is local in the soft Pomeron; the factor $(1 - s_0/\hat{s})^{\beta_g}$ is included to ensure that the Pomeron has sufficiently large mass, which is the necessary condition for applying Regge description for the soft evolution. As we shall see below the parameter β_g determines the gluon momentum distribution in the Pomeron at $x_1^{\pm} \rightarrow x^{\pm}$.

Finally, using the above results we obtain

$$iT_{\text{sea-sea}}^{gg}(\hat{s}, t) = \int \frac{dk^+}{k^+} \frac{dk'^-}{k'^-} \text{Im} T_{\text{soft}}^g(\hat{s}_{\text{soft}}, t) \text{Im} T_{\text{soft}}^g(\hat{s}'_{\text{soft}}, t) iT_{\text{hard}}^{gg}(\hat{s}_{\text{hard}}, t, Q_0^2) \quad (\text{B.13})$$

$$= \int_0^1 \frac{dz^+}{z^+} \frac{dz^-}{z^-} \text{Im} T_{\text{soft}}^g\left(\frac{s_0}{z^+}, t\right) \text{Im} T_{\text{soft}}^g\left(\frac{s_0}{z^-}, t\right) iT_{\text{hard}}^{gg}(z^+ z^- \hat{s}, t, Q_0^2), \quad (\text{B.14})$$

where the following definitions have been used:

$$z^{\pm} = \frac{x_1^{\pm}}{x^{\pm}}, \quad \hat{s}_{\text{soft}} = s_0 \frac{x^+}{x_1^+} = \frac{s_0}{z^+}, \quad \hat{s}'_{\text{soft}} = s_0 \frac{x^-}{x_1^-} = \frac{s_0}{z^-}, \quad \hat{s}_{\text{hard}} = x_1^+ x_1^- s = z^+ z^- \hat{s}. \quad (\text{B.15})$$

In the case of the intermediate parton k being a (anti-)quark, we assume that it originates from local gluon splitting in the soft Pomeron. Thus we neglect the slope of the (non-perturbative) gluon-quark vertex. Using the usual Altarelli-Parisi kernel $P_g^q(z) = \frac{1}{2}(z^2 + (1-z)^2)$ for the gluon light cone momentum partition between the quark and the anti-quark, we get the corresponding amplitude $T_{\text{sea-sea}}^{qq}(\hat{s}, t)$ as

$$iT_{\text{sea-sea}}^{qq}(\hat{s}, t) = \int_0^1 \frac{dz^+}{z^+} \frac{dz^-}{z^-} \text{Im} T_{\text{soft}}^q\left(\frac{s_0}{z^+}, t\right) \text{Im} T_{\text{soft}}^g\left(\frac{s_0}{z^-}, t\right) iT_{\text{hard}}^{qq}(z^+ z^- \hat{s}, t, Q_0^2), \quad (\text{B.16})$$

where the imaginary part of the amplitude $\text{Im} T_{\text{soft}}^q$ for the soft Pomeron exchange between the constituent parton and the quark $q \in \{u, d, s, \bar{u}, \bar{d}, \bar{s}\}$ is expressed via $\text{Im} T_{\text{soft}}^g$ as

$$\text{Im} T_{\text{soft}}^q(\hat{s}_{\text{soft}}, t) = \gamma_{qg} \int d\xi P_g^q(\xi) \text{Im} T_{\text{soft}}^g(\xi \hat{s}_{\text{soft}}, t), \quad (\text{B.17})$$

with γ_{qg} representing the quark-gluon vertex value and ξ being the ratio of the quark and the parent gluon light cone momentum, $\xi = k^+/k_g^+$; the mass squared of the Pomeron between the initial constituent parton and the gluon is then

$$(p - k_g)^2 \simeq s_0 \frac{p^+}{k_g^+} = \xi \hat{s}_{\text{soft}}. \quad (\text{B.18})$$

The full amplitude for the semi-hard scattering is the sum of the different terms discussed above, i.e.

$$\begin{aligned} iT_{\text{sea-sea}}(\hat{s}, t) &= \sum_{jk} iT_{\text{sea-sea}}^{jk}(\hat{s}, t) \\ &= \sum_{jk} \int_0^1 \frac{dz^+}{z^+} \frac{dz^-}{z^-} \text{Im} T_{\text{soft}}^j\left(\frac{s_0}{z^+}, t\right) \text{Im} T_{\text{soft}}^k\left(\frac{s_0}{z^-}, t\right) iT_{\text{hard}}^{jk}(z^+ z^- \hat{s}, t, Q_0^2), \end{aligned} \quad (\text{B.19})$$

where j, k denote the types (flavors) of the initial partons for the perturbative evolution (quarks or gluons).

The discontinuity of the amplitude $T_{\text{sea-sea}}(\hat{s}, t)$ on the right-hand cut in the variable \hat{s} defines the contribution of the cut diagram of the fig. B.1. Cutting procedure amounts here to replace the hard parton-parton scattering amplitude $iT_{\text{hard}}^{jk}(\hat{s}_{\text{hard}}, t, Q_0^2)$ in (B.19) by $2\text{Im} T_{\text{hard}}^{jk}(\hat{s}_{\text{hard}}, t, Q_0^2)$, whereas the contributions of the soft parton cascades $\text{Im} T_{\text{soft}}^j$ stay unchanged as they are already defined by the discontinuities in the corresponding variables \hat{s}_{soft} and \hat{s}'_{soft} . So the cut diagram contribution is just $2\text{Im} T_{\text{sea-sea}}(\hat{s}, t)$. At $t = 0$ it defines the cross section for the semi-hard parton-parton scattering:

$$\sigma_{\text{sea-sea}}(\hat{s}) = \frac{1}{2\hat{s}} 2\text{Im} T_{\text{sea-sea}}(\hat{s}, 0) = \sum_{jk} \int_0^1 dz^+ dz^- E_{\text{soft}}^j(z^+) E_{\text{soft}}^k(z^-) \sigma_{\text{hard}}^{jk}(z^+ z^- \hat{s}, Q_0^2), \quad (\text{B.20})$$

where we used the explicit expressions (2.16), (B.11), (B.17) for T_{hard}^{jk} , T_{soft}^j , and the functions E_{soft}^j are defined as

$$E_{\text{soft}}^g(z) = 8\pi s_0 \gamma_{\text{part}} \gamma_g z^{-\alpha_{\text{soft}}(0)} (1-z)^{\beta_g} \quad (\text{B.21})$$

$$E_{\text{soft}}^q(z) = \gamma_{qg} \int_z^1 d\xi P_g^q(\xi) E_{\text{soft}}^g\left(\frac{z}{\xi}\right). \quad (\text{B.22})$$

It is easy to see that $E_{\text{soft}}^j(z)$ has the meaning of the momentum distribution of parton j at the scale Q_0^2 for an elementary interaction, i.e. parton distribution **in the soft Pomeron**. Introducing the gluon splitting probability w_{split} and the coupling $\tilde{\gamma}_g$ via

$$\gamma_{qg} \gamma_g = w_{\text{split}} \tilde{\gamma}_g, \quad \gamma_g = (1 - w_{\text{split}}) \tilde{\gamma}_g, \quad (\text{B.23})$$

the light cone momentum conservation reads

$$1 = \int_0^1 dz \sum_j z E_{\text{soft}}^j(z) = 8\pi s_0 \gamma_{\text{part}} \tilde{\gamma}_g \int_0^1 dz z^{1-\alpha_{\text{soft}}(0)} (1-z)^{\beta_g} \quad (\text{B.24})$$

and therefore

$$\tilde{\gamma}_g = \frac{1}{8\pi s_0 \gamma_{\text{part}}} \frac{\Gamma(3 - \alpha_{\text{soft}}(0) + \beta_g)}{\Gamma(2 - \alpha_{\text{soft}}(0)) \Gamma(1 + \beta_g)} \quad (\text{B.25})$$

B.2 Parton Evolution

In this appendix, we discuss the properties of the evolution function E_{QCD} , describing the perturbative evolution of partons.

The evolution function $E_{\text{QCD}}^{jm}(z, Q_0^2, Q^2)$ satisfies the usual DGLAP equation

$$\frac{dE_{\text{QCD}}^{jm}(Q_0^2, Q^2, x)}{d \ln Q^2} = \sum_k \int_x^1 \frac{dz}{z} \frac{\alpha_s}{2\pi} \tilde{P}_k^m(z) E_{\text{QCD}}^{jk}\left(\frac{x}{z}, Q_0^2, Q^2\right) \quad (\text{B.26})$$

with the initial condition $E_{\text{QCD}}^{jm}(Q_0^2, Q_0^2, z) = \delta_j^m \delta(1-z)$. Here $\tilde{P}_k^m(z)$ are the usual Altarelli-Parisi splitting functions, regularized at $z \rightarrow 1$ by the contribution of virtual emissions.

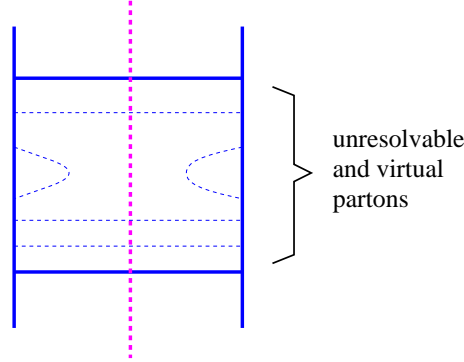


Figure B.2: Unresolvable emissions are summed over, providing the so-called Sudakov form factor.

One can introduce the concept of “resolvable” parton emission, i.e. an emission of a final (s -channel) parton with a finite share of the parent parton light cone momentum $(1-z) > \epsilon = p_{\perp \text{res}}^2 / Q^2$ (with finite relative transverse momentum $p_{\perp}^2 = Q^2(1-z) > p_{\perp \text{res}}^2$) [58] and use the so-called Sudakov form factor, corresponding to the contribution of any number of virtual and unresolvable emissions (i.e. emissions with $(1-z) < \epsilon$) - see fig. B.2.

$$\Delta^k(Q_0^2, Q^2) = \exp \left\{ \int_{Q_0^2}^{Q^2} \frac{dq^2}{q^2} \int_{1-\epsilon}^1 dz \frac{\alpha_s}{2\pi} \tilde{P}_k^k(z) \right\} \quad (\text{B.27})$$

This can also be interpreted as the probability of no resolvable emission between Q_0^2 and Q^2 .

Then E_{QCD}^{jm} can be expressed via $\bar{E}_{\text{QCD}}^{jm}$, corresponding to the sum of any number (but at least one) resolvable emissions, allowed by the kinematics:

$$E_{\text{QCD}}^{jm}(z, Q_0^2, Q^2) = \delta_j^m \delta(1-z) \Delta^j(Q_0^2, Q^2) + \bar{E}_{\text{QCD}}^{jm}(z, Q_0^2, Q^2), \quad (\text{B.28})$$

where $\bar{E}_{\text{QCD}}^{jm}(z, Q_0^2, Q^2)$ satisfies the integral equation

$$\begin{aligned} \bar{E}_{\text{QCD}}^{jm}(x, Q_0^2, Q^2) &= \int_{Q_0^2}^{Q^2} \frac{dQ_1^2}{Q_1^2} \left[\sum_k \int_x^{1-\epsilon} \frac{dz}{z} \frac{\alpha_s}{2\pi} P_k^m(z) \bar{E}_{\text{QCD}}^{jk}\left(\frac{x}{z}, Q_0^2, Q_1^2\right) + \right. \\ &\quad \left. + \Delta^j(Q_0^2, Q_1^2) \frac{\alpha_s}{2\pi} P_j^m(x) \right] \Delta^m(Q_1^2, Q^2) \end{aligned} \quad (\text{B.29})$$

Here $P_j^k(z)$ are the Altarelli-Parisi splitting functions for real emissions, i.e. without δ -function and regularization terms at $z \rightarrow 1$.

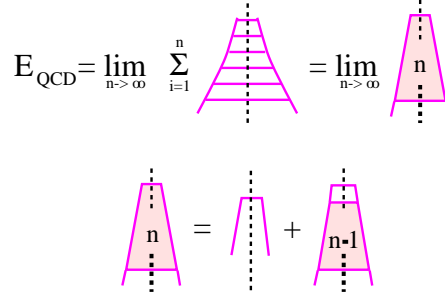


Figure B.3: The calculation of \bar{E}_{QCD} .

Eq. (B.29) can be solved iteratively, expressing $\bar{E}_{\text{QCD}}^{jm}$ as the contribution of at most n ($n \rightarrow \infty$) resolvable emissions (of an ordered ladder with at most n ladder rungs) - see fig. B.3:

$$\bar{E}_{\text{QCD}}^{jm}(Q_0^2, Q^2, x) = \lim_{n \rightarrow \infty} E_{\text{QCD}}^{(n)jm}(Q_0^2, Q^2, x), \quad (\text{B.30})$$

with

$$\begin{aligned} E_{\text{QCD}}^{(n)jm}(x, Q_0^2, Q^2) &= \int_{Q_0^2}^{Q^2} \frac{dQ_1^2}{Q_1^2} \left[\sum_k \int_x^{1-\epsilon} \frac{dz}{z} \frac{\alpha_s}{2\pi} P_k^m(z) E_{\text{QCD}}^{(n-1)jk}\left(\frac{x}{z}, Q_0^2, Q_1^2\right) \right] \\ &\times \Delta^m(Q_1^2, Q^2) + E_{\text{QCD}}^{(1)jm}(x, Q_0^2, Q^2) \end{aligned} \quad (\text{B.31})$$

$$E_{\text{QCD}}^{(1)jm}(x, Q_0^2, Q^2) = \int_{Q_0^2}^{Q^2} \frac{dQ_1^2}{Q_1^2} \Delta^j(Q_0^2, Q_1^2) \Delta^m(Q_1^2, Q^2) \frac{\alpha_s}{2\pi} P_j^m(z) \quad (\text{B.32})$$

So the procedure amounts to only considering resolvable emissions, but to multiply each propagator with Δ^j , which is the reason for the appearance of Δ^j in eqs. (B.29), (B.31-B.32).

B.3 Time-Like Parton Splitting

We discuss here the algorithm for Monte Carlo generation of time-like parton emission on the basis of the eq. (6.25).

The standard procedure is to apply the Monte Carlo rejection method [27]. We consider the splitting of a parton j with a maximal virtuality $Q_{j\text{max}}^2$ given by the preceding process. For the proposal function, we define the limits in z for given Q_j^2 using an approximate formula

$$p_\perp^2 \simeq z(1-z)Q_j^2 - zQ_l^2 - (1-z)Q_k^2 \quad (\text{B.33})$$

instead of the exact one, eq. (6.28), with the lowest possible virtualities for daughter partons $Q_k^2 = Q_l^2 = p_{\perp\text{fin}}^2$, which gives

$$z_{\text{min/max}}(Q_j^2) = \frac{1}{2} \pm \frac{1}{2} \sqrt{1 - \frac{4p_{\perp\text{fin}}^2}{Q_j^2}}. \quad (\text{B.34})$$

Further, we define upper limits,

$$\begin{aligned}\bar{P}_g^g(z) &= 3 \left\{ \frac{1}{z} + \frac{1}{1-z} \right\}, \\ \bar{P}_g^q(z) &= \frac{N_f}{2}, \\ \bar{P}_q^g(z) &= \frac{4}{3} \frac{2}{1-z},\end{aligned}\tag{B.35}$$

for the splitting functions,

$$\begin{aligned}\frac{1}{2} P_g^g(z) &= 3 \frac{(1-z(1-z))^2}{z(1-z)}, \\ \frac{1}{2} \sum_{i \in \{u, d, s, \bar{u}, \bar{d}, \bar{s}\}} P_g^i(z) &= \frac{N_f}{2} (z^2 + (1-z)^2), \\ P_q^g(z) &= \frac{4}{3} \frac{1+z^2}{1-z},\end{aligned}\tag{B.36}$$

with N_f being the number of active quark flavors. Integrating these three functions $\bar{P}_j^k(z)$ over z from $z_{\min} = z_{\min}(Q_j^2)$ to $z_{\max} = z_{\max}(Q_j^2)$ as

$$I_j^k(Q_j^2) = \int_{z_{\min}}^{z_{\max}} dz \bar{P}_j^k(z),\tag{B.37}$$

one obtains

$$I_g^g(Q_j^2) = 3 \left(\ln \left(\frac{z_{\max}}{z_{\min}} \right) + \ln \left(\frac{1-z_{\min}}{1-z_{\max}} \right) \right)\tag{B.38}$$

$$I_g^q(Q_j^2) = \frac{n_f}{2} (z_{\max} - z_{\min})\tag{B.39}$$

$$I_q^g(Q_j^2) = \frac{8}{3} \ln \left(\frac{1-z_{\min}}{1-z_{\max}} \right).\tag{B.40}$$

Defining $I_j(Q_j^2)$ as

$$I_j(Q_j^2) = \{I_g^g(Q_j^2) + I_g^q(Q_j^2)\} \delta_j^g + I_q^g(Q_j^2) \delta_j^q,\tag{B.41}$$

we propose the value Q_j^2 based upon the probability distribution

$$f_j(Q_j^2) = -\frac{\alpha_{\max}}{2\pi} I_j(Q_j^2) \frac{1}{Q_j^2},\tag{B.42}$$

with $\alpha_{\max} = \alpha_s(p_{\perp \min}^2) = \alpha_s(p_{\perp \text{fin}}^2)$. The flavor k of the daughter parton is then chosen according to partial contributions $I_j^k(Q_j^2)$ in (B.41), and the value of z according to the functions $\bar{P}_j^k(z)$.

The proposed values for $Q_j^2 = Q^2$, k , and z are accepted according to the probability

$$\frac{\alpha_s(p_{\perp}^2)}{\alpha_{\max}} w_j^k,\tag{B.43}$$

with $p_{\perp}^2 = z(1-z)Q_j^2$ and

$$w_g^g = (1-z(1-z))^2,\tag{B.44}$$

$$w_g^q = z^2 + (1-z)^2,\tag{B.45}$$

$$w_q^g = (1+z^2)/2.\tag{B.46}$$

Otherwise, the proposal is rejected and one looks for another splitting with $Q_{j \max}^2 = Q_j^2$.

Appendix C

Hadron-Hadron Amplitudes

In this appendix, we discuss the hadron-hadron scattering amplitude $T_{h_1 h_2}$, where h_1 and h_2 represent any pair of hadrons.

C.1 Neglecting Valence Quark Scatterings

We start with the general expression for hadron-hadron scattering amplitude, eq. (2.31),

$$i T_{h_1 h_2}(s, t) = \sum_{n=1}^{\infty} \frac{1}{n!} \int \prod_{l=1}^n \left[\frac{d^4 k_l}{(2\pi)^4} \frac{d^4 k'_l}{(2\pi)^4} \frac{d^4 q_l}{(2\pi)^4} \right] N_{h_1}^{(n)}(p, k_1, \dots, k_n, q_1, \dots, q_n) \\ \times \prod_{l=1}^n [i T_{1\mathbb{P}}(\hat{s}_l, q_l^2)] N_{h_2}^{(n)}(p', k'_1, \dots, k'_n, -q_1, \dots, -q_n) (2\pi)^4 \delta^{(4)}\left(\sum_{k=1}^n q_k - q\right), \quad (\text{C.1})$$

with $t = q^2$, $s = (p + p')^2 \simeq p^+ p'^-$, and with p, p' being the 4-momenta of the initial hadrons. We consider for simplicity identical parton constituents (neglecting valence quark scatterings) and take $T_{1\mathbb{P}}$ to be the sum of the soft Pomeron exchange amplitude (see eq. (2.5)) and the semi-hard sea-sea scattering amplitude (see eq. (??)):

$$T_{1\mathbb{P}}(\hat{s}_l, q_l^2) = T_{\text{soft}}(\hat{s}_l, q_l^2) + T_{\text{sea-sea}}(\hat{s}_l, q_l^2), \quad (\text{C.2})$$

with $\hat{s}_l = (k_l + k'_l)^2 \simeq k_l^+ k_l'^-$. The momenta k_l, k'_l and q_l denote correspondingly the 4-momenta of the initial partons for the l -th scattering and the 4-momentum transfer in that partial process. The factor $1/n!$ takes into account the identical nature of the n scattering contributions. $N_h^{(n)}(p, k_1, \dots, k_n, q_1, \dots, q_n)$ denotes the contribution of the vertex for n -parton coupling to the hadron h .

We assume that the initial partons k_l, k'_l are characterized by small virtualities $k_l^2 \sim -s_0$, $k_l'^2 \sim -s_0$, and therefore by small transverse momenta $k_{l\perp}^2 < s_0$, $k_{l\perp}'^2 < s_0$, so that the general results of the analysis made in [3, 14] are applicable for the hadron-parton vertices $N_h^{(n)}$. Using

$$d^4 k_l = \frac{1}{2} dk_l^+ dk_l^- d^2 k_{l\perp}, \quad d^4 q_l = \frac{1}{2} dq_l^+ dq_l^- d^2 q_{l\perp}, \quad (\text{C.3})$$

we can perform the integrations over $k_l^-, k_{l\perp}, q_l^-$ and $k_l'^+, k_{l\perp}', q_l^+$ separately for the upper and the lower vertexes by making use of

$$q_l^2 \simeq -q_{l\perp}^2, \quad k_l^-, q_l^- \ll k_l'^-, \quad k_l'^+, q_l^+ \ll k_l^+, \quad (\text{C.4})$$

as well as the fact that the integrals $dk_l^+, dk_l'^-$ are restricted by the physical region

$$0 < k_l^+ \leq p^+, \quad \sum_l k_l^+ \leq p^+, \quad (\text{C.5})$$

(similar for $k_l'^-$) [14]. We shall consider explicitly the upper vertex as for the lower one the derivation is identical. The integrals over k_l^-, q_l^- are defined by the discontinuities of the analytic amplitude $N_h^{(n)}$ with respect to the singularities in the corresponding energy invariants

$$\begin{aligned} s_1^+ &= (p - k_1)^2 \simeq -p^+ k_1^-, \\ &\dots \\ s_n^+ &= (p - k_1 - \dots - k_n)^2, \end{aligned} \quad (\text{C.6})$$

and

$$\begin{aligned} s_{q_1}^+ &= (p + q_1)^2 \simeq p^+ q_1^-, \\ &\dots \\ s_{q_{n-1}}^+ &= (p + q_1 + \dots + q_{n-1})^2. \end{aligned} \quad (\text{C.7})$$

As the processes corresponding to large values of $s_l^+, s_{q_l}^+$ need an explicit treatment (the so-called enhanced diagrams, see chapter 5), we only get contributions from the region of large $k_l^+ \sim p^+$, so that

$$s_l^+ \simeq -p^+(k_1^- + \dots + k_l^-) \sim s_0 \left(\frac{p^+}{k_1^+} + \dots + \frac{p^+}{k_l^+} \right) < M_0^2, \quad (\text{C.8})$$

where M_0^2 is some minimal mass for the Pomeron asymptotics to be applied. The similar argument holds for the momenta q_l^- , such that

$$s_{q_l}^+ \simeq p^+(q_1^- + \dots + q_l^-) < M_0^2. \quad (\text{C.9})$$

Using

$$dq_l^- = \frac{ds_{q_l}^+}{p^+}, \quad dk_l^- = \frac{dk_l^2}{k_l^+}, \quad (\text{C.10})$$

we get

$$\begin{aligned} &\int \prod_{l=1}^n \left[\frac{d^4 k_l}{(2\pi)^4} \right] \prod_{l=1}^{n-1} \left[\frac{dq_l^-}{2\pi} \right] N_{h_1}^{(n)}(p, k_1, \dots, k_n, q_1, \dots, q_n) \\ &= \int \prod_{l=1}^n \left[\frac{dk_l^2 dk_l^+ d^2 k_{l\perp}}{2(2\pi)^4 k_l^+} \Theta(s_l^+) \right] \prod_{l=1}^{n-1} \left[\frac{ds_{q_l}^+}{2\pi p^+} \Theta(s_{q_l}^+) \right] \\ &\quad \times \text{disc}_{s_1^+, \dots, s_n^+, s_{q_1}^+, \dots, s_{q_{n-1}}^+} N_{h_1}^{(n)}(p, k_1, \dots, k_n, q_1, \dots, q_n) \Theta \left(1 - \sum_{j=1}^n x_j^+ \right) \\ &\equiv \frac{1}{(p^+)^{n-1}} \int_0^1 \prod_{l=1}^n \frac{dx_l^+}{x_l^+} F_{h_1}^{(n)}(x_1^+, \dots, x_n^+, q_{1\perp}^2, \dots, q_{n\perp}^2) \Theta \left(1 - \sum_{j=1}^n x_j^+ \right). \end{aligned} \quad (\text{C.11})$$

The only difference of the formula eq. (C.11) from the traditional expression for $F_h^{(n)}$ in [3, 14] is the fact that we keep explicitly the integrations over the light cone momentum shares of the constituent partons $x_l^+ = k_l^+/p^+$. Further we assume that the dependences on the light cone

momentum fractions x_l^+ and on the momentum transfers along the Pomerons $q_l^2 \simeq -q_{l\perp}^2$ factorize in $F_h^{(n)}$, and we use the Gaussian parameterization for the latter one,

$$F_h^{(n)}(x_1^+, \dots, x_n^+, q_{1\perp}^2, \dots, q_{n\perp}^2) = \tilde{F}_h^{(n)}(x_1^+, \dots, x_n^+) \exp\left(-R_h^2 \sum_{j=1}^n q_{j\perp}^2\right), \quad (\text{C.12})$$

where the parameter R_h^2 is known as the hadron Regge slope [14]. Based on the above discussion and a corresponding treatment of the lower part of the diagram, eq. (B.2) can be rewritten as

$$\begin{aligned} iT_{h_1 h_2}(s, t) &= \sum_{n=1}^{\infty} \frac{1}{n!} \int \prod_{l=1}^{n-1} \left[\frac{d^2 q_{l\perp}}{8\pi^2 s} \right] \int_0^1 \prod_{l=1}^n \frac{dx_l^+}{x_l^+} \frac{dx_l^-}{x_l^-} \tilde{F}_{h_1}^{(n)}(x_1^+, \dots, x_n^+) \tilde{F}_{h_2}^{(n)}(x_1^-, \dots, x_n^-) \\ &\times \prod_{l=1}^n [iT_{1\mathbb{P}}(\hat{s}_l, -q_{l\perp}^2) \exp(-[R_{h_1}^2 + R_{h_2}^2] q_{l\perp}^2)] \Theta\left(1 - \sum_{j=1}^n x_j^+\right) \Theta\left(1 - \sum_{j=1}^n x_j^-\right) \end{aligned} \quad (\text{C.13})$$

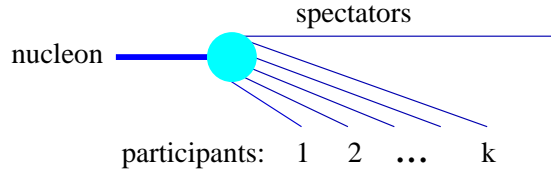


Figure C.1: Nucleon Fock state.

The formula (C.13) can be also obtained using the parton momentum Fock state expansion of the hadron eigenstate [5]

$$|h\rangle = \sum_{k=1}^{\infty} \frac{1}{k!} \int_0^1 \prod_{l=1}^k dx_l f_k(x_1, \dots, x_k) \delta\left(1 - \sum_{j=1}^k x_j\right) a^+(x_1) \cdots a^+(x_k) |0\rangle, \quad (\text{C.14})$$

where $f_k(x_1, \dots, x_k)$ is the probability amplitude for the hadron h to consist of k constituent partons with the light cone momentum fractions x_1, \dots, x_k and $a^+(x)$ is the creation operator for a parton with the fraction x . $f_k(x_1, \dots, x_k)$ satisfies the normalization condition

$$\sum_{k=1}^{\infty} \frac{1}{k!} \int_0^1 \prod_{l=1}^k dx_l |f_k(x_1, \dots, x_k)|^2 \delta\left(1 - \sum_{j=1}^k x_j\right) = 1 \quad (\text{C.15})$$

Then, for the contribution of n pair-like scatterings between the parton constituents of the projectile and target hadrons one obtains eq. (C.13), as shown in [5], with

$$\frac{1}{n!} \tilde{F}_h^{(n)}(x_1, \dots, x_n) = \sum_{k=n}^{\infty} \frac{1}{k!} \frac{k!}{n! (k-n)!} \int_0^1 \prod_{l=n+1}^k dx_l |f_k(x_1, \dots, x_k)|^2 \delta\left(1 - \sum_{j=1}^k x_j\right) \quad (\text{C.16})$$

representing the “inclusive” momentum distributions of n “participating” parton constituents, involved in the scattering process. From the normalization condition (C.15) follows the momentum conservation constraint

$$\int_0^1 dx x \tilde{F}_h^{(1)}(x) = 1 \quad (\text{C.17})$$

To get further simplifications, we assume that $\tilde{F}_{h_1(h_2)}^{(n)}(x_1, \dots, x_n)$ can be represented in a factorized form as a product of the contributions $F_{\text{part}}^h(x_l)$, depending on the momentum shares x_l of the “participating” or “active” parton constituents, and on the function $F_{\text{remn}}^h\left(1 - \sum_{j=1}^n x_j\right)$, representing the contribution of all “spectator” partons, sharing the remaining share $1 - \sum_j x_j$ of the initial light cone momentum (see fig. C.1). So we have

$$\tilde{F}_h^{(n)}(x_1, \dots, x_n) = \prod_{l=1}^n F_{\text{part}}^h(x_l) F_{\text{remn}}^h\left(1 - \sum_{j=1}^n x_j\right) \quad (\text{C.18})$$

The participating parton constituents are assumed to be quark-anti-quark pairs (not necessarily of identical flavors), such that the baryon numbers of the projectile and of the target are conserved. So we have $x = x_q + x_{\bar{q}}$ with x_q and $x_{\bar{q}}$ being the light-cone momentum fractions of the quark and the anti-quark. The function F_{part}^h may thus be written as

$$F_{\text{part}}^h(x) = \int dx_q dx_{\bar{q}} \bar{F}_{\text{part}}^h(x_q, x_{\bar{q}}) \delta(x - x_q - x_{\bar{q}}). \quad (\text{C.19})$$

In case of soft or semi-hard Pomerons, \bar{F}_{part}^h is taken as a product of two asymptotics $x_i^{-\alpha_q}$, $i = q, \bar{q}$, so we have

$$F_{\text{part}}^h(x) = \gamma_h x^{-\alpha_{\text{part}}}, \quad (\text{C.20})$$

with $\alpha_{\text{part}} = 2\alpha_q - 1$. The parameter α_q defines the probability to slow down the constituent (“dressed”) (anti-)quark; it is related to the Regge intercept of the $q\bar{q}$ -trajectory [59]: $\alpha_q = \alpha_{\mathbb{R}}(0) \simeq 0.5$. The remnant function F_{remn}^h defines the probability to slow down the initial hadron quark configuration; it is assumed to be of the form

$$F_{\text{remn}}^h(x) = x^{\alpha_{\text{remn}}^h}, \quad (\text{C.21})$$

with an adjustable parameter α_{remn}^h . Using (C.18-C.21), the eq. (C.13) can be rewritten as

$$\begin{aligned} iT_{h_1 h_2}(s, t) &= 8\pi^2 s \sum_{n=1}^{\infty} \frac{1}{n!} \int_0^1 \prod_{l=1}^n dx_l^+ dx_l^- \prod_{l=1}^n \left[\frac{1}{8\pi^2 \hat{s}_l} \int d^2 q_{l\perp} iT_{1\mathbb{P}}^{h_1 h_2}(x_l^+, x_l^-, s, -q_{l\perp}^2) \right] \\ &\times F_{\text{remn}}^{h_1}\left(1 - \sum_{j=1}^n x_j^+\right) F_{\text{remn}}^{h_2}\left(1 - \sum_{j=1}^n x_j^-\right) \delta^{(2)}\left(\sum_{k=1}^n \vec{q}_{k\perp} - \vec{q}_{\perp}\right). \end{aligned} \quad (\text{C.22})$$

with

$$T_{1\mathbb{P}}^{h_1 h_2}(x_l^+, x_l^-, s, -q_{l\perp}^2) = T_{1\mathbb{P}}(\hat{s}_l, -q_{l\perp}^2) F_{\text{part}}^{h_1}(x_l^+) F_{\text{part}}^{h_2}(x_l^-) \exp(-[R_{h_1}^2 + R_{h_2}^2] q_{l\perp}^2) \quad (\text{C.23})$$

representing the contributions of “elementary interactions plus external legs”.

C.2 Including Valence Quark Hard Scatterings

To include valence quark hard scatterings one has to replace the inclusive parton momentum distributions

$$\frac{1}{n!} \tilde{F}_h^{(n)}(x_1, \dots, x_n) \quad (\text{C.24})$$

in (C.13) by the momentum distributions

$$\frac{1}{n_v! (n - n_v)!} \tilde{F}_h^{(n, n_v) i_1, \dots, i_{n_v}}(x_{v_1}, \dots, x_{v_{n_v}}, x_{n_v+1}, \dots, x_n), \quad (\text{C.25})$$

corresponding to the case of n_v partons being valence quarks with flavors i_1, \dots, i_{n_v} (taken at the virtuality scale Q_0^2) and other $n - n_v$ partons being usual non-valence participants (quark-anti-quark pairs). One has as well to take into account different contributions for scatterings between a pair of valence quarks or between a valence quark and a non-valence participant. In particular, for a single hard scattering on a valence quark we have to use

$$\tilde{F}_h^{(1,1)}(x_v) = q_{\text{val}}^i(x_v), \quad (\text{C.26})$$

where q_{val}^i is the momentum distribution of a valence quark of flavor i at the scale Q_0^2 . In order to conserve the initial hadron baryon content and to keep the simple factorized structure (C.18), we associate a “quasi-spectator” anti-quark to each valence quark interaction, defining the joint contribution $\bar{F}_{\text{part}}^i(x_v, x_{\bar{q}})$ of the valence quark with the flavor i and the anti-quark. Thus we have

$$\begin{aligned} \tilde{F}_h^{(n, n_v) i_1, \dots, i_{n_v}}(x_{v_1}, \dots, x_{v_{n_v}}, x_{n_{v+1}}, \dots, x_n) \\ = \prod_{l=1}^{n_v} \left[\int_{x_{v_l}}^1 dx_l \bar{F}_{\text{part}}^{h, i_l}(x_{v_l}, x_l - x_{v_l}) \right] \prod_{m=n_v+1}^n F_{\text{part}}^h(x_m) F_{\text{remn}}^h \left(1 - \sum_{k=1}^n x_k \right), \end{aligned} \quad (\text{C.27})$$

where x_l is the sum of the momentum fractions of l^{th} valence quark and the corresponding anti-quark; we allow here formally any number of valence quark participants (based on the fact that multiple valence type processes give negligible contribution to the scattering amplitude). By construction the integral over $x_{\bar{q}}$ of the function $\tilde{F}_h^{(1,1)i}(x_v, x_{\bar{q}})$ gives the inclusive momentum distribution of the valence quark i . Thus the function \bar{F}_{part}^i has to meet the condition

$$\int_0^{1-x_v} dx_{\bar{q}} \bar{F}_{\text{part}}^{h, i}(x_v, x_{\bar{q}}) F_{\text{remn}}^h(1 - x_v - x_{\bar{q}}) = q_{\text{val}}^i(x_v, Q_0^2) \quad (\text{C.28})$$

Assuming that the anti-quark momentum distribution behaves as $(x_{\bar{q}})^{-\alpha_R}$, and using the above-mentioned parameterization for F_{remn}^h , we get

$$\bar{F}_{\text{part}}^{h, i}(x_v, x_{\bar{q}}) = N^{-1} q_{\text{val}}^i(x_v, Q_0^2) (1 - x_v)^{\alpha_{\mathbb{R}} - 1 - \alpha_{\text{remn}}} (x_{\bar{q}})^{-\alpha_{\mathbb{R}}}, \quad (\text{C.29})$$

with the normalization factor

$$N = \frac{\Gamma(1 + \alpha_{\text{remn}}) \Gamma(1 - \alpha_{\mathbb{R}})}{\Gamma(2 + \alpha_{\text{remn}} - \alpha_{\mathbb{R}})}. \quad (\text{C.30})$$

Now we can write the normalization condition (C.17) for “active” (participating in an interaction) partons as

$$\int_0^1 dx x F_{\text{part}}^h(x) F_{\text{remn}}^h(1 - x) + \sum_i \int_0^1 x_v dx \int_0^x dx_v \bar{F}_{\text{part}}^{h, i}(x_v, x - x_v) F_{\text{remn}}^h(1 - x) = 1, \quad (\text{C.31})$$

which gives

$$\gamma_h = (1 - \langle x_v \rangle) \frac{\Gamma(3 - \alpha_{\text{part}} + \alpha_{\text{remn}}^h)}{\Gamma(2 - \alpha_{\text{part}}) \Gamma(1 + \alpha_{\text{remn}}^h)}, \quad (\text{C.32})$$

with

$$\langle x_v \rangle = \sum_i \int_0^1 x_v dx_v q_{\text{val}}^i(x_v, Q_0^2) \quad (\text{C.33})$$

being the average light cone momentum fraction carried by valence quarks.

C.3 Enhanced Diagrams

In this appendix, we demonstrate how triple Pomeron contributions appear naturally in the Gribov-Regge formalism under certain kinematical conditions, and we derive a formula for the hadron-hadron scattering amplitude in this case.

To introduce enhanced type diagrams let us come back to the process of double soft Pomeron exchange, which is a particular case of the diagram of fig 2.7. The corresponding contribution to the elastic scattering amplitude is given in eqs. (2.31), (C.11) with $n = 2$ and with T_{1P} being replaced by T_{soft} :

$$\begin{aligned}
 iT_{h_1 h_2}^{(2)}(s, t) &= \frac{1}{2} \int \frac{d^4 k_1}{(2\pi)^4} \frac{d^4 k'_1}{(2\pi)^4} \frac{d^4 k_2}{(2\pi)^4} \frac{d^4 k'_2}{(2\pi)^4} \frac{d^4 q_1}{(2\pi)^4} \Theta(s_1^+) \Theta(s_1^-) \Theta(s_2^+) \Theta(s_2^-) \Theta(s_{q_1}^+) \Theta(s_{q_1}^-) \\
 &\quad \times \text{disc}_{s_1^+, s_2^+, s_{q_1}^+} N_{h_1}^{(2)}(p, k_1, k_2, q_1, q - q_1) \\
 &\quad \times \prod_{l=1}^2 [iT_{\text{soft}}(\hat{s}_l, q_l^2)] \text{disc}_{s_1^-, s_2^-, s_{q_1}^-} N_{h_2}^{(2)}(p', k'_1, k'_2, -q_1, -q + q_1) \quad (C.34)
 \end{aligned}$$

see fig. C.2.

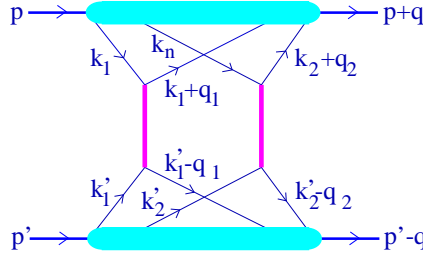


Figure C.2: Double Pomeron exchange.

We are now interested in the contribution with some of the invariants

$$\begin{aligned}
 s_1^+ &= (p - k_1)^2 \simeq -p^+ k_1^-, \\
 s_2^+ &= (p - k_1 - k_2)^2 \simeq -p^+ (k_1^- + k_2^-), \\
 s_{q_1}^+ &= (p + q_1)^2 \simeq p^+ q_1^-,
 \end{aligned} \quad (C.35)$$

being large, implying k_i^-, q_1^- to be not too small. As was shown in [14], one can restrict the integration region to $s_i^+ \leq s_{q_1}^+$, because $s_i^+ \gg s_{q_1}^+$, ($k_i^- \gg q_1^-$) either correspond to processes with exchange of more than two Pomerons or to the Pomeron self-coupling, the latter one just renormalizing the Pomeron amplitude. Then from

$$k_i^2, k_i'^2, (k_1' - q_1)^2, (k_1 + q_1)^2, (k_2 - q_1 - q)^2 \sim -s_0 \quad (C.36)$$

it follows that

$$k_i^- \sim -\frac{s_0}{k_i^+}, \quad k_i'^+ \sim -\frac{s_0}{k_i'^-}, \quad q_1^+ \sim -\frac{s_0}{k_1'^-}, \quad q_1^- \sim \frac{s_0}{k_1^+}, \frac{s_0}{k_2^+} \quad (C.37)$$

and correspondingly $k_1^+ \sim k_2^+$ and the invariants $s_1^+, s_2^+, s_{q_1}^+$ are of the same order. The vertex $N_h^{(2)}$ for large $s_{q_1}^+$ can be described by the soft Pomeron asymptotics and we may write $\text{disc}_{s_1^+, s_2^+, s_{q_1}^+} N_{h_1}^{(2)}(p, k_1, k_2, q_1, q - q_1)$ as a product of the Pomeron-hadron coupling $N_h^{(1)}(p, k, q)$, twice imaginary part of the soft Pomeron exchange amplitude $2\text{Im } T_{\text{soft}}((k - k_{12})^2, q^2)$ with $k_{12} =$

$k_1 + k_2$, and a term $V^{3\mathbb{P}}(k_{12}, k_1, k_2, q, q_1, q - q_1)$ describing the coupling of the three Pomerons¹. So we get

$$\begin{aligned}
& \int \frac{d^4 k_1}{(2\pi)^4} \frac{d^4 k_2}{(2\pi)^4} \frac{dq_1^-}{2\pi} \Theta(s_1^+) \Theta(s_2^+) \Theta(s_{q_1}^+) \text{disc}_{s_1^+, s_2^+, s_{q_1}^+} N_{h_1}^{(2)}(p, k_1, k_2, q_1, q - q_1) \\
&= \int \frac{d^4 k_1}{(2\pi)^4} \frac{d^4 k_2}{(2\pi)^4} \frac{dq_1^-}{2\pi} \Theta(s_1^+) \Theta(s_2^+) \Theta(s_{q_1}^+) \frac{d^4 k}{(2\pi)^4} \frac{d^4 k_{12}}{(2\pi)^4} (2\pi)^4 \delta(k_{12} - k_1 - k_2) \\
&\quad \times N_{h_1}^{(1)}(p, k, q) 2\text{Im} T_{\text{soft}}((k - k_{12})^2, q^2) V^{3\mathbb{P}}(k_{12}, k_1, k_2, q, q_1, q - q_1) \\
&= \int \frac{dk^+ dk^2 d^2 k_{\perp}}{2k^+ (2\pi)^4} \Theta(s_0^+) \text{disc}_{s_0^+} N_{h_1}^{(1)}(p, k, q) \int \frac{dk_{12}^+ dk_{12}^2 d^2 k_{12\perp}}{2k_{12}^+ (2\pi)^4} 2\text{Im} T_{\text{soft}}((k - k_{12})^2, q^2) \\
&\quad \times \int \frac{dk_1^+ dk_1^2 d^2 k_{1\perp}}{2k_1^+ (2\pi)^4} \frac{d(k_{12} - k_1 - q_1 - q)^2}{2\pi(k_{12}^+ - k_1^+)} \Theta(s_1^+) \Theta(s_2^+) \Theta(s_{q_1}^+) \\
&\quad \times V^{3\mathbb{P}}(k_{12}, k_1, k_{12} - k_1, q, q_1, q - q_1)
\end{aligned} \tag{C.38}$$

see fig. C.3, with $s_0^+ = (p - k)^2 \simeq -p^+ k^-$ and $dq_1^- = \frac{1}{k_2^+} d(k_2 - q_1 - q)^2$. Now we can perform the

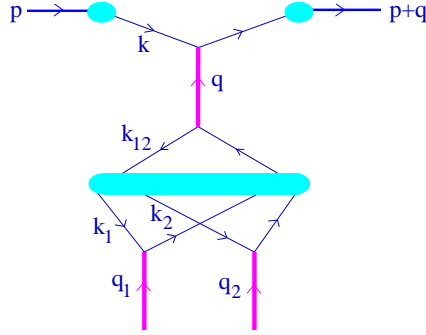


Figure C.3: Three Pomeron coupling.

integrations over $k^2, k_{12}^2, k_1^2, (k_2 - q_1 - q)^2$ assuming their convergence in the region $k_i^2 \sim -s_0$, as well as over $k_{\perp}, k_{12\perp}, k_{1\perp} \leq s_0$ to transform eq. (C.38) to the form

$$\begin{aligned}
& \int dx^+ F_{\text{part}}^{h_1}(x^+) F_{\text{remn}}^{h_1}(1 - x^+) \exp(-R_{h_1}^2 q_{\perp}^2) \int \frac{dx_{12}^+}{x_{12}^+} \frac{1}{2s^+} \text{Im} T_{\text{soft}}(s^+, -q_{\perp}^2) \times \\
& \quad \times \int \frac{dz^+}{x_1^+ (x_{12}^+ - x_1^+) p^+} \tilde{V}^{3\mathbb{P}}(-q_{\perp}^2, -q_{1\perp}^2, -(\vec{q}_{\perp} - \vec{q}_{1\perp})^2)
\end{aligned} \tag{C.39}$$

with

$$x^+ = k^+ / p^+, \tag{C.40}$$

$$x_{12}^+ = k_{12}^+ / p^+, \tag{C.41}$$

$$x_1^+ = k_1^+ / p^+, \tag{C.42}$$

$$x_{12}^+ - x_1^+ = (k_{12}^+ - k_1^+) / p^+ = k_2^+ / p^+, \tag{C.43}$$

$$z^+ = k_1^+ / k_{12}^+ = x_1^+ / x_{12}^+, \tag{C.44}$$

$$s^+ = (k - k_{12})^2 \simeq -k^+ k_{12}^- \simeq s_0 k^+ / k_{12}^+ = s_0 x^+ / x_{12}^+. \tag{C.45}$$

¹ The triple Pomeron vertex is assumed to have nonplanar structure, corresponding to having the two lower Pomerons “in parallel”; the planar triple-Pomeron vertex would correspond to subsequent emission of these Pomerons and gives no contribution in the high energy limit [60].

We used (see eq. (C.11-C.18))

$$\int \frac{dk^2 d^2 k_\perp}{2(2\pi)^4} \Theta(s_0^+) \text{disc}_{s_0^+} N_h^{(1)}(p, k, q) = F_{\text{part}}^h(x^+) F_{\text{remn}}^h(1-x^+) \exp(-R_h^2 q_\perp^2) \quad (\text{C.46})$$

and the definition

$$\begin{aligned} \tilde{V}^{3\text{IP}}(-q_\perp^2, -q_{1\perp}^2, -(\vec{q}_\perp - \vec{q}_{1\perp})^2) &= s_0 \int \frac{dk_{12}^2 d^2 k_{12\perp}}{(2\pi)^4} \frac{dk_1^2 d^2 k_{1\perp}}{(2\pi)^4} \frac{d[(k_{12} - k_1 - q_1 - q)^2]}{2\pi} \\ &\times \Theta(s_1^+) \Theta(s_2^+) \Theta(s_{q_1}^+) V^{3\text{IP}}(k_{12}, k_1, k_{12} - k_1, q, q_1, q - q_1) . \end{aligned} \quad (\text{C.47})$$

We have also taken into account the fact that the triple Pomeron vertex $V^{3\text{IP}}$ has a scalar structure, and we therefore suppose that it can only depend on the invariants

$$k_i^2, (k_1 + q_1)^2, (k_2 - q_1 - q)^2 \sim -s_0, q^2 \simeq -q_\perp^2, q_1^2 \simeq -q_{1\perp}^2, q_2^2 \simeq -(q_\perp - q_{1\perp})^2 \quad (\text{C.48})$$

and on the partition of the light cone momentum k_{12}^+ between the two lower Pomerons,

$$z^+ = k_1^+ / k_{12}^+ = (p' + k_1)^2 / (p' + k_{12})^2.$$

Furthermore, we did assume the flat distribution in z^+ in order to obtain $k_1^+ \sim k_2^+ \sim k_{12}^+ / 2$ (see the discussion above). We use the Gaussian parameterization for the q_i^2 -dependence of $\tilde{V}^{3\text{IP}}$,

$$\tilde{V}^{3\text{IP}}(-q_\perp^2, -q_{1\perp}^2, -q_{2\perp}^2) \equiv r_{3\text{IP}} \exp(-R_{3\text{IP}}^2 [q_\perp^2 + q_{1\perp}^2 + q_{2\perp}^2]), \quad (\text{C.49})$$

where $r_{3\text{IP}}$ is the triple-Pomeron coupling and $R_{3\text{IP}}^2$ is the slope of the triple-Pomeron vertex. The slope $R_{3\text{IP}}^2$ is known to be small and will be neglected in the following.

Now, using (C.34-C.49) for the upper vertex and doing the usual treatment (C.11-C.18) of the lower one, we get for the triple Pomeron amplitude

$$iT_{h_1 h_2}^{3\text{IP}-}(s, t) = \int_0^1 \frac{dx^+}{x^+} \frac{dx^-}{x^-} F_{\text{remn}}^{h_1}(1-x^+) F_{\text{remn}}^{h_2}(1-x^-) iT_{3\text{IP}-}^{h_1 h_2}(x^+, x^-, s, t) \quad (\text{C.50})$$

with

$$\begin{aligned} iT_{3\text{IP}+}^{h_1 h_2}(x^+, x^-, s, t) &= 8\pi^2 x^+ x^- s \frac{r_{3\text{IP}}}{2} \int_{s_0/x^-}^{x^+} \frac{dx_{12}^+}{x_{12}^+} \left[\frac{1}{2s^+} \text{Im} T^{h_1}(x^+, s^+, -q_\perp^2) \right] \\ &\times \int dz^+ \int d^2 q_{1\perp} d^2 q_{2\perp} \int_0^{x^-} dx_1^- dx_2^- \prod_{l=1}^2 \left[\frac{1}{8\pi^2 \hat{s}_l} iT^{h_2}(x_l^-, \hat{s}_l, -q_{l\perp}^2) \right] \\ &\times \delta(x^- - x_1^- - x_2^-) \delta^{(2)}(\vec{q}_\perp - \vec{q}_{1\perp} - \vec{q}_{2\perp}), \end{aligned} \quad (\text{C.51})$$

with

$$T^h(x, \hat{s}, -q_\perp^2) = T_{\text{soft}}^h(x, \hat{s}, -q_\perp^2) = T_{\text{soft}}(\hat{s}, -q_\perp^2) F_{\text{part}}^h(x) \exp(-R_h^2 q_\perp^2) \quad (\text{C.52})$$

and

$$\hat{s}_1 = x_{12}^+ z^+ x_1^- s, \quad \hat{s}_2 = x_{12}^+ (1 - z^+) x_2^- s. \quad (\text{C.53})$$

The sign “-” in “3IP-” refers to the Pomeron “splitting” towards the target hadron (reversed Y-diagram); the lower limit for the integral dx_{12}^+ is due to $x_{12}^- \simeq s_0/x_{12}^+ < x^-$.

C.4 Parton Generation for Triple-Pomeron Diagrams

The inclusion of the triple-Pomeron contributions results only in slight modification of the standard procedure. Now the full contribution of an elementary interaction is

$$G_{1\mathbb{P}}^{h_1 h_2}(x^+, x^-, s, b) + \sum_{\sigma} \sum_{i=0}^2 \widehat{G}_{3\mathbb{P}\sigma(i)}^{h_1 h_2}(x^+, x^-, x^{\text{proj}}, x^{\text{targ}}, s, b), \quad (\text{C.54})$$

where $x^{\text{proj}}, x^{\text{targ}}$ are the corresponding remnant light cone momentum fractions, and with the contributions of different cuts of triple-Pomeron diagrams being obtained from eq. (5.54), together with eqs. (5.54), (5.47-5.49) as

$$\begin{aligned} \widehat{G}_{3\mathbb{P}-(0)}^{h_1 h_2}(x^+, x^-, x^{\text{proj}}, x^{\text{targ}}, s, b) &= \frac{r_{3\mathbb{P}}}{8} \int d^2 b_1 \frac{1}{x^-} G^{h_1}(x^+, x^+ x^- s, |\vec{b} - \vec{b}_1|) \\ &\times \int_0^{x^{\text{targ}}} d\hat{x}^- \int_0^1 dz^+ \int_0^{\hat{x}^- + x^-} dx_1^- G^{h_2}(x_1^-, x_1^- \frac{s_0}{x^-} z^+ s, b_1) \\ &\times G^{h_2}(\hat{x}^- + x^- - x_1^-, (\hat{x}^- + x^- - x_1^-) \frac{s_0}{x^-} (1 - z^+) s, b_1) \\ &\times \frac{F_{\text{remn}}(x^{\text{targ}} - \hat{x}^-)}{F_{\text{remn}}(x^{\text{targ}})} \end{aligned} \quad (\text{C.55})$$

and

$$\begin{aligned} \widehat{G}_{3\mathbb{P}-(1)}^{h_1 h_2}(x^+, x^-, x^{\text{proj}}, x^{\text{targ}}, s, b) &= -\frac{r_{3\mathbb{P}}}{2} \int d^2 b_1 \int_{s_0/(x-s)}^{x^+} \frac{dx_{12}^+}{x_{12}^+} G^{h_1}(x^+, s^+, |\vec{b} - \vec{b}_1|) \\ &\times \int_0^1 dz^+ G^{h_2}(x^-, x_{12}^+ z^+ x^- s, b_1) \\ &\times \int_0^{x^{\text{targ}}} d\hat{x}^- G^{h_2}(\hat{x}^-, x_{12}^+ (1 - z^+) \hat{x}^- s, b_1) \\ &\times \frac{F_{\text{remn}}(x^{\text{targ}} - \hat{x}^-)}{F_{\text{remn}}(x^{\text{targ}})} \end{aligned} \quad (\text{C.56})$$

and

$$\begin{aligned} \widehat{G}_{3\mathbb{P}-(2)}^{h_1 h_2}(x^+, x^-, x^{\text{proj}}, x^{\text{targ}}, s, b) &= \frac{r_{3\mathbb{P}}}{4} \int d^2 b_1 \int_{s_0/(sx^-)}^{x^+} \frac{dx_{12}^+}{x_{12}^+} G^{h_1}(x^+, s^+, |\vec{b} - \vec{b}_1|) \\ &\times \int_0^1 dz^+ \int_0^{x^-} dx_1^- G^{h_2}(x_1^-, \hat{s}_1, b_1) G^{h_2}(x^- - x_1^-, \hat{s}_2, b_1) \end{aligned} \quad (\text{C.57})$$

(similarly for $\widehat{G}_{3\mathbb{P}+(i)}^{h_1 h_2}$). Thus, the elementary process splits into a single elementary scattering contribution – with the weight

$$\widehat{G}_{1\mathbb{P}}^{h_1 h_2} = G_{1\mathbb{P}}^{h_1 h_2} + \sum_{\sigma} \sum_{i=0}^1 \widehat{G}_{3\mathbb{P}\sigma(i)}^{h_1 h_2}, \quad (\text{C.58})$$

and the contribution with all three Pomerons being cut – with the weight

$$\widehat{G}_{3\mathbb{P}+(2)}^{h_1 h_2} + \widehat{G}_{3\mathbb{P}-(2)}^{h_1 h_2}. \quad (\text{C.59})$$

Choosing the first one, one proceeds in the usual way, with the functions $G_{1\mathbb{P}}^{h_1 h_2}$, $G_{\text{soft}}^{h_1 h_2}$, $G_{\text{sea-sea}}^{h_1 h_2}$, $G_{\text{val-sea}}^{h_1 h_2}$, $G_{\text{sea-val}}^{h_1 h_2}$ in eq. (6.4) being replaced by $\widehat{G}_{1\mathbb{P}}^{h_1 h_2}$, $\widehat{G}_{\text{soft}}^{h_1 h_2}$, $\widehat{G}_{\text{sea-sea}}^{h_1 h_2}$, $\widehat{G}_{\text{val-sea}}^{h_1 h_2}$, $\widehat{G}_{\text{sea-val}}^{h_1 h_2}$, where we introduce the functions $\widehat{G}_J^{h_1 h_2}$ via

$$\widehat{G}_J^{h_1 h_2} = G_J^{h_1 h_2} + \widehat{G}_{3\mathbb{P}+(0)J}^{h_1 h_2} + \widehat{G}_{3\mathbb{P}-(0)J}^{h_1 h_2} + \widehat{G}_{3\mathbb{P}-(1)J}^{h_1 h_2} + \widehat{G}_{3\mathbb{P}-(1)J}^{h_1 h_2}, \quad (\text{C.60})$$

with J being “soft”, “sea-sea”, “val-sea” or “sea-val”. Here $\widehat{G}_{3\mathbb{P}-(0)\text{soft}}^{h_1 h_2}$ is given by the eq. (C.55) with $G^{h_1}(x^+, x^+ x^- s, |\vec{b} - \vec{b}_1|)$ being replaced by its soft contribution $G_{\text{soft}}^{h_1}(x^+, x^+ x^- s, |\vec{b} - \vec{b}_1|)$ (see eq. (5.34)), whereas $\widehat{G}_{3\mathbb{P}-(1)\text{soft}}^{h_1 h_2}$ is given in (C.56) with both $G^{h_1}(x^+, s^+, |\vec{b} - \vec{b}_1|)$ and $G^{h_2}(x^-, x_{12}^+ z^+ x^- s, b_1)$ being represented by the soft contributions $G_{\text{soft}}^{h_1/h_2}$. The other functions $\widehat{G}_{3\mathbb{P}+(i)J}^{h_1 h_2}$ are defined similarly to the “soft” case - considering corresponding “sea” and “valence” contributions in the cut Pomerons G^{h_1/h_2} in eq. (C.55-C.56).

For the contribution corresponding to the cases of all three Pomerons being cut, we split the processes into three separate cut Pomeron pieces. Each piece is characterized by the function $\bar{G}_{i\pm}^{h_1 h_2}(\bar{x}^+, \bar{x}^-, s, b_1)$, where $b_1 \simeq b/2$ and

$$\bar{G}_{1-}^{h_1 h_2}(\bar{x}^+, \bar{x}^-, s, b_1) = G^{h_1}(\bar{x}^+, \bar{x}^+ \bar{x}^- s, b_1), \quad \bar{x}^+ = x^+, \bar{x}^- = s_0/(x_{12}^+ s), \quad (\text{C.61})$$

$$\bar{G}_{2-}^{h_1 h_2}(\bar{x}^+, \bar{x}^-, s, b_1) = G^{h_2}(\bar{x}^-, \bar{x}^+ \bar{x}^- s, b_1), \quad \bar{x}^+ = z^+ x_{12}^+, \bar{x}^- = x_1^-, \quad (\text{C.62})$$

$$\bar{G}_{3-}^{h_1 h_2}(\bar{x}^+, \bar{x}^-, s, b_1) = G^{h_2}(\bar{x}^-, \bar{x}^+ \bar{x}^- s, b_1), \quad \bar{x}^+ = (1 - z^+) x_{12}^+, \bar{x}^- = x^- - x_1^-, \quad (\text{C.63})$$

where the variables x_{12}^+, z^+, x_1^- are generated according to the integrand of eq. (C.57) (similar for $\bar{G}_{i+}^{h_1 h_2}$). After that each contribution $\bar{G}_{i\pm}^{h_1 h_2}(\bar{x}^+, \bar{x}^-, s, b_1)$ is treated separately in the usual way, starting from the eq. (6.4), with the functions $G_{1\mathbb{P}}^{h_1 h_2}$, $G_{\text{soft}}^{h_1 h_2}$, $G_{\text{sea-sea}}^{h_1 h_2}$, $G_{\text{val-sea}}^{h_1 h_2}$, $G_{\text{sea-val}}^{h_1 h_2}$ being replaced by $\bar{G}_{i\pm}^{h_1 h_2}(\bar{x}^+, \bar{x}^-, s, b_1)$ and by the corresponding partial contributions of soft G_{soft}^h , “sea-sea”-type $G_{\text{sea-sea}}^h$, and “valence-sea”-type parton scattering $G_{\text{val-sea}}^h$ (see eq. (5.34-5.36)), but without “valence-valence” contribution.

Appendix D

Calculation of Φ and H

D.1 Calculation of Φ_{pp}

Here, we present the detailed calculation of Φ for proton-proton collisions. As shown earlier, Φ_{pp} may be written as

$$\begin{aligned}\Phi_{pp}(x^+, x^-, s, b) &= \sum_{r_1=0}^{\infty} \cdots \sum_{r_N=0}^{\infty} \frac{1}{r_1!} \cdots \frac{1}{r_N!} \int \prod_{\lambda=1}^{r_1+\dots+r_N} dx_{\lambda}^+ dx_{\lambda}^- \\ &\times \prod_{\rho_1=1}^{r_1} -G_{1\rho_1} \cdots \prod_{\rho_N=r_1+\dots+r_{N-1}+1}^{r_1+\dots+r_N} -G_{N\rho_N} \\ &\times F_{\text{remn}}(x^+ - \sum_{\lambda} x_{\lambda}^+) F_{\text{remn}}(x^- - \sum_{\lambda} x_{\lambda}^-),\end{aligned}\tag{D.1}$$

with

$$F_{\text{remn}}(x) = x^{\alpha_{\text{remn}}} \Theta(x) \Theta(1-x),\tag{D.2}$$

and with $G_{i\lambda}$ being of the form

$$G_{i\lambda}(x_{\lambda}^+, x_{\lambda}^-, s, b) = \alpha_i (x_{\lambda}^+ x_{\lambda}^-)^{\beta_i},\tag{D.3}$$

with α_i and β_i being s - and b -dependent parameters. We obtain

$$\begin{aligned}\Phi_{pp}(x^+, x^-, s, b) &= \sum_{r_1=0}^{\infty} \cdots \sum_{r_N=0}^{\infty} \frac{(-\alpha_1)^{r_1}}{r_1!} \cdots \frac{(-\alpha_N)^{r_N}}{r_N!} \\ &\times I_{r_1, \dots, r_N}(x^+) I_{r_1, \dots, r_N}(x^-)\end{aligned}\tag{D.4}$$

with

$$I_{r_1, \dots, r_N}(x) = \int \prod_{\lambda=1}^{r_1+\dots+r_N} dx_{\lambda} \prod_{\rho_1=1}^{r_1} x_{\rho_1}^{\beta_1} \cdots \prod_{\rho_N=r_1+\dots+r_{N-1}+1}^{r_1+\dots+r_N} x_{\rho_N}^{\beta_N} F_{\text{remn}}(x - \sum_{\lambda} x_{\lambda}),\tag{D.5}$$

which amounts to

$$I_{r_1, \dots, r_N}(x) = \int \prod_{\lambda=1}^{r_1+\dots+r_N} [dx_\lambda x_\lambda^{\epsilon_\lambda}] (x - \sum_\lambda x_\lambda)^{\alpha_{\text{remn}}} \theta(x - \sum_\lambda x_\lambda) \theta\left(1 - (x - \sum_\lambda x_\lambda)\right), \quad (\text{D.6})$$

with

$$\epsilon_\lambda = \begin{cases} \beta_1 & \text{for } \lambda \leq r_1 \\ \beta_2 & \text{for } r_1 < \lambda \leq r_1 + r_2 \\ \dots & \\ \beta_N & \text{for } r_1 + \dots + r_{N-1} < \lambda \leq r_1 + \dots + r_N \end{cases}. \quad (\text{D.7})$$

We define new variables,

$$\begin{cases} u_\lambda &= \frac{x_\lambda}{x - x_1 - \dots - x_{\lambda-1}} \\ du_\lambda &= \frac{dx_\lambda}{x - x_1 - \dots - x_{\lambda-1}} \end{cases}, \quad (\text{D.8})$$

which have the following property,

$$\prod_{\alpha=1}^{\lambda-1} (1 - u_\alpha) = \prod_{\alpha=1}^{\lambda-1} \frac{x - \dots - x_\alpha}{x - \dots - x_{\alpha-1}} = \frac{x - \dots - x_{\lambda-1}}{x}, \quad (\text{D.9})$$

and therefore

$$\begin{cases} x_\lambda &= xu_\lambda \prod_{\alpha=1}^{\lambda-1} (1 - u_\alpha) \\ dx_\lambda &= x du_\lambda \prod_{\alpha=1}^{\lambda-1} (1 - u_\alpha) \end{cases}. \quad (\text{D.10})$$

This leads to

$$I_{r_1, \dots, r_N}(x) = \int \prod_{\lambda=1}^{r_1+\dots+r_N} \left\{ du_\lambda u_\lambda^{\epsilon_\lambda} x^{1+\epsilon_\lambda} \prod_{\alpha=1}^{\lambda-1} (1 - u_\alpha)^{1+\epsilon_\alpha} \right\} \left[x \prod_{\lambda=1}^{r_1+\dots+r_N} (1 - u_\lambda) \right]^{\alpha_{\text{remn}}} \quad (\text{D.11})$$

Defining

$$\alpha = \alpha_{\text{remn}} + \sum_{\lambda=1}^{r_1+\dots+r_N} \tilde{\epsilon}_\lambda = \alpha_{\text{remn}} + r_1 \tilde{\beta}_1 + \dots + r_N \tilde{\beta}_N \quad (\text{D.12})$$

and

$$\gamma_\lambda = \alpha_{\text{remn}} + \sum_{\nu=\lambda+1}^{r_1+\dots+r_N} \tilde{\epsilon}_\nu = \begin{cases} \alpha_{\text{remn}} + (r_1 - \lambda) \tilde{\beta}_1 + r_2 \tilde{\beta}_2 + \dots + r_N \tilde{\beta}_N & \text{if } \lambda \leq r_1 \\ \alpha_{\text{remn}} + (r_1 + r_2 - \lambda) \tilde{\beta}_2 + r_3 \tilde{\beta}_3 + \dots + r_N \tilde{\beta}_N & \text{if } r_1 < \lambda \leq r_1 + r_2 \\ \dots & \\ \alpha_{\text{remn}} + (r_1 + \dots + r_N - \lambda) \tilde{\beta}_N & \text{if } \lambda > r_1 + \dots + r_{N-1} \end{cases} \quad (\text{D.13})$$

with

$$\tilde{\beta} = \beta + 1, \quad (\text{D.14})$$

$$\tilde{\epsilon} = \epsilon + 1, \quad (\text{D.15})$$

we find

$$I_{r_1, \dots, r_N}(x) = x^\alpha \int \prod_{\lambda=1}^{r_1 + \dots + r_N} du_\lambda u_\lambda^{\epsilon_\lambda} (1 - u_\lambda)^{\gamma_\lambda} \quad (\text{D.16})$$

The u -integration can be done,

$$\int_0^1 du u^\epsilon (1 - u)^\gamma = \frac{\Gamma(1 + \epsilon) \Gamma(1 + \gamma)}{\Gamma(2 + \epsilon + \gamma)}, \quad (\text{D.17})$$

and we get

$$I_{r_1, \dots, r_N}(x) = x^\alpha \prod_{\lambda=1}^{r_1 + \dots + r_N} \frac{\Gamma(1 + \epsilon_\lambda) \Gamma(1 + \gamma_\lambda)}{\Gamma(2 + \epsilon_\lambda + \gamma_\lambda)} \quad (\text{D.18})$$

Using the relation $1 + \epsilon_\lambda + \gamma_\lambda = \gamma_{\lambda-1}$, we get

$$I_{r_1, \dots, r_N}(x) = x^\alpha \Gamma(1 + \beta_1)^{r_1} \dots \Gamma(1 + \beta_N)^{r_N} \prod_{\lambda=1}^{r_1 + \dots + r_N} \frac{\Gamma(1 + \gamma_\lambda)}{\Gamma(1 + \gamma_{\lambda-1})} \quad (\text{D.19})$$

$$= x^\alpha \Gamma(1 + \beta_1)^{r_1} \dots \Gamma(1 + \beta_N)^{r_N} \frac{\Gamma(1 + \gamma_{r_1 + \dots + r_N})}{\Gamma(1 + \gamma_0)}, \quad (\text{D.20})$$

or

$$I_{r_1, \dots, r_N}(x) = x^{\alpha_{\text{remn}} + r_1 \tilde{\beta}_1 + \dots + r_N \tilde{\beta}_N} \Gamma(\tilde{\beta}_1)^{r_1} \dots \Gamma(\tilde{\beta}_N)^{r_N} \frac{\Gamma(\tilde{\alpha}_{\text{remn}})}{\Gamma(\tilde{\alpha}_{\text{remn}} + r_1 \tilde{\beta}_1 + \dots + r_N \tilde{\beta}_N)}. \quad (\text{D.21})$$

The final expression for Φ_{pp} is therefore

$$\begin{aligned} \Phi_{pp}(x^+, x^-, s, b) &= x^{\alpha_{\text{remn}}} \sum_{r_1=0}^{\infty} \dots \sum_{r_N=0}^{\infty} \left\{ \frac{\Gamma(1 + \alpha_{\text{remn}})}{\Gamma(1 + \alpha_{\text{remn}} + r_1 \tilde{\beta}_1 + \dots + r_N \tilde{\beta}_N)} \right\}^2 \\ &\times \frac{(-\alpha_1 x^{\tilde{\beta}_1} \Gamma^2(\tilde{\beta}_1))^{r_1}}{r_1!} \dots \frac{(-\alpha_N x^{\tilde{\beta}_N} \Gamma^2(\tilde{\beta}_N))^{r_N}}{r_N!} \end{aligned} \quad (\text{D.22})$$

with $x = x^+ x^-$. This is the expression shown in eq. (3.15).

D.2 Calculation of H

The function H is defined as

$$\begin{aligned} H(z^+, z^-) &= \sum_{m=1}^{\infty} \int \prod_{\mu=1}^m dx_\mu^+ dx_\mu^- \frac{1}{m!} \prod_{\mu=1}^m G(x_\mu^+, x_\mu^-, s, b) \\ &\times \delta(1 - z^+ - \sum_{\mu=1}^m x_\mu^+) \delta(1 - z^- - \sum_{\mu=1}^m x_\mu^-). \end{aligned} \quad (\text{D.23})$$

Using the expression

$$G(x_\mu^+, x_\mu^-, s, b) = \sum_{i=1}^N \alpha_i (x_\mu^+ x_\mu^-)^{\beta_i}, \quad (\text{D.24})$$

with the α_i and β_i are functions of the impact parameter b and the energy squared s ,

$$\alpha_i = (\alpha_{D_i} + \alpha_{D_i}^*) s^{\beta_{D_i} + \gamma_{D_i} b^2} e^{-\frac{b^2}{\delta_{D_i}}}, \quad (\text{D.25})$$

$$\beta_i = \beta_{D_i} + \gamma_{D_i} b^2 + \beta_{D_i}^* - \alpha_{\text{part}}, \quad (\text{D.26})$$

with $\alpha_{D_i}^* \neq 0$ and $\beta_{D_i}^* \neq 0$ only if $\alpha_{D_i} = 0$, and using the same method as for the calculation of $\Phi_{pp}(x^+, x^-)$, one may write

$$H(z^+, z^-) = \underbrace{\sum_{r_1=0}^{\infty} \dots \sum_{r_N=0}^{\infty}}_{r_1 + \dots + r_N = 0} \frac{(\alpha_1)^{r_1}}{r_1!} \dots \frac{(\alpha_N)^{r_N}}{r_N!} J_{r_1, \dots, r_N}(z^+) J_{r_1, \dots, r_N}(z^-) \quad (\text{D.27})$$

with

$$J_{r_1, \dots, r_N}(z) = \int \prod_{\lambda=1}^{r_1 + \dots + r_N} [dx_{\lambda} x_{\lambda}^{\epsilon_{\lambda}}] \delta \left(1 - z - \sum_{\lambda=1}^{r_1 + \dots + r_N} x_{\lambda} \right) \quad (\text{D.28})$$

and

$$\epsilon_{\lambda} = \begin{cases} \beta_1 & \text{for } \lambda \leq r_1 \\ \beta_2 & \text{for } r_1 < \lambda \leq r_1 + r_2 \\ \dots & \\ \beta_N & \text{for } r_1 + \dots + r_{N-1} < \lambda \leq r_1 + \dots + r_N \end{cases}. \quad (\text{D.29})$$

One may use the δ function to obtain

$$J_{r_1, \dots, r_N}(z) = \int \prod_{\lambda=2}^{r_1 + \dots + r_N} [dx_{\lambda} x_{\lambda}^{\epsilon_{\lambda}}] \left((1 - z) - \sum_{\lambda=2}^{r_1 + \dots + r_N} x_{\lambda} \right)^{\epsilon_1}. \quad (\text{D.30})$$

Introducing $\tilde{x}_{\alpha} = x_{\alpha+1}$, we define new variables,

$$\begin{cases} u_{\lambda'} &= \frac{\tilde{x}_{\lambda'}}{1 - z - \tilde{x}_1 - \dots - \tilde{x}_{\lambda'-1}} \\ du_{\lambda'} &= \frac{d\tilde{x}_{\lambda'}}{1 - z - \tilde{x}_1 - \dots - \tilde{x}_{\lambda'-1}} \end{cases}, \quad (\text{D.31})$$

which have the following property,

$$\prod_{\alpha=1}^{\lambda'-1} (1 - u_{\alpha}) = \prod_{\alpha=1}^{\lambda'-1} \frac{1 - z - \dots - \tilde{x}_{\alpha}}{1 - z - \dots - \tilde{x}_{\alpha-1}} = \frac{1 - z - \dots - \tilde{x}_{\lambda'-1}}{1 - z}, \quad (\text{D.32})$$

and therefore

$$\begin{cases} \tilde{x}_{\lambda'} &= (1 - z) u_{\lambda'} \prod_{\alpha=1}^{\lambda'-1} (1 - u_{\alpha}) \\ d\tilde{x}_{\lambda'} &= (1 - z) du_{\lambda'} \prod_{\alpha=1}^{\lambda'-1} (1 - u_{\alpha}) \end{cases}. \quad (\text{D.33})$$

This leads to

$$\begin{aligned}
J_{r,s,t}(z) &= \int \prod_{\lambda'=1}^{r_1+\dots+r_N-1} \left\{ du_{\lambda'} u_{\lambda'}^{\epsilon_{\lambda'+1}} (1-z)^{1+\epsilon_{\lambda'+1}} \prod_{\alpha=1}^{\lambda'-1} (1-u_{\alpha})^{1+\epsilon_{\lambda'+1}} \right\} \\
&\times \left[(1-z) \prod_{\lambda'=1}^{r_1+\dots+r_N-1} (1-u_{\lambda'}) \right]^{\epsilon_1}
\end{aligned} \tag{D.34}$$

Defining

$$\alpha' = \epsilon_1 + \sum_{\lambda'=1}^{r_1+\dots+r_N-1} \tilde{\epsilon}_{\lambda'+1} = r_1 \tilde{\beta}_1 + \dots + r_N \tilde{\beta}_N - 1 \tag{D.35}$$

and

$$\begin{aligned}
\gamma_{\lambda'} &= \epsilon_1 + \sum_{\nu=\lambda'+1}^{r_1+\dots+r_N-1} \tilde{\epsilon}_{\nu+1} \\
&= \begin{cases} \epsilon_1 + (r_1 - 1 - \lambda') \tilde{\beta}_1 + r_2 \tilde{\beta}_2 + \dots + r_N \tilde{\beta}_N & \text{if } \lambda' \leq r_1 - 1 \\ \epsilon_1 + (r_1 + r_2 - 1 - \lambda') \tilde{\beta}_2 + r_3 \tilde{\beta}_3 + \dots + r_N \tilde{\beta}_N & \text{if } r_1 - 1 < \lambda' \leq r_1 + r_2 - 1 \\ \dots & \\ \epsilon_1 + (r_1 + \dots + r_N - 1 - \lambda') \tilde{\beta}_N & \text{if } \lambda' > r_1 + \dots + r_{N-1} - 1 \end{cases}
\end{aligned} \tag{D.36}$$

with

$$\tilde{\beta} = \beta + 1, \tag{D.38}$$

$$\tilde{\epsilon} = \epsilon + 1, \tag{D.39}$$

we find

$$J_{r_1, \dots, r_N}(z) = (1-z)^{\alpha'} \int \prod_{\lambda'=1}^{r_1+\dots+r_N-1} du_{\lambda'} u_{\lambda'}^{\epsilon_{\lambda'+1}} (1-u_{\lambda'})^{\gamma_{\lambda'}} \tag{D.40}$$

The u -integration can be done,

$$\int_0^1 du u^{\epsilon} (1-u)^{\gamma} = \frac{\Gamma(1+\epsilon)\Gamma(1+\gamma)}{\Gamma(2+\epsilon+\gamma)} \tag{D.41}$$

and we get

$$J_{r_1, \dots, r_N}(z) = (1-z)^{\alpha'} \prod_{\lambda'=1}^{r_1+\dots+r_N-1} \frac{\Gamma(1+\epsilon_{\lambda'+1})\Gamma(1+\gamma_{\lambda'})}{\Gamma(2+\epsilon_{\lambda'+1}+\gamma_{\lambda'})} \tag{D.42}$$

Using the relation $1 + \epsilon_{\lambda'+1} + \gamma_{\lambda'} = \gamma_{\lambda'-1}$, we get, if $r_1 \neq 0$,

$$J_{r_1, \dots, r_N}(z) = (1-z)^{\alpha'} \Gamma(\tilde{\beta}_1)^{r_1-1} \Gamma(\tilde{\beta}_2)^{r_2} \dots \Gamma(\tilde{\beta}_N)^{r_N} \prod_{\lambda'=1}^{r_1+\dots+r_N-1} \frac{\Gamma(1+\gamma_{\lambda'})}{\Gamma(1+\gamma_{\lambda'-1})} \tag{D.43}$$

$$= (1-z)^{\alpha'} \Gamma(\tilde{\beta}_1)^{r_1-1} \Gamma(\tilde{\beta}_2)^{r_2} \dots \Gamma(\tilde{\beta}_N)^{r_N} \frac{\Gamma(1+\gamma_{r_1+\dots+r_N-1})}{\Gamma(1+\gamma_0)} \tag{D.44}$$

$$= (1-z)^{\alpha'} \Gamma(\tilde{\beta}_1)^{r_1-1} \Gamma(\tilde{\beta}_2)^{r_2} \dots \Gamma(\tilde{\beta}_N)^{r_N} \frac{\Gamma(\tilde{\beta}_1)}{\Gamma(r\tilde{\beta}_1 + \dots + r_N \tilde{\beta}_N)}. \tag{D.45}$$

If $r_1 = 0$ and $r_2 \neq 0$, we get

$$J_{r_1, \dots, r_N}(z) = (1-z)^{\alpha'} \Gamma(\tilde{\beta}_2)^{r_2-1} \Gamma(\tilde{\beta}_3)^{r_3} \dots \Gamma(\tilde{\beta}_N)^{r_N} \frac{\Gamma(\tilde{\beta}_2)}{\Gamma(r_2\tilde{\beta}_2 + \dots + r_N\tilde{\beta}_N)}, \quad (\text{D.46})$$

and so on, which corresponds finally to

$$J_{r_1, \dots, r_N}(z) = (1-z)^{r_1\tilde{\beta}_1 + \dots + r_N\tilde{\beta}_N - 1} \frac{\Gamma(\tilde{\beta}_1)^{r_1} \dots \Gamma(\tilde{\beta}_N)^{r_N}}{\Gamma(r_1\tilde{\beta}_1 + \dots + r_N\tilde{\beta}_N)}. \quad (\text{D.47})$$

The final expression for H is therefore

$$\begin{aligned} H(z^+, z^-) &= \underbrace{\sum_{r_1=0}^{\infty} \dots \sum_{r_N=0}^{\infty}}_{r_1 + \dots + r_N \neq 0} \frac{[(1-z^+)(1-z^-)]^{r_1\tilde{\beta}_1 + \dots + r_N\tilde{\beta}_N - 1}}{\Gamma(r_1\tilde{\beta}_1 + \dots + r_N\tilde{\beta}_N)^2} \\ &\quad \times \frac{(\alpha_1 \Gamma(\tilde{\beta}_1)^2)^{r_1}}{r_1!} \dots \frac{(\alpha_N \Gamma(\tilde{\beta}_N)^2)^{r_N}}{r_N!} \end{aligned} \quad (\text{D.48})$$

D.3 Calculation of Φ_{AB}

The expression for the virtual emissions in case of nucleus-nucleus collisions is given as

$$\begin{aligned} \Phi_{AB}(X^+, X^-, s, b) &= \sum_{l_1=0}^{\infty} \dots \sum_{l_{AB}=0}^{\infty} \int \prod_{k=1}^{AB} \left\{ \prod_{\lambda=1}^{l_k} d\tilde{x}_{k,\lambda}^+ d\tilde{x}_{k,\lambda}^- \right\} \prod_{k=1}^{AB} \left\{ \frac{1}{l_k!} \prod_{\lambda=1}^{l_k} -G(\tilde{x}_{k,\lambda}^+, \tilde{x}_{k,\lambda}^-, s, b) \right\} \\ &\quad \times \prod_{i=1}^A F_{\text{remn}} \left(x_i^+ - \sum_{\pi(k)=i} \tilde{x}_{k,\lambda}^+ \right) \prod_{j=1}^B F_{\text{remn}} \left(x_j^- - \sum_{\tau(k)=j} \tilde{x}_{k,\lambda}^- \right), \end{aligned} \quad (\text{D.49})$$

where $X^+ = \{x_1^+ \dots x_A^+\}$, $X^- = \{x_1^- \dots x_B^-\}$ and $\pi(k)$ and $\tau(k)$ represent the projectile or target nucleon linked to pair k . Using the expression

$$G(\tilde{x}_{k,\lambda}^+, \tilde{x}_{k,\lambda}^-, s, b) = \sum_{i=1}^N \underbrace{\alpha_i (\tilde{x}_{k,\lambda}^+ \tilde{x}_{k,\lambda}^-)^{\beta_i}}_{G_{i,k,\lambda}}, \quad (\text{D.50})$$

with the α_i and β_i are functions of the impact parameter b and the energy squared s ,

$$\alpha_i = (\alpha_{D_i} + \alpha_{D_i}^*) s^{\beta_{D_i} + \gamma_{D_i} b^2} e^{-\frac{b^2}{\delta_{D_i}}}, \quad (\text{D.51})$$

$$\beta_i = \beta_{D_i} + \gamma_{D_i} b^2 + \beta_{D_i}^* - \alpha_{\text{part}}, \quad (\text{D.52})$$

with $\alpha_{D_i}^* \neq 0$ and $\beta_{D_i}^* \neq 0$ only if $\alpha_{D_i} = 0$. The remnant function F_{remn} is given as

$$F_{\text{remn}}(x) = x^{\alpha_{\text{remn}}} \Theta(x) \Theta(1-x). \quad (\text{D.53})$$

We have (see calculation of Φ_{pp})

$$\dots \sum_{l_k=0}^{\infty} \dots \frac{1}{l_k!} \prod_{\lambda=1}^{l_k} -G(s, \tilde{x}_{k,\lambda}^+, \tilde{x}_{k,\lambda}^-, b) = \dots \sum_{l_k=0}^{\infty} \dots \frac{1}{l_k!} \prod_{\lambda=1}^{l_k} (-G_{1,k,\lambda} - \dots - G_{N,k,\lambda}) \quad (\text{D.54})$$

$$\begin{aligned} &= \dots \sum_{r_{1,k}=0}^{\infty} \dots \sum_{r_{N,k}=0}^{\infty} \dots \frac{1}{r_{1,k}! \dots r_{N,k}!} \\ &\quad \times \prod_{\rho_1=1}^{r_{1,k}} -G_{1,k,\rho_1} \dots \prod_{\rho_N=r_{1,k}+\dots+r_{N-1,k}+1}^{r_{1,k}+\dots+r_{N,k}} -G_{N,k,\rho_N}. \end{aligned} \quad (\text{D.55})$$

So eq. (D.49) can be written as

$$\begin{aligned} \Phi_{AB}(X^+, X^-, s, b) &= \sum_{r_{1,1} \dots r_{N,1}} \dots \sum_{r_{1,AB} \dots r_{N,AB}} \prod_{k=1}^{AB} \frac{1}{r_{1,k}! \dots r_{N,k}!} \int \prod_{k=1}^{AB} \left\{ \prod_{\lambda=1}^{r_{1,k}+\dots+r_{N,k}} d\tilde{x}_{k,\lambda}^+ d\tilde{x}_{k,\lambda}^- \right\} \\ &\quad \times \prod_{k=1}^{AB} \left\{ \prod_{\rho_1=1}^{r_{1,k}} -\alpha_1(\tilde{x}_{k,\rho_1}^+ \tilde{x}_{k,\rho_1}^-)^{\beta_1} \dots \prod_{\rho_N=r_{1,k}+\dots+r_{N-1,k}+1}^{r_{1,k}+\dots+r_{N,k}} -\alpha_N(\tilde{x}_{k,\rho_N}^+ \tilde{x}_{k,\rho_N}^-)^{\beta_N} \right\} \\ &\quad \times \prod_{i=1}^A F_{\text{remn}} \left(x_i^+ - \sum_{\pi(k)=i} \tilde{x}_{k,\lambda}^+ \right) \prod_{j=1}^B F_{\text{remn}} \left(x_j^- - \sum_{\tau(k)=j} \tilde{x}_{k,\lambda}^- \right), \end{aligned} \quad (\text{D.56})$$

which leads to

$$\begin{aligned} \Phi_{AB}(X^+, X^-, s, b) &= \sum_{r_{1,1} \dots r_{N,1}} \dots \sum_{r_{1,AB} \dots r_{N,AB}} \prod_{k=1}^{AB} \frac{(-\alpha_1)^{r_{1,k}}}{r_{1,k}!} \dots \frac{(-\alpha_N)^{r_{N,k}}}{r_{N,k}!} \\ &\quad \times I_R^+(X^+) I_R^-(X^-), \end{aligned} \quad (\text{D.57})$$

where

$$I_R^\sigma(X) = \int \prod_{k=1}^{AB} \prod_{\lambda=1}^{r_{1,k}+\dots+r_{N,k}} d\tilde{x}_{k,\lambda} (\tilde{x}_{k,\lambda})^{\epsilon_{k,\lambda}} \prod_{i=1}^{P^\sigma} F_{\text{remn}} \left(x_i - \sum_{\kappa^\sigma(k)=i} \tilde{x}_{k,\lambda} \right), \quad (\text{D.58})$$

with $R = \{r_{j,k}\}$, $P^+ = A$, $P^- = B$, $\kappa^+(k) = \pi(k)$, and $\kappa^-(k) = \tau(k)$. Using the property

$$\prod_{k=1}^{AB} = \prod_{i=1}^{P^\sigma} \prod_{\kappa^\sigma(k)=i}, \quad (\text{D.59})$$

one can write

$$\begin{aligned} I_R^\sigma(X) &= \prod_{i=1}^{P^\sigma} \left\{ \int \prod_{\kappa^\sigma(k)=i} \prod_{\lambda=1}^{r_{1,k}+\dots+r_{N,k}} d\tilde{x}_{k,\lambda} (\tilde{x}_{k,\lambda})^{\epsilon_{k,\lambda}} \right. \\ &\quad \left. \times F_{\text{remn}} \left(x_i - \sum_{\kappa^\sigma(k)=i} \tilde{x}_{k,\lambda} \right) \right\}. \end{aligned} \quad (\text{D.60})$$

Let us rename the $\tilde{x}_{k,\lambda}$ linked to the remnant i as $\tilde{x}_1, \tilde{x}_2, \dots, \tilde{x}_{r_{1,i}^\sigma + \dots + r_{N,i}^\sigma}$, where $r_{p,i}^\sigma$ is per definition the number of Pomerons of type p linked to remnant i . So we get for the term in brackets

$$\int \prod_{\nu=1}^{r_{1,i}^\sigma + \dots + r_{N,i}^\sigma} d\tilde{x}_\nu \tilde{x}_\nu^{\epsilon_\nu} F_{\text{remn}} \left(x_i - \sum_{\nu=1}^{r_{1,i}^\sigma + \dots + r_{N,i}^\sigma} \tilde{x}_\nu \right). \quad (\text{D.61})$$

This is exactly the corresponding I for proton-proton scattering. So we have

$$I_R^\sigma(X) = \prod_{i=1}^{P^\sigma} x_i^{\alpha_{\text{remn}} + r_{1,i}^\sigma \tilde{\beta}_1 + \dots + r_{N,i}^\sigma \tilde{\beta}_N} \Gamma(\tilde{\beta}_1)^{r_{1,i}^\sigma} \dots \Gamma(\tilde{\beta}_N)^{r_{N,i}^\sigma} g \left(r_{1,i}^\sigma \tilde{\beta}_1 + \dots + r_{N,i}^\sigma \tilde{\beta}_N \right), \quad (\text{D.62})$$

with

$$g(z) = \frac{\Gamma(1 + \alpha_{\text{remn}})}{\Gamma(1 + \alpha_{\text{remn}} + z)}, \quad (\text{D.63})$$

and

$$\tilde{\beta} = \beta + 1. \quad (\text{D.64})$$

Since we have

$$r_{p,i}^\sigma = \sum_{\kappa^\sigma(k)=i} r_{p,k}, \quad (\text{D.65})$$

we find finally

$$\begin{aligned} \Phi_{AB}(X^+, X^-, s, b) = & \sum_{r_{1,1} \dots r_{N,1}} \dots \sum_{r_{1,AB} \dots r_{N,AB}} \prod_{k=1}^{AB} \frac{(-\alpha_1)^{r_{1,k}}}{r_{1,k}!} \dots \frac{(-\alpha_N)^{r_{N,k}}}{r_{N,k}!} \\ & \prod_{i=1}^A (x_i^+)^{\alpha_{\text{remn}}} \prod_{\pi(k)=i} \left(\Gamma(\tilde{\beta}_1)(x_i^+)^{\tilde{\beta}_1} \right)^{r_{1,k}} \dots \left(\Gamma(\tilde{\beta}_N)(x_i^+)^{\tilde{\beta}_N} \right)^{r_{N,k}} g \left(\sum_{\pi(k)=i} r_{1,k} \tilde{\beta}_1 + \dots + r_{N,k} \tilde{\beta}_N \right) \\ & \prod_{j=1}^B (x_j^-)^{\alpha_{\text{remn}}} \prod_{\tau(k)=j} \left(\Gamma(\tilde{\beta}_1)(x_j^-)^{\tilde{\beta}_1} \right)^{r_{1,k}} \dots \left(\Gamma(\tilde{\beta}_N)(x_j^-)^{\tilde{\beta}_N} \right)^{r_{N,k}} g \left(\sum_{\tau(k)=j} r_{1,k} \tilde{\beta}_1 + \dots + r_{N,k} \tilde{\beta}_N \right) \end{aligned} \quad (\text{D.66})$$

D.4 Exponentiation of Φ_{AB}

We first replace in eq. (D.66) the function $g(z)$ by the “exponentiated” function $g_e(z)$,

$$\begin{aligned} g_e \left(\sum_{\kappa^\sigma(k)=i} r_{1,k} \tilde{\beta}_1 + \dots + r_{N,k} \tilde{\beta}_N \right) &= \exp \left\{ -\epsilon_e \left(\sum_{\kappa^\sigma(k)=i} r_{1,k} \tilde{\beta}_1 + \dots + r_{N,k} \tilde{\beta}_N \right) \right\} \\ &= \prod_{\kappa^\sigma(k)=i} \left(e^{-\epsilon_e \tilde{\beta}_1} \right)^{r_{1,k}} \dots \left(e^{-\epsilon_e \tilde{\beta}_N} \right)^{r_{N,k}}, \end{aligned} \quad (\text{D.67})$$

and we obtain

$$\begin{aligned}
\Phi_{eAB}(X^+, X^-, s, b) = & \prod_{i=1}^A (x_i^+)^{\alpha_{\text{remn}}} \prod_{j=1}^B (x_j^-)^{\alpha_{\text{remn}}} \\
& \sum_{\substack{r_{1,1} \dots r_{1,AB} \\ \dots}} \prod_{k=1}^{AB} \frac{(-\alpha_1)^{r_{1,k}}}{r_{1,k}!} \left\{ \prod_{i=1}^A \prod_{\pi(k)=i} \left(D_1 (x_i^+)^{\tilde{\beta}_1} \right)^{r_{1,k}} \prod_{j=1}^B \prod_{\tau(k)=j} \left(D_1 (x_j^-)^{\tilde{\beta}_1} \right)^{r_{1,k}} \right\} \\
& \sum_{r_{N,1} \dots r_{N,AB}} \prod_{k=1}^{AB} \frac{(-\alpha_N)^{r_{N,k}}}{r_{N,k}!} \left\{ \prod_{i=1}^A \prod_{\pi(k)=i} \left(D_N (x_i^+)^{\tilde{\beta}_N} \right)^{r_{N,k}} \prod_{j=1}^B \prod_{\tau(k)=j} \left(D_N (x_j^-)^{\tilde{\beta}_N} \right)^{r_{N,k}} \right\}
\end{aligned} \tag{D.68}$$

with

$$D_j = \Gamma(\tilde{\beta}_j) e^{-\epsilon_e \tilde{\beta}_j}. \tag{D.69}$$

And using again the property (D.59), we can write

$$\begin{aligned}
\Phi_{eAB}(X^+, X^-, s, b) = & \prod_{i=1}^A (x_i^+)^{\alpha_{\text{remn}}} \prod_{j=1}^B (x_j^-)^{\alpha_{\text{remn}}} \\
& \times \sum_{r_{1,1} \dots r_{1,AB}} \prod_{k=1}^{AB} \frac{\left(-\alpha_1 D_1^2 (x_{\pi(k)}^+ x_{\tau(k)}^-)^{\tilde{\beta}_1} \right)^{r_{1,k}}}{r_{1,k}!} \\
& \times \dots \\
& \times \sum_{r_{N,1} \dots r_{N,AB}} \prod_{k=1}^{AB} \frac{\left(-\alpha_N D_N^2 (x_{\pi(k)}^+ x_{\tau(k)}^-)^{\tilde{\beta}_N} \right)^{r_{N,k}}}{r_{N,k}!}.
\end{aligned} \tag{D.70}$$

Now the sum can be performed and we get the final expression for the “exponentiated” Φ ,

$$\Phi_{eAB}(X^+, X^-, s, b) = \prod_{i=1}^A (x_i^+)^{\alpha_{\text{remn}}} \prod_{j=1}^B (x_j^-)^{\alpha_{\text{remn}}} \prod_{k=1}^{AB} e^{-\tilde{G}(x_{\pi(k)}^+ x_{\tau(k)}^-)},$$

with

$$\tilde{G}(x) = \sum_{i=1}^N \tilde{\alpha}_i x^{\tilde{\beta}_i}, \tag{D.71}$$

where

$$\tilde{\alpha}_i = \alpha_i \Gamma(\tilde{\beta}_i)^2 e^{-2\epsilon_e \tilde{\beta}_i}, \tag{D.72}$$

$$\tilde{\beta}_i = \beta_i + 1, \tag{D.73}$$

and

$$\alpha_i = (\alpha_{D_i} + \alpha_{D_i}^*) s^{\beta_{D_i} + \gamma_{D_i} b^2} e^{-\frac{b^2}{\delta_{D_i}}}, \tag{D.74}$$

$$\beta_i = \beta_{D_i} + \gamma_{D_i} b^2 + \beta_{D_i}^* - \alpha_{\text{part}}, \tag{D.75}$$

with $\alpha_{D_i}^* \neq 0$ and $\beta_{D_i}^* \neq 0$ only if $\alpha_{D_i} = 0$.

Bibliography

- [1] K. Werner, Phys. Rep. **232**, 87 (1993).
- [2] L. McLerran and R. Venugopalan, Phys. Rev. **D49**, 2233; 3352 (1994), hep-ph/9311205.
- [3] V. Gribov, Sov. Phys. JETP **26**, 414 (1968).
- [4] M. Braun, Yad. Fiz. (Rus) **52**, 257 (1990).
- [5] V. A. Abramovskii and G. G. Leptoukh, Sov.J.Nucl.Phys. **55**, 903 (1992).
- [6] T. Sjostrand and M. van Zijl, Phys. Rev. **D36**, 2019 (1987).
- [7] D. Amati, A. Stanghellini, and S. Fubini, Nuovo Cim. **26**, 896 (1962).
- [8] G. Altarelli, Phys. Rep. **81**, 1 (1982).
- [9] E. Reya, Phys. Rep. **69**, 195 (1981).
- [10] G. Altarelli and G. Parisi, Nucl. Phys. **B126**, 298 (1977).
- [11] L. N. Lipatov, Sov. Phys. JETP **63**, 904 (1986).
- [12] M. G. Ryskin and Y. M. Shabelski, Yad. Fiz. (Rus.) **55**, 2149 (1992).
- [13] A. Donnachie and P. Landshoff, Phys. Lett. B **332**, 433 (1994).
- [14] M. Baker and K. A. Ter-Martirosyan, Phys. Rep. **28**, 1 (1976).
- [15] V. Abramovskii, V. Gribov, and O. Kancheli, Sov.J.Nucl.Phys. **18**, 308 (1974).
- [16] R. J. Glauber, *in Lectures on theoretical physics* (N.Y.: Inter-science Publishers, 1959).
- [17] V. Gribov, Sov. Phys. JETP **29**, 483 (1969).
- [18] P. Murthy et al., Nucl. Phys. **B92**, 269 (1975).
- [19] A. B. Kaidalov, L. A. Ponomarev, and K. A. Ter-Martirosian, Sov.J.Nucl.Phys **44**, 468 (1986).
- [20] A. Capella, U. Sukhatme, C.-I. Tan, and J. T. T. Van, Phys. Rept. **236**, 225 (1994).
- [21] A. B. Kaidalov and K. A. Ter-Martirosyan, Phys. Lett. **117B**, 247 (1982).
- [22] M. Hladik, *Nouvelle approche pour la diffusion multiple dans les interactions noyau-noyau aux énergies ultra-relativistes*, PhD thesis, Université de Nantes, 1998.
- [23] A. Capella, J. Kaplan, and J. T. T. Van, Nucl. Phys. **B105**, 333 (1976).
- [24] L. V. Gribov, E. M. Levin, and M. G. Ryskin, Phys.Rep. **100**, 1 (1983).

- [25] A. H. Mueller and J. Qui, Nucl. Phys. **B268**, 427 (1986).
- [26] J. F. Owens, Rev. Mod. Phys. **59**, 465 (1987).
- [27] T. Sjostrand, Nucl. Phys. **B248**, 469 (1984).
- [28] Y. L. Dokshitzer, V. A. Khoze, A. H. Mueller, and S. I. Troian, Gif-sur-Yvette, France: Ed. Frontieres (1991) 274 p. (Basics of).
- [29] R. K. Ellis, W. J. Stirling, and B. R. Webber, *OCD and Collider Physics* (Cambridge University Press, 1996).
- [30] M. Bengtsson and T. Sjostrand, Phys. Lett. **B185**, 435 (1987).
- [31] B. Andersson, G. Gustafson, G. Ingelman, and T. Sjostrand, Phys. Rep. **97**, 31 (1983).
- [32] D. A. Morris, Nuc. Phys. **B288**, 717 (1987).
- [33] D. A. Morris, *The relativistic string in the CALTECH-II model of hadronization and electron - positron annihilation*, PhD thesis, California Institute of Technology, Pasadena, CA, USA, 1990.
- [34] H. Drescher, *Les processus durs et la fragmentation dans un modèle unifié pour les interactions aux énergies ultra-relativistes*, PhD thesis, Université de Nantes, 1999.
- [35] X. Atru and G. Menessier, Nucl. Phys. **B70**, 93 (1974).
- [36] TASSO, M. Althoff *et al.*, Z. Phys. **C22**, 307 (1984).
- [37] DELPHI, P. Abreu *et al.*, Z. Phys. **C73**, 11 (1996).
- [38] OPAL, G. Alexander *et al.*, Z. Phys. **C72**, 191 (1996).
- [39] S. L. Wu, Phys. Rep. **107**, 59 (1984).
- [40] TPC/Two Gamma, H. Aihara *et al.*, Phys. Rev. Lett. **52**, 577 (1984).
- [41] S. Klein *et al.*, Phys. Rev. Lett. **58**, 644 (1987).
- [42] JADE, W. Bartel *et al.*, Z. Phys. **C33**, 23 (1986).
- [43] S. Catani, Y. L. Dokshitzer, M. Olsson, G. Turnock, and B. R. Webber, Phys. Lett. **B269**, 432 (1991).
- [44] A. H. Mueller, Phys. Rep. **73**, 237 (1981).
- [45] M. Gluck, E. Reya, and M. Stratmann, Nucl. Phys. **B422**, 37 (1994).
- [46] B. Potter, Eur. Phys. J. direct **C5**, 1 (1999), hep-ph/9707319.
- [47] M. Gluck, E. Reya, and A. Vogt, Z. Phys. **C67**, 433 (1995).
- [48] M. Gluck, E. Reya, and I. Schienbein, Phys. Rev. **D60**, 054019 (1999), hep-ph/9903337.
- [49] M. Gluck, E. Reya, and M. Stratmann, Eur. Phys. J. **C2**, 159 (1998), hep-ph/9711369.
- [50] A. Rostovtsev, M. G. Ryskin, and R. Engel, Phys. Rev. **D59**, 014021 (1999), hep-ph/9807268.
- [51] H1 Collaboration, Aid *et al.*, preprint DESY 96-039 (1996).
- [52] ZEUS, M. Derrick *et al.*, Z. Phys. **C72**, 399 (1996), hep-ex/9607002.

- [53] NMC Collaboration, Arneodo et al., Phys. Lett. **364B**, 107 (1995).
- [54] H1 Collaboration, Abt et al., Z. Phys. **C63**, 377 (1994).
- [55] H1 Collaboration, Adloff et al., Nucl. Phys. **B485**, 3 (1996).
- [56] G. Giacomelli and M. Jacob, Phys. Rep. **55**, 1 (1979).
- [57] K. Werner, H. Drescher, E. Furler, M. Hladik, and S. Ostapchenko, Semihard processes in nuclear collisions, in *Proc. of the "3rd International Conference on Physics and Astrophysics of Quark-Gluon Plasma", Jaipur, India, March 17-21, 1997*, 1997.
- [58] B. R. Webber, Nucl. Phys. **B238**, 492 (1984).
- [59] A. B. Kaidalov and K. A. Ter-Martirosian, Sov. J. Nucl. Phys. **39**, 979 (1984).
- [60] K. G. Boreskov, A. B. Kaidalov, S. M. Kiselev, and N. Y. Smorodinskaya, Sov. J. Nucl. Phys. **53**, 356 (1991).